Design of Novel Antigens and Immunogens to Improve Influenza Vaccines

Daniel Reed Ellis

A dissertation

submitted in partial fulfillment of the

Requirements for the degree of

Doctor of Philosophy

University of Washington

2021

Reading Committee:

Neil P. King, Chair

David Baker

Andrew T. McGuire

Program Authorized to Offer Degree:

Molecular and Cellular Biology

@Copyright 2021

Daniel R Ellis

University of Washington

Abstract

Design of Novel Antigens and Immunogens to Improve Influenza Vaccines

Daniel Reed Ellis

Chair of the supervisory committee:

Neil P. King

Department of Biochemistry

The ability to design complex oligomeric proteins has recently been broadly expanded, leading to the design of smaller oligomeric structures to much larger self-assembling protein nanoparticles of similar sizes to viruses, with such advances having extensive applications in vaccinology. Here, I present both the translation of designed protein nanoparticles for vaccine development and the use of Rosetta modeling to redesign viral antigens to favor desirable oligomeric or conformational states. The described work most heavily focuses on applications towards influenza vaccines, including the use of particulate display of hemagglutinin (HA) to simultaneously target its head and stem domains, the conformational stabilization of neuraminidase (NA), and the tailored particulate display of the HA head domain in distinct conformational states and/or geometric spacings to alter its immunogenicity. Additional stories are presented involving SARS-CoV-2 and human papillomavirus (HPV), which, respectively, explore stabilization of the SARS-CoV-2 receptor binding domain (RBD) and the presentation of linear peptide HPV epitopes on different designed nanoparticles in diverse arrangements and valencies.

Thanks

For funding, I would like to thank the Open Philanthropy Project, the Bill and Melinda Gates Foundation, the Seattle Structural Genomics Center for Infectious Disease, and the National Institutes of Health for a multitude of grants, gifts, and other support that allowed this research to happen.

I would like to largely thank Seyhan Boyoglu-Barnum and Julia Lederhofer, both of whom made massive contributions to the work shown here and hugely share responsibility for its success. As well, I thank Masaru Kanekiyo for similarly massive contributions, leadership and extensive mentorship. Further, I would like to thank Masaru Kanekiyo and Barney S. Graham for hosting a research visit to the Vaccine Research Center and the National Institutes of Health, which was vital for accelerating this work. I would also like to thank so many others at the Vaccine Research Center who have contributed to this work.

I would like to thank all members of the King Lab, both past and present, for all their support, help and friendship for so many years. As well, I would like to thank everyone in the core facilities at the Institute for Protein Design, most particularly Brooke Fiala, Lauren Carter, Rashmi Ravichandran, Michael Murphy and Deleah Pettie, for providing intensive support that is a backbone for so much of this work. Similarly, I would like to thank Lance Stewart and Ratika Krishnamurty for their hard work at maintaining funding for this work. I would like to thank Young-Jun Park, Oliver Acton and David Veesler for their extensive contributions to structural work that has been absolutely vital for these projects. Importantly, I would like to thank Neil P. King for so much time and support that was key for my growth as a scientist, and for always being patiently open to crazy ideas that might not really make a lot of sense but are still interesting to think about.

I would like to thank my parents, Sue and Tom, my sister, Kerri, and my grandparents John and Doris, whose support has been so important in achieving all described here. I would like to thank Rose McCarty for helping with proofreading this thesis. I would like to thank my housemate Hadley Scherer for support, and my dog, Oliver, who has no idea that he helped with this. Finally and most importantly, I would like to thank my wife, Catie, who has always been there to support me and cheer me on when I need it, and let me know it is OK to step away and take breaks to enjoy the moment when things get too stressful.

Table of Contents

Preface

Vaccinology has strongly grown since the 19th century as a “black box” science, with small advances providing massive medical progress (Plotkin 2014). Live-attenuated and inactivated vaccines have greatly reduced the burden of infectious diseases on the world, as best exemplified by the elimination of smallpox and the extreme diminishment of polio. However, many diseases were not surmountable by early vaccinology attempts. An understanding of how human immunodeficiency virus (HIV) eludes effective humoral responses was previously lacking (Francis and Petricciani 1985). Inactivated vaccines against respiratory syncytial virus (RSV) detrimentally failed (Ruckwardt, Morabito, and Graham 2019). Influenza could be fought by targeting narrow selections of viruses with inactivated vaccines, but not by targeting the family as a whole to prevent unexpected seasonal strains or pandemics (Wei et al. 2020).

Advances in recombinant vaccine technologies, virological and immunological understandings, and structural biology of antigen-antibody complexes have provided possible answers for these and other outstanding challenges in infectious disease prevention (Kanekiyo, Ellis, and King 2019). While the development of an effective HIV vaccine still appears highly challenging, the characterization of diverse broadly neutralizing antibodies (bNAbs) has provided detailed inspiration and blueprints for vaccination strategies (Klasse et al. 2020; Ward and Wilson 2017). Structural understandings of the metastability of the RSV F glycoprotein have shown why early vaccines failed and how to stabilize RSV F in the correct prefusion conformation (Ruckwardt, Morabito, and Graham 2019; McLellan et al. 2013). This progress will likely lead to the first highly effective RSV vaccines, and has further inspired vaccine design for other paramyxoviruses (Stewart-Jones et al. 2018), pneumoviruses (Battles et al. 2017) and coronaviruses (Hsieh et al. 2020; Pallesen et al. 2017). Numerous broadly protective antibodies have been characterized against distinct epitopes on multiple glycoproteins of influenza viruses (Wu and Wilson 2020). Further, there is a greater understanding of how hypervariability, immunodominance, and pre-existing immunity can complicate the induction of such antibodies (Knight et al. 2020). Protein subunit vaccines appear particularly promising in this growing age of structure-based vaccine design given their recombinant customizability and proven scalability (Kanekiyo, Ellis, and King 2019). Despite subunit vaccines providing improved precision in vaccine design strategies, this class of vaccines is often considered inherently less immunogenic than live-attenuated and inactivated vaccines. Strategies to generally transcend this issue are needed, with particulate display of antigens (Irvine and Read 2020) and/or coformulation with adjuvants (Kwissa, Kasturi, and Pulendran 2007) often investigated.

Attempts to improve the breadth or effectiveness of influenza vaccines have been particularly interesting given how many diverse strategies appear useful for providing progress (Kanekiyo, Ellis, and King 2019; Rockman et al. 2020). Modifications have been made to the HA protein to subvert issues caused by hypervariability and immunodominance, most notably through removing or obscuring the HA head domain to direct responses towards more conserved regions, such as the HA stem domain (Yassine et al. 2015; Impagliazzo et al. 2015; Nachbagauer et al. 2020), HA receptor binding site (Bajic et al. 2020), HA head interface (Bajic et al. 2019) and/or neuraminidase (NA) antigen (Zheng et al. 2020; Broecker et al. 2019). Further, the use of naturally existing self-assembling protein nanoparticles to multivalently

display HA-based subunit antigens has been particularly influential for improving the potency of protein-based vaccines (Kanekiyo et al. 2013; Yassine et al. 2015; Kanekiyo et al. 2019).

Irrespective to progress in vaccinology, large advancements have been made in the last two decades in computational protein design in terms of computing power, algorithms, and conceptual strategies (Leman et al. 2020; Huang, Boyken, and Baker 2016). It is now possible to design proteins of diverse folds and complex secondary structure arrangements completely *de novo* (Rocklin et al. 2017; Dou et al. 2018; Marcos et al. 2018). The capability to design novel protein-protein interfaces has provided access to a massive possible space of self-assembling protein oligomers (Gonen et al. 2015; Fallas et al. 2017; Boyken et al. 2016; Chen et al. 2019; Shen et al. 2018). This space contains a universe of possible cubic nanoparticle structures with tetrahedral, octahedral, or icosahedral symmetry, which can generally resemble smaller viral capsids (King et al. 2012; King et al. 2014; Hsia et al. 2016; Bale et al. 2016; Divine et al. 2020). In contrast to viral capsids or naturally existing protein nanoparticles, designed nanoparticle structures can be constructed with highly customized features including controlled pore sizes, precisely placed genetic termini, and integration of multiple distinct protein components (Ueda et al. 2020). This tailorability has allowed these novel nanoparticles to be used for vaccine design through the multivalent display of subunit antigens, with early studies demonstrating enhanced immunogenicity of displayed antigens, similar to natural protein nanoparticles, while providing many more ways to design and produce immunogens (Bruun et al. 2018; Marcandalli et al. 2019; Brouwer et al. 2019; Antanasijevic et al. 2020; Walls et al. 2020). Therefore, there is ample room both to use novel designed protein nanoparticles to immediately develop vaccines and to further explore how finer structural details of multivalent antigen display can correlate with desirable immunogenicities.

The work described in this thesis provides advancements at the intersection of structure-based vaccinology and computational protein design, which most directly contributes to the development of novel influenza vaccines as well as nanoparticle-based vaccinology in general. In one project, I helped design and produced nanoparticle immunogens that displayed the same quadrivalent set of HA antigens used in current commercial vaccines. In multiple animal models, the designed particles were found to elicit antibody responses that potently targeted the head domain similarly or superiorly to current commercial vaccines. Most importantly, the designed nanoparticle vaccines were found to elicit significantly higher antibody responses against the HA stem domain than commercial vaccines, which were found to broadly protect against diverse heterologous influenza viruses. One of the designed particles is currently set to enter a phase I clinical trial in the spring of 2021, which will be sponsored by the National Institutes of Health (NIH). I also assisted in the technology transfer process and helped consult with the NIH regarding the manufacturing of this vaccine.

A second project focused on improving the immunogenicity of the HA head domain in the context of nanoparticle-based vaccines, which provided two distinct novel methods of modulating responses against the head. The head domain was genetically fused to a designed nanoparticle, with the genetic fusion mediated by a separate modularly extendable domain that is rigidly attached to the nanoparticle surface. As well, designed interactions could be introduced between the HA heads and the extension domain to rigidly hold the head in its native-like closed trimeric state. By altering the length of the extension domain and whether heads were stabilized in the closed state, the head domain immunogenicity could be altered to impact both humoral

breadth and neutralizing potency. Between these results and the surprising stem-directed results shown in the previously-mentioned project, one takeaway of my thesis work is that the precise geometric details of how antigens are displayed on particulate surfaces has the potential to prioritize focus on distinct epitopes and to generally alter the quality of elicited antibody responses.

A third influenza-based project focused on the structure and stability of the tetrameric influenza NA antigen, which is not functionally represented in current vaccines due to inadequacies in both the stability of the antigen and regulations on how much is included in vaccines. Our collaborators showed that different commonly-used recombinant NAs experience conformational heterogeneity, with many NAs forming a previously unreported “open” state while others form the classically observed “closed” tetrameric structure. Based on this analysis, I developed a homology-directed design strategy using Rosetta to transfer stabilizing substitutions from more stable NA strains into less stable strains, which successfully showed conformational stabilization of the closed state by strengthening the interface between NA protomers. Stabilized NAs showed greatly improved thermal stabilities and affinities to protective antibodies, suggesting that these designed antigens could be useful starting points for greater studies of NA’s antigenicity and immunogenicity.

Outside of influenza, two other projects are described here that relate to the study and development of nanoparticle vaccines. One involves the first study of our designed protein nanoparticles as immunogens, which involved the display of a model peptide antigen from human papillomavirus on a set of nanoparticles to alter the geometries and valencies in which the antigen was displayed. This study showed that increased valency and nanoparticle size were generally correlated with improved immunogenicity of the peptide antigen. The other project involved stabilization of the SARS-CoV-2 receptor binding domain (RBD) and characterization of the effects of this stabilization on immunogens containing the RBD, both for manufacturability and immunogenicity. The stabilizing mutations to the RBD were found to not impact immunogenicity of the RBD, however thermal and solution stability was notably improved, particularly when the RBD was displayed on nanoparticles.

Beyond the described work, my research has involved multiple additional projects that will not be described here in detail. Most importantly, I led early efforts to refine the process of *in vitro* assembly for diverse two-component nanoparticles that are now widely used for preclinical studies and will soon be tested in clinical trials. In studying these nanoparticles, it became apparent that many of the components alone, most often the pentameric components, were poorly stable and/or not producible in workable yields. To fix this, I designed stabilizing mutations to improve expression yields and protein solubility, and in some cases remove reactive unpaired cysteines, which was largely inspired by homology-based comparisons with related proteins of the same pentameric fold. The improved workability of these proteins has widened the bottleneck of possible preclinical immunogenicity studies while enabling the scalable manufacturing of two nanoparticles, I53-50 (Bale et al. 2016) and I53_dn5 (Ueda et al. 2020), for clinical studies involving RSV (Marcandalli et al. 2019), SARS-CoV-2 (Walls et al. 2020), and influenza. Further, insights obtained in refining protocols for *in vitro* assembly seeded detailed studies of the cooperativity of two-component protein nanoparticles and the encapsulation of macromolecules (Bale et al. 2016). To further describe projects not discussed in this thesis, I also explored many additional combinations of influenza HA antigens displayed

on nanoparticles, including the display of HAs from viruses that represent possible pandemic threats and designed stem-only antigens. I also helped design multiple nanoparticle immunogens that display spike proteins from diverse coronaviruses to help support early research into broadly-reactive vaccines against coronaviruses, both before and during the COVID-19 pandemic. As well, I developed preliminary protein-protein interface design protocols for building interfaces between repetitive protein structures using minimal orthogonal and isosteric contacts, which could allow for simplified methods of encoding highly-specific oligomeric interactions.

This work has only been possible because of the highly collaborative environment at the Institute for Protein Design and connections to other laboratories at the University of Washington, NIH Vaccine Research Center, and Fred Hutchinson Cancer Research Center. Maintaining productive collaborations involves a massive amount of time, energy, and investment in communication, and the projects described here all progressed fruitfully because those involved recognized this. Given that the field of vaccinology requires such diverse specializations, the progress of this field will be directly connected with the successful implementation of interdisciplinary collaborations.

References

Antanasijevic, Aleksandar, George Ueda, Philip J. M. Brouwer, Jeffrey Copps, Deli Huang, Joel D. Allen, Christopher A. Cottrell, et al. 2020. “Structural and Functional Evaluation of de Novo-Designed, Two-Component Nanoparticle Carriers for HIV Env Trimer Immunogens.” *PLoS Pathogens* 16 (8): e1008665.

Bajic, Goran, Max J. Maron, Yu Adachi, Taishi Onodera, Kevin R. McCarthy, Charles E. McGee, Gregory D. Sempowski, et al. 2019. “Influenza Antigen Engineering Focuses Immune Responses to a Subdominant but Broadly Protective Viral Epitope.” *Cell Host & Microbe* 25 (6): 827–35.e6.

Bajic, Goran, Max J. Maron, Timothy M. Caradonna, Ming Tian, Adam Mermelstein, Daniela Fera, Garnett Kelsoe, Masayuki Kuraoka, and Aaron G. Schmidt. 2020. “Structure-Guided Molecular Grafting of a Complex Broadly Neutralizing Viral Epitope.” *ACS Infectious Diseases* 6 (5): 1182–91.

Bale, Jacob B., Shane Gonen, Yuxi Liu, William Sheffler, Daniel Ellis, Chantz Thomas, Duilio Cascio, et al. 2016. “Accurate Design of Megadalton-Scale Two-Component Icosahedral Protein Complexes.” *Science* 353 (6297): 389–94.

Battles, Michael B., Vicente Más, Eduardo Olmedillas, Olga Cano, Mónica Vázquez, Laura Rodríguez, José A. Melero, and Jason S. McLellan. 2017. “Structure and Immunogenicity of Pre-Fusion-Stabilized Human Metapneumovirus F Glycoprotein.” *Nature Communications* 8 (1): 1528.

Boyken, Scott E., Zibo Chen, Benjamin Groves, Robert A. Langan, Gustav Oberdorfer, Alex Ford, Jason M. Gilmore, et al. 2016. “De Novo Design of Protein Homo-Oligomers with Modular Hydrogen-Bond Network-Mediated Specificity.” *Science* 352 (6286): 680–87.

Broecker, Felix, Allen Zheng, Nungruthai Suntronwong, Weina Sun, Mark J. Bailey, Florian Krammer, and Peter Palese. 2019. “Extending the Stalk Enhances Immunogenicity of the Influenza Virus Neuraminidase.” *Journal of Virology* 93 (18). https://doi.org/10.1128/JVI.00840-19.

Brouwer, Philip J. M., Aleksandar Antanasijevic, Zachary Berndsen, Anila Yasmeen, Brooke Fiala, Tom P. L. Bijl, Ilja Bontjer, et al. 2019. “Enhancing and Shaping the Immunogenicity of Native-like HIV-1 Envelope Trimers with a Two-Component Protein Nanoparticle.” *Nature Communications* 10 (1): 4272.

Bruun, Theodora U. J., Anne-Marie C. Andersson, Simon J. Draper, and Mark Howarth. 2018. “Engineering a Rugged Nanoscaffold To Enhance Plug-and-Display Vaccination.” *ACS Nano* 12 (9): 8855–66.

Chen, Zibo, Scott E. Boyken, Mengxuan Jia, Florian Busch, David Flores-Solis, Matthew J. Bick, Peilong Lu, et al. 2019. “Programmable Design of Orthogonal Protein Heterodimers.” *Nature* 565 (7737):

106–11.
Divine, Robby, Ha V. Dang, George Ueda, Jorge A. Fallas, Ivan Vulovic, William Sheffler, Shally Saini, et al. 2020. “Designed Proteins Assemble Antibodies into Modular Nanocages.” *bioRxiv : The Preprint Server for Biology*, December. https://doi.org/10.1101/2020.12.01.406611.
Dou, Jiayi, Anastassia A. Vorobieva, William Sheffler, Lindsey A. Doyle, Hahnbeom Park, Matthew J. Bick, Binchen Mao, et al. 2018. “De Novo Design of a Fluorescence-Activating β-Barrel.” *Nature* 561 (7724): 485–91.
Fallas, Jorge A., George Ueda, William Sheffler, Vanessa Nguyen, Dan E. McNamara, Banumathi Sankaran, Jose Henrique Pereira, et al. 2017. “Computational Design of Self-Assembling Cyclic Protein Homo-Oligomers.” *Nature Chemistry* 9 (4): 353–60.
Francis, D. P., and J. C. Petricciani. 1985. “The Prospects for and Pathways toward a Vaccine for AIDS.” *The New England Journal of Medicine* 313 (25): 1586–90.
Gonen, Shane, Frank DiMaio, Tamir Gonen, and David Baker. 2015. “Design of Ordered Two-Dimensional Arrays Mediated by Noncovalent Protein-Protein Interfaces.” *Science* 348 (6241): 1365–68.
Hsia, Yang, Jacob B. Bale, Shane Gonen, Dan Shi, William Sheffler, Kimberly K. Fong, Una Nattermann, et al. 2016. “Design of a Hyperstable 60-Subunit Protein Dodecahedron. [corrected].” *Nature* 535 (7610): 136–39.
Hsieh, Ching-Lin, Jory A. Goldsmith, Jeffrey M. Schaub, Andrea M. DiVenere, Hung-Che Kuo, Kamyab Javanmardi, Kevin C. Le, et al. 2020. “Structure-Based Design of Prefusion-Stabilized SARS-CoV-2 Spikes.” *Science* 369 (6510): 1501–5.
Huang, Po-Ssu, Scott E. Boyken, and David Baker. 2016. “The Coming of Age of de Novo Protein Design.” *Nature* 537 (7620): 320–27.
Impagliazzo, Antonietta, Fin Milder, Harmjan Kuipers, Michelle V. Wagner, Xueyong Zhu, Ryan M. B. Hoffman, Ruud van Meersbergen, et al. 2015. “A Stable Trimeric Influenza Hemagglutinin Stem as a Broadly Protective Immunogen.” *Science* 349 (6254): 1301–6.
Irvine, Darrell J., and Benjamin J. Read. 2020. “Shaping Humoral Immunity to Vaccines through Antigen-Displaying Nanoparticles.” *Current Opinion in Immunology* 65 (August): 1–6.
Kanekiyo, Masaru, Daniel Ellis, and Neil P. King. 2019. “New Vaccine Design and Delivery Technologies.” *The Journal of Infectious Diseases* 219 (Suppl_1): S88–96.
Kanekiyo, Masaru, M. Gordon Joyce, Rebecca A. Gillespie, John R. Gallagher, Sarah F. Andrews, Hadi M. Yassine, Adam K. Wheatley, et al. 2019. “Mosaic Nanoparticle Display of Diverse Influenza Virus Hemagglutinins Elicits Broad B Cell Responses.” *Nature Immunology* 20 (3): 362–72.
Kanekiyo, Masaru, Chih-Jen Wei, Hadi M. Yassine, Patrick M. McTamney, Jeffrey C. Boyington, James R. R. Whittle, Srinivas S. Rao, Wing-Pui Kong, Lingshu Wang, and Gary J. Nabel. 2013. “Self-Assembling Influenza Nanoparticle Vaccines Elicit Broadly Neutralizing H1N1 Antibodies.” *Nature* 499 (7456): 102–6.
King, Neil P., Jacob B. Bale, William Sheffler, Dan E. McNamara, Shane Gonen, Tamir Gonen, Todd O. Yeates, and David Baker. 2014. “Accurate Design of Co-Assembling Multi-Component Protein Nanomaterials.” *Nature* 510 (7503): 103–8.
King, Neil P., William Sheffler, Michael R. Sawaya, Breanna S. Vollmar, John P. Sumida, Ingemar André, Tamir Gonen, Todd O. Yeates, and David Baker. 2012. “Computational Design of Self-Assembling Protein Nanomaterials with Atomic Level Accuracy.” *Science* 336 (6085): 1171–74.
Klasse, P. J., Gabriel Ozorowski, Rogier W. Sanders, and John P. Moore. 2020. “Env Exceptionalism: Why Are HIV-1 Env Glycoproteins Atypical Immunogens?” *Cell Host & Microbe* 27 (4): 507–18.
Knight, Matthew, Siriruk Changrob, Lei Li, and Patrick C. Wilson. 2020. “Imprinting, Immunodominance, and Other Impediments to Generating Broad Influenza Immunity.” *Immunological Reviews* 296 (1): 191–204.
Kwissa, Marcin, Sudhir Pai Kasturi, and Bali Pulendran. 2007. “The Science of Adjuvants.” *Expert Review of Vaccines* 6 (5): 673–84.
Leman, Julia Koehler, Brian D. Weitzner, Steven M. Lewis, Jared Adolf-Bryfogle, Nawsad Alam, Rebecca F. Alford, Melanie Aprahamian, et al. 2020. “Macromolecular Modeling and Design in Rosetta: Recent Methods and Frameworks.” *Nature Methods* 17 (7): 665–80.
Marcandalli, Jessica, Brooke Fiala, Sebastian Ols, Michela Perotti, Willem de van der Schueren, Joost Snijder, Edgar Hodge, et al. 2019. “Induction of Potent Neutralizing Antibody Responses by a Designed Protein Nanoparticle Vaccine for Respiratory Syncytial Virus.” *Cell* 176 (6): 1420–31.e17.

Marcos, Enrique, Tamuka M. Chidyausiku, Andrew C. McShan, Thomas Evangelidis, Santrupti Nerli, Lauren Carter, Lucas G. Nivón, et al. 2018. “De Novo Design of a Non-Local β-Sheet Protein with High Stability and Accuracy.” *Nature Structural & Molecular Biology* 25 (11): 1028–34.

McLellan, Jason S., Man Chen, M. Gordon Joyce, Mallika Sastry, Guillaume B. E. Stewart-Jones, Yongping Yang, Baoshan Zhang, et al. 2013. “Structure-Based Design of a Fusion Glycoprotein Vaccine for Respiratory Syncytial Virus.” *Science* 342 (6158): 592–98.

Nachbagauer, Raffael, Jodi Feser, Abdollah Naficy, David I. Bernstein, Jeffrey Guptill, Emmanuel B. Walter, Franceso Berlanda-Scorza, et al. 2020. “A Chimeric Hemagglutinin-Based Universal Influenza Virus Vaccine Approach Induces Broad and Long-Lasting Immunity in a Randomized, Placebo-Controlled Phase I Trial.” *Nature Medicine*, December. https://doi.org/10.1038/s41591-020-1118-7.

Pallesen, Jesper, Nianshuang Wang, Kizzmekia S. Corbett, Daniel Wrapp, Robert N. Kirchdoerfer, Hannah L. Turner, Christopher A. Cottrell, et al. 2017. “Immunogenicity and Structures of a Rationally Designed Prefusion MERS-CoV Spike Antigen.” *Proceedings of the National Academy of Sciences of the United States of America* 114 (35): E7348–57.

Plotkin, Stanley. 2014. “History of Vaccination.” *Proceedings of the National Academy of Sciences of the United States of America* 111 (34): 12283–87.

Rocklin, Gabriel J., Tamuka M. Chidyausiku, Inna Goreshnik, Alex Ford, Scott Houliston, Alexander Lemak, Lauren Carter, et al. 2017. “Global Analysis of Protein Folding Using Massively Parallel Design, Synthesis, and Testing.” *Science* 357 (6347): 168–75.

Rockman, Steven, Karen L. Laurie, Simone Parkes, Adam Wheatley, and Ian G. Barr. 2020. “New Technologies for Influenza Vaccines.” *Microorganisms* 8 (11). https://doi.org/10.3390/microorganisms8111745.

Ruckwardt, Tracy J., Kaitlyn M. Morabito, and Barney S. Graham. 2019. “Immunological Lessons from Respiratory Syncytial Virus Vaccine Development.” *Immunity* 51 (3): 429–42.

Shen, Hao, Jorge A. Fallas, Eric Lynch, William Sheffler, Bradley Parry, Nicholas Jannetty, Justin Decarreau, et al. 2018. “De Novo Design of Self-Assembling Helical Protein Filaments.” *Science* 362 (6415): 705–9.

Stewart-Jones, Guillaume B. E., Gwo-Yu Chuang, Kai Xu, Tongqing Zhou, Priyamvada Acharya, Yaroslav Tsybovsky, Li Ou, et al. 2018. “Structure-Based Design of a Quadrivalent Fusion Glycoprotein Vaccine for Human Parainfluenza Virus Types 1-4.” *Proceedings of the National Academy of Sciences of the United States of America* 115 (48): 12265–70.

Ueda, George, Aleksandar Antanasijevic, Jorge A. Fallas, William Sheffler, Jeffrey Copps, Daniel Ellis, Geoffrey B. Hutchinson, et al. 2020. “Tailored Design of Protein Nanoparticle Scaffolds for Multivalent Presentation of Viral Glycoprotein Antigens.” *eLife* 9 (August). https://doi.org/10.7554/eLife.57659.

Walls, Alexandra C., Brooke Fiala, Alexandra Schäfer, Samuel Wrenn, Minh N. Pham, Michael Murphy, Longping V. Tse, et al. 2020. “Elicitation of Potent Neutralizing Antibody Responses by Designed Protein Nanoparticle Vaccines for SARS-CoV-2.” *bioRxiv : The Preprint Server for Biology*, August. https://doi.org/10.1101/2020.08.11.247395.

Ward, Andrew B., and Ian A. Wilson. 2017. “The HIV-1 Envelope Glycoprotein Structure: Nailing down a Moving Target.” *Immunological Reviews* 275 (1): 21–32.

Wei, Chih-Jen, Michelle C. Crank, John Shiver, Barney S. Graham, John R. Mascola, and Gary J. Nabel. 2020. “Next-Generation Influenza Vaccines: Opportunities and Challenges.” *Nature Reviews. Drug Discovery* 19 (4): 239–52.

Wu, Nicholas C., and Ian A. Wilson. 2020. “Structural Biology of Influenza Hemagglutinin: An Amaranthine Adventure.” *Viruses* 12 (9). https://doi.org/10.3390/v12091053.

Yassine, Hadi M., Jeffrey C. Boyington, Patrick M. McTamney, Chih-Jen Wei, Masaru Kanekiyo, Wing-Pui Kong, John R. Gallagher, et al. 2015. “Hemagglutinin-Stem Nanoparticles Generate Heterosubtypic Influenza Protection.” *Nature Medicine* 21 (9): 1065–70.

Zheng, Allen, Weina Sun, Xiaoli Xiong, Alec W. Freyn, Julia Peukes, Shirin Strohmeier, Raffael Nachbagauer, John A. G. Briggs, Florian Krammer, and Peter Palese. 2020. “Enhancing Neuraminidase Immunogenicity of Influenza A Viruses by Rewiring RNA Packaging Signals.” *Journal of Virology* 94 (16). https://doi.org/10.1128/JVI.00742-20.

Chapter 1: Elicitation of broadly protective immunity to influenza viruses by multivalent hemagglutinin nanoparticle vaccines

Summary

Influenza vaccines that confer broad and durable protection against diverse virus strains would have a major impact on global health. However, next-generation vaccine design efforts have been complicated by challenges including the genetic plasticity of the virus and the immunodominance of certain epitopes in its glycoprotein antigens. Here we show that computationally designed, two-component nanoparticle immunogens induce potently neutralizing and broadly protective antibody responses against a wide variety of influenza viruses. The nanoparticle immunogens display 20 hemagglutinin (HA) trimers in a highly immunogenic array, and their assembly *in vitro* enables precisely controlled co-display of multiple distinct HAs in defined ratios. Nanoparticle immunogens displaying the four HAs of licensed quadrivalent influenza vaccines (QIV) elicited hemagglutination inhibition and neutralizing antibody responses to vaccine-matched strains that were equivalent or superior to commercial QIV in mice, ferrets, and nonhuman primates. The nanoparticle immunogens—but not QIV—simultaneously induced broadly protective antibody responses to heterologous viruses, including H5N1 and H7N9, by targeting the subdominant yet conserved HA stem. Unlike previously reported influenza vaccine candidates, our nanoparticle immunogens can alter the intrinsic immunodominance hierarchy of HA to induce both potent receptor-blocking and broadly cross-reactive stem-directed antibody responses and are attractive candidates for a next-generation influenza vaccine that could replace current seasonal vaccines.

Introduction

Influenza viruses cause an estimated 290,000–650,000 deaths annually despite the availability of licensed vaccines[1]. HAs of the strains currently circulating in humans belong to the H1N1 and H3N2 subtypes of group 1 and 2 influenza A viruses, respectively, as well as the B/Yamagata/16/1988-like (B/Yam) and B/Victoria/2/1987-like (B/Vic) lineages of influenza B viruses[2,3]. Most current seasonal influenza vaccines comprise antigens from each of these four branches and provide protection against symptomatic infection ranging from about 60% down to less than 10%, varying from year to year[4]. Vaccine-mediated protection largely derives from eliciting antibodies to hemagglutinin (HA), the immunodominant surface glycoprotein of influenza viruses. Current vaccines induce narrow, strain-specific responses predominantly targeting the hypervariable head domain of HA. As a result, vaccine performance is blunted when antigenic mismatches occur between the vaccine and circulating strains arising from mispredictions or egg-adapted mutations introduced during vaccine manufacturing[5–9]. These challenges require continual updating of the vaccine strains and annual vaccine reformulation. Furthermore, current seasonal vaccines do not protect against pandemic strains or subtypes such as H5N1 or H7N9[10–12]. Four influenza pandemics have occurred since 1900 with varying levels of severity[13], including the recent 2009 H1N1 pandemic and the 1918 pandemic, which claimed 50–100 million lives[14]. In the absence of novel interventions, it is inevitable that they will continue to reoccur[15–17].

HA is a homotrimeric class I fusion protein, consisting of a head domain that facilitates host cell attachment by binding cell-surface sialosides and a stem domain containing the membrane fusion machinery[18,19]. Both the head and stem contain highly conserved epitopes that are targeted by broadly neutralizing antibodies (bnAbs) capable of protecting against infection by diverse influenza viruses in animal models[18,20,21]. A few such bnAbs are currently being evaluated in human clinical trials for their prophylactic and therapeutic potential[22]. However, bnAbs are rarely elicited and instead, antibodies targeting immunodominant hypervariable epitopes in the head domain often dominate the response to HA, resulting in strain-specific immunity and limited breadth of protection[23–25]. Because of the subdominant nature and broader cross-reactive potential of epitopes in the HA stem, several antigen design efforts have focused on removing or obscuring the head domain to elicit improved stem-focused responses[26–32].

Orderly arrays of antigen on submicron particles are efficiently recognized by the immune system and induce robust humoral responses[33]. The utility of non-viral self-assembling proteins for displaying complex antigens was initially demonstrated by displaying native-like HA trimers on *H. pylori* ferritin nanoparticles, which increased the overall immunogenicity of HA and improved the breadth of vaccine-elicited antibody responses[34]. To further improve breadth across multiple homotypic and heterosubtypic strains, ferritin-based display has been combined with re-designed HA antigens, including headless trimeric HA stems and antigenically optimized HAs[26,28,29,35]. More recently, ferritin was used as a scaffold for co-displaying the monomeric receptor-binding domains (RBDs) from multiple H1 HAs on the same nanoparticle surface[36]. These “mosaic” nanoparticles elicited antibody responses of greater breadth and potency than corresponding mixtures or “cocktails” of nanoparticles each displaying individual RBDs. However, spontaneous assembly of the homomeric ferritin scaffold in cells during secretion precludes the production of mosaic nanoparticles co-displaying multiple trimeric HA antigens.

Recent advances in computational design methods have made possible the predictive design of novel self-assembling protein complexes with structures tailored to specific applications[37–42]. In addition to designed homomeric assemblies of exceptional stability[43], designed two-component complexes constructed from multiple copies of two distinct protein building blocks have been used to generate nanoparticle immunogens. Multivalent antigen display on these nanoparticles enhanced the potency of vaccine-elicited immune responses against a malaria antigen[43], prefusion-stabilized respiratory syncytial virus (RSV) F[44], HIV-1 envelope[44–46], and most recently the SARS-CoV-2 RBD[47]. Assembly of the two-component nanoparticles *in vitro* from independently purified components could in theory enable facile, scalable, and stoichiometrically-controlled co-display of multiple antigenic variants of a wide variety of oligomeric antigens.

Here we use *in vitro* assembly to produce cocktail and mosaic nanoparticle immunogens (co-)displaying multiple trimeric HA ectodomains and evaluate their immunogenicity and protective efficacy against diverse influenza viruses in mice, ferrets, and nonhuman primates. We find that these immunogens possess unique antigenic and immunogenic properties, and have the potential to induce protective responses against seasonal and pandemic strains effective over multiple years without reformulation.

Immunogen design, *in vitro* assembly, and characterization

We genetically fused HA ectodomains from the four strains in licensed 2017-2018 seasonal influenza vaccines to the N terminus of I53_dn5B, the trimeric component of the two-component icosahedral nanoparticle I53_dn5 (**Fig. 1.1a**; H1: A/Michigan/45/2015, H3: A/Hong Kong/4801/2014, B/Yam: B/Phuket/3073/2013, B/Vic: B/Brisbane/60/2008; ref. 42). The four proteins were individually produced in mammalian cells and purified by affinity chromatography and size-exclusion chromatography (SEC). The SEC profiles were consistent with the expected size of the trimeric fusion proteins (**Fig. S1.1a**), and SDS-PAGE indicated that the preparations contained exclusively uncleaved HA-I53_dn5B fusion proteins (**Fig. S1.1b**).

To produce a mosaic nanoparticle co-displaying quadrivalent seasonal HAs (qsMosaic-I53_dn5), the purified trimeric HA-I53_dn5B components were mixed in equimolar amounts prior to addition of purified I53_dn5A pentamer to induce nanoparticle assembly (**Fig. 1.1a**). In parallel, nanoparticles individually displaying each HA ectodomain were produced by separately assembling each of the four HA-I53_dn5B trimers with I53_dn5A pentamer. During the purification of each nanoparticle by SEC, nearly all of the protein eluted in an early peak corresponding to the assembled icosahedral complex, with only minor amounts of residual, unassembled components eluting later (**Fig. S1.1c,d**). The nanoparticles bound head- and stem-directed mAbs specific to the HA trimers displayed, including qsMosaic-I53_dn5, which bound mAbs specific to H1, H3, and influenza B HAs (**Fig. 1.1b**). The size and morphology of each nanoparticle, including I53_dn5 nanoparticles without HA, was evaluated by analytical SEC (**Fig. 1.1c**), dynamic light scattering (**Fig. S1.1e**), and negative stain electron microscopy (**Fig. 1.1d**), which confirmed assembly to the intended icosahedral architecture with no evidence of aggregation. A single-particle cryo-EM reconstruction of the H1-I53_dn5 nanoparticle to 6.6 Å resolution established the integrity of the I53_dn5 nanoparticle core and indicated marked flexibility between the displayed HA ectodomains and the underlying nanoparticle scaffold despite the use of a minimal (two-residue) linker (**Fig. 1.1e** and **Fig. S1.1f–h**). We therefore used localized reconstruction[48] to determine a 3.3 Å reconstruction of the displayed H1 HA, demonstrating full retention of the native structure of the genetically fused antigen (**Fig. 1.1e** and **Fig. S1.1i**). Finally, hydrogen-deuterium exchange mass spectrometry revealed no significant differences in the local structural order of H1-I53_dn5 and an H1-foldon fusion protein, a well-characterized research reagent[49], further confirming the integrity of the HA displayed on the nanoparticle (**Fig. S1.2**). These data demonstrate that *in vitro* assembly yielded monodisperse I53_dn5-based nanoparticles with the expected size, morphology, and antigenicity.

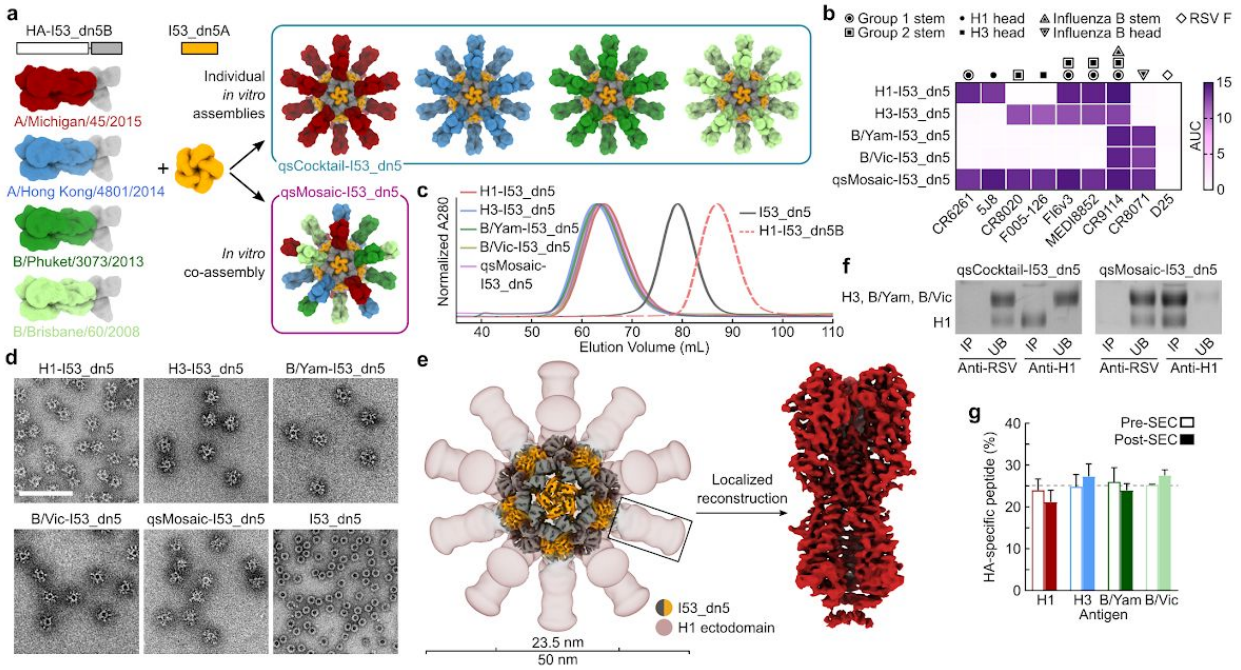

Figure 1.1 | Design, *in vitro* assembly, and characterization of cocktail and mosaic HA nanoparticle immunogens. a, Schematics of the components and *in vitro* assembly of nanoparticle immunogens displaying HA. Trimeric HA-I53_dn5B fusions were secreted from HEK293F cells, while the I53_dn5A pentamer was expressed in *E. coli*. **b,** Antigenic characterization of purified nanoparticle immunogens by ELISA. Symbols indicate the specificity of each mAb. AUC, area under the curve. **c,** Analytical SEC of purified nanoparticle immunogens, compared to I53_dn5 nanoparticles lacking displayed antigen and trimeric H1-I53_dn5B, using a Sephacryl S-500 HR 16/60 column. **d,** Negative stain electron micrographs of purified nanoparticle immunogens and I53_dn5 (scale bar, 200 nm). **e,** 3D reconstruction of the H1-I53_dn5 nanoparticle immunogen and localized reconstruction of H1 MI15 obtained using single-particle cryo-EM. For the nanoparticle immunogen, high (grey/orange) and low (red) contour 3D representations are overlaid to enable visualization of the I53_dn5 scaffold and the displayed HA, respectively. The density corresponding to the low contour representation was smoothed using a 16 Å low-pass filter for clarity. **f,** Immunoprecipitation of qsCocktail-I53_dn5 and qsMosaic-I53_dn5 using RSV F-specific (MPE8) and H1-specific (5J8) mAbs. IP, immunoprecipitated; UB, unbound. **g,** Quantitation of HA antigen content in assembled qsMosaic-I53_dn5 nanoparticles before and after preparative SEC by peptide mass spectrometry. The dashed grey line represents the expected peptide content from each HA, and error bars represent the s.d. of measurements across four unique peptides from each HA.

We prepared a quadrivalent seasonal cocktail containing equimolar amounts of the four individual HA-displaying nanoparticles (qsCocktail-I53_dn5; **Fig. 1.1a**) and used two distinct assays to confirm co-assembly only in the case of qsMosaic-I53_dn5. First, we immunoprecipitated each nanoparticle using the H1-specific mAb 5J8 (ref. 50) and exploited the unique mobility of the H1-I53_dn5B band during non-reducing SDS-PAGE to track the fate of H1-containing nanoparticles. While immunoprecipitation of qsCocktail-I53_dn5 nanoparticles recovered only H1-I53_dn5B and not the other HA-I53_dn5B proteins, the same procedure resulted in complete pull-down of all the HA-I53_dn5B proteins in qsMosaic-I53_dn5 nanoparticles (**Fig. 1.1f**). No pull-down was seen when immunoprecipitation was performed with

an irrelevant, RSV F-specific mAb. This result indicates that co-assembly of qsMosaic-I53_dn5 is very efficient—as expected if there is no preferential incorporation or exclusion of specific HAs during assembly (**Fig. S1.3a,b**)—and confirms that subunit exchange did not occur in the qsCocktail-I53_dn5 nanoparticle. Second, we devised a sandwich biolayer interferometry (BLI) experiment in which each nanoparticle was captured by immobilized H1-specific mAb and subsequently evaluated for binding to H3- or influenza B-specific mAbs. qsMosaic-I53_dn5 nanoparticles were bound by the H3- and B-specific mAbs, indicating co-display, while qsCocktail-I53_dn5 nanoparticles were not (**Fig. S1.3c**).

We used quantitative mass spectrometry to measure the relative amount of each HA in co-assembled qsMosaic-I53_dn5 nanoparticles before and after purification by SEC. Quantitating unique peptides for each HA antigen revealed that the equimolar HA content used in the *in vitro* assembly reaction was maintained in the purified nanoparticle (**Fig. 1.1g**). Post-SEC specific HA content was also maintained in additional mosaic nanoparticles in which we substantially altered the stoichiometric ratios of the four HA-I53_dn5B components (**Fig. S1.3d**). Together, these data demonstrate that *in vitro* assembly enables co-display of multiple oligomeric antigens in defined ratios. We note, however, that the symmetric nature of the I53_dn5 nanoparticle scaffold does not allow the controlled placement of antigens in specific locations on the nanoparticle, and we expect that the antigen content of each individual nanoparticle will assume a distribution centered on the overall antigen content (**Fig. S1.3a**).

Vaccine-elicited antibody responses against vaccine-matched antigens and viruses

We next performed a series of *in vivo* experiments in mice, ferrets, and nonhuman primates (NHPs) to compare the immunogenicity of qsCocktail-I53_dn5 and qsMosaic-I53_dn5 to commercial 2017-2018 QIV. Throughout our studies, we matched the total protein dose of each nanoparticle immunogen to the HA content of QIV. After three immunizations with each immunogen formulated with AddaVax, a squalene-based oil-in-water emulsion chemically equivalent to the licensed adjuvant MF59 (ref. 51), we measured antigen-specific antibody, hemagglutination inhibition (HAI), and reporter-based microneutralization (see **Methods**) titers against vaccine-matched or slightly mismatched viruses and HAs (**Fig. 1.2a**). HA-specific antibody titers induced by both nanoparticle immunogens were equivalent or superior to those induced by QIV, with larger increases observed in mice and ferrets than in NHPs in most cases (**Fig. S1.4a–c**). Similarly, in mice and ferrets qsCocktail-I53_dn5 and qsMosaic-I53_dn5 elicited higher HAI titers than QIV against vaccine-matched B/Yam virus and were comparable against H1N1, H3N2, and a slightly mismatched B/Vic virus (**Fig. 1.2b**). The three immunogens induced roughly equivalent HAI activity against these viruses in NHPs. The increases in microneutralization titer afforded by the nanoparticle immunogens over QIV were more variable, in some cases exceeding an order of magnitude, but overall exhibited the same trend of being comparable to each other and equivalent or superior to QIV (**Fig. 1.2c**). We also observed I53_dn5 nanoparticle scaffold-specific antibodies in animals immunized with either nanoparticle immunogen. Additional immunogenicity studies in mice without adjuvant (**Fig. S1.4d**) and using updated versions of the three immunogens containing the 2018-2019 vaccine strains (**Fig. S1.5a–d**) yielded similar results. These data establish that qsCocktail-I53_dn5 and qsMosaic-I53_dn5 elicit vaccine-matched antibody responses that are equivalent or superior to

current commercial influenza vaccines.

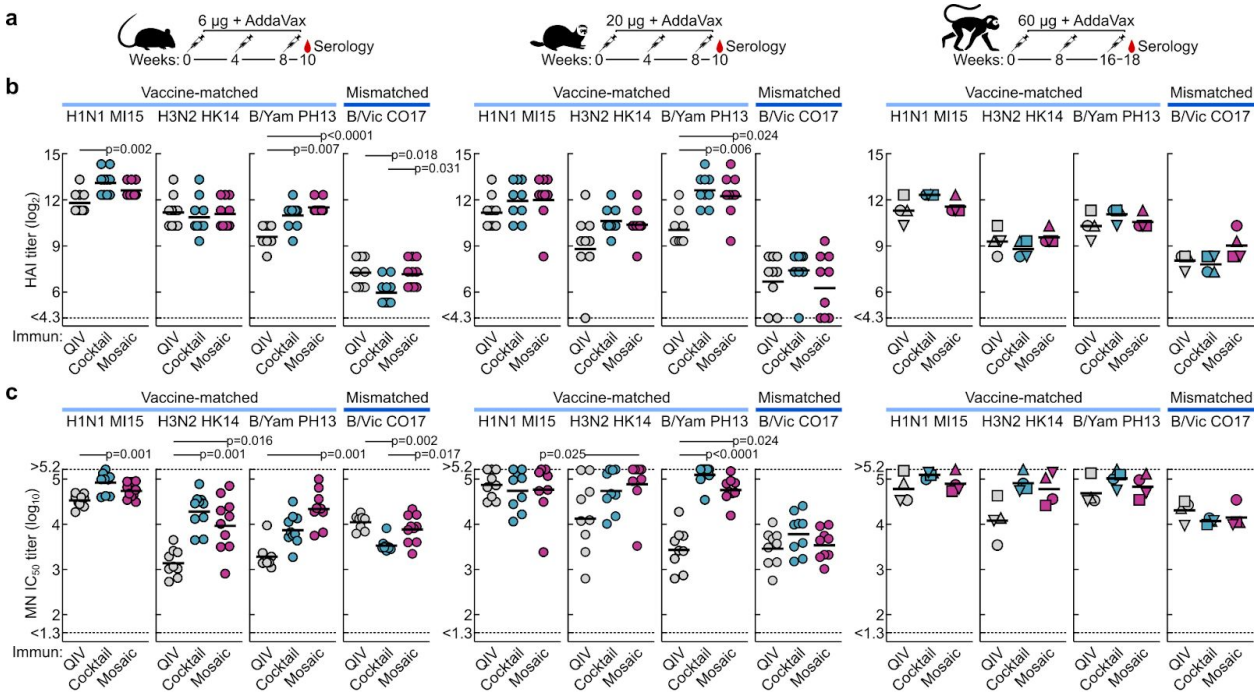

Figure 1.2 | Vaccine-elicited antibody responses against vaccine-matched viruses in mice, ferrets, and NHPs. a, Immunization schemes for mouse, ferret, and NHP studies. All immunizations were given intramuscularly with AddaVax. Groups of BALB/cJ mice (*N* = 10), Finch ferrets (*N* = 9), and rhesus macaques (*N* = 4) were used in each experiment. **b,** Hemagglutination inhibition (HAI) and **c,** microneutralization (MN) titers in immune sera. Microneutralization titers are reported as half maximal inhibitory dilution (IC_{50}). Each symbol represents an individual animal and the horizontal bar indicates the geometric mean of the group. Individual NHPs are identified by unique symbols. Statistical analysis was performed using nonparametric Kruskal–Wallis test with Dunn's multiple comparisons. All animal experiments except for NHPs were performed at least twice and representative data are shown.

Neutralization of and protection against historical H1N1 and H3N2 viruses

We next tested sera from ferrets immunized with QIV, qsCocktail-I53_dn5, and qsMosaic-I53_dn5 for their ability to neutralize a panel of H1N1 and H3N2 viruses that represent historical antigenic drift and shift[52] (**Fig. 1.3a, Fig. S1.6**). H1N1 microneutralization showed a clear demarcation between pre- and post-2009 viruses, with much lower neutralization activity overall against pre-2009 viruses possessing HAs antigenically distant from the vaccine-strain H1. Nevertheless, both nanoparticle immunogens elicited roughly equivalent or superior neutralizing activity to QIV for all H1N1 strains tested, which translated to slightly higher global geometric mean titers (GMT) across 10 viruses. Historical H3N2 microneutralization decreased more gradually, in keeping with the continuous antigenic drift of this lineage, and both nanoparticle immunogens elicited ~10-fold higher levels of neutralizing activity than QIV against viruses dating back to 2002, resulting in significant increases in global GMT.

Encouraged by these results, we compared the ability of QIV, qsCocktail-I53_dn5, and qsMosaic-I53_dn5 to protect against lethal challenges with highly divergent H1N1 and H3N2 viruses. Mice were immunized with AddaVax-adjuvanted or unadjuvanted immunogens and subsequently challenged with heterologous A/Puerto Rico/8/1934 (H1N1) or mismatched A/Philippines/2/1982 (H3N2) viruses (**Fig. 1.3b,c**). All mice receiving mock immunizations succumbed to disease and had to be euthanized by 9 days post-infection. When adjuvanted, both nanoparticle immunogens provided complete or near-complete protection (97% in aggregate across the four groups), while QIV afforded partial protection against both H1N1 (70%) and H3N2 (60%) challenges. Remarkably, in the absence of adjuvant, mice immunized with qsMosaic-I53_dn5 were almost completely protected from heterologous H1N1 challenge (90%) and partially protected from mismatched H3N2 challenge (50%), while qsCocktail-I53_dn5 provided partial protection in both cases (55% and 44%, respectively). In contrast, unadjuvanted QIV provided negligible protection (20% and 0%, respectively). Pseudovirus neutralization titers against the challenge strains, measured using sera collected 6 to 8 weeks prior to challenge, showed a clear correlation with protection, with all protected animals having IC_{50} titers above 100 (**Figure 1.3b,c**).

Together, these data establish that both qsCocktail-I53_dn5 and qsMosaic-I53_dn5 elicit more broadly neutralizing antibody responses and protective immunity against mismatched H1N1 and H3N2 viruses than current commercial influenza vaccines. This effect was magnified in the absence of adjuvant. These findings suggest the nanoparticle immunogens might confer multi-season protection without requiring annual vaccine reformulation.

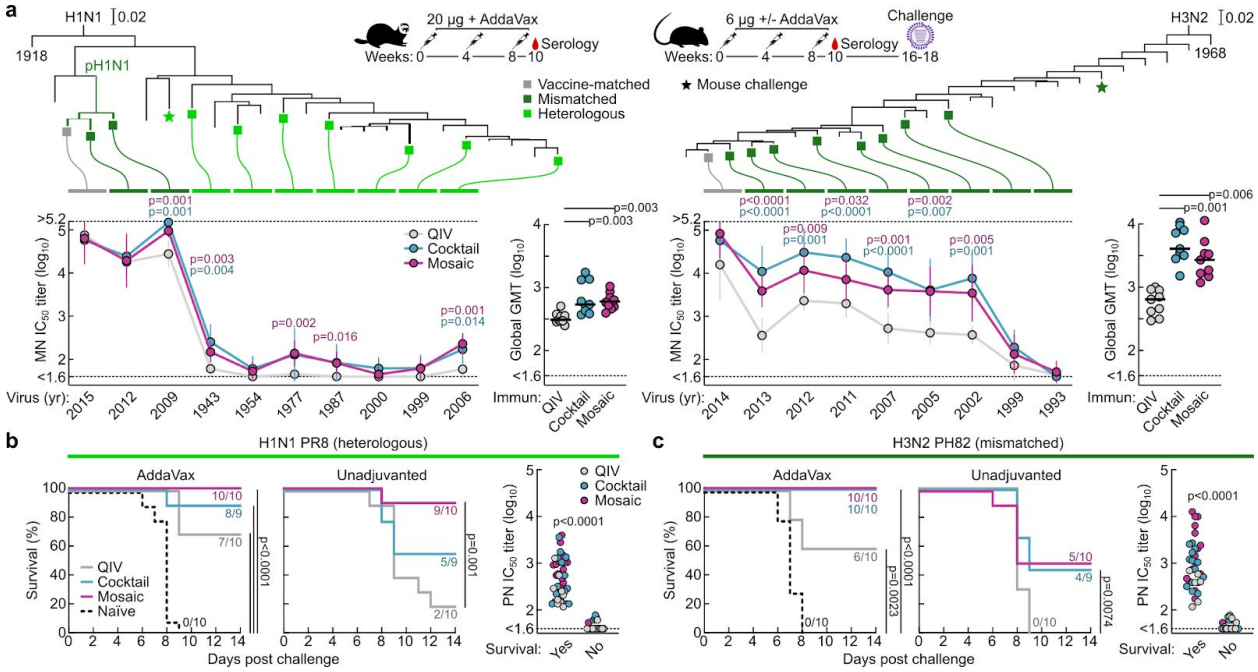

Figure 1.3 | Neutralization of and protection against historical H1N1 and H3N2 viruses. a, Experimental scheme for ferret and mouse studies. Groups of Finch ferrets (*N* = 9) and BALB/cJ mice (*N* = 9–10) were used in each experiment. Phylogenetic trees of HA sequences of selected human H1N1 (left) and H3N2 (right) viruses are shown. Neutralization breadth of ferret immune sera across representative panels of historical H1N1 and H3N2 viruses, along with geometric mean IC_{50} titers ±

geometric s.d. for each group are shown (bottom). Means of geometric mean IC_{50} titers across 10 H1N1 or 9 H3N2 viruses for each individual animal are plotted as global GMT to the right of each neutralization breadth plot. Statistical analysis was performed using nonparametric Kruskal–Wallis test with Dunn's multiple comparisons. Ferret experiments were performed twice and representative data are shown. Heterologous H1N1 (**b**) and mismatched H3N2 (**c**) virus challenges in immunized mice. Viruses were given intranasally and mice were monitored for 14 days post infection. Statistical test to compare multiple Kaplan–Meier curves was performed using Mantel-Cox log-rank test with Bonferroni correction. Pseudotype neutralizing (PN) antibody IC_{50} titers were grouped based on survival outcomes and plotted to the right of survival curves. Each symbol represents an individual animal and is color-coded by vaccine. Mouse challenge experiments were performed once.

Vaccine-elicited heterosubtypic antibody responses and protective immunity

Current commercial influenza vaccines are limited in their ability to protect against many widely circulating zoonotic strains, making influenza a major pandemic threat[53]. We compared the ability of QIV, qsCocktail-I53_dn5, and qsMosaic-I53_dn5 to provide immunity against heterosubtypic influenza A viruses in mice, ferrets, and NHPs. We found that both nanoparticle immunogens elicited cross-reactive antibody responses to HAs from heterosubtypic group 1 (H5N1 and H6N1) and group 2 (H7N9 and H10N8) viruses, whereas QIV elicited low—in some cases undetectable—levels of such antibodies (**Fig. 1.4a–c**). The ability of the nanoparticle immunogens to induce heterosubtypic antibody responses is not limited to the 2017-2018 vaccine composition, as we observed similar cross-reactive antibody responses in mice immunized with nanoparticle immunogens updated with the 2018-2019 vaccine strains (**Fig. S1.6e**).

To assess whether these cross-reactive antibody responses were protective, we carried out several challenge studies with H5N1 and H7N9 viruses in mice and ferrets. First, we immunized mice with each of the three immunogens either with or without AddaVax and challenged them with lethal doses of heterosubtypic A/Vietnam/1203/2004 (H5N1) or A/Anhui/1/2013 (H7N9) virus 8–10 weeks after the last immunization. As expected, all animals receiving mock immunizations succumbed to disease, and QIV provided negligible protection (12% in aggregate across the four experiments; **Fig. 1.4d**). Strikingly, qsCocktail-I53_dn5 conferred partial protection (73% in aggregate) and qsMosaic-I53_dn5 nearly complete protection (92% in aggregate) against these heterosubtypic challenges, even in the absence of adjuvant (67% and 87%, respectively). Similar results were obtained with adjuvant in ferrets, where the nanoparticle immunogens provided robust protection against both H5N1 and H7N9 challenge (88% combined), whereas commercial QIV (33% combined) and mock immunization (17%) provided only weak protection (**Fig. 1.4e**). Viral RNA quantification in lung tissues by RT-qPCR revealed that the animals receiving qsMosaic-I53_dn5 had significantly lower amounts of H5N1 or H7N9 viral RNA than those immunized with commercial QIV (**Fig. 1.4e, right**).

To determine whether vaccine-elicited serum antibodies alone could confer protection against heterosubtypic challenge, we performed passive transfer experiments in mice. We passively immunized three mice with 10 mg of purified immunoglobulin (Ig) from each immunized NHP 24 h prior to infection with H5N1 or H7N9 virus (**Fig. 1.4f)**. We included ten mice passively immunized with Ig purified from influenza-naïve NHPs as negative controls and another ten

mice passively immunized with FI6v3, a potent stem-directed human bnAb[54], as positive controls. All mice that received Ig from qsCocktail-I53_dn5- or qsMosaic-I53_dn5-immunized animals, as well as the animals that received FI6v3, showed no weight loss and were protected from disease, with the exception of one mouse receiving Ig from an NHP immunized with qsCocktail-I53_dn5 (**Fig. 1.4f**). In contrast, all mice that received naïve Ig succumbed to disease and had to be euthanized by 8 days post-infection, while the mice that received Ig from QIV-immunized NHPs showed significant weight loss and only partial protection against H5N1 (42%) and H7N9 (25%) challenge.

To better understand the role of multivalent antigen display in the remarkable antibody responses elicited by qsCocktail-I53_dn5 and qsMosaic-I53_dn5 in mice, ferrets, and NHPs, we performed another immunization experiment in mice in which we included a non-assembling version of these immunogens. This non-assembling control immunogen was identical to qsCocktail-I53_dn5 and qsMosaic-I53_dn5 except that the trimeric components lacked the computationally designed interface that drives nanoparticle assembly (**Fig. S1.7a–d**; ref. 42). While the non-assembling immunogen elicited microneutralization titers against vaccine-matched viruses that were similar to qsCocktail-I53_dn5 and qsMosaic-I53_dn5, the cross-reactive antibody responses elicited against H5N1 and H7N9 HAs were more than 10- and 100-fold lower, respectively, and were similar to those induced by commercial QIV (**Fig. S1.7e–g**).

Together, these data demonstrate that qsCocktail-I53_dn5 and qsMosaic-I53_dn5 elicit broadly protective antibody responses against a wide variety of influenza viruses, including known pandemic threats, in contrast to currently available influenza vaccines. Formation of the nanoparticle architecture displaying an orderly array of HA antigens is required, since an equivalent dose of non-assembling HA trimeric components and the I53_dn5A pentamer elicited a negligible cross-reactive response.

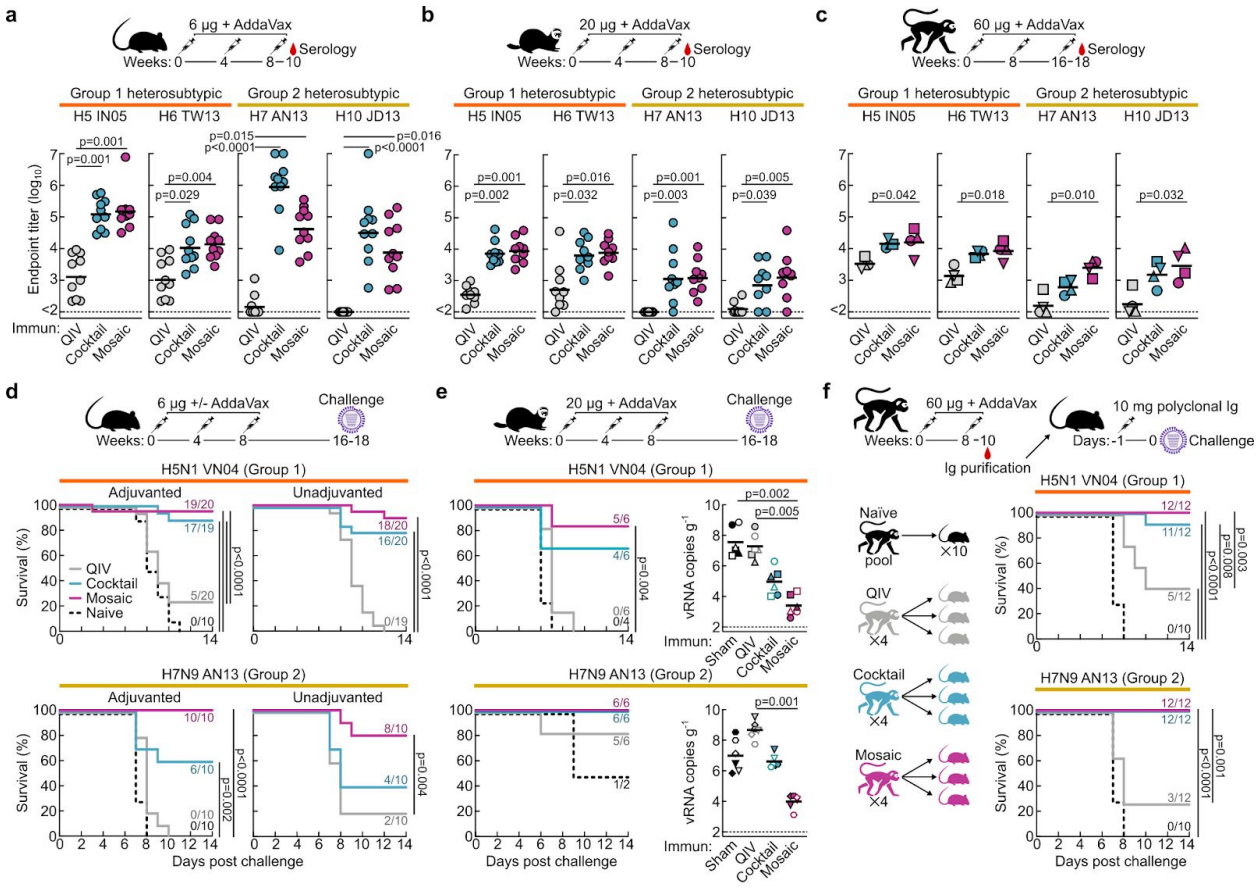

Figure 1.4 | Vaccine-elicited heterosubtypic antibody responses and protective immunity. Cross-reactive antibody responses to heterosubtypic HA antigens in **a,** mice, **b,** ferrets, and **c,** NHPs. Immunization schemes are shown at the top of each panel. ELISA antibody titers are expressed as endpoint dilutions. Each symbol represents an individual animal and the horizontal bar indicates the geometric mean of each group of BALB/cJ mice (*N* = 10), Finch ferrets (*N* = 9), and rhesus macaques (*N* = 4). Individual NHPs are identified by unique symbols. All animal immunization experiments except for NHP were performed at least twice and representative data are shown. Statistical analysis was performed using nonparametric Kruskal–Wallis test with Dunn's multiple comparisons. **d,** Heterosubtypic influenza virus challenge in immunized mice. Immunized mice were challenged with either H5N1 (top) or H7N9 virus (bottom) intranasally. **e,** Heterosubtypic influenza virus challenge in immunized ferrets. Immunized ferrets were challenged with either H5N1 (top) or H7N9 virus (bottom) intranasally. Three ferrets from each group were euthanized at day 4 post challenge to measure viral RNA in lung tissue (right). Individual ferrets are identified by unique symbols. Right and left caudal lung lobes are indicated as closed and open symbols, respectively. **f,** Heterosubtypic influenza virus challenge after passive transfer of purified NHP immune Ig in mice. Polyclonal Ig from immunized NHPs was purified and administered intraperitoneally to recipient BALB/cAnNHsd mice prior to infection with H5N1 (top) or H7N9 (bottom) virus. Control Ig was purified from pooled naïve sera and given to 10 mice. Statistical test to compare multiple Kaplan–Meier curves was carried out by using Mantel-Cox log-rank test with Bonferroni correction. Mouse challenge experiments were performed twice, while ferret experiments and passive transfer experiments were performed once, and representative data are shown.

Molecular basis for vaccine-elicited broad antibody responses against heterosubtypic influenza viruses

We performed several experiments to better understand the molecular and structural determinants of the broadly protective immunity induced by qsCocktail-I53_dn5 and qsMosaic-I53_dn5. First, we measured serum antibody binding to stabilized stem trimers of group 1 and group 2 HAs, which comprise only the conserved stem domain[26,28]. Stem-directed antibodies elicited by both qsCocktail-I53_dn5 and qsMosaic-I53_dn5 were significantly higher than those induced by QIV in all three animal species (**Fig. 1.5a**). We next assessed whether these stem-directed antibodies contribute to virus neutralization by performing microneutralization assays in the presence of competitor proteins to deplete certain antibody specificities. Analysis of sera from NHPs immunized with qsMosaic-I53_dn5 revealed that neutralizing activity against the vaccine-matched H1N1 virus was depleted by vaccine-matched full-length HA ectodomain but not by an H1 HA stem, suggesting that antibodies targeting epitopes outside of the stem domain account for most of the neutralizing activity, as expected (**Fig. 1.5b**). In contrast, neutralizing activity against a heterosubtypic H5N1 virus was fully depleted by both vaccine-matched H1 HA and an H1 HA stem, indicating that stem-directed antibodies are solely responsible for the observed heterosubtypic neutralization.

We directly visualized the epitopes recognized by nanoparticle immunogen-elicited antibodies in individual NHPs using recently developed methods for single-particle EM analysis of polyclonal antibody responses[55,56]. We found that the polyclonal response to vaccine-matched H1 HA comprises at least three classes of antibodies targeting the RBD, the vestigial esterase (VE) domain, and the stem, respectively (**Fig. 1.5c** and **Fig. S1.8**). While each class included multiple specificities recognizing distinct epitopes or having different angles of approach, the vast majority of complexes we visualized contained antibodies recognizing the head domain of H1 HA. We also performed single-particle cryo-EM analysis of H5 HA in complex with polyclonal Fab fragments prepared from antibodies elicited by qsMosaic-I53_dn5. Strikingly, we saw only stem-directed antibodies bound to the H5 HA trimer, unambiguously demonstrating recognition of this conserved supersite (**Fig. 1.5d**). 3D classification of the data revealed H5 HA trimers with polyclonal stem-directed Fabs bound to one, two, or all three HA subunits, from which we obtained 3D reconstructions with average resolutions ranging from 3.6 to 4.1 Å (**Fig. 1.5d** and **Fig. S1.9**). Although the resolution of the Fab components is much lower than the nominal resolution due to polyclonal heterogeneity, the maps clearly indicate the existence of multiple vaccine-elicited antibody classes featuring distinct angles of approach to the epitope defined by the HA fusion peptide, helix A, and the hydrophobic groove surrounding $Trp21_{HA2}$. The data suggest at least one common class of vaccine-elicited antibodies recognizes this epitope in a manner reminiscent of the human bnAbs MEDI8852 and 56.a.09, which both belong to the $V_H6\text{-}1+D_H3\text{-}3$ class of multi-donor human bnAbs[57,58] (**Fig. 1.5e**). These findings corroborate our serological analyses and establish that although most vaccine-elicited antibodies recognize the vaccine-matched HA head, the heterosubtypic protection we observe likely derives from the simultaneous elicitation of stem-targeted bnAbs.

To study how pre-existing immunity could influence antibody responses to the nanoparticle immunogens, three of the NHPs from the commercial QIV and qsMosaic-I53_dn5 groups were boosted 63 weeks later (week 99) with a single dose of an updated version of qsMosaic-I53_dn5 co-displaying the HAs from 2018-2019 seasonal influenza vaccines. All

animals had high levels of neutralizing antibodies against vaccine-matched strains at week 99 that were strongly boosted upon immunization with updated qsMosaic-I53_dn5 (**Fig. S1.10**). Prior to the immunization at week 99, animals pre-immunized with commercial QIV had near-baseline levels of H1 and H3 stem-directed antibodies, while animals pre-immunized with qsMosaic-I53_dn5 maintained robust stem-directed titers. Two weeks after the boost (week 101), the NHPs pre-immunized with commercial QIV showed strongly elevated anti-stem antibody titers that were similar to the animals pre-immunized with qsMosaic-I53_dn5 (**Fig. 1.5f**). These data demonstrate that qsMosaic-I53_dn5 stimulates robust stem-directed antibody responses even in the context of high levels of pre-existing immunity against the immunodominant head of HA.

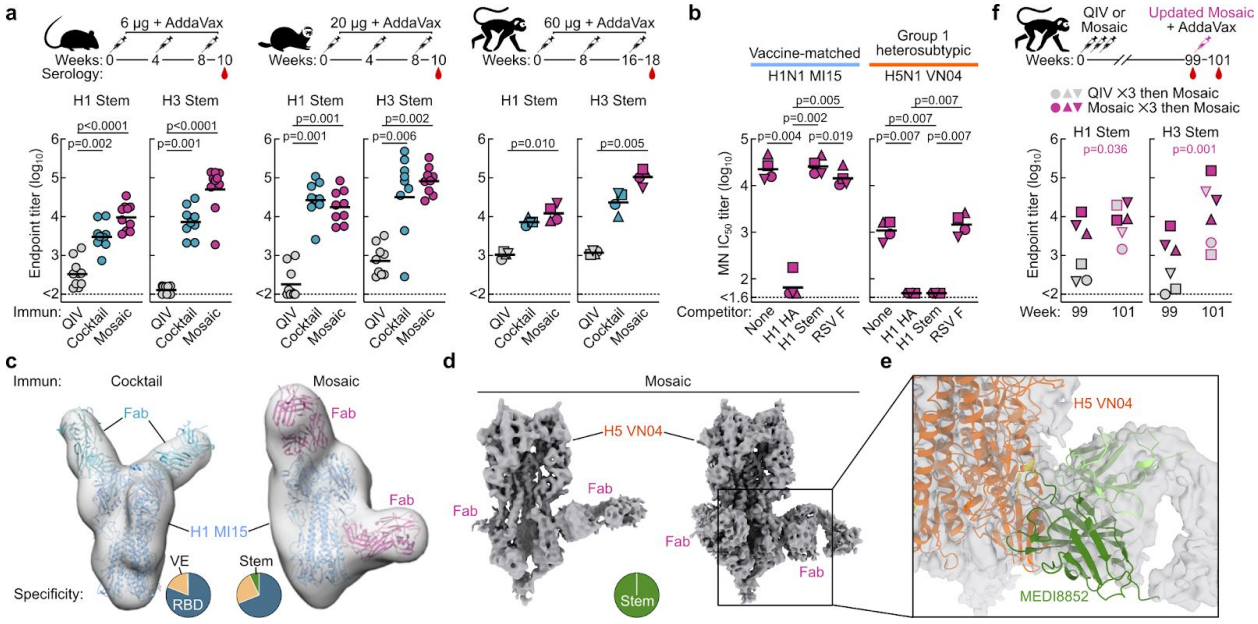

Figure 1.5 | Molecular basis for nanoparticle immunogen-induced protection against heterosubtypic influenza viruses. a, Serum antibody titers to H1 (CA09) and H3 (WI05) HA stem antigens in mice, ferrets, and NHPs. Immunization schemes are shown at the top. Antibody titers are expressed as endpoint dilutions. Each symbol represents an individual animal and the horizontal bar indicates the geometric mean of each group of BALB/cJ mice (*N* = 10), Finch ferrets (*N* = 9), and rhesus macaques (*N* = 4). Individual NHPs are identified by unique symbols. All animal immunization experiments except for NHP were performed at least twice and representative data are shown. **b,** Serum microneutralization activity in the presence of competitor proteins. Immune sera were evaluated directly or pre-incubated with either H1 MI15 HA, H1 HA stem, or irrelevant RSV F proteins prior to evaluation of MI15 (H1N1) and VN04 (H5N1) neutralization. Microneutralization titers are reported as half maximal inhibitory dilution (IC_{50}). Statistical analysis was performed using nonparametric Kruskal–Wallis test with Dunn's multiple comparisons. **c,** Selected EM reconstructions of negatively stained vaccine-matched H1 HA-foldon in complex with polyclonal antibody Fab fragments elicited by qsCocktail-I53_dn5 (left) and qsMosaic-I53_dn5 (right). Frequency of HA/Fab complexes observed by EM containing Fab fragments bound to RBD, VE, and stem domains are shown as pie charts. The coordinates of an H1 HA crystal structure (PDB 1RUZ) and a Fab fragment (PDB 3GBN) were fitted into the EM densities. Light blue ribbons, H1 HA; cyan ribbons, polyclonal Fabs elicited by qsCocktail-I53_dn5; magenta ribbons, polyclonal Fabs elicited by qsMosaic-I53_dn5. **d,** Two independent cryo-EM reconstructions of heterosubtypic H5 HA-foldon in complex with polyclonal antibody Fab fragments elicited by

qsMosaic-I53_dn5. Note the nearly orthogonal angles of approach adopted by the Fabs in the two reconstructions. **e,** Close-up view showing that one of the dominant antibody recognition modes resembles that of MEDI8852 by forming putative contacts with helix A and the fusion peptide. The coordinates of an H5 HA crystal structure in complex with MEDI8852 Fab (PDB 5JW4) were fitted into the EM densities. **f,** Serum antibody titers to H1 and H3 HA stem antigens in NHPs with pre-existing influenza immunity. Immunization scheme is shown at the top of the panel. NHPs (N = 3) that had been immunized three times with either QIV 2017-2018 or qsMosaic-I53_dn5 2017-2018 were boosted 63 weeks later (week 99) with a single dose (60 μg) of updated qsMosaic-I53_dn5 2018-2019, which contains different H3 and B/Vic strains (**Fig. S1.10**). All immunizations were given intramuscularly with AddaVax. Antibody titers are expressed as endpoint dilutions. Individual NHPs are identified by unique symbols. Statistical analysis between the two timepoints was performed using paired t test.

Discussion

The manifest consequences of the SARS-CoV-2 pandemic emphasize the importance of efforts to mitigate the next influenza pandemic by establishing universal influenza immunity. We have developed nanoparticle vaccines that elicit potent vaccine-matched HAI activity as well as protective stem-directed neutralizing antibodies against distantly related—including heterosubtypic—viruses in multiple animal models. These results go beyond previous next-generation influenza vaccine concepts, which have been reported to enhance either stem-directed responses[26–29,32,59], the potency and breadth of HAI within specific subtypes[34,35,60,61], or both types of responses within specific subtypes[62,63]. Since both HAI and stem-directed antibodies have been shown as independent immune correlates of protection against influenza infection in humans[64], a vaccine candidate capable of eliciting both would have advantages over approaches eliciting one or the other. The broad, antibody-mediated protection conferred by qsCocktail-I53_dn5 and qsMosaic-I53_dn5 suggests that they may be able to provide consistent year-to-year protection against seasonal influenza viruses, even in the event of antigenic mismatches in the hypervariable head domain. In contrast to universal vaccine approaches targeting only the HA stem, eliciting HAI responses against seasonal influenza strains with nanoparticle vaccines displaying full-length HAs justifies head-to-head evaluation against conventional licensed vaccines, which will facilitate clinical development. These unique features make our nanoparticle immunogens attractive candidates for clinical evaluation as supraseasonal vaccines[12] that may eventually replace current seasonal vaccines.

Defining the immunological or structural basis for the singular breadth elicited by our nanoparticle vaccines will require further investigation. The induction of protective levels of stem-directed antibodies by both qsCocktail-I53_dn5 and qsMosaic-I53_dn5 despite the presence of the immunodominant head domain—but not by QIV or a non-assembling control immunogen—suggests that some aspect of HA presentation on the I53_dn5 scaffold alters the intrinsic immunodominance hierarchy of HA[23,65]. Several potential factors may contribute to this effect, such as the geometric relationship between neighboring HAs on the nanoparticle surface[33,42,45], preferential antigen uptake or retention kinetics by macrophages and follicular dendritic cells[66], or the presence of T helper epitopes within the subunits of the I53_dn5 nanoparticle[67–69]. Intriguingly, across our many *in vivo* studies, qsMosaic-I53_dn5 subtly yet consistently outperformed qsCocktail-I53_dn5 by most measures, including protective efficacy. Additional studies will be required to determine if this observation holds for mosaic and cocktail

immunogens displaying different combinations of HAs and antigens other than HA.

We demonstrated the apparent epitope and angle of approach of a major class of vaccine-elicited, cross-reactive, polyclonal NHP antibodies are remarkably similar to human multi-donor V_H6-1+D_H3-3–class antibodies[57,58], the broadest and most potent stem-directed human bnAbs[52]. Precursors of this class of bnAb are in theory found in ~99% of the human population[70] and can be amplified by heterologous stimuli such as pandemic influenza vaccines[58,71]. While this observation is encouraging, it remains to be seen whether more frequently observed stem-directed antibodies, such as those derived from V_H1-69 genes, interfere with the elicitation of the broader and more potent V_H6-1+D_H3-3 antibodies in humans upon immunization with our nanoparticle vaccines, or whether other forms of pre-existing influenza immunity would alter the breadth of responses.

Our work establishes *in vitro* assembly as a key advantage of designed two-component nanoparticles[38,39,42], as it enables facile and scalable co-display of multiple antigenic variants in stoichiometrically-controlled ratios. This property could be used to generate nanoparticle vaccine candidates co-displaying additional combinations of HAs for specific purposes. For example, incorporating additional HAs from co-circulating H3N2 or influenza B viruses could consolidate protective immunity against drifted seasonal strains. Including HAs from non-circulating subtypes, such as H5N1 and H7N9, may yield pandemic preparedness vaccines that provide broad protection against known and unknown pandemic threats[12]. While identifying the combinations and ratios of displayed HAs that elicit the broadest and most potent protective immunity will require further investigation, our data suggest that even displaying the four HAs of current seasonal influenza vaccines on I53_dn5, as we have done here, may provide moderate protection to unforeseen pandemic influenza viruses, which could provide the time needed for vaccine manufacturing in the event of an emerging threat[12]. The modularity of designed two-component nanoparticles could be a powerful tool in the development of next-generation influenza vaccines.

Motivated by the data presented here, a variant of qsMosaic-I53_dn5 with updated HA antigens is being produced under current Good Manufacturing Practice (cGMP) conditions for a planned Phase I clinical trial. In addition to evaluating the safety and reactogenicity of the nanoparticle vaccine, data from this trial should address several key questions raised by the current study, such as whether the protective stem-directed responses we observed in naïve animals can also be elicited in humans in the face of pre-existing immunity. While animal models can be devised to investigate some aspects of this question (reviewed in ref. 72) and our data in pre-immunized NHPs suggests that anti-stem responses can be efficiently boosted by qsMosaic-I53_dn5, human clinical trials will be needed to fully assess the impact of complex and individualized influenza exposure histories and immunological imprinting[73,74]. Furthermore, although the sialoside-binding knockout mutation (Y98F) we included in our HAs may result in a slightly reduced affinity to antibodies that target the sialoside-binding pocket using extended CDRH3 loops, these antibodies are rare and almost exclusively found in humans. Future clinical studies will address whether this mutation impacts the elicitation of these rare antibodies. Finally, detailed serological analyses in human subjects will also define the potential for

qsMosaic-I53_dn5 to provide multi-season protection.

Understanding the mechanistic basis responsible for the exceptionally broad immune responses elicited by the nanoparticle immunogens described here may bring us a step closer to the ultimate goal of developing a universal influenza vaccine[75]. More generally, our work suggests that precisely designed two-component nanoparticles may be useful for generating vaccines that induce broadly protective immunity against other rapidly evolving pathogens and pandemic threats.

Contributors and acknowledgements
I would like to thank Seyhan Boyoglu-Barnum, Neil P. King, Masaru Kanekiyo and Barney Graham for their leadership and extensive contributions to this project. I would also like to thank Rebecca A. Gillespie, Geoffrey B. Hutchinson, Young-Jun Park, Syed M. Moin, Oliver J. Acton, Rashmi Ravichandran, Mike Murphy, Deleah Pettie, Nick Matheson, Lauren Carter, Adrian Creanga, Michael J. Watson, Sally Kephart, Sila Ataca, John R. Vaile, George Ueda, Michelle C. Crank, Lance Stewart, Kelly K. Lee, Miklos Guttman, David Baker, John R. Mascola and David Veesler for direct contributions to this project. As well, I would like to thank K. Foulds, A. Noe, S.-F. Kao, V. Ficca, N. Nji, D. Flebbe, and E. McCarthy (VRC) for help with nonhuman primate experiments; A. Taylor, H. Bao, C. Chiedi, M. Dillon, L. Gilman, and G. Sarbador, E. McCarthy, J.-P. Todd, Diana Scorpio (VRC) for help with mouse, ferret, and nonhuman primate experiments; H. Andersen, N. Jones, and G. Patel (Bioqual) for help with influenza challenge studies; R. Webby (St. Jude Children's Research Hospital) for providing influenza reverse genetics plasmids; Y. Tsybovsky and T. Stephens (Frederick National Laboratory for Cancer Research) for initial EM screening; A. Reers and P. Myler (Seattle Children's Research Institute) for assistance with protein production; and members of the King laboratory and the Influenza Program at the VRC for comments on the manuscript. This study was supported by the intramural research program of the Vaccine Research Center, National Institute of Allergy and Infectious Diseases, National Institutes of Health (M.K. and B.S.G.); a generous gift from the Open Philanthropy Project (D.B. and N.P.K.); a generous gift from the Audacious Project (D.B. and N.P.K.); the National Institute of General Medical Sciences (R01GM120553, D.V.); the National Institute of Allergy and Infectious Diseases (DP1AI158186 and HHSN272201700059C to DV); a Pew Biomedical Scholars Award (D.V.); an Investigators in the Pathogenesis of Infectious Disease Award from the Burroughs Wellcome Fund (D.V.); and the University of Washington Arnold and Mabel Beckman cryo-EM center. Molecular graphics and analyses performed with UCSF ChimeraX, developed by the Resource for Biocomputing, Visualization, and Informatics at the University of California, San Francisco, with support from National Institutes of Health R01-GM129325 and the Office of Cyber Infrastructure and Computational Biology, National Institute of Allergy and Infectious Diseases.

Supplemental figures

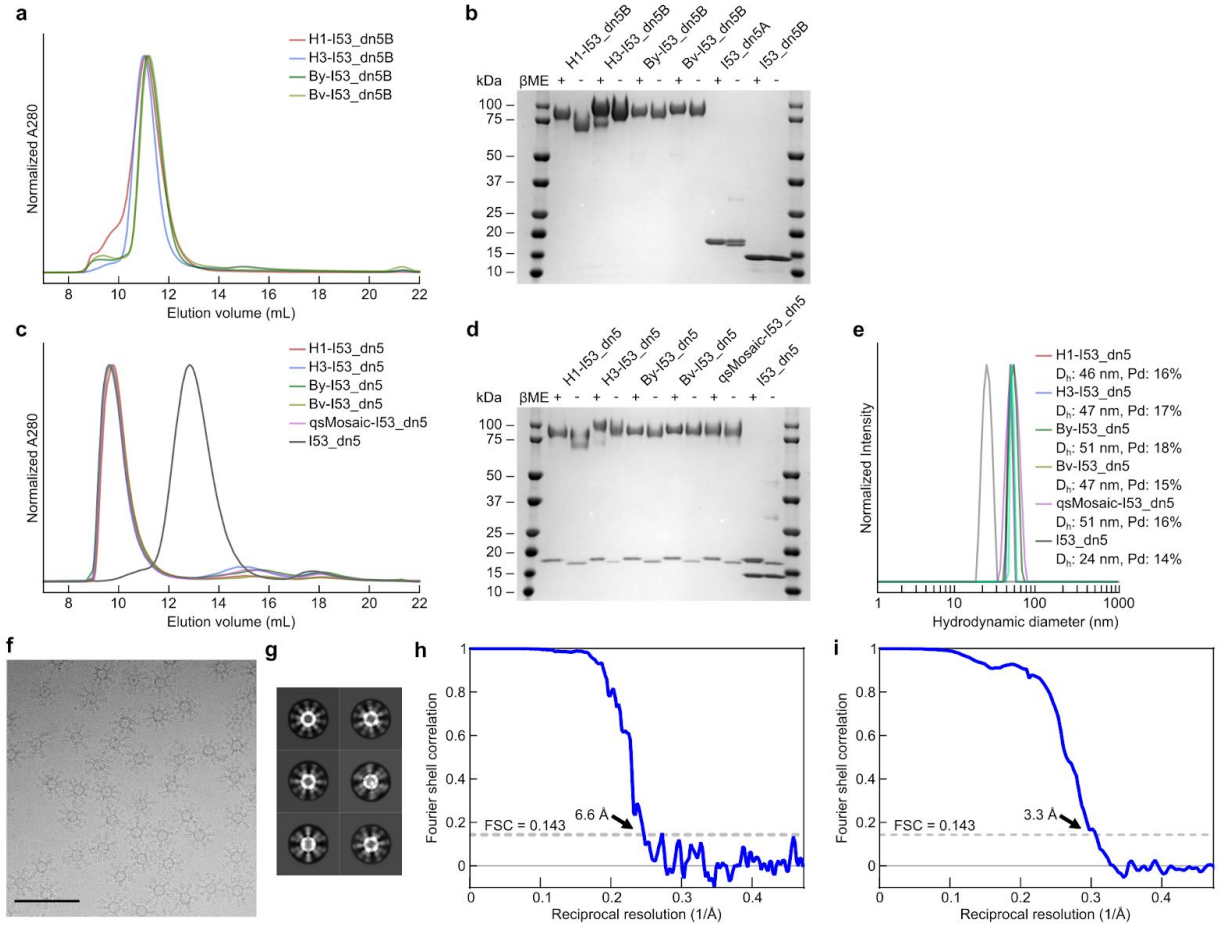

Fig. S1.1 | Production and characterization of HA-I53_dn5 components and nanoparticle immunogens. a, SEC purification of seasonal HAs fused to I53_dn5B trimeric components, using a Superdex 200 Increase 10/300 GL column. **b,** Reducing and non-reducing SDS-PAGE of SEC-purified trimeric HA-I53_dn5B fusions, pentameric I53_dn5A component, and I53_dn5B trimer lacking fused HA. **c,** SEC purification of nanoparticle immunogens after *in vitro* assembly, including I53_dn5 lacking displayed antigen, using a Superose 6 Increase 10/300 GL column. The nanoparticle immunogens elute at the void volume of the column, while I53_dn5 is resolved. Residual, unassembled trimeric and pentameric components elute around 15 mL and 18 mL, respectively. **d,** Reducing and non-reducing SDS-PAGE of SEC-purified nanoparticle immunogens and I53_dn5. **e,** Dynamic light scattering (DLS) of SEC-purified nanoparticle immunogens, including I53_dn5. **f,** Representative electron micrograph of H1-I53_dn5 embedded in vitreous ice. Scale bar, 100 nm. **g,** 2D class averages obtained using single-particle cryo-EM. **h,** Gold-standard Fourier shell correlation curve for the H1-I53_dn5 density map presented in Fig. 1.1e. **i,** Gold-standard Fourier shell correlation curve for the localized reconstruction of H1 MI15 presented in Fig. 1.1e.

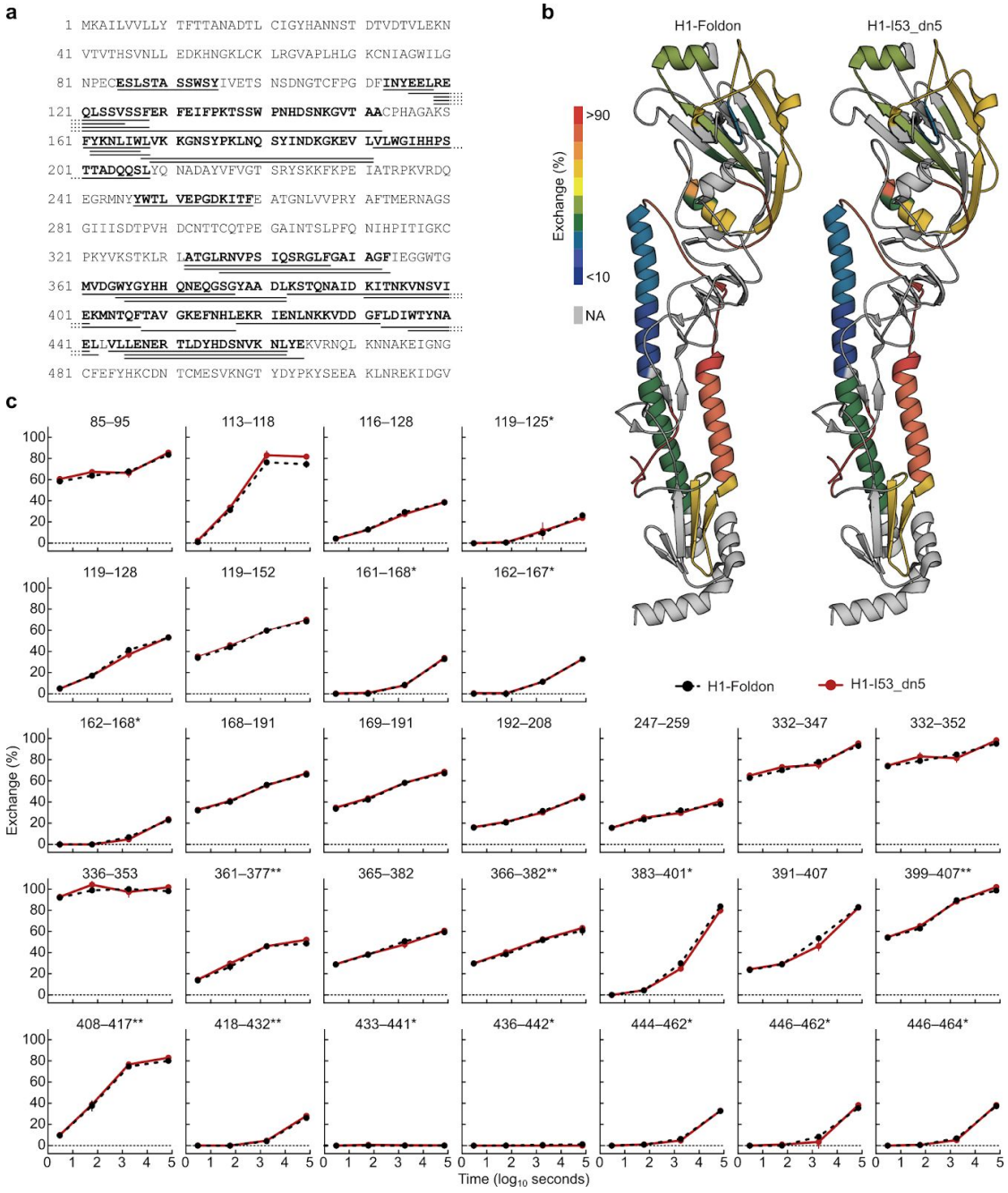

Fig. S1.2 | Hydrogen-deuterium exchange mass spectrometry (HDX-MS) of H1-foldon trimer and H1-I53_dn5 nanoparticle. a, Amino acid sequence of H1 ectodomain expressed as a genetic fusion to both foldon and I53_dn5B. Underlined sequences correspond to peptides analyzed by HDX-MS. **b,** Hydrogen-deuterium exchange percentages after 20 h for both samples mapped onto the structure of H1 HA (PDB 3LZG). **c,** Kinetics of hydrogen-deuterium exchange for both samples at multiple timepoints up to 20 h. *, peptides where a negative percent exchange was corrected to zero (< 2% magnitude correction); **, peptides that were missing a replicate at the 30 min timepoint.

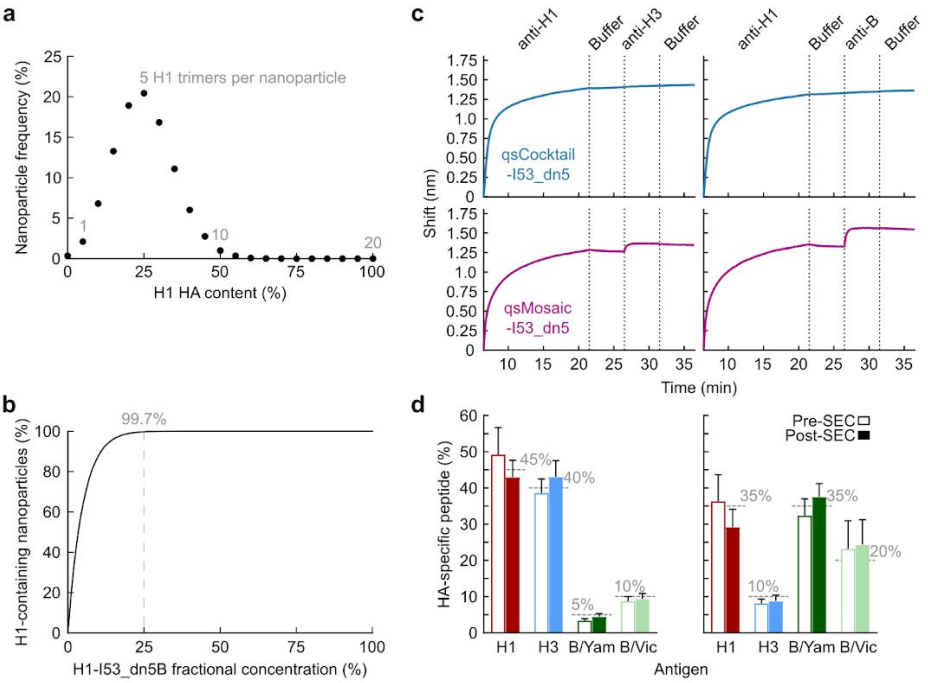

S1.3 | Controllable co-display of multiple antigenic variants on two-component nanoparticle immunogens. a, Numerical approximation of the H1 HA content of individual qsMosaic-I53_dn5 nanoparticles assuming an equimolar quadrivalent *in vitro* assembly reaction (i.e., 25% of the input HA-I53_dn5B trimers bear H1 HA) and random incorporation of each HA-I53_dn5B trimer at each of the 20 trimeric positions into the nanoparticle. A distribution centered on 25% valency (5 H1 HA trimers per nanoparticle) is observed. **b,** Calculation of the fraction of individual mosaic nanoparticles displaying at least one H1 HA trimer as a function of the fractional concentration of H1-I53-dn5B in the *in vitro* assembly reaction ([H1]), expressed as: $1 - (1 - [H1])^{20}$. At the 25% fractional concentration used to assemble qsMosaic-I53_dn5, 99.7% of the individual nanoparticles are expected to display at least one H1 HA trimer. **c,** Sandwich BLI comparing qsCocktail-I53_dn5 and qsMosaic-I53_dn5. Biotinylated 5J8 immobilized on streptavidin probes was used to capture H1-containing nanoparticles from each sample. The captured particles were then exposed to antibodies specific to H3 (CR8020; left) or influenza B HA (CR8071; right). **d,** Quantitation of HA antigen content in two distinct qsMosaic-I53_dn5 nanoparticles with non-uniform antigen ratios before and after preparative SEC by peptide mass spectrometry. Dashed grey lines represent the fractional concentration of each HA in the *in vitro* assembly reactions used to prepare the mosaic nanoparticle immunogens, and error bars represent the standard deviation of measurements across four unique peptides from each HA.

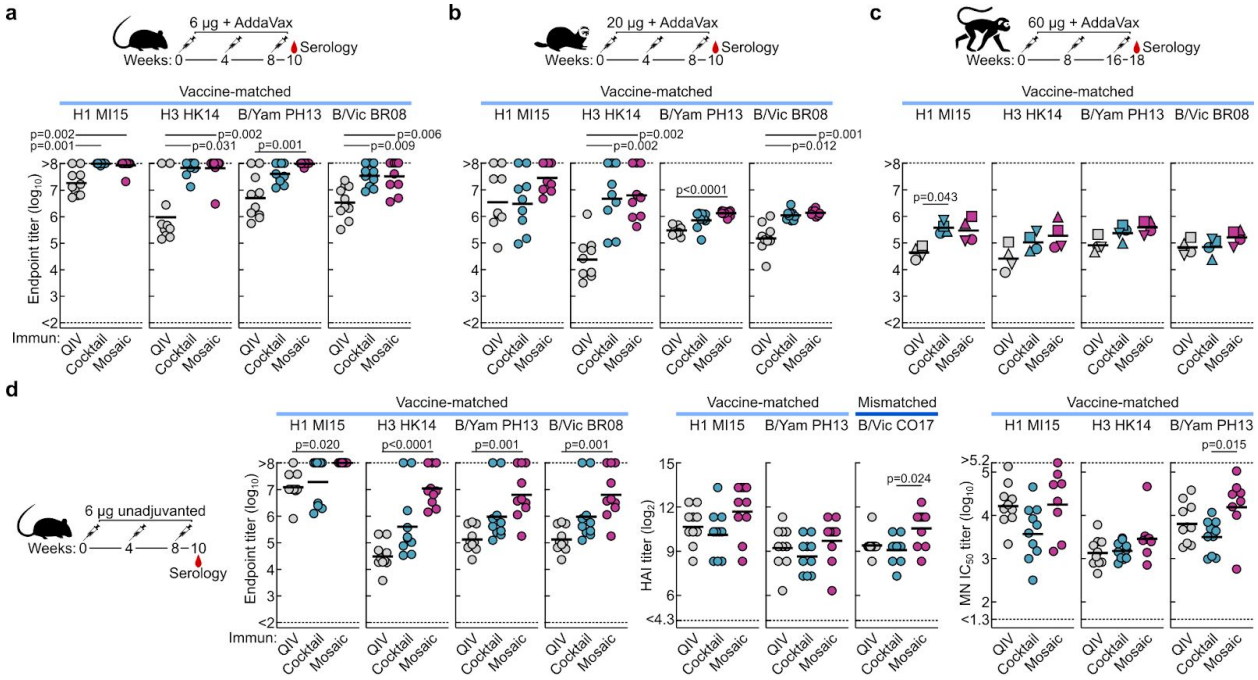

Fig. S1.4 | Vaccine-elicited antibody responses against vaccine-matched antigens. HA-specific antibody titers in immunized mice (**a**), ferrets (**b**), and NHPs (**c**). Immunization schemes are shown at the top of each panel. All immunizations were given intramuscularly with AddaVax. Groups of BALB/cJ mice (*N* = 10), Finch ferrets (*N* = 9), and rhesus macaques (*N* = 4) were used in each experiment. ELISA antibody titers are expressed as endpoint dilutions. Each symbol represents an individual animal and the horizontal bar indicates the geometric mean of the group. Individual NHPs are identified by unique symbols. **d,** Antibody responses against vaccine-matched antigens and viruses elicited by unadjuvanted vaccines in immunized mice. Immunization scheme is shown. All immunizations were given intramuscularly. Groups of BALB/cJ mice (*N* = 10) were used. HA-specific ELISA binding antibody (left), hemagglutination inhibition (HAI) (middle), and microneutralization titers (right) in immune sera are shown. Microneutralization titers are reported as half maximal inhibitory dilution (IC_{50}). Each symbol represents an individual animal and the horizontal bar indicates the geometric mean of the group. Statistical analysis was performed using nonparametric Kruskal–Wallis test with Dunn's multiple comparisons. All animal experiments except for NHP were performed at least twice and representative data are shown.

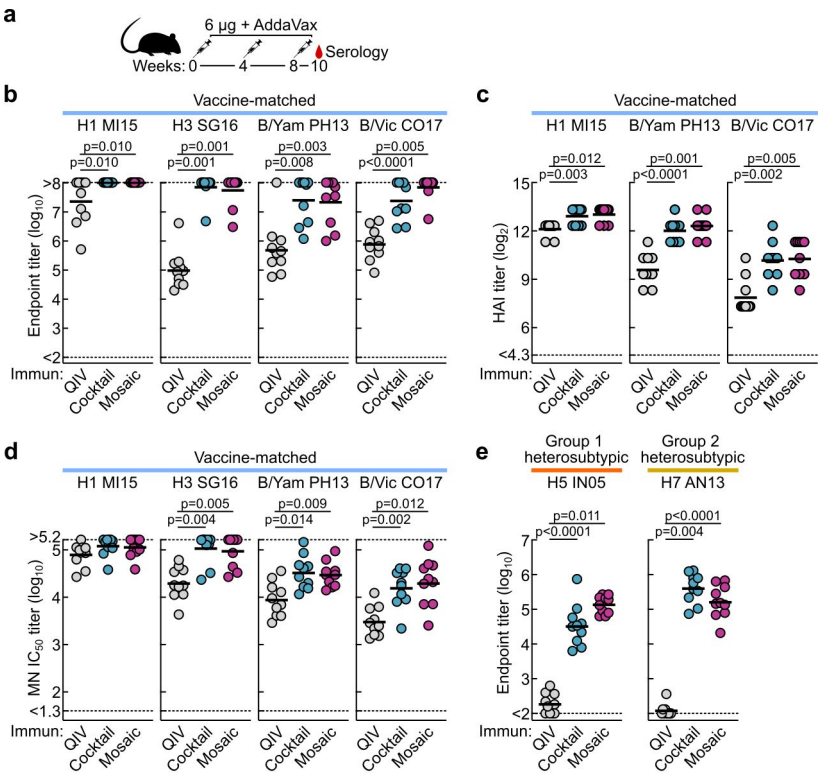

Fig. S1.5 | Antibody responses against vaccine-matched antigens and viruses elicited by 2018-2019 vaccines. a, Immunization scheme. The commercial QIV, qsCocktail-I53_dn5, and qsMosaic-I53_dn5 vaccines used in this study comprised the WHO-recommended 2018-2019 vaccine strains. All immunizations were given intramuscularly with AddaVax. Groups of BALB/cJ mice (*N* = 10) were used. **b,** HA-specific antibody, **c,** hemagglutination inhibition (HAI), and **d,** microneutralization titers in immune sera. Microneutralization titers are reported as half maximal inhibitory dilution (IC_{50}). **e,** Heterosubtypic HA-specific antibody titers in immune sera. Each symbol represents an individual animal and the horizontal bar indicates the geometric mean of the group. Statistical analysis was performed using nonparametric Kruskal–Wallis test with Dunn's multiple comparisons. The animal experiment was performed once.

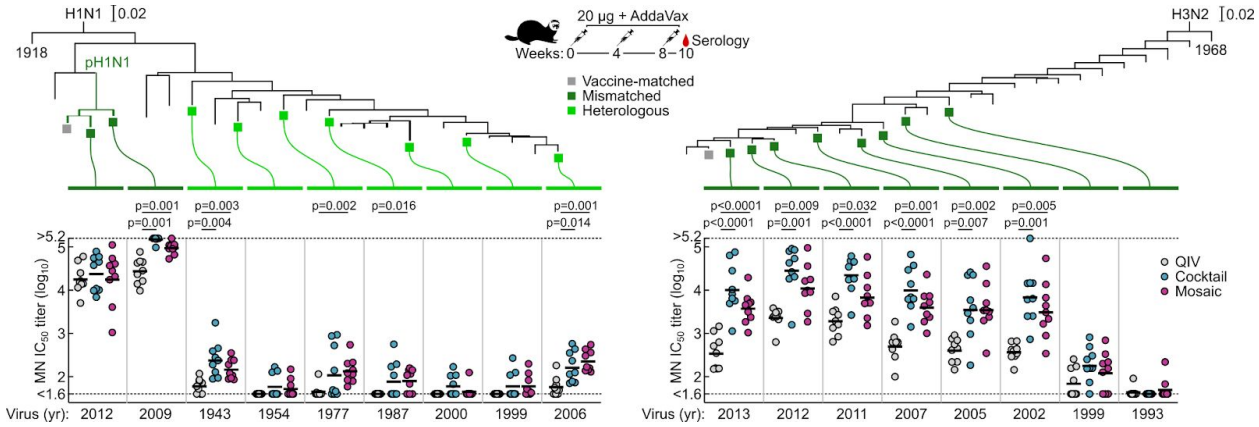

Fig. S1.6 | Neutralization of historical H1N1 and H3N2 viruses. Immunization scheme for ferret study is shown. Groups of Finch ferrets (*N* = 9) were used. Neutralization of representative panels of historical H1N1 and H3N2 viruses by ferret immune sera. Phylogenetic trees of HA sequences of human H1N1 (left) and H3N2 (right) viruses are shown. Each symbol represents an individual animal and the horizontal bar indicates the geometric mean of the group. Statistical analysis was performed using nonparametric Kruskal–Wallis test with Dunn's multiple comparisons. Ferret experiments were performed twice and representative data are shown.

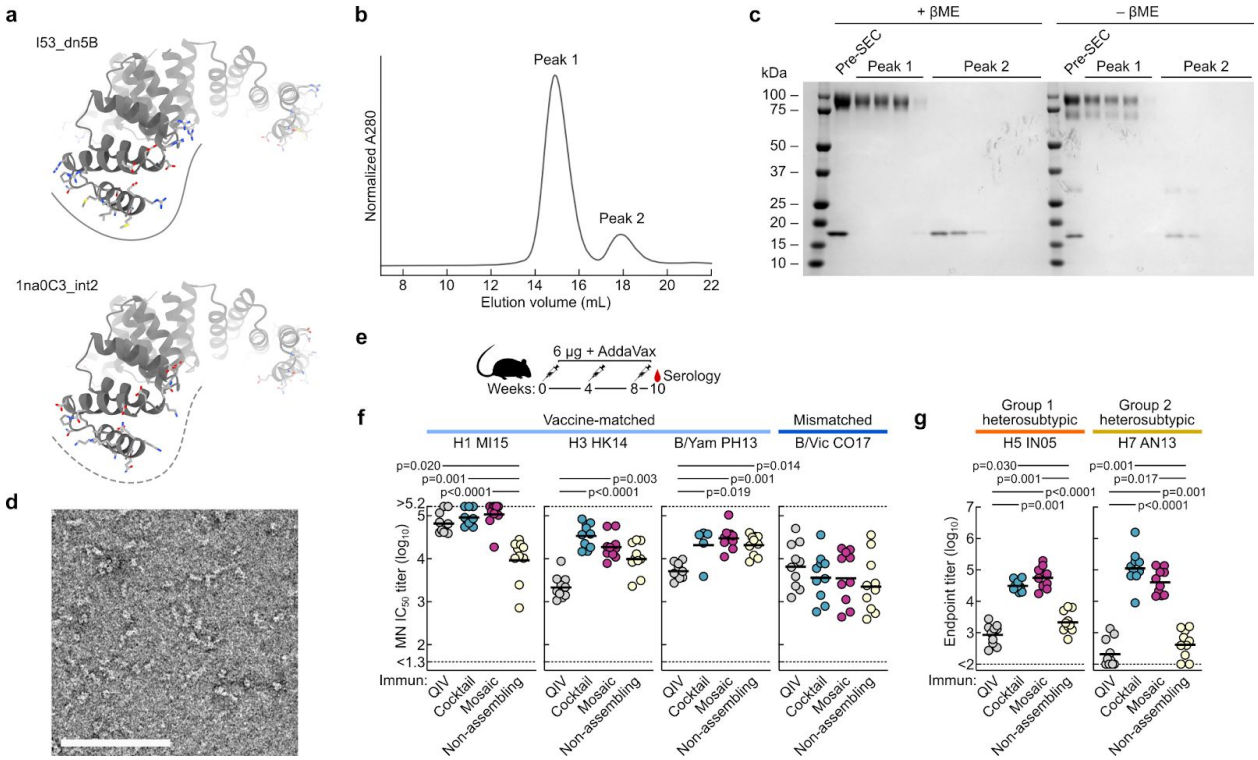

Fig. S1.7 | Antibody responses elicited by a non-assembling immunogen. a, Model of the I53_dn5B trimer, with the computationally designed interface that drives nanoparticle assembly indicated by the solid line (top), and the 1na0C3_int2 trimer, in which the interface mutations were reverted to their original identities (bottom). The dotted line indicates the inability of this molecule to drive nanoparticle assembly. **b,** Analytical SEC of the non-assembling immunogen (a mixture of four HA-1na0C3_int2 trimers with pentameric I53_dn5A) using a Superose 6 Increase 10/300 GL column. Only unassembled oligomeric components were observed. **c,** Reducing and non-reducing SDS-PAGE analysis of the non-assembling immunogen before and after analytical SEC. **d,** Negative stain EM of the non-assembling immunogen, which confirmed the absence of higher-order structures indicated by analytical SEC. Scale bar, 100 nm. **e,** Immunization scheme in mice. All immunizations were given intramuscularly with AddaVax. Groups of BALB/cJ mice (N = 10) were used in the experiment. **f,** Microneutralization titers in immune sera against vaccine-matched or slightly mismatched viruses. Microneutralization titers are reported as half maximal inhibitory dilution (IC_{50}). **g,** Cross-reactive antibody titers in immune sera. Each symbol represents an individual animal and the horizontal bar indicates the geometric mean of the group. Statistical analysis was performed using nonparametric Kruskal–Wallis test with Dunn's multiple comparisons. The animal experiment was performed once.

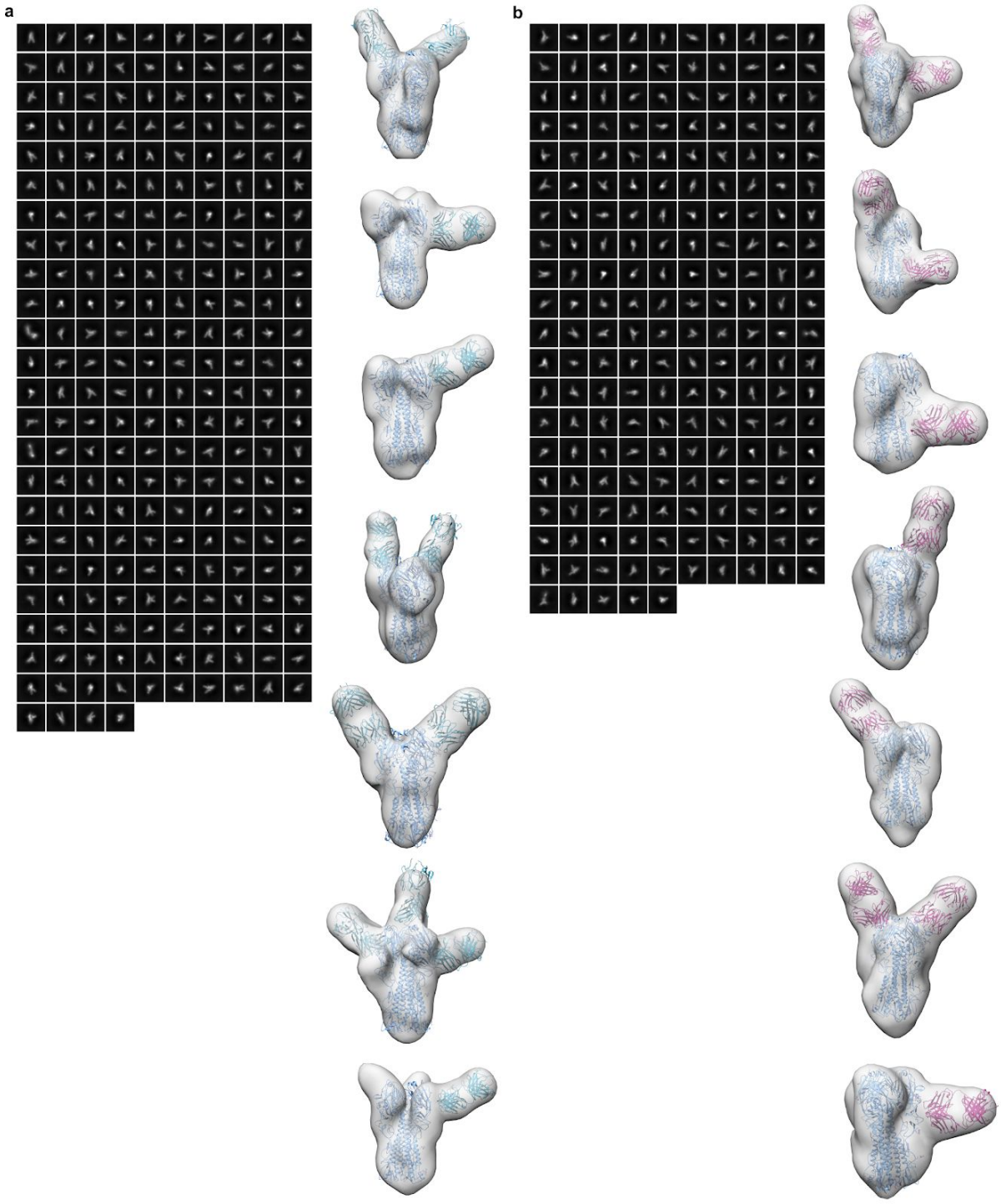

Fig. S1.8 | NS-EM analysis of H1 HA complexed with polyclonal antibody Fabs prepared from NHPs immunized with qsCocktail-I53_dn5 or qsMosaic-I53_dn5. a, NS-EM analysis of Fabs obtained from qsCocktail-I53_dn5-immunized NHPs in complex with recombinant H1 MI15 HA trimers. Two-dimensional classifications were generated by using 847,873 particles collected from 4,112 micrographs. The frequencies of complexes containing Fab fragments bound to RBD (81%), VE (18%), or stem (1%) domains are presented as pie charts in Fig. 1.5c. **b,** NS-EM analysis of Fabs obtained from qsMosaic-I53_dn5-immunized NHPs in complex with recombinant H1 MI15 HA trimers. Two-dimensional classifications were generated by using 997,557 particles collected from 3,237 micrographs. The

frequencies of complexes containing Fab fragments bound to RBD (69%), VE (24%), or stem (7%) domains are presented as pie charts in Fig. 1.5c. Left side of each panel shows representative reference-free 2D class averages. Right side of each panel shows seven representative 3D reconstructions of HA–Fab complexes. Single complexes containing Fabs of multiple specificities were counted once against each specificity. The coordinates of an H1 HA crystal structure (PDB 1RUZ) and a Fab fragment (PDB 3GBN) were fitted into the EM densities. Light blue ribbons, H1 HA; violet or turquoise ribbons, Fabs.

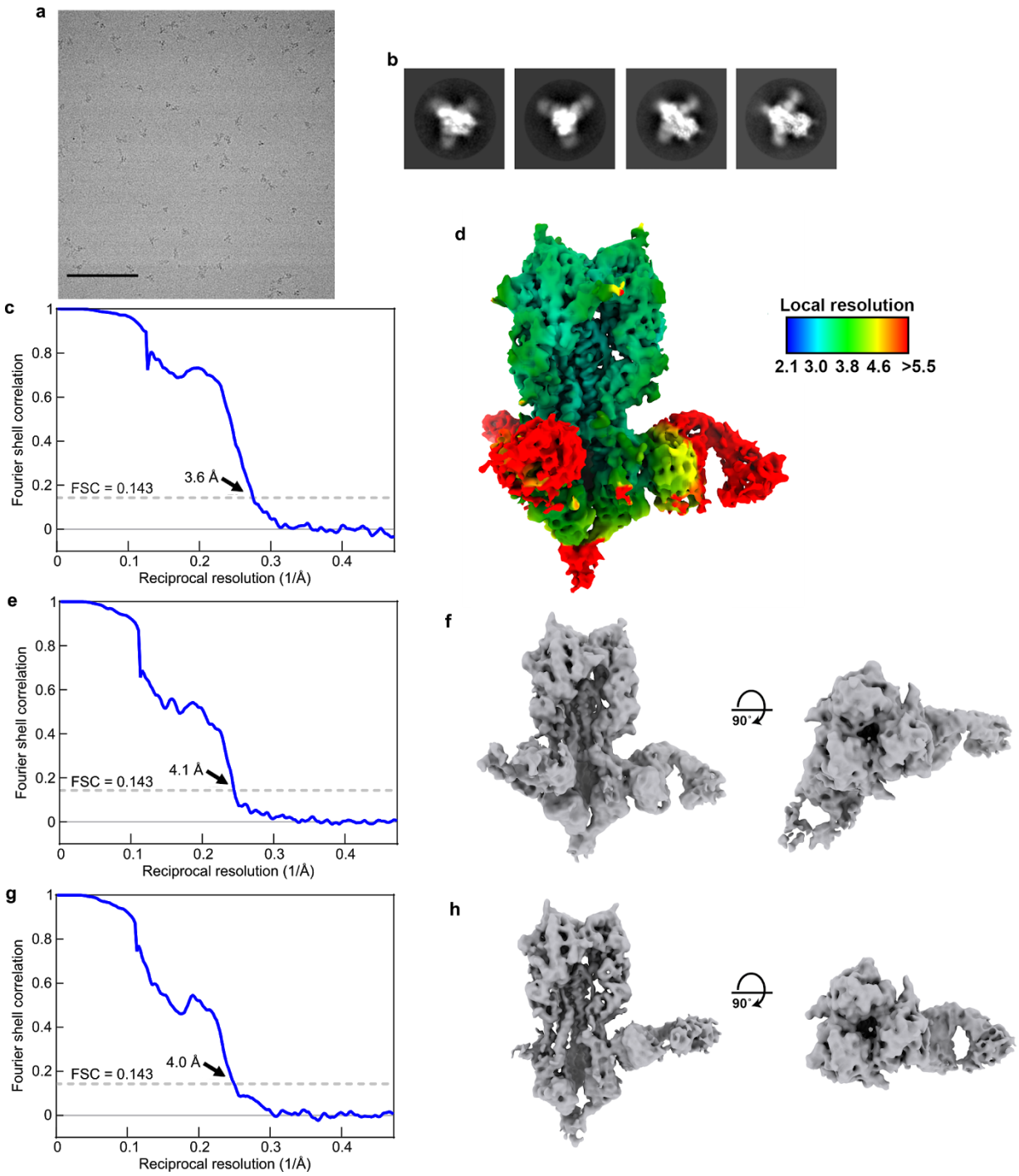

Fig. S1.9 | CryoEM analysis of heterosubtypic H5 HA in complex with polyclonal antibody Fab fragments prepared from NHP immunized with qsMosaic-I53_dn5. a, Representative cryo-electron micrograph. Scale bar, 100 nm. **b,** Reference-free 2D class averages. **c,** Gold-standard Fourier shell correlation (FSC) curve for the asymmetric reconstruction shown in **d**. **d,** Asymmetric cryo-EM reconstruction of H5 HA–Fab complexes with Fab fragments bound to all three HA subunits at 3.6 Å resolution. The reconstruction is the same as that shown in the right panel in Fig. 1.5d, but here is colored by local resolution. **e,** FSC curve for the asymmetric reconstruction shown in **f**. **f,** Two orthogonal orientations of an asymmetric cryo-EM reconstruction of H5 HA–Fab complexes with Fab fragments bound to two HA subunits at 4.1 Å resolution. **g,** FSC curve for the asymmetric reconstruction shown in **h**.

h, Two orthogonal orientations of an asymmetric cryo-EM reconstruction of H5 HA–Fab complexes with Fab fragments bound to one HA subunit at 4.0 Å resolution. The reconstruction is the same as that shown in the left panel in Fig. 51.d.

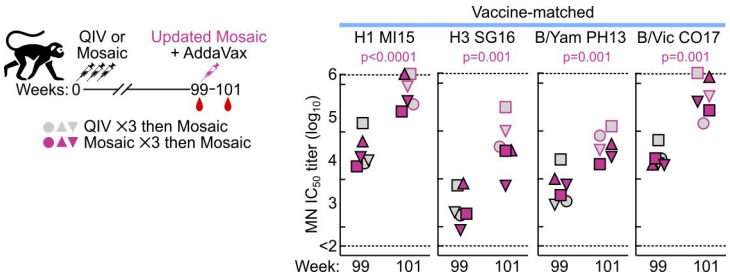

Fig. S1.10 | Vaccine-elicited antibody responses against vaccine-matched viruses in NHPs with preexisting influenza immunity. Immunization scheme for NHP study shown on the left. NHPs (*N* = 3) had been immunized three times with either QIV 2017-2018 or qsMosaic-I53_dn5 2017-2018 were boosted 63 weeks later with a single dose (60 μg) of updated qsMosaic-I53_dn5 2018-2019. All immunizations were given intramuscularly with AddaVax. Microneutralization titers are reported as half maximal inhibitory dilution (IC_{50}). Each symbol represents an individual animal and the horizontal bar indicates the geometric mean of the group. Individual NHPs are identified by unique symbols. Statistical analysis was performed using paired t test.

Materials and Methods

Gene synthesis and vector construction

Plasmids for expression of the I53_dn5A pentamer were prepared in pET29b as previously described[42]. Genes for expression of HA fusions to nanoparticle trimeric components were codon optimized for expression in human cells and cloned into the CMV/R (VRC 8400) mammalian expression vector by Genscript. All HA fusions to the I53_dn5B trimer contained full-length HA ectodomains including native secretion signals, and the H1 and H3 HAs contained an additional mutation (Y98F) to knock out sialic acid binding to facilitate expression and purification[76]. HA ectodomain sequences preceded a short linker sequence followed by the I53_dn5B trimer sequence with a C-terminal flexible linker, WELQut protease recognition sequence, and a hexa-histidine tag.

Protein expression and purification

All HA-I53_dn5B trimers, as well as mAbs CR6261 (ref. 77), 5J8 (ref. 78), CR8020 (ref. 79), F005-126 (ref. 80), F045-092 (ref. 81), MEDI8552 (ref. 57), FI6v3 (ref. 54), CR9114 and CR8071 (ref. 82), CT149 (ref. 83), D25 (ref. 84), and MPE8 (ref. 85) were expressed in Expi293F cells (ThermoFisher Scientific) by transient transfection using PEI MAX (Polysciences) or ExpiFectamine™ 293 (ThermoFisher Scientific). mAbs were purified by protein A affinity chromatography using established methods. Recombinant HA ectodomain trimers fused to T4 fibritin foldon were produced and purified as described previously[34]. The protein-containing supernatants from cells expressing HA-I53_dn5B fusion proteins were further clarified by vacuum filtration (0.22 μm, Millipore Sigma). Prior to immobilized metal affinity chromatography, a background of 50 mM Tris pH 8.0 and 350 mM NaCl was added to the clarified supernatant using concentrated solutions of 1 M Tris pH 8.0 and 5 M NaCl, respectively. For each liter of supernatant, 4 ml of Ni^{2+} Sepharose Excel resin (GE) was rinsed into PBS using a gravity column and then added to the supernatant, followed by overnight shaking at 4°C. The resin was collected 16–24 h later using a gravity column, then washed

twice with 50 mM Tris pH 8.0, 500 mM NaCl, 30 mM imidazole prior to elution of His-tagged protein using 50 mM Tris pH 8.0, 500 mM NaCl, 300 mM imidazole. Eluates were concentrated and applied to a HiLoad 16/600 Superdex 200 pg column or a Superdex 200 Increase 10/300 GL column pre-equilibrated with PBS for preparative size exclusion chromatography. Peaks corresponding to trimeric species were identified based on elution volume and SDS-PAGE (both reducing and non-reducing) of elution fractions. Fractions containing pure HA-I53_dn5B were pooled and the protein quantified using UV/vis spectroscopy. Purified protein was either stored at 4°C until use or flash-frozen in liquid nitrogen and stored at -80°C.

Single colonies of *E. coli* cells transformed with plasmid encoding the I53_dn5A pentamer were picked and grown in TB medium with 50 μg L^{-1} kanamycin at 37°C overnight. Subsequently, liquid cultures were diluted 1:40 in TB medium and grown at 37°C until OD_{600} reached 0.5–0.8. Isopropyl-thio-β-D-galactopyranoside (IPTG) was then added to a concentration of 1 mM and the growth temperature reduced to 18°C to induce protein expression, or cultures were left at 37°C for an additional 5 h before lowering the temperature to 18°C leading to auto-induction by virtue of galactose in the media according to the Studier protocols[86]. Expression proceeded for 20 h at 18°C, at which point the cell cultures were harvested by centrifugation. Cell pellets were resuspended in 50 mM Tris pH 8.0, 250 mM NaCl, 20 mM imidazole, 1 mM dithiothreitol (DTT), 0.1 mg ml^{-1} DNase, 0.1 mg ml^{-1} RNase, and EDTA-free protease inhibitors (Pierce) and lysed by sonication or microfluidization. I53_dn5A protein was purified from the soluble fraction of cell lysates by immobilized metal affinity chromatography using HisTrap HP columns (GE). After application of clarified cell lysate supernatants, the column was washed with 20 column volumes of 50 mM Tris pH 8.0, 250 mM NaCl, 20 mM imidazole, 1 mM DTT. I53_dn5A was eluted using a linear gradient of imidazole up to a final concentration of 500 mM. Protein was concentrated to 1 ml, and 3-[(3-Cholamidopropyl)dimethylammonio]-1-propanesulfonate (CHAPS) was added to 0.75% (w/v) to remove endotoxin. The protein was sterile-filtered at 0.22 μm and purified by preparative SEC using a Superdex 200 Increase 10/300 GL equilibrated in 25 mM Tris pH 8.0, 150 mM NaCl, 5% glycerol. The peak corresponding to the pentamer was identified based on elution volume and SDS-PAGE (both reducing and non-reducing) of eluted fractions. Fractions containing pure I53_dn5A pentamer were pooled and the protein quantified using UV/vis spectroscopy. The samples were confirmed to be low in endotoxin (< 100 EU mg^{-1}) using the Limulus Amebocyte Lysate (LAL) assay (Charles River), then flash-frozen in liquid nitrogen and stored at -80°C within 6 hours of purification to prevent oxidation of cysteines.

***In vitro* assembly and purification of nanoparticle immunogens**

To assemble nanoparticle immunogens bearing multiple copies of single HA antigens (e.g., H1-I53_dn5), individual HA-bearing trimeric components were mixed with pentameric I53_dn5A at a molar ratio of 1:1 (subunit:subunit) at concentrations ranging from 15–40 μM (subunit) by pipetting. Assembly reactions were prepared at room temperature and incubated for 30 min before purification by SEC on a Superose 6 Increase 10/300 GL. The nanoparticle immunogens eluted at the void volume of the column. Fractions were analyzed by SDS-PAGE (both reducing and non-reducing) before pooling and sterile filtering at 0.22 μm.

For H1- and H3-bearing components, the assembly reactions consisted of pentameric components and HA-bearing trimeric components buffered in either PBS or 25 mM Tris pH 8.0, 150 mM NaCl, 5% glycerol. After assembly and incubation, the samples were centrifuged for 10 min at 14,000 rpm at 4°C and the nanoparticle immunogens purified by SEC using a Superose 6 Increase 10/300 GL column pre-equilibrated with 25 mM Tris pH 8.0, 150 mM NaCl, 5% glycerol.

For B/Vic- and B/Yam-bearing components, half of the volume of the assembly solution consisted of an additional buffer solution with high ionic strength to maintain nanoparticle immunogen solubility. The solutions used were 25 mM Tris pH 8.0, 1.85 M NaCl, 5% glycerol for B/Vic and 25 mM Tris pH 8.0, 3.85 M NaCl, 5% glycerol for B/Yam, which respectively brought NaCl in the assembly reactions to approximately 1 M and 2 M. In these cases the HA-bearing trimeric component was first added to the high-salt buffer prior to addition of the pentameric component. After assembly and incubation, the samples were centrifuged for 10 min at 14,000 rpm at room temperature and the nanoparticle immunogens purified by SEC using a Superose 6 Increase 10/300 GL column pre-equilibrated with either 25 mM Tris pH 8.0, 1 M NaCl, 5% glycerol for B/Vic-I53_dn5 or 25 mM Tris pH 8.0, 2 M NaCl, 5% glycerol for B/Yam-I53_dn5.

For mosaic nanoparticles with equal amounts of each seasonal HA (qsMosaic-I53_dn5), all four HA-bearing trimeric components (in PBS) were first mixed in equimolar amounts. Tris pH 8.0, 1.85 M NaCl, 5% glycerol was added such that the final NaCl in the *in vitro* assembly reaction would be 1 M. The pentameric component was added and the solution was mixed vigorously by pipetting. After assembly and incubation, the samples were centrifuged for 10 min at 14,000 rpm at 4°C and the nanoparticle immunogens purified by SEC using a Superose 6 Increase 10/300 GL column pre-equilibrated with 25 mM Tris pH 8.0, 150 mM NaCl, 5% glycerol.

After purification and evaluation of nanoparticle immunogen quality by SDS-PAGE, UV/vis spectroscopy, negative stain EM, DLS, and LAL assay (< 100 EU mg^{-1}), samples were flash-frozen in liquid nitrogen and stored at -80°C.

Dynamic light scattering

Light scattering analysis was conducted using an UNcle (UNchained Labs) at 25°C. For each sample, 10 acquisitions (5 s per acquisition) were obtained using auto-attenuation of the laser. Increased viscosity due to the inclusion of 5% glycerol in the H1-I53_dn5, H3-I53_dn5, B/Yam-I53_dn5, B/Vic-I53_dn5, qsMosaic-I53_dn5 and I53_dn5 nanoparticles was accounted for in the software.

Negative stain and cryo-electron microscopy of immunogens

To image nanoparticles and non-assembling immunogens by negative stain EM, protein samples were diluted to 0.020–0.075 mg ml^{-1} in 25 mM Tris pH 8.0 with NaCl concentrations ranging from 0.15–2 M. 300 mesh copper grids (Ted Pella) were glow discharged immediately before use. Six µL of sample was applied to the grid for 1 min, then briefly dipped in a droplet of water before blotting away excess liquid with Whatman No. 1 filter paper. Grids were stained with 6 µL of 0.75% (w/v) uranyl formate stain, immediately blotting away excess, then stained

again with another 6 µL for 30 s. Grids were imaged on a Morgagni transmission electron microscope with a Gatan camera, and Gatan Digital Micrograph software was used to take images.

To obtain a cryo-EM single particle reconstruction of the H1-I53_dn5 nanoparticle, 3 µl of 0.7 mg ml^{-1} H1-I53_dn5 was loaded onto a freshly glow-discharged (30 s at 20 mA) Protochips C-flat grid (2.0 µm hole, 200 mesh) by multiple blotting strategy[87] prior to plunge freezing using a vitrobot Mark IV (ThermoFisher Scientific) using a blot force of 0 and 7 second blot time at 100% humidity and 25°C. Data was collected using the Leginon software[88] on an FEI Titan Krios transmission electron microscope, equipped with a Gatan K2 Summit direct electron detector and Gatan Quantum GIF energy filter, operated in zero-loss mode with a slit width of 20 eV. The dose rate was adjusted to 8 counts $pixel^{-1}$ s^{-1}, and each movie was acquired in counting mode fractionated in 50 frames of 200 ms. 803 micrographs were collected in a single session with a defocus range between -1.2 µm and -2.5 µm. Movie frame alignment, estimation of the microscope contrast-transfer function parameters and particle picking were carried out using Warp[89]. 2D and 3D classification (without applying symmetry) were performed using RELION 3.0. A total of 20,827 particles of the best class were selected and subjected to 3D refinement in CryoSPARC applying icosahedral symmetry which led to a reconstruction at 6.6 Å resolution. We subsequently implemented a previously reported localized reconstruction strategy[48] (along with extensive 3D classification using Relion) to determine a reconstruction of the H1 MI15 HA at 3.3 Å resolution using Relion (applying C3 symmetry). An atomic model of H1 MI15 HA was built using Coot[90], refined using Rosetta[91,92], and validated used Molprobity[93], Phenix[94], Privateer[95] and EMRinger[96]. Reported resolutions are based on the gold-standard Fourier shell correlation (FSC) of 0.143 criterion and Fourier shell correlation curves were corrected for the effects of soft masking by high-resolution noise substitution[97].

Immunoprecipitation

qsCocktail-I53_dn5 and qsMosaic-I53_dn5 samples were mixed with either MPE8 (anti-RSV F) or 5J8 (anti-H1) to final concentrations of 4 µM (each subunit) of immunogen and 0.20 mg ml^{-1} of mAb. The final buffers contained 2 M NaCl and 0.05% Tween-20 in addition to other buffering agents. The solution was allowed to mix at room temperature for 1 h and then added to recently washed and dried magnetic protein G Dynabeads (Thermo Fisher). The mixture was incubated for 1.5 h and resin was separated from the supernatant magnetically. Beads were washed twice and returned to the same volume used during the binding process, then heated to 95°C for 10 min in the presence of SDS loading dye to detach bound protein. Proteins were then analyzed by SDS-PAGE.

Antigenic characterization

ELISA was used to measure binding of H1-I53_dn5, H3-I53_dn5, B/Yam-I53_dn5, B/Vic-I53_dn5, and qsMosaic-I53_dn5 nanoparticles to mAbs CR6261, 5J8, CR8020, F005-126, MEDI8852, FI6v3, CR9114, CR8071, and D25 (anti-RSV F). 96-well plates were coated with 2 µmol ml-1 nanoparticles (0.1 ml $well^{-1}$) and incubated at 4°C overnight. Plates were then blocked with PBS containing 5% skim milk at 37°C for 30 min. mAbs were serially diluted in four-fold steps and added to the wells for 1 h. Horseradish peroxidase

(HRP)-conjugated anti-human or anti-mouse IgG (Southern Biotech) was added and incubated at 37°C for 30 min. The wells were developed with 3,3′,5′,5-tetramethylbenzidine (TMB) substrate (KPL), and the reactions were stopped by adding 1 M H_2SO_4 before measuring absorbance at 450 nm with a Spectramax Paradigm plate reader (Molecular Devices).

Mass spectrometry quantification of HA content in qsMosaic-I53_dn5

Label-free quantitation was performed by peptide mass spectrometry to determine the relative abundance of each HA present in the mosaic nanoparticle samples. Each mosaic nanoparticle, either before or after SEC purification, along with a standard mixture of each purified HA-I53_dn5B fusion protein at equimolar concentrations (1:1:1:1), was denatured and reduced using guanidine hydrochloride and DTT. Samples were then alkylated with iodoacetamide, deglycosylated with N-glycanase (New England Biolabs), and digested overnight with LysC protease (ThermoFisher scientific). LC-MS was performed using a Waters Acquity UPLC coupled to a Thermo LTQ-OT using data-dependent acquisition. Peptides were resolved over a Waters CSH C18 1.7 µm, 2.1 × 100 mm column with a linear gradient from 3% to 40% B over 30 minutes (A: 0.1% formic acid; B: acetonitrile with 0.1% formic acid). Peptides were identified from MS/MS data using Protein Prospector using a score cutoff of 15 (http://prospector.ucsf.edu/). Due to the high sequence identity between the HA constructs, only four peptides unique to each specific HA were observed that could be used for label-free quantitation. The integrated peak areas for these peptides relative to the areas from an equimolar mixture of each HA were used to estimate the total abundance of each HA within the mosaic nanoparticle samples.

Hydrogen-deuterium exchange mass spectrometry

For each timepoint, 30 pM of H1 HA-foldon and H1-I53_dn5 were incubated in deuterated buffer (85% D_2O, pH* 7.4) for 3; 60; 1,800; or 72,000 s at room temperature and subsequently mixed with an equal volume of ice-cold quench buffer (4 M urea, 200 mM tris(2-chlorethyl) phosphate (TCEP), 0.2% formic acid) to a final pH* of 2.5. Samples were immediately frozen in liquid nitrogen and stored at 80°C until analysis. Fully deuterated samples were prepared by digesting 30 pmol of undeuterated H1-foldon over a pepsin column, followed by concentration under vacuum, resuspension in deuterated buffer at 65°C for 1 h, then quenching and freezing. Zero timepoint samples were prepared as described previously[98]. Inline pepsin digestion was performed and analyzed by LC-IMS-MS utilizing a Waters Synapt G2-Si Q-TOF mass spectrometer as previously described[98]. Deuterium uptake analysis was performed using HD-Examiner (Sierra Analytics) followed by HX-Express v3.13 (refs. 99,100). The percent exchange was normalized to the zero timepoint and fully deuterated reference samples. Internal exchange standards (Pro-Pro-Pro-Ile [PPPI] and Pro-Pro-Pro-Phe [PPPF]) were included in each reaction to ensure that conditions were consistent throughout all of the labeling reactions.

Animal experiments

All animal experiments were reviewed and approved by the Institutional Animal Care and Use Committee of the VRC, NIAID, NIH. All animals were housed and cared for in accordance with local, state, federal, and institutional policies of NIH and American Association for Accreditation of Laboratory Animal Care.

Immunization and challenge studies

The 2017-2018 and 2018-2019 QIVs used were split virion vaccines manufactured in embryonated chicken eggs (Afluria®, Seqirus). Throughout our studies, we matched the total protein dose of each nanoparticle immunogen to the HA content of QIV. The HA antigens make up approximately 62% of the total peptidic mass of the nanoparticle immunogens. The HA content of commercial QIV was determined by the manufacturer using the standard SRD assay, and the total protein content of the nanoparticle vaccine preparations was measured by UV/vis absorbance. BALB/cJ mice (Jackson Laboratory) were immunized intramuscularly (i.m.) with 6 μg of commercial QIV 2017-2018 (Afluria®, Seqirus), qsCocktail-I53_dn5, or qsMosaic-I53_dn5 in the presence or absence of AddaVax™ (InvivoGen) at weeks 0, 4, and 8. Formulated vaccines were given 50 μl into each hind leg. Serum samples were collected before and after each immunization and used for immunological assays. For challenge studies, mice were infected intranasally at Bioqual with 10×, 25×, 10×, and 10× the experimentally determined 50% lethal dose (LD_{50}) of H1N1, H5N1, H3N2, and H7N9 viruses, respectively. The animals were monitored twice daily for development of clinical signs and weighed daily for 14 days. Any animals that had lost 20% or more of their initial body weight were euthanized. Finch ferrets (*Mustela putorius*) were immunized i.m. with 20 μg of commercial QIV 2017-2018, qsCocktail-I53_dn5, or qsMosaic-I53_dn5 with AddaVax three times at weeks 0, 4, and 8. Immunogens were formulated in 500 μL per ferret and injected into limbs. Serum samples were collected periodically before and after immunization and used for immunological assays. Ferrets were infected intranasally at Bioqual with 25× and 10× LD_{50} of H5N1 and H7N9 viruses, respectively. Clinical signs of infection, weight, and body temperatures were recorded twice daily for 14 days. Ferrets that showed signs of severe disease (prolonged fever, diarrhea; nasal discharge interfering with eating, drinking or breathing; severe lethargy; or neurological signs) or that had > 20% weight loss were euthanized immediately. Rhesus macaques (*Macaca mulatta*) were immunized i.m. with 60 μg of commercial QIV 2017-2018, qsCocktail-I53_dn5, or qsMosaic-I53_dn5 with AddaVax three times at weeks 0, 8, and 16. Immunogens were prepared in 1.0 ml volumes per NHP and injected into limbs. Some of the NHPs that were immunized three times with either 2017-2018 commercial QIV (N = 3) or qsMosaic-I53_dn5 (N = 3) were boosted 63 weeks later with a single dose of an updated version of qsMosaic-I53_dn5 containing the 2018-2019 seasonal strains. Serum samples were collected periodically before and after immunization and used for immunological assays.

ELISA

Antigen-specific IgG levels in immune sera were measured by ELISA. The plates were coated with 2 μg ml^{-1} of recombinant HA-foldon proteins and incubated at 4°C overnight. Plates were then blocked with PBS containing 5% skim milk at 37°C for 1 h. mAbs and immune sera were serially diluted in four-fold steps and added to the wells for 1 h. Horseradish peroxidase (HRP)-conjugated anti-human or anti-mouse IgG (Southern Biotech) was added and incubated at 37°C for 1 h. The wells were developed with 3,3′,5′,5-tetramethylbenzidine (TMB) substrate (KPL), and the reactions were stopped by adding 1 M H_2SO_4 before measuring absorbance at 450 nm with a Spectramax Paradigm plate reader (Molecular Devices). Sera from mice immunized with PBS or an irrelevant antigen (DS-Cav1-I53_dn5; ref. 42), ferrets immunized with

PBS, and NHPs prior to immunization were used as negative controls, and did not yield signal above background.

Reporter-based microneutralization assay

All reporter viruses were prepared as described previously[52]. Briefly, all H1N1 and H3N2 viruses were made with a modified PB1 segment expressing the TdKatushka reporter gene (R3ΔPB1) and propagated in MDCK-SIAT-PB1 cells, while H5N1 reporter virus was made with a modified HA segment expressing the reporter (R3ΔHA) and produced in cells stably expressing H5 HA. Replication-restricted reporter influenza viruses encoding influenza B HA and NA coding regions were rescued using plasmids expressing the open reading frames of influenza B HA and NA genes flanked by genome packaging signals of influenza A HA[101] and NA segments[102], respectively. These viruses have a PB1 segment modified to express the TdKatushka2 reporter gene and encode the internal genes of influenza A (A/WSN/1933, H1N1) virus. Rescued viruses were propagated in MDCK-SIAT1-PB1 in the presence of TPCK-treated trypsin (1 μg ml^{-1}, Sigma) at 34°C. Virus stocks were stored at -80°C. Mouse sera were treated with receptor destroying enzyme (RDE II; Denka Seiken) and heat-inactivated before use in neutralization assays. Immune sera or mAbs were serially diluted and incubated for 1 h at 37°C with pre-titrated viruses. Serum-virus mixtures were then transferred to 96-well plates (PerkinElmer), and 1.0×10^4 MDCK-SIAT1-PB1 cells[52,103] were added into each well. After overnight incubation at 37°C, the number of fluorescent cells in each well was counted automatically using a Celigo image cytometer (Nexcelom Biosciences).

Pseudovirus neutralization assay

Pseudovirus neutralization assays were carried out using luciferase-encoding lentiviruses pseudotyped with influenza HA and NA, as described previously[104,105]. The HA and NA sequences used to generate the pseudoviruses were derived from H1N1 PR8 and H3N2 PH82. Briefly, mouse sera were treated with receptor destroying enzyme (RDE (II); SEIKEN Accurate Chemical and Scientific) and heat-inactivated before use in assays. Immune sera were serially diluted and incubated with pre-titrated HA-NA pseudotyped viruses for 30 min at room temperature. Serum-pseudovirus mixtures were then transferred to 96-well white/black isoplates (PerkinElmer), and 12,000 293A cells were added into each well of the plate. After overnight incubation at 37°C, wells were supplemented with 100 μl of fresh Dulbecco's Modified Eagle Medium including 5% fetal bovine serum (Fisher Scientific) and 5,000 units ml^{-1} penicillin-streptomycin (Gibco), and the plates were incubated in a static 37°C, 5% CO_2, humidified incubator for 48 h. Cells were lysed with cell culture lysis buffer (Promega) and luciferase activity in the lysate was measured using Luciferase kit (Promega). Luminescence was measured with a Spectramax L luminometer (Molecular Devices). IC_{50} values, defined as the serum dilution or antibody concentration that gives 50% reduction in virus-infected cells, were calculated from neutralization curves using a four-parameter nonlinear regression model and plotted with GraphPad Prism (v8.0).

Hemagglutination inhibition assay

HAI titer to vaccine-matched viruses were tested with immune sera. The reporter influenza viruses H1N1 MI15, H3N2 HK14, B/Vic CO17, and B/Yam PH13 were propagated in

Madin-Darby canine kidney (MDCK) cells. Immune sera were treated with receptor-destroying enzyme (RDE II; Denka Seiken) before use in HAI assays. Immune sera were serially diluted and incubated with viruses (four hemagglutination unit per well) and then incubated with 0.5% turkey or guinea pig (for H3N2 HK14 virus only) red blood cells (Lampire Biological Laboratories) for 30 min at room temperature. The HAI titer of the sample was determined based on the well with the last non-agglutinated appearance, immediately before an agglutination was observed.

Passive transfer

To generate hyper-immune Ig for passive transfer, the immune serum samples from each NHP were diluted 1:50 with PBS, added to protein A columns, and incubated overnight at 4°C. After washing the columns briefly, captured antibodies were eluted with low-pH IgG elution buffer (ThermoFisher Scientific) and the eluates were immediately neutralized by adding 1 M Tris-HCl (pH 8.0) to a final concentration of 100 mM. Purified polyclonal antibodies were dialyzed two times against PBS, concentrated to ~20 mg ml^{-1} and stored at -80°C until use. BALB/cAnNHsd mice (Envigo) were given intraperitoneally 0.2 mg of FI6v3 (approximately 10 mg kg^{-1}) or 10 mg of purified polyclonal Ig from individual NHPs. Twenty-four hours later, the mice were infected intranasally with 25× or 10× LD_{50} of H5N1 or H7N9 viruses at Bioqual. The animals were monitored twice daily for development of clinical signs of infection and weighed daily for 14 days. Any animals that lost 20% or more of their initial body weight were euthanized.

Preparation of polyclonal immunoglobulin antigen-binding fragments

To generate polyclonal Fab fragments for epitope mapping, the immune serum samples from each NHP were diluted with PBS and applied to protein A columns. After washing the columns, captured antibodies were eluted with 0.1 M glycine pH 3.5, and the eluates were immediately neutralized by adding Tris-HCl (pH 8.0) to a final concentration of 50 mM. Purified IgG was buffer-exchanged into PBS and concentrated to approximately 25 mg ml^{-1}, and 250 µL of 2× digestion buffer (40 mM sodium phosphate pH 6.5, 20 mM EDTA, 40 mM cysteine) was added. 500 µL of resuspended immobilized papain resin (ThermoFisher Scientific) freshly washed in 1× digestion buffer (20 mM sodium phosphate, 10 mM EDTA, 20 mM cysteine, pH 6.5) was further added, and samples were shaken for 5 h at 37°C. The supernatant was separated from resin and mixed with 1 ml of 20 mM Tris pH 8.0. Resin was washed twice with 500 µL of 20 mM Tris pH 8.0 and supernatants from the washes were pooled with the original supernatant to increase sample yield. Pooled supernatants were sterile-filtered at 0.22 µm and applied to protein A columns. Unbound fractions were pooled, concentrated to approximately 10 mg ml^{-1}, and dialyzed twice against 25 mM Tris pH 8.0 to remove excess phosphates and cysteine prior to sample preparation for EM. Final samples were confirmed by SDS-PAGE, flash-frozen, and stored at -80°C.

Electron microscopy polyclonal epitope mapping (EMPEM)

To prepare H1 HA/polyclonal Fab fragment complexes, 150-fold molar excesses of qsCocktail- or qsMosaic-I53_dn5-elicited antibody Fab fragments were incubated with H1 HA-foldon for 1 h at room temperature, and the complexes were purified on a Superdex 200 Increase 10/300 GL column. The purified complexes were adsorbed onto glow-discharged carbon-coated copper

mesh grids for 60 s, stained with 2% uranyl formate for 30 s, and allowed to air dry. Grids were imaged using an FEI Tecnai Spirit 120 kV electron microscope equipped with a Gatan Ultrascan 4000 CCD Camera. The pixel size at the specimen level was 1.60 Å. Data collection was performed using Leginon[88] with the majority of the data processing carried out in Appion[106]. 4,112 and 3,237 micrographs were collected for qsCocktail-I53_dn5- and qsMosaic-I53_dn5-elicited Fab/HA complexes respectively. The parameters of the contrast transfer function (CTF) were estimated using CTFFIND4 (ref. 107). All particles were picked in a reference-free manner using DoG Picker[108]. Reference-free 2D classification was used to select homogeneous subsets of particles using CryoSPARC[109]. 847,873 and 997,557 particles were subjected for 2D classification of qsCocktail-I53_dn5- and qsMosaic-I53_dn5-elicited Fab/HA complexes, respectively. During the 2D classification, 2D classes were visually inspected and particles from classes not showing clear structural features of Fab/HA complexes were discarded. The remaining particles were subsequently subjected to three rounds of ab initio 3D reconstructions and 3D classifications without any symmetry imposed using CryoSPARC. Only receptor binding domain, vestigial esterase domain, and stem-directed Abs were included in the calculations. Particles from these classes were separately subjected to 3D refinement using CryoSPARC. The head-binding Fabs of the different classes were similar, but most classes showed obvious asymmetric features. All 3D reconstructions were compared to three classes of structurally characterized anti-HA antibodies: (i) receptor binding domain-targeted Abs CH65 (PDB: 5UGY), C05 (PDB: 4FP8), F045-092 (PDB: 4O58), HC63 (PDB: 1KEN), 2G1 (PDB: 4HG4), 8M2 (PDB: 4HFU), 5J8 (PDB: 4M5Z), 1F1 (PDB: 4GXU), and S139/1 (PDB: 4GMS); (ii) vestigial esterase domain-targeted Abs H5M9 (PDB: 4MHJ) and CR8071 (PDB: 4FQJ); and (iii) stem-binding Abs C179 (PDB: 4HLZ), CR6261 (PDB: 3GBN), CR8043 (PDB: 4NM8), CR8020 (PDB: 3SDY), CR9114 (PDB: 4FQI), FI6v3 (PDB: 3ZTJ), MEDI8852 (PDB: 5JW4), and 39.29 (PDB: 4KVN). Estimates of the fraction of particles containing receptor binding domain-, vestigial esterase domain-, and stem-binding Fabs were based on the number of particles clustered in each group. Particles containing Fabs bound to multiple sites were counted against each site.

H5 HA/polyclonal Fab fragment complexes were prepared and verified by negative stain electron microscopy as described above and then pooled and concentrated. 3 µl of 0.1 mg ml^{-1} H5 HA in complex with qsMosaic-I53_dn5-elicited antibody Fab fragments was loaded onto a freshly glow-discharged (30 s at 20 mA) 1.2/1.3 UltraFoil grid (300 mesh) with a thin layer of evaporated continuous carbon prior to plunge freezing using a vitrobot Mark IV (ThermoFisher Scientific) using a blot force of -1 and 2.5 second blot time at 100% humidity and 25°C. Data were acquired using the an FEI Titan Krios transmission electron microscope operated at 300 kV and equipped with a Gatan K2 Summit direct detector and Gatan Quantum GIF energy filter, operated in zero-loss mode with a slit width of 20 eV. Automated data collection was carried out using Leginon at a nominal magnification of 130,000× with a pixel size of 0.525 Å. The dose rate was adjusted to 8 counts/pixel/s, and each movie was acquired in super-resolution mode fractionated in 50 frames of 200 ms. 2,374 micrographs were collected using beam-image shift with a defocus range between -1.0 and -2.5 µm. Movie frame alignment, estimation of the microscope contrast-transfer function parameters, particle picking, and extraction were carried out using Warp. Particle images were extracted with a box size of 800 $pixels^2$ binned to 400

pixels^2 yielding a pixel size of 1.05 Å. Two rounds of reference-free 2D classification were performed using CryoSPARC to select well-defined particle images. These selected particles were subjected to 3D refinement in CryoSPARC applying C3 symmetry using a map generated from a crystal structure of H5 HA (PDB 5JW4) low-pass filtered at 30 Å resolution. For beam tilt correction, the micrographs were grouped into beam tilt groups using beam-image shift values from Leginon. Beam tilt refinement was performed in Relion3.0 (ref. 110). CTF refinement was used to refine per-particle defocus values. Particle images were subjected to the Bayesian polishing procedure implemented in Relion3.0 (ref. 111). After determining a refined 3D structure, the particles were then subjected to 3D classification without refining angles and shifts using a soft mask on three Fab regions and with a tau value of 20 using Relion. 3D refinements were carried out using non-uniform refinement along with per-particle defocus refinement in CryoSPARC[112]. Local resolution estimation, filtering, and sharpening was carried out using CryoSPARC. Reported resolutions are based on the gold-standard Fourier shell correlation (FSC) of 0.143 criterion and Fourier shell correlation curves were corrected for the effects of soft masking by high-resolution noise substitution.

Statistics and Reproducibility

Multi-group comparisons were performed using nonparametric Kruskal-Wallis test with Dunn's post-hoc analysis in Prism 8 (GraphPad) unless mentioned otherwise. Differences were considered significant when P values were less than 0.05. Statistical test to compare multiple Kaplan–Meier curves was carried out by using Mantel-Cox log-rank test with Bonferroni correction. Statistical methods and P value ranges can be found in the Figures and Figure legends.

Data availability

All images and data were generated and analyzed by the authors, and will be made available by the corresponding authors (B.S.G., N.P.K., and M.K.) upon reasonable request. Structural models and density maps have been deposited in the Protein Data Bank and Electron Microscopy Data Bank under accession numbers EMD-22935 (H1-I53_dn5 nanoparticle), EMD-22937 and PDB 7KNA (localized reconstruction of H1 HA), EMD-22940 (H5 HA bound to 3 polyclonal Fabs), EMD-22939 (H5 HA bound to 2 polyclonal Fabs), and EMD-22938 (H5 HA bound to 1 polyclonal Fab).

References

1. Iuliano, A. D. *et al.* Estimates of global seasonal influenza-associated respiratory mortality: a modelling study. *Lancet* **391**, 1285–1300 (2018).
2. Bedford, T. *et al.* Global circulation patterns of seasonal influenza viruses vary with antigenic drift. *Nature* **523**, 217–220 (2015).
3. Francis, M. E., King, M. L. & Kelvin, A. A. Back to the Future for Influenza Preimmunity-Looking Back at Influenza Virus History to Infer the Outcome of Future Infections. *Viruses* **11**, E122 (2019).
4. Flannery, B. *et al.* Interim Estimates of 2017-18 Seasonal Influenza Vaccine Effectiveness - United States, February 2018. *MMWR Morb. Mortal. Wkly. Rep.* **67**, 180–185 (2018).
5. Belongia, E. A. *et al.* Variable influenza vaccine effectiveness by subtype: a systematic

review and meta-analysis of test-negative design studies. *Lancet Infect. Dis.* **16**, 942–951 (2016).
6. Wu, N. C. *et al.* Preventing an Antigenically Disruptive Mutation in Egg-Based H3N2 Seasonal Influenza Vaccines by Mutational Incompatibility. *Cell Host Microbe* **25**, 836–844.e5 (2019).
7. Raymond, D. D. *et al.* Influenza immunization elicits antibodies specific for an egg-adapted vaccine strain. *Nat. Med.* **22**, 1465–1469 (2016).
8. Garretson, T. A., Petrie, J. G., Martin, E. T., Monto, A. S. & Hensley, S. E. Identification of human vaccinees that possess antibodies targeting the egg-adapted hemagglutinin receptor binding site of an H1N1 influenza vaccine strain. *Vaccine* **36**, 4095–4101 (2018).
9. Zost, S. J. *et al.* Contemporary H3N2 influenza viruses have a glycosylation site that alters binding of antibodies elicited by egg-adapted vaccine strains. *Proc. Natl. Acad. Sci. U. S. A.* **114**, 12578–12583 (2017).
10. Yamayoshi, S. & Kawaoka, Y. Current and future influenza vaccines. *Nat. Med.* **25**, 212–220 (2019).
11. Neumann, G. & Kawaoka, Y. Predicting the Next Influenza Pandemics. *J. Infect. Dis.* **219**, S14–S20 (2019).
12. Kanekiyo, M. & Graham, B. S. Next-Generation Influenza Vaccines. *Cold Spring Harb. Perspect. Med.* (2020) doi:10.1101/cshperspect.a038448.
13. Hope-Simpson, R. E. & Golubev, D. B. A new concept of the epidemic process of influenza A virus. *Epidemiol. Infect.* **99**, 5–54 (1987).
14. Johnson, N. P. A. S. & Mueller, J. Updating the accounts: global mortality of the 1918-1920 'Spanish' influenza pandemic. *Bull. Hist. Med.* **76**, 105–115 (2002).
15. Fineberg, H. V. Pandemic preparedness and response--lessons from the H1N1 influenza of 2009. *N. Engl. J. Med.* **370**, 1335–1342 (2014).
16. Gilbert, J. A. Seasonal and pandemic influenza: global fatigue versus global preparedness. *Lancet Respir Med* **6**, 94–95 (2018).
17. Taubenberger, J. K., Kash, J. C. & Morens, D. M. The 1918 influenza pandemic: 100 years of questions answered and unanswered. *Sci. Transl. Med.* **11**, eaau5485 (2019).
18. Wu, N. C. & Wilson, I. A. Influenza Hemagglutinin Structures and Antibody Recognition. *Cold Spring Harb. Perspect. Med.* (2019) doi:10.1101/cshperspect.a038778.
19. Harrison, S. C. Viral membrane fusion. *Virology* **479-480**, 498–507 (2015).
20. Corti, D. *et al.* Tackling influenza with broadly neutralizing antibodies. *Curr. Opin. Virol.* **24**, 60–69 (2017).
21. Crowe, J. E. Antibody Determinants of Influenza Immunity. *J. Infect. Dis.* **219**, S21–S29 (2019).
22. Sedeyn, K. & Saelens, X. New antibody-based prevention and treatment options for influenza. *Antiviral Res.* **170**, 104562 (2019).
23. Tan, H.-X. *et al.* Subdominance and poor intrinsic immunogenicity limit humoral immunity targeting influenza HA stem. *J. Clin. Invest.* **129**, 850–862 (2019).
24. Ellebedy, A. H. *et al.* Induction of broadly cross-reactive antibody responses to the influenza HA stem region following H5N1 vaccination in humans. *Proc. Natl. Acad. Sci. U. S. A.* **111**, 13133–13138 (2014).
25. Andrews, S. F. *et al.* Immune history profoundly affects broadly protective B cell responses

to influenza. *Sci. Transl. Med.* **7**, 316ra192 (2015).
26. Yassine, H. M. *et al.* Hemagglutinin-stem nanoparticles generate heterosubtypic influenza protection. *Nat. Med.* **21**, 1065–1070 (2015).
27. Impagliazzo, A. *et al.* A stable trimeric influenza hemagglutinin stem as a broadly protective immunogen. *Science* **349**, 1301–1306 (2015).
28. Corbett, K. S. *et al.* Design of Nanoparticulate Group 2 Influenza Virus Hemagglutinin Stem Antigens That Activate Unmutated Ancestor B Cell Receptors of Broadly Neutralizing Antibody Lineages. *MBio* **10**, e02810–18 (2019).
29. Boyoglu-Barnum, S. *et al.* Glycan repositioning of influenza hemagglutinin stem facilitates the elicitation of protective cross-group antibody responses. *Nat. Commun.* **11**, 791 (2020).
30. Steel, J. *et al.* Influenza virus vaccine based on the conserved hemagglutinin stalk domain. *MBio* **1**, e00018–10 (2010).
31. Bommakanti, G. *et al.* Design of an HA2-based Escherichia coli expressed influenza immunogen that protects mice from pathogenic challenge. *Proc. Natl. Acad. Sci. U. S. A.* **107**, 13701–13706 (2010).
32. Krammer, F., Pica, N., Hai, R., Margine, I. & Palese, P. Chimeric hemagglutinin influenza virus vaccine constructs elicit broadly protective stalk-specific antibodies. *J. Virol.* **87**, 6542–6550 (2013).
33. Bachmann, M. F. *et al.* The influence of antigen organization on B cell responsiveness. *Science* **262**, 1448–1451 (1993).
34. Kanekiyo, M. *et al.* Self-assembling influenza nanoparticle vaccines elicit broadly neutralizing H1N1 antibodies. *Nature* **499**, 102–106 (2013).
35. Darricarrère, N. *et al.* Development of a Pan-H1 Influenza Vaccine. *J. Virol.* **92**, e01349–18 (2018).
36. Kanekiyo, M. *et al.* Mosaic nanoparticle display of diverse influenza virus hemagglutinins elicits broad B cell responses. *Nat. Immunol.* **20**, 362–372 (2019).
37. King, N. P. *et al.* Computational design of self-assembling protein nanomaterials with atomic level accuracy. *Science* **336**, 1171–1174 (2012).
38. King, N. P. *et al.* Accurate design of co-assembling multi-component protein nanomaterials. *Nature* **510**, 103–108 (2014).
39. Bale, J. B. *et al.* Accurate design of megadalton-scale two-component icosahedral protein complexes. *Science* **353**, 389–394 (2016).
40. Hsia, Y. *et al.* Design of a hyperstable 60-subunit protein icosahedron. *Nature* **535**, 136–139 (2016).
41. Fallas, J. A. *et al.* Computational design of self-assembling cyclic protein homo-oligomers. *Nat. Chem.* **9**, 353–360 (2017).
42. Ueda, G. *et al.* Tailored Design of Protein Nanoparticle Scaffolds for Multivalent Presentation of Viral Glycoprotein Antigens. *Elife* **9**, e57659 (2020).
43. Bruun, T. U. J., Andersson, A.-M. C., Draper, S. J. & Howarth, M. Engineering a Rugged Nanoscaffold To Enhance Plug-and-Display Vaccination. *ACS Nano* **12**, 8855–8866 (2018).
44. Marcandalli, J. *et al.* Induction of Potent Neutralizing Antibody Responses by a Designed Protein Nanoparticle Vaccine for Respiratory Syncytial Virus. *Cell* **176**, 1420–1431.e17 (2019).
45. Brouwer, P. J. M. *et al.* Enhancing and shaping the immunogenicity of native-like HIV-1

envelope trimers with a two-component protein nanoparticle. *Nat. Commun.* **10**, 4272 (2019).
46. Antanasijevic, A. *et al.* Structural and functional evaluation of de novo-designed, two-component nanoparticle carriers for HIV Env trimer immunogens. *PLoS Pathog.* (2020) doi:10.1371/journal.ppat.1008665.
47. Walls, A. C. *et al.* Elicitation of potent neutralizing antibody responses by designed protein nanoparticle vaccines for SARS-CoV-2. *Cell* (2020) doi:10.1016/j.cell.2020.10.043.
48. Ilca, S. L. *et al.* Localized reconstruction of subunits from electron cryomicroscopy images of macromolecular complexes. *Nat. Commun.* **6**, 8843 (2015).
49. Krammer, F. *et al.* A carboxy-terminal trimerization domain stabilizes conformational epitopes on the stalk domain of soluble recombinant hemagglutinin substrates. *PLoS One* **7**, e43603 (2012).
50. Krause, J. C. *et al.* A broadly neutralizing human monoclonal antibody that recognizes a conserved, novel epitope on the globular head of the influenza H1N1 virus hemagglutinin. *J. Virol.* **85**, 10905–10908 (2011).
51. O'Hagan, D. T. MF59 is a safe and potent vaccine adjuvant that enhances protection against influenza virus infection. *Expert Rev. Vaccines* **6**, 699–710 (2007).
52. Creanga, A. *et al.* A comprehensive influenza reporter virus panel for high-throughput deep profiling of neutralizing antibodies. *bioRxiv* (2020) doi:10.1101/2020.02.24.963611.
53. Cowling, B. J. *et al.* Protective efficacy of seasonal influenza vaccination against seasonal and pandemic influenza virus infection during 2009 in Hong Kong. *Clin. Infect. Dis.* **51**, 1370–1379 (2010).
54. Corti, D. *et al.* A neutralizing antibody selected from plasma cells that binds to group 1 and group 2 influenza A hemagglutinins. *Science* **333**, 850–856 (2011).
55. Nogal, B. *et al.* Mapping Polyclonal Antibody Responses in Non-human Primates Vaccinated with HIV Env Trimer Subunit Vaccines. *Cell Rep.* **30**, 3755–3765.e7 (2020).
56. Bianchi, M. *et al.* Electron-Microscopy-Based Epitope Mapping Defines Specificities of Polyclonal Antibodies Elicited during HIV-1 BG505 Envelope Trimer Immunization. *Immunity* **49**, 288–300.e8 (2018).
57. Kallewaard, N. L. *et al.* Structure and Function Analysis of an Antibody Recognizing All Influenza A Subtypes. *Cell* **166**, 596–608 (2016).
58. Joyce, M. G. *et al.* Vaccine-Induced Antibodies that Neutralize Group 1 and Group 2 Influenza A Viruses. *Cell* **166**, 609–623 (2016).
59. Wei, C.-J. *et al.* Induction of broadly neutralizing H1N1 influenza antibodies by vaccination. *Science* **329**, 1060–1064 (2010).
60. Giles, B. M. & Ross, T. M. A computationally optimized broadly reactive antigen (COBRA) based H5N1 VLP vaccine elicits broadly reactive antibodies in mice and ferrets. *Vaccine* **29**, 3043–3054 (2011).
61. Chen, M.-W. *et al.* Broadly neutralizing DNA vaccine with specific mutation alters the antigenicity and sugar-binding activities of influenza hemagglutinin. *Proc. Natl. Acad. Sci. U. S. A.* **108**, 3510–3515 (2011).
62. Broecker, F. *et al.* A mosaic hemagglutinin-based influenza virus vaccine candidate protects mice from challenge with divergent H3N2 strains. *NPJ Vaccines* **4**, 31 (2019).
63. Sun, W. *et al.* Development of Influenza B Universal Vaccine Candidates Using the 'Mosaic'

Hemagglutinin Approach. *J. Virol.* **93**, e00333-19 (2019).
64. Ng, S. *et al.* Novel correlates of protection against pandemic H1N1 influenza A virus infection. *Nat. Med.* **25**, 962–967 (2019).
65. Angeletti, D. *et al.* Defining B cell immunodominance to viruses. *Nat. Immunol.* **18**, 456–463 (2017).
66. Tokatlian, T. *et al.* Innate immune recognition of glycans targets HIV nanoparticle immunogens to germinal centers. *Science* **363**, 649–654 (2019).
67. Russell, S. M. & Liew, F. Y. T cells primed by influenza virion internal components can cooperate in the antibody response to haemagglutinin. *Nature* **280**, 147–148 (1979).
68. Scherle, P. A. & Gerhard, W. Functional analysis of influenza-specific helper T cell clones in vivo. T cells specific for internal viral proteins provide cognate help for B cell responses to hemagglutinin. *J. Exp. Med.* **164**, 1114–1128 (1986).
69. Milich, D. R., McLachlan, A., Thornton, G. B. & Hughes, J. L. Antibody production to the nucleocapsid and envelope of the hepatitis B virus primed by a single synthetic T cell site. *Nature* **329**, 547–549 (1987).
70. 1000 Genomes Project Consortium *et al.* An integrated map of genetic variation from 1,092 human genomes. *Nature* **491**, 56–65 (2012).
71. Andrews, S. F. *et al.* Preferential induction of cross-group influenza A hemagglutinin stem-specific memory B cells after H7N9 immunization in humans. *Sci Immunol* **2**, eaan2676 (2017).
72. Jang, H. & Ross, T. M. Preexisting influenza specific immunity and vaccine effectiveness. *Expert Rev. Vaccines* **18**, 1043–1051 (2019).
73. Fonville, J. M. *et al.* Antibody landscapes after influenza virus infection or vaccination. *Science* **346**, 996–1000 (2014).
74. Gostic, K. M., Ambrose, M., Worobey, M. & Lloyd-Smith, J. O. Potent protection against H5N1 and H7N9 influenza via childhood hemagglutinin imprinting. *Science* **354**, 722–726 (2016).
75. Erbelding, E. J. *et al.* A Universal Influenza Vaccine: The Strategic Plan for the National Institute of Allergy and Infectious Diseases. *J. Infect. Dis.* **218**, 347–354 (2018).
76. Whittle, J. R. R. *et al.* Flow cytometry reveals that H5N1 vaccination elicits cross-reactive stem-directed antibodies from multiple Ig heavy-chain lineages. *J. Virol.* **88**, 4047–4057 (2014).
77. Throsby, M. *et al.* Heterosubtypic neutralizing monoclonal antibodies cross-protective against H5N1 and H1N1 recovered from human IgM+ memory B cells. *PLoS One* **3**, e3942 (2008).
78. Hong, M. *et al.* Antibody recognition of the pandemic H1N1 Influenza virus hemagglutinin receptor binding site. *J. Virol.* **87**, 12471–12480 (2013).
79. Ekiert, D. C. *et al.* A highly conserved neutralizing epitope on group 2 influenza A viruses. *Science* **333**, 843–850 (2011).
80. Iba, Y. *et al.* Conserved neutralizing epitope at globular head of hemagglutinin in H3N2 influenza viruses. *J. Virol.* **88**, 7130–7144 (2014).
81. Lee, P. S. *et al.* Receptor mimicry by antibody F045-092 facilitates universal binding to the H3 subtype of influenza virus. *Nat. Commun.* **5**, 3614 (2014).
82. Dreyfus, C. *et al.* Highly conserved protective epitopes on influenza B viruses. *Science* **337**,

1343–1348 (2012).
83. Wu, Y. *et al.* A potent broad-spectrum protective human monoclonal antibody crosslinking two haemagglutinin monomers of influenza A virus. *Nat. Commun.* **6**, 7708 (2015).
84. Kwakkenbos, M. J. *et al.* Generation of stable monoclonal antibody-producing B cell receptor-positive human memory B cells by genetic programming. *Nat. Med.* **16**, 123–128 (2010).
85. Corti, D. *et al.* Cross-neutralization of four paramyxoviruses by a human monoclonal antibody. *Nature* **501**, 439–443 (2013).
86. Studier, F. W. & William Studier, F. Protein production by auto-induction in high-density shaking cultures. *Protein Expr. Purif.* **41**, 207–234 (2005).
87. Snijder, J. *et al.* Vitrification after multiple rounds of sample application and blotting improves particle density on cryo-electron microscopy grids. *J. Struct. Biol.* **198**, 38–42 (2017).
88. Suloway, C. *et al.* Automated molecular microscopy: the new Leginon system. *J. Struct. Biol.* **151**, 41–60 (2005).
89. Tegunov, D. & Cramer, P. Real-time cryo-electron microscopy data preprocessing with Warp. *Nat. Methods* **16**, 1146–1152 (2019).
90. Emsley, P., Lohkamp, B., Scott, W. G. & Cowtan, K. Features and development of Coot. *Acta Crystallogr. D Biol. Crystallogr.* **66**, 486–501 (2010).
91. Frenz, B. *et al.* Automatically Fixing Errors in Glycoprotein Structures with Rosetta. *Structure* **27**, 134–139.e3 (2019).
92. Wang, R. Y.-R. *et al.* Automated structure refinement of macromolecular assemblies from cryo-EM maps using Rosetta. *Elife* **5**, e17219 (2016).
93. Chen, V. B. *et al.* MolProbity: all-atom structure validation for macromolecular crystallography. *Acta Crystallogr. D Biol. Crystallogr.* **66**, 12–21 (2010).
94. Liebschner, D. *et al.* Macromolecular structure determination using X-rays, neutrons and electrons: recent developments in Phenix. *Acta Crystallogr D Struct Biol* **75**, 861–877 (2019).
95. Agirre, J. *et al.* Privateer: software for the conformational validation of carbohydrate structures. *Nat. Struct. Mol. Biol.* **22**, 833–834 (2015).
96. Barad, B. A. *et al.* EMRinger: side chain-directed model and map validation for 3D cryo-electron microscopy. *Nat. Methods* **12**, 943–946 (2015).
97. Scheres, S. H. W. & Chen, S. Prevention of overfitting in cryo-EM structure determination. *Nat. Methods* **9**, 853–854 (2012).
98. Verkerke, H. P. *et al.* Epitope-Independent Purification of Native-Like Envelope Trimers from Diverse HIV-1 Isolates. *J. Virol.* **90**, 9471–9482 (2016).
99. Guttman, M., Weis, D. D., Engen, J. R. & Lee, K. K. Analysis of overlapped and noisy hydrogen/deuterium exchange mass spectra. *J. Am. Soc. Mass Spectrom.* **24**, 1906–1912 (2013).
100. Weis, D. D., Engen, J. R. & Kass, I. J. Semi-automated data processing of hydrogen exchange mass spectra using HX-Express. *J. Am. Soc. Mass Spectrom.* **17**, 1700–1703 (2006).
101. Martínez-Sobrido, L. *et al.* Hemagglutinin-pseudotyped green fluorescent protein-expressing influenza viruses for the detection of influenza virus neutralizing

antibodies. *J. Virol.* **84**, 2157–2163 (2010).
102. Gao, Q. *et al.* The influenza A virus PB2, PA, NP, and M segments play a pivotal role during genome packaging. *J. Virol.* **86**, 7043–7051 (2012).
103. Bloom, J. D., Gong, L. I. & Baltimore, D. Permissive secondary mutations enable the evolution of influenza oseltamivir resistance. *Science* **328**, 1272–1275 (2010).
104. Kong, W.-P. *et al.* Protective immunity to lethal challenge of the 1918 pandemic influenza virus by vaccination. *Proc. Natl. Acad. Sci. U. S. A.* **103**, 15987–15991 (2006).
105. Yang, Z.-Y. *et al.* Immunization by avian H5 influenza hemagglutinin mutants with altered receptor binding specificity. *Science* **317**, 825–828 (2007).
106. Lander, G. C. *et al.* Appion: an integrated, database-driven pipeline to facilitate EM image processing. *J. Struct. Biol.* **166**, 95–102 (2009).
107. Rohou, A. & Grigorieff, N. CTFFIND4: Fast and accurate defocus estimation from electron micrographs. *J. Struct. Biol.* **192**, 216–221 (2015).
108. Voss, N. R., Yoshioka, C. K., Radermacher, M., Potter, C. S. & Carragher, B. DoG Picker and TiltPicker: software tools to facilitate particle selection in single particle electron microscopy. *J. Struct. Biol.* **166**, 205–213 (2009).
109. Punjani, A., Rubinstein, J. L., Fleet, D. J. & Brubaker, M. A. cryoSPARC: algorithms for rapid unsupervised cryo-EM structure determination. *Nat. Methods* **14**, 290–296 (2017).
110. Zivanov, J. *et al.* New tools for automated high-resolution cryo-EM structure determination in RELION-3. *Elife* **7**, e42166 (2018).
111. Zivanov, J., Nakane, T. & Scheres, S. H. W. A Bayesian approach to beam-induced motion correction in cryo-EM single-particle analysis. *IUCrJ* **6**, 5–17 (2019).
112. Punjani, A., Zhang, H. & Fleet, D. J. Non-uniform refinement: Adaptive regularization improves single particle cryo-EM reconstruction. *bioRxiv* (2019) doi:10.1101/2019.12.15.877092.

Chapter 2: Design of a modular nanoparticle platform for tunable antibody responses against the influenza hemagglutinin head domain

Summary

Influenza vaccines are characteristic in their elicitation of narrowly-specific responses against the head domain of the hemagglutinin glycoprotein (HA). Multiple broadly-conserved epitopes are present on the head domain, which motivates the design of vaccines to better prioritize inclusion of responses against these regions. Here we use structure-based computational protein design strategies to design a nanoparticle-based platform that allows for multiple levels of control over epitopes prioritized in responses against the HA head domain. HA head domains can either be presented as monomers or in their native-like closed trimeric formation that structurally occludes access to the interface region between heads. Further, the designed platform features a rigidly-bridging extension domain that can modularly be shrunk or extended to precisely control spacing between antigens. Smaller spacings between adjacent head antigens on the nanoparticle surface was found to be correlated with improved neutralization potency as well as binding breadth across diverse H1N1 HAs. This platform has potential for the greater study of humoral responses against the HA head, as well as a starting point for the design of next-generation head-directed influenza vaccines.

Introduction

Influenza vaccines maintain massive biomedical importance, both for the clinical prevention of disease and the general study of vaccinology. The influenza hemagglutinin (HA) glycoprotein is most notably relevant, which is a homotrimeric class I fusion protein responsible for both receptor binding to sialic acids and cell entry (Wu and Wilson 2020; Harrison 2015). The head contains an upper receptor binding domain (RBD) which presents an apical receptor binding site (RBS) and a lower “vestigial esterase” subdomain, while the stem domain holds metastable membrane fusion machinery. The HA head is the predominant target of antibodies elicited by existing commercial influenza vaccines (Krammer and Palese 2015). HA head-directed polyclonal antibody responses are often capable of neutralizing virions by blocking receptor binding, which has long been measurable using the hemagglutinin inhibition (HAI) assay (Rimmelzwaan and McElhaney 2008). However, the head domain of HA is characteristic for both possessing a combination of hypervariability and immunodominance (Knight et al. 2020). This combination of properties is considered largely responsible for current vaccines eliciting antibody responses that are narrow in specificity, which necessitates regular updates to vaccine formulations when circulating viruses mutate (Knight et al. 2020; Belongia et al. 2016).

In spite of the hypervariability of the head domain, monoclonal antibodies have been recently isolated from infected and/or vaccinated patients that are capable of recognizing broadly-conserved regions in the head domain, which can inspire future improved vaccine designs (Wu and Wilson 2020). Multiple RBS-directed antibodies have been isolated that can broadly neutralize viruses within the same HA subtype (Whittle et al. 2011; Schmidt et al. 2013; Hong et al. 2013; Xu et al. 2013), with a few also capable of cross-neutralization between diverse subtypes (P. S. Lee et al. 2012; Ekiert et al. 2012; P. S. Lee et al. 2014). Most recently, antibodies have been isolated that recognize normally-occluded parts of the interface between

head domains, which, despite not possessing neutralizing activity, are capable of providing broad protection across diverse influenza A subtypes in preclinical studies (J. Lee et al. 2016; Bangaru et al. 2019; Watanabe et al. 2019). Further conserved epitopes have been recognized on the head which have potential for hosting neutralizing responses within individual subtypes (Raymond et al. 2018; Bangaru et al. 2018; Turner et al. 2019; Zhu et al. 2013).

Attempts to improve the focus of head-directed antibody responses towards desired epitopes have been investigated by modification to the HA head or it's presentation to the immune system, both with and without consideration of known broadly conserved epitopes. HA antigens have been redesigned to include a collection of variable epitopes that are present in diverse viruses, thereby enhancing breadth through direct inclusion of broadly-representative epitopes (Giles and Ross 2011; Allen, Ray, and Ross 2018; Sautto, Kirchenbaum, and Ross 2018). Conversely, other approaches have attempted to prioritize recognition of conserved regions of the head domain, either through hyperglycosylation (Bajic et al. 2019) or antigenic diversity that is leveraged to highlight conserved epitopes using prime-boost immunization regimens (Broecker et al. 2019; Sun et al. 2019) or particulate co-display of diverse antigens (Kanekiyo et al. 2019). While promising, all such strategies directly rely on exploiting antigenic identities of the included head antigens to prioritize responses. Greater understandings of how to influence responses against desired epitopes on any single arbitrary HA head without modifications to its base antigenicity could provide vital information for the development of improved head-directed influenza vaccines.

The oligomeric organization of antigens has long been shown to be vital for determining their immunogenicity (Irvine and Read 2020). Early studies have demonstrated the importance of antigen oligomerization for eliciting quality immune responses, with repetitiveness antigen display every 5-10nm proposed to be ideally immunogenic (M. F. Bachmann and Zinkernagel 1996; Martin F. Bachmann and Jennings 2010; M. F. Bachmann and Zinkernagel 1997; Dintzis, Dintzis, and Vogelstein 1976). Antigen spacing on virion structures has been argued to have a key impact on the immunogenicity of many viruses (Schiller and Chackerian 2014; Harris et al. 2013; Klein and Bjorkman 2010), with some preclinical vaccines also proposed to be immunologically impacted by geometric factors of displayed antigens (Brouwer et al. 2019). More recent studies have utilized the precision of DNA origami to study detailed effects of antigen spacing and valency on antibody avidity (Shaw et al. 2019) and B cell activation (Veneziano et al. 2020). However, the ability to both study the structural correlates of immunogenicity and specifically leverage such spatial properties for immunogen design has been inherently difficult due to inherent structural flexibilities in many particulate or oligomeric systems.

Recent advances in designed protein nanoparticles have allowed for tailored placement of desirable features, such as genetic termini, which provides opportunities for constructing more precisely defined immunogens to better understand this relationship (Ueda et al. 2020). Here, we build on this nanoparticle platform to further design a model system for bespoke presentation of the HA head domain on the surface of protein nanoparticles that allows for control over both the local oligomeric state of head domains and their precise rigid spatial organization. Alterations to both features allows for tuned immunogenicity of different epitopes on the HA head, in all providing novel approaches to vaccine development for influenza, and likely other pathogens, through finely-customized particulate immunogen design.

Results

We aimed to design a platform that could allow for customizable targeting of different epitopes on the HA head domain of an arbitrary individual strain while minimally altering key antigenic sites on the head itself. HA is split into two genetic units, with HA1 largely containing the head domain and HA2 presenting the majority of the stem domain. HA natively forms as a trimer in which the HA2 region contains the majority of interprotomeric contacts, while the head domains maintain relatively smaller numbers of contacts with other heads and can experience separated “breathing” (Benton et al. 2020; Das et al. 2018). When expressed on their own without the stem domain, HA head domains are subsequently monomeric. Even when attached to other multimeric structures, such as protein nanoparticles, HA head domains do not natively form reliable contacts and leave inter-head interface regions largely exposed (Kanekiyo et al. 2019). Given that broadly conserved epitopes present at the HA head interface could either be considered desirable targets or limitations to the focus on more valuable epitopes that can host neutralizing responses, we envisioned a modular way of controlling whether the HA head was monomeric or held in the closed trimeric state observed in common ectodomain structures, all in the absence of HA2. Two possible strategies were considered: design of interactions between HA head domains and a different rigid trimeric base which imitates HA2, and design of interactions within head domains to favor the trimeric state.

To further gain control over epitopes targeted on head domain, we hypothesized that precise control of the geometry in which head domains are displayed on a nanoparticle surface could be used to preferentially highlight different epitopes for humoral focus. Given that spatial features of multivalent antigens arrays, whether on pathogens or other designed surfaces, have been suggested to influence humoral responses, we outlined a strategy for displaying the HA head in distinct rigid spacings. Symmetrical helical bundles can contain structurally repeating motifs, such as heptads which repeat structurally identical backbones every seven amino acids. This modularity can be exploited by protein design to concatenate heptad repeats into rigid units with arbitrary lengths. A redesigned C3 homotrimeric GCN4 helical bundle features such heptad repeats, and as well has been observed to closely match the backbone geometry of the apical portion of HA2 that natively contacts head domains (Harbury, Kim, and Alber 1994); (Impagliazzo et al. 2015). Therefore, we sought to use this helical bundle to mediate a connection between HA heads and a protein nanoparticle surface that could support heads in their native closed trimerized state, while reengineering the length of the bundle to alter spacing between the HA heads and the nanoparticle surface.

A preliminary trimeric head (“TriHead”) design was developed using the H1N1 strain A/New Caledonia/20/1999 (NC99), which sequentially features the receptor binding domain (RBD) of the HA head (residues 56-264 containing Y98F mutation for simplified production) (Kanekiyo et al. 2019), followed by the modified trimeric GCN4 bundle, and subsequently the trimeric component of the I53_dn5 nanoparticle (I53_dn5B) (Ueda et al. 2020). The RBD was connected to the GCN4 bundle using a flexible seven-residue Gly-Ser linker. The N-terminal portion of GCN4 was redesigned to match residues that normally contact the HA head with the intention that the RBDs may naturally recognize this interface to drive trimerization. The I53_dn5 nanoparticle was selected due to the N-terminus of I53_dn5B containing helical regions that closely match the C-terminal end of GCN4, and the hydrophobic core both helical structures

containing a similar pattern of hydrophobic residues. Rather than connecting the two domains using a flexible genetic linker, the C-terminal end of GCN4 was merged with the N-terminal helices of the I53_dn5 trimer by replacing terminal hydrophobic residues GCN4 with complementary positions in the I53_dn5B N-terminal helix to blend them into one continuous helix. This design was successfully secreted from HEK293F cells, purified by immobilized metal affinity chromatography and confirmed as a trimer by size exclusion chromatography (SEC) (not shown). To infer whether RBDs formed the closed trimeric state, binding to the non-neutralizing interface-directed antibody D2 H1-1/H3-1 (J. Lee et al. 2016) was measured using biolayer interferometry (BLI) which demonstrated that the interface region was solvent exposed and accessible for antibody recognition (**Figure 2.1B**). This is not surprising, as many more interactions between the HA head and HA2 are normally needed to support the closed conformation observed in ectodomain crystal structures.

We next asked whether strengthened interactions with the redesigned GCN4 bundle could favor the trimerized closed state of the RBDs. Computational modeling with Rosetta was used to identify a favorable disulfide bond between the RBD and the N-terminal portion of the GCN4 bundle. This construct was expressed and purified and similarly identified as a trimer, however binding to D2 H1-1/H3-1 was still detected (data not shown). Designed interactions between the RBDs appeared necessary for maintaining trimerized closure. Rosetta was therefore used to build hydrophobic interfaces between the RBDs, while not directly mutating epitopes contacted by D2 H1-1/H3-1 or other interface-directed antibodies (Bangaru et al. 2019); (Watanabe et al. 2019). Multiple designs were ordered and successfully expressed, with a leading candidate (**Figure 2.1A**) scaled-up and purified by SEC to confirm the overall trimeric state. In contrast to previous constructs, this design did not bind to D2 H1-1/H3-1 despite the epitope remaining intact (**Figure 2.1B**), while antigenicity of the RBS was confirmed intact as expected.

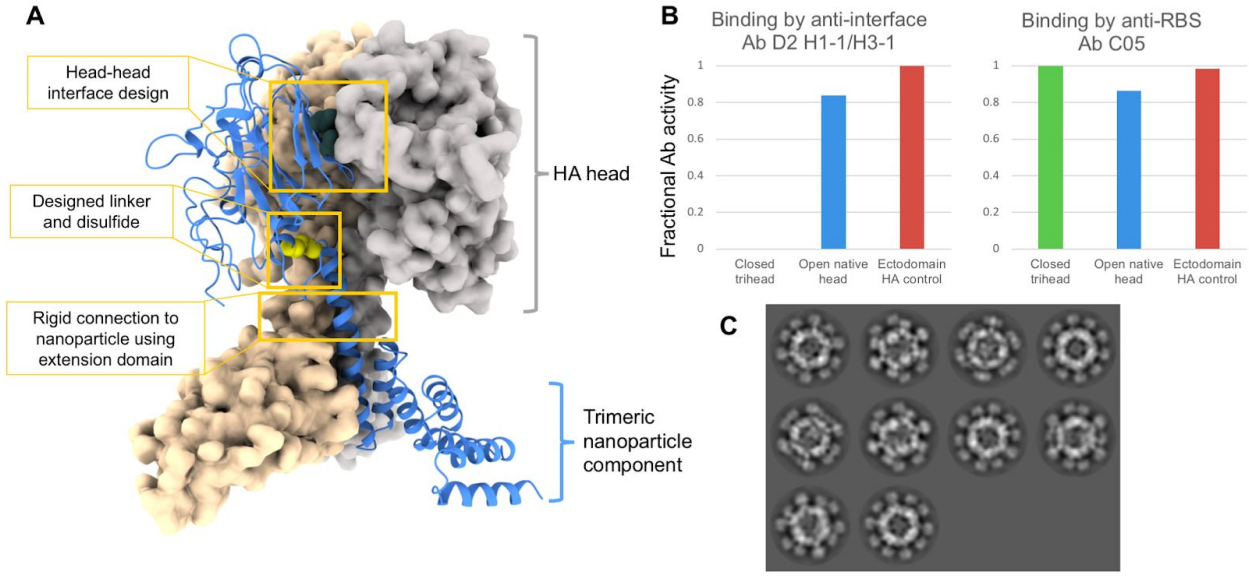

Figure 2.1: Design and characterization of nanoparticle components rigidly displaying closed trimeric HA heads (“TriHead”). **A)** Design model of the initial successful TriHead design, which features a rigid helical extension from the nanoparticle N-terminus, a designed linker to connect to the HA head, a disulfide between the head and the N-terminal nanoparticle extension, and a hydrophobic interface designed

between the individual head domains. **B)** Fractional binding of anti-HA antibodies to the final TriHead design (“Closed trihead”, green), the original design lacking the designed disulfide and head-head interface (“open native head”, blue), and trimeric HA ectodomain fused to foldon (“Ectodomain HA control”, red) as measured by BLI. The D2 H1-1/H3-1 antibody recognizes an epitope at the head-head interface and is not neutralizing, while C05 recognizes the highly conserved receptor binding site. **C)** 2D class averages of the initial TriHead design after assembled as a nanoparticle, obtained by cryo-EM.

Purified protein for this design was mixed with the complementary I53_dn5A.1 pentameric component (Ueda et al. 2020) to drive nanoparticle assembly, and purified nanoparticles were analyzed by cryo-EM (**Figure 2.1C, Figure 2.2A**). 2D class averages showed density consistent with closed trimeric RBDs rigidly attached to the nanoparticle surface, further confirming success of the design. 3D reconstruction resolved density at 8.1Å, with the size of the density confirmed to match closed trimeric RBDs (**Figure 2.2A**). While clear secondary structure could be resolved for the nanoparticle interior, there was a notable drop in local resolution for the RBDs, suggesting that a small amount of flexibility is present between the nanoparticle and the antigens.

Structural effects of alterations to the extendable GCN4-based domain were next studied. Two additional sequences were designed to provide different rigid spacings of TriHeads. One construct (“Closed/Rigid-1”) was designed that removed a heptad repeat from the original TriHead design (“Closed/Rigid-2”), while a third construct was designed that added four additional heptad repeats to greatly lengthen the extendable region (“Closed/Rigid-3”). Further, a fourth construct was designed that introduced a Gly-Ser linker directly in between the C-terminal end of the GCN4 domain and I53_dn5B (“Closed/Flexible”), which was intended to maintain trimeric closure of RBDs while allowing significant flexibility between the antigens and the nanoparticle surface. After producing and assembling all designs into nanoparticles, negative stain EM averages were collected for all three new constructs, in addition to the original design lacking the designed disulfide and inter-RBD interface (“Open/Flexible”). Low resolution 3D reconstructions of both the Closed/Rigid-1 and Closed/Rigid-3 designs demonstrated significant rigidity between the TriHead antigens and nanoparticle surface, however with striking differences in the spacing of TriHeads (**Figure 2.2A**). In contrast, both the Closed/Flexible and Open/Flexible constructs did not show clear density for the antigens, therefore validating the desired flexibility between antigens and the nanoparticle surface of these constructs.

A study was initiated in mice to understand the effects of both RBD trimeric closure and antigen spacing on immunogenicity. BALB/c mice were immunized three times with equimolar doses of nanoparticle immunogens from all five groups, with serum collected two weeks after the third immunization (**Figure 2.2B**). Enzyme-linked immunosorbent assay (ELISA) binding titers against matched NC99 HAs represented in the immunogens reached the upper limit of detection, suggesting strong inherent immunogenicity of all constructs (**Figure 2.2C**). However, differences in the quality of immunogenicity against NC99 viruses was resolved by testing microneutralization (**Figure 2.2D**). Between all three immunogens with rigidly-spaced antigens, stronger neutralizing titers were observed for groups with shorter GCN4 regions. Neutralizing titers elicited by the Closed/Rigid-1 immunogen also far exceeded those elicited by both the Closed/Flexible and Open/Flexible immunogens. Neutralizing antibodies against the RBD most commonly work by blocking receptor binding (Krammer et al. 2020), suggesting that the

combination of closure, rigidity and shortened GCN4 region may assist direction of humoral responses towards the apical region of the RBD near the RBS. Breadth of binding titers was also measured against two mismatched H1N1 viruses (**Figure 2.2C**), in which closer spacings similarly demonstrated improvements to breadth. In contrast to strain-matched neutralizing titers, maximal breadth of binding was observed by the Open/Flexible group, suggesting that responses against the interface region could assist breadth in ways consistent with broadly cross-reactive interface-directed antibodies. In all, the multiple levels of control provided by the customizability of this platform allows for tuning of responses against the HA head to preferentially include or focus on particular epitopes.

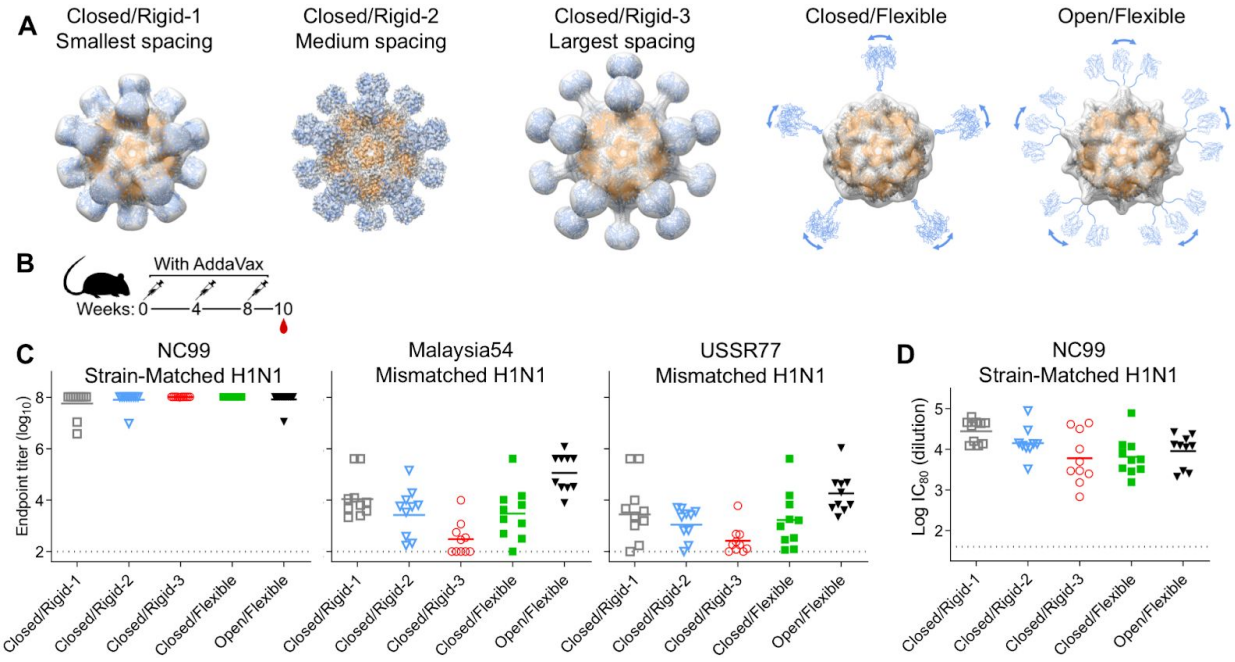

Figure 2.2: Structural and immunogenic characterization of immunogens displaying head domains in different states of closure and/or geometric spacings. **A)** 3D class averages of five HA-head based nanoparticle immunogens obtained by negative stain EM or cryo-EM. Structural characterization of the Closed/Flexible and Open/Flexible constructs could not resolve the head antigens, and head antigens shown for these constructs are representative cartoons to demonstrate flexibility. Models of nanoparticles and antigens are all rigid body fits. **B)** Immunization schedule in mice, with immunizations on weeks 0, 4 and 8 with serum collection on week 10. All immunizations contained equimolar amounts of the HA head, with all doses near 1.5ug. **C)** Week 10 ELISA endpoint binding titers against HAs from diverse H1N1 strains, including strain-matched NC99 HA, and mismatched Malaysia54 and USSR77 HAs. **D)** Week 10 strain-matched microneutralization titers against H1N1 NC99 virus. Data plotted are titers for which 80% of virus entry to host cells was inhibited.

Discussion

As structure-based vaccine design has grown largely in the last decade, the ability to focus antibody responses on arbitrary epitopes has long been desired for many pathogens. Most utilized strategies have aimed to focus antibodies on desirable epitopes by removing focus on undesirable epitopes, either by removing or obscuring their base antigenicity through domain deletions or hyperglycosylation. While promising in some circumstances, this arithmetic

approach inherently involves removing parts of antigens that could participate valuably in polyclonal responses. The results presented here demonstrate an advancement in the structural precision used for the design of nanoparticle immunogens, which generally opens opportunities for vaccine development for influenza and other pathogens, alternatively to traditional epitope-focused antigen design strategies. To our knowledge, this research describes the most rigid attachment of a glycoprotein antigen to a protein nanoparticle to date. Beyond this, the approach used is particularly versatile in the use of helical bundles with modular units of heptad repeats to mediate between two rigidly attached bodies, which allows for different rigid spacings of antigens to be investigated on nanoparticle surfaces. The rigidity of antigenic spacings achieved, as validated by electron microscopy, was vital for demonstrating how geometric properties of the studied immunogens can correlate with their immunogenicity. Given the clear differences in neutralization between distinct rigidly-designed immunogens, it is likely that these geometric differences are responsible for shifting responses to particular epitopes of the head, such as the apical region that features the RBS. In comparison with other published research, it is becoming more clear that leverage of finer details in the particulate display of antigens can be an alternative strategy for epitope-focused immunogen design that does not require direct alterations to base antigenicity.

For influenza vaccines, the described research most directly provides novel methods for altering the immunogenicity of the head domain, and could further inspire epitope-targeted vaccine design against other parts of the virus. Head-directed responses are highly valuable, with HAI currently the most clinically-proven correlate of protection and commercial vaccines largely relying on antibody responses with measurable HAI activity. The ability to directly improve on the potency and/or breadth of head-directed responses could allow for improved and even universal influenza vaccines. Here, we present modular strategies for altering the immunogenicity of the head domain of a single strain of HA without modifications to key exterior antigenic regions, which stands in contrast to other published strategies for head-directed vaccines (Giles and Ross 2011; Allen, Ray, and Ross 2018; Sautto, Kirchenbaum, and Ross 2018; Bajic et al. 2019; Broecker et al. 2019; Sun et al. 2019). This sets up the ability to amend the proposed strategies of controlling head closure and antigen spacing to arbitrary HA sequences, with amendability to diverse vaccine target product profiles. Further investigations into the precise epitopes targeted on the head domain in different designed immunogens and how this correlates with neutralization and protection will be vital for a greater understanding of this strategy. As well, further generalization of geometry-leveraged epitope prioritization using nanoparticle display to target the HA stem region or conserved regions of the neuraminidase glycoprotein would be exceedingly valuable.

Contributors and acknowledgements

I would like to thank Seyhan Boyoglu-Barnum, Young-Jun Park, Yaroslav Tsybovsky, David Veesler, Neil P. King and Masaru Kanekiyo for their leadership and extensive contributions to this project. I would also like to thank Rebecca A. Gillespie, Geoffrey B. Hutchinson, Rashmi Ravichandran, Mike Murphy, Deleah Pettie, Nick Matheson, Lauren Carter, Adrian Creanga and Barney S. Graham for direct contributions to this project.

Materials and Methods

Protein expression and purification

All designed HA head constructs were expressed by transient transfection in Expi293F cells (ThermoFisher Scientific) at a density of 2.5×10^6 cells/ml using the ExpiFectamine™ 293 Transfection Kit (ThermoFisher Scientific). The supernatants were harvested 5 days post-transfection and centrifuged at 4000 rpm to remove cell debris. Proteins were purified from clarified supernatants by immobilized metal affinity chromatography (IMAC) using either Ni^{2+}- or Co^{2+}-containing resin. For Ni^{2+}-based IMAC, clarified supernatants were incubated for 2 h at room temperature with Ni^{2+} Sepharose High Performance histidine-tagged protein purification resin (Cytiva) and bound protein eluted using 50 mM Tris pH 8.0, 0.5 M NaCl, 300 mM imidazole. For Co^{2+}-based resin, clarified supernatants were flowed over Talon resin (Takara), and bound protein eluted in 20 mM Tris pH 8.0, 300 mM NaCl, 300 mM imidazole. Eluted proteins were further purified by SEC into phosphate-buffered saline (PBS) or 25 mM Tris pH 8.0, 150 mM NaCl, 5% glycerol using a Superdex 200 Increase 10/300 column (Cytiva).

Negative stain EM sample preparation and analysis

NS-EM and particle image averaging was used to assess whether the head domains of recombinant NA proteins adopted the open or closed tetrameric structure. Proteins were diluted to between 0.1–0.2 mg/mL using either 10 mM HEPES pH 7.0, 150 mM NaCl or 10 mM Tris pH 7.5, 150 mM NaCl. Samples were adsorbed to glow-discharged carbon-coated copper grids. The grids were either washed with a drop of the same buffer three times and stained with 0.75% uranyl formate, or blotted and stained directly with 0.75% uranyl formate. Images were recorded with sampling ranging between 1.9 Å/pixel and 2.2 Å/pixel, depending on the microscope. Data were collected on either an FEI Tecnai T20 electron microscope equipped with an FEI Eagle CCD camera and operated at 200 kV using SerialEM (Takaba, Maki-Yonekura, and Yonekura 2020), or on an FEI Tecnai 12 Spirit 120kV electron microscope equipped with a Gatan Ultrascan 4000 CCD camera. Particles were selected from the micrographs automatically using either in-house software (Yaroslav Tsybovsky, unpublished) or were picked in a reference-free manner in cisTEM (Grant, Rohou, and Grigorieff 2018). For the latter datasets, particles were extracted after correcting for the effect of the CTF for each micrograph with cisTEM (Grant, Rohou, and Grigorieff 2018). Depending on user, dataset, and microscope, particles were either extracted into 120×120-pixel boxes with a final pixel size of 2.2 Å/pixel or extracted with a box size of 176×176 pixels and binned to a final box size of 44×44 pixels (to a pixel size of 6.4 Å/pixel). Reference-free 2D classification was performed using either Relion 1.4 or Relion 3.1 (Zivanov et al. 2018; Scheres 2015).

Protein-protein interface design using Rosetta

All calculations in Rosetta were made using versions v2017.18-dev59451, v2019.21-dev60746, or v2019.45-dev61026. For design of interfaces between HA heads, residue positions were manually selected in the head-head interface of a model of a closely-related strain to NC99 (PDB ID 5UG0). The three-fold symmetry axis of the symmetric HA trimer was aligned with [0,0,1] and a single protomer was saved in .pdb format. A design protocol was written using RosettaScripts (Fleishman et al. 2011) that takes the aligned protomer and a custom resfile as inputs, with the resfile dictating the side chain identities and conformations sampled during design. Briefly, the protocol applies two rounds of design based on the input resfile, with side

chain and backbone energy minimization applied after each design step. Both design and minimization steps were allowed to repack or minimize residues within 5 Å of all mutable or packable residues listed in the resfile. Multiple resfiles were set up to diversify allowed residue identities at each position to lead trajectories towards different solutions. Design models and scores were manually inspected to identify interactions across the interface that appeared structurally feasible. Favorable interactions were iteratively retested in resfiles and manually refined to finalize a diverse set of designs.

Biolayer interferometry

BLI binding assays were performed on an Octet Red instrument at 25°C with shaking at 1,000 RPM in the presence of 25mM Tris pH 8.0, 150mM NaCl and 5% glycerol. Anti-hIgG Capture (AHC) tips were loaded with human D2 H1-1/H3-1 or C05 at 0.02mg/mL for 300s prior to a baseline for 60s, association with trimeric components at 500nM for 600s, and dissociation for 300s.

Cryo-electron microscopy sample preparation, data collection, and image processing

Nanoparticle samples were diluted to 1–1.5 μM in buffer (10 mM Tris, pH 7.5, 150 mM NaCl) and 3 μL sample loaded onto a freshly glow-discharged 1.2/1.2 UltrAuFoil grid (300 mesh) prior to plunge freezing using a vitrobot Mark IV (ThermoFisher Scientific) with a blot force of -1 and 3.5–4.5 s blot time at 100% humidity and 4°C. Data were acquired on an FEI Glacios transmission electron microscope operated at 200 kV and equipped with a Gatan K2 Summit direct detector. Automated data collection was carried out using Leginon (Suloway et al. 2005) at a nominal magnification of 36,000× with a pixel size of 1.16 Å. The dose rate was adjusted to 8 counts/pixel/s, and each movie was acquired in counting mode fractionated in 50 frames of 200 ms. Reference-free 2D and 3D classification were performed using cryoSPARC (Punjani et al. 2017).

References

Allen, James D., Satyajit Ray, and Ted M. Ross. 2018. “Split Inactivated COBRA Vaccine Elicits Protective Antibodies against H1N1 and H3N2 Influenza Viruses.” *PloS One* 13 (9): e0204284.

Bachmann, Martin F., and Gary T. Jennings. 2010. “Vaccine Delivery: A Matter of Size, Geometry, Kinetics and Molecular Patterns.” *Nature Reviews. Immunology* 10 (11): 787–96.

Bachmann, M. F., and R. M. Zinkernagel. 1996. “The Influence of Virus Structure on Antibody Responses and Virus Serotype Formation.” *Immunology Today* 17 (12): 553–58.

———. 1997. “Neutralizing Antiviral B Cell Responses.” *Annual Review of Immunology* 15: 235–70.

Bajic, Goran, Max J. Maron, Yu Adachi, Taishi Onodera, Kevin R. McCarthy, Charles E. McGee, Gregory D. Sempowski, et al. 2019. “Influenza Antigen Engineering Focuses Immune Responses to a Subdominant but Broadly Protective Viral Epitope.” *Cell Host & Microbe* 25 (6): 827–35.e6.

Bangaru, Sandhya, Shanshan Lang, Michael Schotsaert, Hillary A. Vanderven, Xueyong Zhu, Nurgun Kose, Robin Bombardi, et al. 2019. “A Site of Vulnerability on the Influenza Virus Hemagglutinin Head Domain Trimer Interface.” *Cell* 177 (5): 1136–52.e18.

Bangaru, Sandhya, Heng Zhang, Iuliia M. Gilchuk, Thomas G. Voss, Ryan P. Irving, Pavlo Gilchuk, Pranathi Matta, et al. 2018. “A Multifunctional Human Monoclonal Neutralizing Antibody That Targets a Unique Conserved Epitope on Influenza HA.” *Nature Communications* 9 (1): 2669.

Belongia, Edward A., Melissa D. Simpson, Jennifer P. King, Maria E. Sundaram, Nicholas S. Kelley, Michael T. Osterholm, and Huong Q. McLean. 2016. “Variable Influenza Vaccine Effectiveness by Subtype: A Systematic Review and Meta-Analysis of Test-Negative Design Studies.” *The Lancet*

Infectious Diseases 16 (8): 942–51.
Benton, Donald J., Steven J. Gamblin, Peter B. Rosenthal, and John J. Skehel. 2020. “Structural Transitions in Influenza Haemagglutinin at Membrane Fusion pH.” *Nature* 583 (7814): 150–53.
Broecker, Felix, Sean T. H. Liu, Nungruthai Suntronwong, Weina Sun, Mark J. Bailey, Raffael Nachbagauer, Florian Krammer, and Peter Palese. 2019. “A Mosaic Hemagglutinin-Based Influenza Virus Vaccine Candidate Protects Mice from Challenge with Divergent H3N2 Strains.” *NPJ Vaccines* 4 (July): 31.
Brouwer, Philip J. M., Aleksandar Antanasijevic, Zachary Berndsen, Anila Yasmeen, Brooke Fiala, Tom P. L. Bijl, Ilja Bontjer, et al. 2019. “Enhancing and Shaping the Immunogenicity of Native-like HIV-1 Envelope Trimers with a Two-Component Protein Nanoparticle.” *Nature Communications* 10 (1): 4272.
Das, Dibyendu Kumar, Ramesh Govindan, Ivana Nikić-Spiegel, Florian Krammer, Edward A. Lemke, and James B. Munro. 2018. “Direct Visualization of the Conformational Dynamics of Single Influenza Hemagglutinin Trimers.” *Cell* 174 (4): 926–37.e12.
Dintzis, H. M., R. Z. Dintzis, and B. Vogelstein. 1976. “Molecular Determinants of Immunogenicity: The Immunon Model of Immune Response.” *Proceedings of the National Academy of Sciences of the United States of America* 73 (10): 3671–75.
Ekiert, Damian C., Arun K. Kashyap, John Steel, Adam Rubrum, Gira Bhabha, Reza Khayat, Jeong Hyun Lee, et al. 2012. “Cross-Neutralization of Influenza A Viruses Mediated by a Single Antibody Loop.” *Nature* 489 (7417): 526–32.
Fleishman, Sarel J., Andrew Leaver-Fay, Jacob E. Corn, Eva-Maria Strauch, Sagar D. Khare, Nobuyasu Koga, Justin Ashworth, et al. 2011. “RosettaScripts: A Scripting Language Interface to the Rosetta Macromolecular Modeling Suite.” *PloS One* 6 (6): e20161.
Giles, Brendan M., and Ted M. Ross. 2011. “A Computationally Optimized Broadly Reactive Antigen (COBRA) Based H5N1 VLP Vaccine Elicits Broadly Reactive Antibodies in Mice and Ferrets.” *Vaccine* 29 (16): 3043–54.
Grant, Timothy, Alexis Rohou, and Nikolaus Grigorieff. 2018. “cisTEM, User-Friendly Software for Single-Particle Image Processing.” *eLife* 7 (March): e35383.
Harbury, P. B., P. S. Kim, and T. Alber. 1994. “Crystal Structure of an Isoleucine-Zipper Trimer.” *Nature* 371 (6492): 80–83.
Harris, Audray K., Joel R. Meyerson, Yumiko Matsuoka, Oleg Kuybeda, Amy Moran, Donald Bliss, Suman R. Das, et al. 2013. “Structure and Accessibility of HA Trimers on Intact 2009 H1N1 Pandemic Influenza Virus to Stem Region-Specific Neutralizing Antibodies.” *Proceedings of the National Academy of Sciences of the United States of America* 110 (12): 4592–97.
Harrison, Stephen C. 2015. “Viral Membrane Fusion.” *Virology* 479-480 (May): 498–507.
Hong, Minsun, Peter S. Lee, Ryan M. B. Hoffman, Xueyong Zhu, Jens C. Krause, Nick S. Laursen, Sung-Il Yoon, et al. 2013. “Antibody Recognition of the Pandemic H1N1 Influenza Virus Hemagglutinin Receptor Binding Site.” *Journal of Virology* 87 (22): 12471–80.
Impagliazzo, Antonietta, Fin Milder, Harmjan Kuipers, Michelle V. Wagner, Xueyong Zhu, Ryan M. B. Hoffman, Ruud van Meersbergen, et al. 2015. “A Stable Trimeric Influenza Hemagglutinin Stem as a Broadly Protective Immunogen.” *Science* 349 (6254): 1301–6.
Irvine, Darrell J., and Benjamin J. Read. 2020. “Shaping Humoral Immunity to Vaccines through Antigen-Displaying Nanoparticles.” *Current Opinion in Immunology* 65 (August): 1–6.
Kanekiyo, Masaru, M. Gordon Joyce, Rebecca A. Gillespie, John R. Gallagher, Sarah F. Andrews, Hadi M. Yassine, Adam K. Wheatley, et al. 2019. “Mosaic Nanoparticle Display of Diverse Influenza Virus Hemagglutinins Elicits Broad B Cell Responses.” *Nature Immunology* 20 (3): 362–72.
Klein, Joshua S., and Pamela J. Bjorkman. 2010. “Few and Far between: How HIV May Be Evading Antibody Avidity.” *PLoS Pathogens* 6 (5): e1000908.
Knight, Matthew, Siriruk Changrob, Lei Li, and Patrick C. Wilson. 2020. “Imprinting, Immunodominance, and Other Impediments to Generating Broad Influenza Immunity.” *Immunological Reviews* 296 (1): 191–204.
Krammer, Florian, and Peter Palese. 2015. “Advances in the Development of Influenza Virus Vaccines.” *Nature Reviews. Drug Discovery* 14 (3): 167–82.
Krammer, Florian, Jerry P. Weir, Othmar Engelhardt, Jacqueline M. Katz, and Rebecca Jane Cox. 2020. “Meeting Report and Review: Immunological Assays and Correlates of Protection for next-Generation Influenza Vaccines.” *Influenza and Other Respiratory Viruses* 14 (2): 237–43.

Lee, Jiwon, Daniel R. Boutz, Veronika Chromikova, M. Gordon Joyce, Christopher Vollmers, Kwanyee Leung, Andrew P. Horton, et al. 2016. “Molecular-Level Analysis of the Serum Antibody Repertoire in Young Adults before and after Seasonal Influenza Vaccination.” *Nature Medicine* 22 (12): 1456–64.
Lee, Peter S., Nobuko Ohshima, Robyn L. Stanfield, Wenli Yu, Yoshitaka Iba, Yoshinobu Okuno, Yoshikazu Kurosawa, and Ian A. Wilson. 2014. “Receptor Mimicry by Antibody F045-092 Facilitates Universal Binding to the H3 Subtype of Influenza Virus.” *Nature Communications* 5 (April): 3614.
Lee, Peter S., Reiko Yoshida, Damian C. Ekiert, Naoki Sakai, Yasuhiko Suzuki, Ayato Takada, and Ian A. Wilson. 2012. “Heterosubtypic Antibody Recognition of the Influenza Virus Hemagglutinin Receptor Binding Site Enhanced by Avidity.” *Proceedings of the National Academy of Sciences of the United States of America* 109 (42): 17040–45.
Punjani, Ali, John L. Rubinstein, David J. Fleet, and Marcus A. Brubaker. 2017. “cryoSPARC: Algorithms for Rapid Unsupervised Cryo-EM Structure Determination.” *Nature Methods* 14 (3): 290–96.
Raymond, Donald D., Goran Bajic, Jack Ferdman, Pirada Suphaphiphat, Ethan C. Settembre, M. Anthony Moody, Aaron G. Schmidt, and Stephen C. Harrison. 2018. “Conserved Epitope on Influenza-Virus Hemagglutinin Head Defined by a Vaccine-Induced Antibody.” *Proceedings of the National Academy of Sciences of the United States of America* 115 (1): 168–73.
Rimmelzwaan, Guus F., and Janet E. McElhaney. 2008. “Correlates of Protection: Novel Generations of Influenza Vaccines.” *Vaccine* 26 Suppl 4 (September): D41–44.
Sautto, Giuseppe A., Greg A. Kirchenbaum, and Ted M. Ross. 2018. “Towards a Universal Influenza Vaccine: Different Approaches for One Goal.” *Virology Journal* 15 (1): 17.
Scheres, Sjors H. W. 2015. “Semi-Automated Selection of Cryo-EM Particles in RELION-1.3.” *Journal of Structural Biology* 189 (2): 114–22.
Schiller, John, and Bryce Chackerian. 2014. “Why HIV Virions Have Low Numbers of Envelope Spikes: Implications for Vaccine Development.” *PLoS Pathogens* 10 (8): e1004254.
Schmidt, Aaron G., Huafeng Xu, Amir R. Khan, Timothy O’Donnell, Surender Khurana, Lisa R. King, Jody Manischewitz, et al. 2013. “Preconfiguration of the Antigen-Binding Site during Affinity Maturation of a Broadly Neutralizing Influenza Virus Antibody.” *Proceedings of the National Academy of Sciences of the United States of America* 110 (1): 264–69.
Shaw, Alan, Ian T. Hoffecker, Ioanna Smyrlaki, Joao Rosa, Algirdas Grevys, Diane Bratlie, Inger Sandlie, Terje Einar Michaelsen, Jan Terje Andersen, and Björn Högberg. 2019. “Binding to Nanopatterned Antigens Is Dominated by the Spatial Tolerance of Antibodies.” *Nature Nanotechnology* 14 (2): 184–90.
Suloway, Christian, James Pulokas, Denis Fellmann, Anchi Cheng, Francisco Guerra, Joel Quispe, Scott Stagg, Clinton S. Potter, and Bridget Carragher. 2005. “Automated Molecular Microscopy: The New Leginon System.” *Journal of Structural Biology* 151 (1): 41–60.
Sun, Weina, Ericka Kirkpatrick, Megan Ermler, Raffael Nachbagauer, Felix Broecker, Florian Krammer, and Peter Palese. 2019. “Development of Influenza B Universal Vaccine Candidates Using the ‘Mosaic’ Hemagglutinin Approach.” *Journal of Virology* 93 (12). https://doi.org/10.1128/JVI.00333-19.
Takaba, Kiyofumi, Saori Maki-Yonekura, and Koji Yonekura. 2020. “Collecting Large Datasets of Rotational Electron Diffraction with ParallEM and SerialEM.” *Journal of Structural Biology* 211 (2): 107549.
Turner, Hannah L., Jesper Pallesen, Shanshan Lang, Sandhya Bangaru, Sarah Urata, Sheng Li, Christopher A. Cottrell, et al. 2019. “Potent Anti-Influenza H7 Human Monoclonal Antibody Induces Separation of Hemagglutinin Receptor-Binding Head Domains.” *PLoS Biology* 17 (2): e3000139.
Ueda, George, Aleksandar Antanasijevic, Jorge A. Fallas, William Sheffler, Jeffrey Copps, Daniel Ellis, Geoffrey B. Hutchinson, et al. 2020. “Tailored Design of Protein Nanoparticle Scaffolds for Multivalent Presentation of Viral Glycoprotein Antigens.” *eLife* 9 (August). https://doi.org/10.7554/eLife.57659.
Veneziano, Rémi, Tyson J. Moyer, Matthew B. Stone, Eike-Christian Wamhoff, Benjamin J. Read, Sayak Mukherjee, Tyson R. Shepherd, et al. 2020. “Role of Nanoscale Antigen Organization on B-Cell Activation Probed Using DNA Origami.” *Nature Nanotechnology* 15 (8): 716–23.
Watanabe, Akiko, Kevin R. McCarthy, Masayuki Kuraoka, Aaron G. Schmidt, Yu Adachi, Taishi Onodera, Keisuke Tonouchi, et al. 2019. “Antibodies to a Conserved Influenza Head Interface Epitope Protect by an IgG Subtype-Dependent Mechanism.” *Cell* 177 (5): 1124–35.e16.
Whittle, James R. R., Ruijun Zhang, Surender Khurana, Lisa R. King, Jody Manischewitz, Hana Golding, Philip R. Dormitzer, et al. 2011. “Broadly Neutralizing Human Antibody That Recognizes the

Receptor-Binding Pocket of Influenza Virus Hemagglutinin." *Proceedings of the National Academy of Sciences of the United States of America* 108 (34): 14216–21.
Wu, Nicholas C., and Ian A. Wilson. 2020. "Influenza Hemagglutinin Structures and Antibody Recognition." *Cold Spring Harbor Perspectives in Medicine* 10 (8). https://doi.org/10.1101/cshperspect.a038778.
Xu, Rui, Jens C. Krause, Ryan McBride, James C. Paulson, James E. Crowe Jr, and Ian A. Wilson. 2013. "A Recurring Motif for Antibody Recognition of the Receptor-Binding Site of Influenza Hemagglutinin." *Nature Structural & Molecular Biology* 20 (3): 363–70.
Zhu, Xueyong, Yong-Hui Guo, Tao Jiang, Ya-Di Wang, Kwok-Hung Chan, Xiao-Feng Li, Wenli Yu, et al. 2013. "A Unique and Conserved Neutralization Epitope in H5N1 Influenza Viruses Identified by an Antibody against the A/Goose/Guangdong/1/96 Hemagglutinin." *Journal of Virology* 87 (23): 12619–35.
Zivanov, Jasenko, Takanori Nakane, Björn O. Forsberg, Dari Kimanius, Wim Jh Hagen, Erik Lindahl, and Sjors Hw Scheres. 2018. "New Tools for Automated High-Resolution Cryo-EM Structure Determination in RELION-3." *eLife* 7 (November): e42166.

Chapter 3: Structure-based design of stabilized recombinant influenza neuraminidase tetramers

Summary

Influenza virus neuraminidase (NA) is a major antiviral drug target and has recently reemerged as a key target of antibody-mediated protective immunity. Here we show that recombinant NAs across all non-bat subtypes adopt various tetrameric conformations, including a previously unreported “open” state that may help explain poorly understood variations in NA stability across viral strains and subtypes. We used homology-directed protein design to uncover the structural principles underlying these distinct tetrameric conformations and stabilize multiple recombinant NAs in the “closed” state. In addition to improving thermal stability, conformational stabilization improved affinity to protective antibodies elicited by viral infection, including a broadly reactive antibody targeting the catalytic site, revealing complex yet direct connections between the stability, conformational state, and antigenicity of NA. Our findings provide a deeper understanding of NA structure and stability as well as a roadmap towards structure-based discovery of NA-directed therapeutics and vaccines.

Introduction

Influenza viruses are negative-sense RNA viruses in the family *Orthomyxoviridae*. The two major viral glycoproteins hemagglutinin (HA) and neuraminidase (NA) facilitate viral entry and egress from host cells, respectively. NA is an enzyme that binds and cleaves sialosides from glycans on the host cell surface to facilitate the release of nascent viral particles from infected cells, and is also proposed to assist other stages in the virus replication cycle (McAuley et al. 2019; Vahey and Fletcher 2019). Like HA, influenza A NAs are divided into subtypes that are clustered into the phylogenetically defined groups 1 (N1, N4, N5, and N8) and 2 (N2, N3, N6, N7, and N9), whereas influenza B NAs are clustered in a separate branch (Krammer et al., 2018). NA is a homotetrameric, type II integral membrane protein with a short cytoplasmic N-terminal domain. The C-terminal catalytic domain folds into a disulfide-stabilized and glycosylated six-bladed beta propeller and is supported by a hypervariable stalk domain (Colman, 1994; Colman et al., 1983). Published crystal structures of NA catalytic domains, either proteolytically released from viruses or produced recombinantly, have consistently shown that four identical subunits interact non-covalently to form a globular “head” with four-fold symmetry (McAuley et al., 2019; Varghese et al., 1983). The head features deep pockets on the exterior face of each protomer comprising the catalytic residues. One active site loop, commonly referred to as the ‘150-loop’, stretches from the inter-subunit interface to a corner of the catalytic pocket and has been observed to adopt distinct conformations that appear to be influenced by the binding of small molecule inhibitors (Amaro et al., 2011; Russell et al., 2006). The adjacent ‘430-loop’ is also predicted to be relatively dynamic and capable of regulating binding events in the active site (Amaro et al., 2009; Kwon et al., 2018). NA contains several Ca^{2+} binding sites, one of which is highly conserved and supports the periphery of the catalytic pocket on each protomer, while another site at the four-fold axis is frequently, but not universally, observed across various subtypes (Air, 2012). Ca^{2+} ions have been shown to assist catalytic activity (McAuley et al., 2019) and have been resolved to varying degrees in crystal structures, with reports and predictions of increased structural flexibility in their absence (Han et al., 2020; Smith

et al., 2006). These observations, combined with remote epistatic effects that impact sialoside binding and resistance to catalytic inhibitors, highlight the relatively plastic conformational landscape of NA (Duan et al., 2014; Fujisaki et al., 2012; McKimm-Breschkin et al., 2013, 2019; Zanin et al., 2017).

While multiple studies have shown that antibodies against NA correlate with immunity against influenza viruses (Couch et al., 2013; Kilbourne et al., 1968; Memoli et al., 2016; Monto et al., 2015; Murphy et al., 1972; Schulman et al., 1968), substantial gaps remain in our knowledge of NA-directed immunity, particularly in terms of the relationships between NA structure, conformational stability, and antigenicity. The antigenicity of NA has long been detailed using monoclonal antibodies (mAbs) isolated from immunized and/or infected mice, which provided an initial understanding of its distinct antigenic regions—some of which span adjacent protomers—as well as mechanisms of both enzymatic inhibition and protection (Colman et al., 1987; Gulati et al., 2002; Jiang et al., 2016; Malby et al., 1994; Saito et al., 1994). Although an NA-based vaccine, extracted from viral membranes and inactivated by formalin, was evaluated in humans in a Phase I clinical trial 25 years ago and improved humoral NA-directed inhibition compared to commercial vaccines (Hocart et al., 1995; Kilbourne et al., 1995), only preclinical studies of NA-based vaccines have been reported since (Broecker et al., 2019; Liu et al., 2015; Smith et al., 2017; Wohlbold et al., 2015). More recently, studies comparing antibodies elicited by infection or immunization with split virus vaccines in humans as well as mice have clearly demonstrated that infection results in substantially more robust NA-directed humoral responses (Chen et al., 2018). Protective human mAbs have most frequently been isolated from infected individuals, with the recent exception of mAbs isolated from a minority of subjects receiving H7N9 vaccines that generated detectable anti-NA responses (Chen et al. 2018; Gilchuk et al. 2019; Madsen et al. 2020; Stadlbauer et al. 2019). These studies have further defined NA epitopes targeted by protective antibodies, most notably leading to the isolation from an H3N2-infected individual of broadly cross-reactive and protective antibodies that bind the catalytic site (Stadlbauer et al., 2019). The disconnect between infection- and vaccine-elicited responses appears to be due to existing vaccine manufacturing processes causing NA to unfold and lose its native structure (Chen et al., 2018), suggesting that there is substantial room to improve the composition and stability of NA-based immunogens.

Despite the atomic structure of NA having been known for decades, its conformational stability in solution has not been fully understood or explored. In agreement with crystal structures, tomographic models of NA on the surface of virions have shown a compact, “closed” four-fold symmetric arrangement of the catalytic domains (Harris et al., 2006, 2013). In contrast to other sialidases that share the same six-bladed propeller fold and can function as monomers (Taylor, 1996), it has frequently been reported that tetramer formation is a prerequisite for the function of influenza NA (Bucher and Kilbourne, 1972; Dai et al., 2016; McMahon et al., 2020; da Silva et al., 2013; Sultana et al., 2011). Consequently, catalytic activity is often considered an important indicator of the biologically relevant conformation (Sultana et al., 2014). Interestingly, NA stability against denaturing conditions, measured by enzymatic activity, differs markedly between viral strains and subtypes, with N1 strains generally being less stable than N2 (Rajendran et al., 2017; Sultana et al., 2014). Differences in NA immunogenicity have also been observed between N1 and N2 strains, and have been suggested to reflect variations in stability (Rajendran et al., 2017; Sultana et al., 2014). Recent attempts to understand and improve NA

stability have shown some promise, and have suggested connections between exposure to Ca^{2+} ions, antigenicity, oligomerization, and general stability (McMahon et al., 2020; Wang et al., 2019; Zhu et al., 2019).

Here we characterize a previously unreported "open" tetrameric conformation adopted by recombinant NAs and provide a general structure-based design strategy for stabilizing the closed tetrameric state. Closed versions of engineered recombinant N1 NAs have improved stability and affinity to infection-elicited protective antibodies relative to their wild-type counterparts, providing new opportunities to design and discover NA-based vaccines and therapeutics.

Results

The Tetrameric Conformation of Recombinant NA Proteins Varies Across Influenza Strains and Subtypes

We expressed and purified recombinant NA proteins from every non-bat influenza A subtype and two influenza B viruses using a previously described format (Xu et al., 2008) in which the cytosolic, transmembrane, and stalk domains of the wild-type (WT) NA (residues 1–82, N1 numbering) were replaced by affinity purification tags, a tetramerization domain derived from human vasodilator-stimulated phosphoprotein (hVASP) (Kühnel et al., 2004), a thrombin protease cleavage site, and a two-residue GG linker (**Figure 3.1A–B**). The recombinant proteins, secreted from mammalian cells and purified from clarified supernatants, yielded homogeneous size exclusion chromatography (SEC) profiles featuring a major peak corresponding to the estimated elution volume of a tetramer, with minimal aggregation (**Figure S3.1A**). However, two-dimensional (2D) class averages obtained by electron microscopy analysis of negatively stained samples revealed unexpected structural heterogeneity (**Figure 3.1C**). Two tested NAs each from the N2 subtype and influenza B viruses, as well as representative NAs from N3 and N5 formed "closed" tetrameric structures in which the head domains packed tightly and resembled the four-fold symmetric structure classically observed by X-ray crystallography. In contrast, representative NAs from the N1 and N6 subtypes formed "open" tetramers in which the head domains did not form a single, compact structure. These NAs instead exhibited a clover-like appearance characterized by a thin stalk tethered to independent densities corresponding to the four globular head domains. Representative NAs from the N4, N7, N8, and N9 subtypes, in addition to a third tested N2 strain, formed mixtures of open and closed tetramers.

We explored whether destabilization of the closed tetrameric conformation was due to the conditions the proteins experienced during negative stain electron microscopy (NS-EM). To determine the structure of NA in solution, the WT NA from the H1N1 strain A/California/07/2009 (abbreviated as N1-CA09-WT) was vitrified and imaged by cryoelectron microscopy (cryo-EM). 2D classification of the data revealed heterogeneity consistent with the NS-EM data, with N1-CA09-WT forming a variety of poorly ordered open tetramers (**Figure 3.1D**). No 2D classes matched the crystallographically observed, four-fold symmetric closed conformation (van der Vries et al., 2012). However, several 2D classes indicated that adjacent head domains formed dimers reminiscent of conformations observed in distantly related proteins with the same six-bladed propeller fold, such as the hemagglutinin (H), hemagglutinin-neuraminidase (HN), and G proteins of paramyxoviruses (Aguilar et al., 2016; Yuan et al., 2005).

We tested whether several commonly used biochemical and biophysical techniques could discern the structural differences we observed by EM. We found no clear correlation between SEC profiles and the conformations observed by NS-EM (**Figure S3.1A**). Although NA contains an interprotomeric Ca^{2+} binding site that thermally stabilizes the protein (Wang et al., 2019), the addition of 1 mM $CaCl_2$ to purified N1-CA09-WT prior to NS-EM did not result in tetramer closure, indicating that potential Ca^{2+} deficiency does not explain the conformational differences between different recombinant NAs (**Figure 3.1E**). Importantly, all NAs tested were catalytically active (**Figure S3.1B**), although levels of catalytic activity varied, with no clear correlation to the conformational states observed by EM.

We also determined the thermal stabilities of multiple NAs using nano differential scanning fluorimetry (nanoDSF), monitoring intrinsic tryptophan fluorescence (**Figure 3.1F** and **S3.1C**). While Ca^{2+} did not influence tetrameric closure, it is possible it could alter other aspects of NA stability. All measurements were performed in buffers containing either 1 mM $CaCl_2$ or 5 mM ethylenediaminetetraacetic acid (EDTA). Thermal stability varied widely across the recombinant NAs analyzed. NAs from representative N3 and N5 (identified as closed by NS-EM) and N8 (mixed) strains were found to have the highest thermal stability, with melting temperatures (T_m) above 60°C regardless of buffer additives (**Figure 3.1F**). However, N8-JD13-WT (A/Jiangxi Donghu/346/2013) had an incomplete yet clear transition between 46 and 52°C, depending on the buffer additive, which may be a partial unfolding event or the unfolding of a minor population of less stable species. Another closed NA, N2-WI05-WT (A/Wisconsin/67/2005), was less stable but also relatively insensitive to Ca^{2+}, with T_ms of 55.1°C in the presence of Ca^{2+} and 49.0°C in 5 mM EDTA. In contrast, the open N1-CA09-WT and N1-MI15-WT (A/Michigan/45/2015), and particularly the mixed N4-DB16-WT (A/Redknot/Delaware Bay/310/2016), showed much greater sensitivities to Ca^{2+}. These NAs had T_ms below 50°C in the presence of EDTA, which increased 12.5–23°C in the presence of Ca^{2+}. N1-CA09-WT stood out as having low thermal stability in both conditions. These data indicate that the thermal stabilities of recombinant NAs can vary over a wide range, and suggest that Ca^{2+} contributes less to the stability of NAs that tend to form closed tetramers, possibly because head tetramerization has an independent stabilizing effect.

Together, these data establish that the head domains of many influenza NAs, when expressed as recombinant tetramers, do not form the compact structure with four-fold symmetry observed crystallographically, and that several non-structural readouts, including catalytic activity, do not reflect these differences.

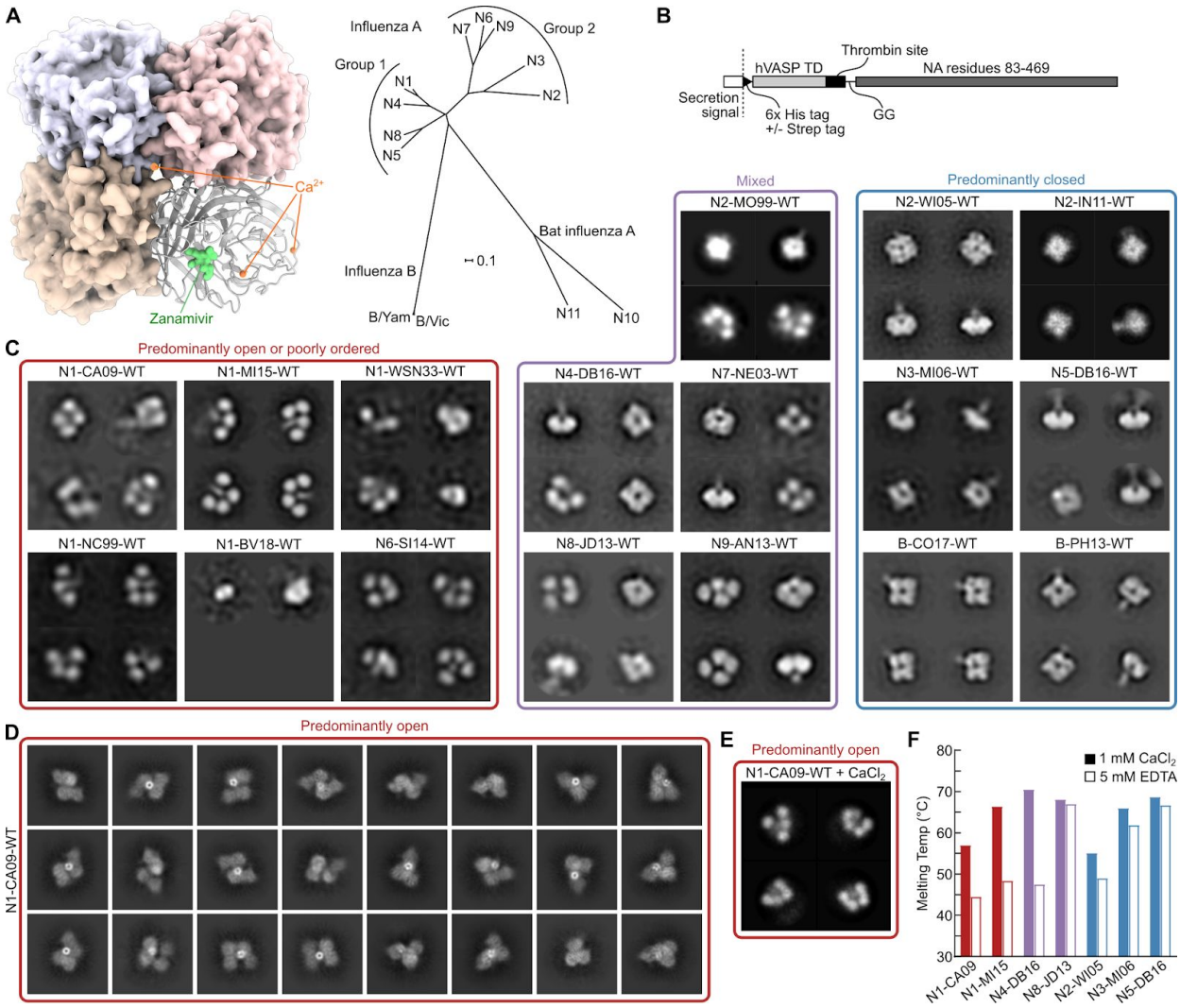

Figure 3.1. The Tetrameric Conformation of Recombinant NA Proteins Varies Across Influenza Strains and Subtypes

(A) NA structure and phylogeny. (Left) Model of NA structure as observed crystallographically, featuring a bound NA inhibitor (Zanamivir, green) and Ca^{2+} ions (orange). Model from PDB ID 4B7Q with the Ca^{2+} ion near the four-fold axis placed using an alignment with PDB ID 3NSS. (Right) Phylogenetic tree of NA of influenza A and B viruses. Scale bar, 0.1 amino acid substitutions per site.

(B) Construct diagram for recombinant NA proteins used in this work. The globular head domain of NA (residues 83–469, N1 numbering) was genetically fused to the hVASP tetramerization domain (TD) by a flexible GG linker and a thrombin protease cleavage site. All constructs contained an N-terminal hexahistidine tag, and some constructs additionally contained a Strep Tag.

(C) NS-EM 2D class averages of NA. (Left) NA preparations from strains that show predominantly open or poorly ordered tetramers. (Middle) NA preparations from strains that show mixtures of closed and open tetramers. (Right) NA preparations from strains that show predominantly closed tetramers similar to those classically observed in NA crystal structures.

(D) Cryo-EM 2D class averages of recombinant N1-CA09-WT.

(E) NS-EM 2D class averages of recombinant N1-CA09-WT in the presence of 1 mM $CaCl_2$.

(F) Melting temperatures of representative open, mixed, and closed recombinant NAs (see also **Figure S3.1**).

Stabilization of the Closed Tetrameric State of N1 NA CA09

Although high-resolution structural data for NA in its native context in the virion membrane is not yet available, cryo-electron tomographic reconstructions at modest resolution suggest that NA on the surface of H1N1 CA09 virions forms closed tetramers (Harris et al., 2013). Furthermore, the protective mAb CD6, isolated from a mouse infected with H1N1 virus, binds a quaternary epitope spanning two subunits of the NA tetramer, suggesting that the closed state of the tetramer is present on virions and is antigenically relevant (Wan et al., 2015). Inspired by these observations and the potential utility of recombinant NA antigens with improved stability, we set out to stabilize N1 NA in the closed tetrameric state.

The inter-protomer interface of N1-CA09-WT (PDB ID 4B7Q) has 3,172 $Å^2$ of buried surface area between each protomer, but features many aqueous cavities and non-ideal polar contacts. We attempted to design closed N1-CA09 tetramers by stabilizing this interface using homology-directed mutations inspired by NAs we identified as closed, as well as novel mutations identified purely by structural modeling (**Figure 3.2A**). Based on our data indicating that recombinant N2, N3, and N5 NAs form predominantly closed tetramers, we analyzed structural differences between representative NAs from each of these subtypes and N1-CA09-WT. Due to the higher sequence similarity of N4 to N1 NAs, an N4 NA structure was also included in this analysis even though it adopted a mixture of the open and closed states. To organize our design strategy, we identified residues involved in interprotomer interactions by visual inspection and categorized them into four “spaces” (**Figure 3.2B**). Space A is distal to the four-fold axis, near the CD6 epitope, and features an aqueous cavity surrounding I99 (N1 numbering, unless otherwise clarified). Space B is largely solvent-exposed and on the “underside” of NA, opposite the active site, surrounding Q408. Space C is at the four-fold axis and features residues that have been observed to bind Ca^{2+} ions, such as D113. Space D surrounds E165 between spaces B and C, and is also partially solvent-exposed towards the underside of the molecule.

To take advantage of the sequence differences between N1-CA09-WT and NAs from other subtypes, we developed a computational pipeline for homology-directed design using the Rosetta macromolecular modeling software (Fleishman et al., 2011; Leman et al., 2020). The protocol models sidechain repacking and conservative backbone movement surrounding homology-inspired mutations while maintaining four-fold symmetry in the closed tetrameric state. Potential interface-stabilizing mutations derived from closed NAs were modeled in Rosetta both individually and in combination within each space. Combinations of mutations included sets derived entirely from a single subtype or from multiple subtypes. In parallel, design trajectories that allowed Rosetta to identify novel mutations without restriction to naturally-observed substitutions were performed. Interestingly, we noted a tendency in these latter design trajectories for Rosetta to converge on mutations found naturally in N2, N3, N4, and N5 NAs instead of novel mutations. Mutations were discarded if they buried polar groups that were natively solvent-exposed or involved in hydrogen bonds, an important consideration when designing polar interactions (Boyken et al., 2016; Maguire et al., 2018). To prevent undesired alterations to antigenicity, mutations to surface-exposed residues were not frequently considered. Final mutation sets for each space were chosen according to several structure-based metrics and visual inspection. Thirty-two designs were selected for experimental

characterization, comprising designs with mutations contained to each individual space as well as across multiple spaces.

Genes for each stabilized NA protein (sNAp) were synthesized as genetic fusions to the hVASP tetramerization domain (**Figure 3.1B**) and transfected into mammalian cells to assess expression. Nine designs that were detectable in cell culture supernatants by SDS-PAGE were purified by affinity chromatography and analyzed by NS-EM. The success of each design was judged by its qualitative appearance and semi-quantitative counts of particles assigned to open, closed, or misformed/aggregated 2D classes. Of the nine designs analyzed by NS-EM, only one (N1-CA09-sNAp-94) contained a substantial population of closed structures, with approximately half of the particles classified as closed based on the 2D class averages (**Figure 3.2C**). Determining which mutations were most responsible for this partial closure was difficult because N1-CA09-sNAp-94 featured 10 mutations across all four spaces targeted, with mutations originating from all four NA subtypes analyzed in addition to novel mutations identified by Rosetta. To improve this design towards complete stabilization of the closed state, one additional N2- and N3-inspired mutation was added that appended an individual methyl group to a valine in space A (V177I; N1-CA09-sNAp-114), which resulted in predominantly closed particles by NS-EM (**Figure 3.2C**). Although a small number of particles in the open state were still detectable by EM, the vast majority of N1-CA09-sNAp-114 tetramers adopted the closed state.

Two additional rounds of design were performed to remove unproductive mutations from N1-CA09-sNAp-114 while maintaining closure and maximizing expression levels. Space C mutations derived from N4 NA were removed without deleterious effects, reverting the native Ca^{2+}-binding residues in this space to their original identities, and the N5-inspired combination of C161V and S172A was added to remove an unpaired cysteine and slightly repack space D, which greatly improved expression (N1-CA09-sNAp-130). N1-CA09-sNAp-155, which reverted an unnecessary mutation at the surface-exposed position 453 of N1-CA09-sNAp-130, maintained closure with similar expression to N1-CA09-WT and had its stabilizing mutations maximally buried to maintain proper antigenicity (**Figure 3.2C**). Relative to N1-CA09-WT, N1-CA09-sNAp-155 features four mutations in space A, three in space B, and three in space D. sNAp-130 and sNAp-155 were used interchangeably as representative sNAps for N1 CA09.

We used several assays to determine if closing the N1 CA09 tetramer physically stabilized the protein. nanoDSF of N1-CA09-WT and N1-CA09-sNAp-155 showed that the tetramer-stabilizing mutations increased the T_m by 9.5 and 19.1°C in the presence of $CaCl_2$ and EDTA, respectively (**Figure 3.2D**). Sensitivity to Ca^{2+} was substantially decreased, with only a 2.9°C difference between Ca^{2+}- and EDTA-containing conditions. This finding is consistent with our earlier observation that the thermal stability of closed tetramers tended to be less dependent on Ca^{2+} (**Figure 3.1F**). Monitoring static light scattering (SLS) also revealed an increase in aggregation temperature for N1-CA09-sNAp-155 of 9.7°C in the presence of Ca^{2+} (**Figure 3.2E**). Interestingly, neither protein aggregated in the presence of EDTA. Finally, hydrogen-deuterium exchange mass spectrometry (HDX-MS) was used to collect data on a small set of deuterium-exposed peptides from both N1-CA09-WT and N1-CA09-sNAp-130, which indicated multiple regions of differential stability (**Figure S3.2A**). Several peptides were identified near the inter-protomer interface and the catalytic pocket that showed decreased deuterium uptake for the sNAp, including one peptide that includes the main catalytic residue (Y402) and another

peptide containing the substrate-binding residue R368. These observations indicate that the sites experience a reduction in solvent accessibility or an increase in local ordering that are consistent with the sNAp adopting a more “closed” conformation compared to N1-CA09-WT. One peptide (residues 215–224) was more dynamic in the sNAp. A small portion of this peptide is included in a beta-sheet that contains two stabilizing mutations, which could have caused the increase in exchange at early timepoints relative to N1-CA09-WT. Importantly, N1-CA09-sNAp-130 was catalytically active, exhibiting activity that was comparable to N1-CA09-WT (**Figure S3.2B**).

While the V177I mutation suggested that improved packing in space A assists closure, the results from other less successful design attempts were compared to evaluate the contributions of other mutations (**Figure 3.2F**). Reversion of the three space B mutations in N1-CA09-sNAp-130 did not decrease tetrameric closure (N1-CA09-sNAp-131), although it did reveal a role for these mutations in increasing sNAp expression. Strikingly, reversion of the single N5-derived space D mutation E165S from N1-CA09-sNAp-c155 resulted in a roughly equal mixture of open and closed tetramers (N1-CA09-sNAp-c134). Together, these data demonstrate that combining mutations in spaces A and D can drive complete closure of CA09 NA.

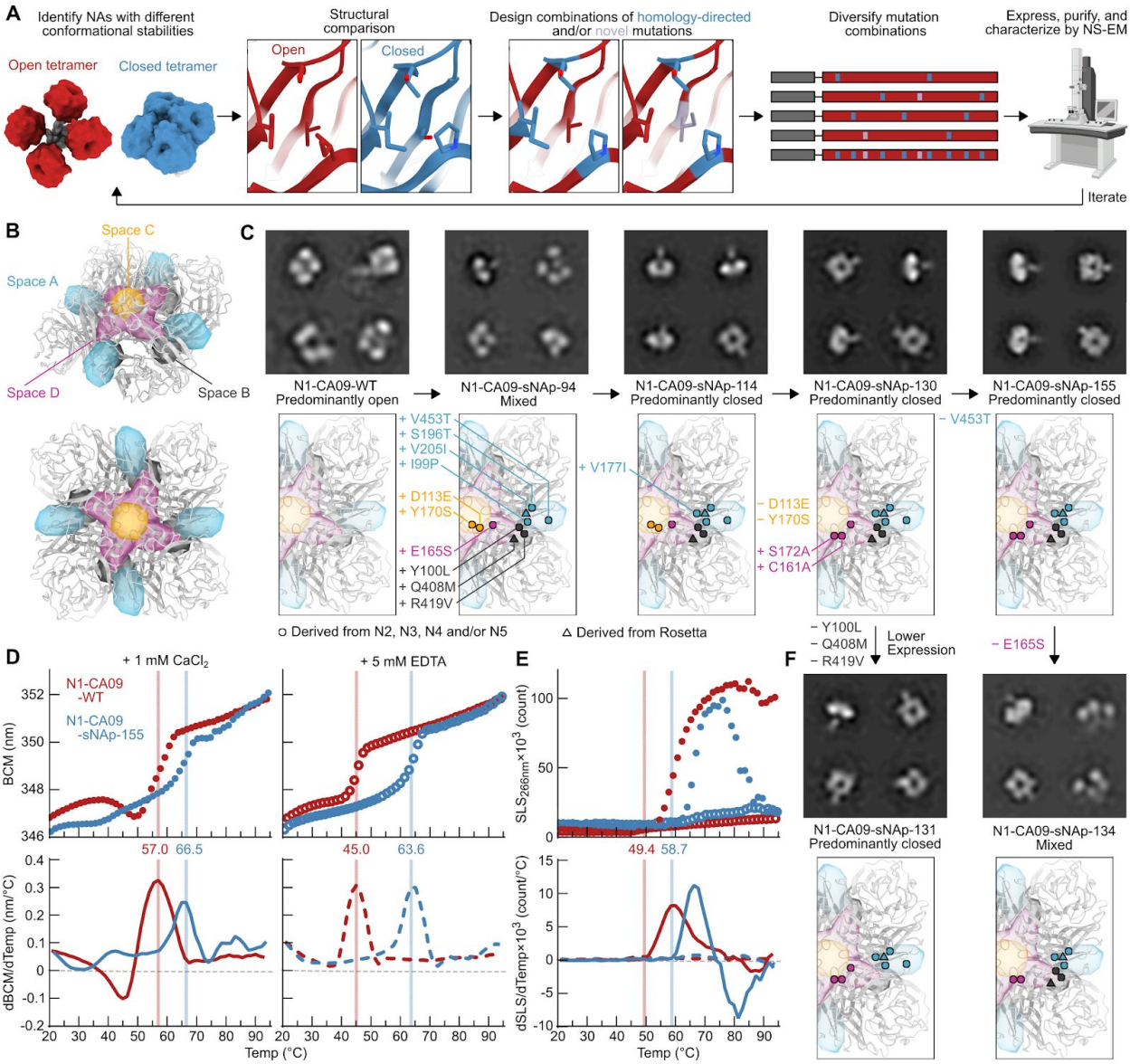

Figure 3.2. Stabilization of the Closed Tetrameric State of N1 NA CA09

(A) Design and analysis pipeline for stabilization of closed tetrameric NAs using homology-directed mutations and computational protein design. Models constructed using PDB-IDs 4B7Q, 6BR5, and 1USE.

(B) Structural depiction of the four different spaces in NA targeted for design. Two views of the CA09 NA tetramer are shown.

(C) NS-EM 2D class averages (top) and designed mutations (bottom) in a series of CA09 NA mutants that exhibit varying degrees of tetramer closure.

(D) Thermal denaturation of N1-CA09-WT and N1-CA09-sNAp-c155 in the presence of 1 mM $CaCl_2$ (closed circles and solid lines) or 5 mM EDTA (open circles and dashed lines), monitored by intrinsic tryptophan fluorescence. Top panels show raw data, while lower panels show smoothed first derivatives used to calculate melting temperatures. The barycentric mean (BCM) of the fluorescence emission spectra is plotted.

(E) SLS during thermal denaturation of N1-CA09-WT and N1-CA09-sNAp-c155 in the presence of 1 mM $CaCl_2$ or 5 mM EDTA, with aggregation temperatures shown for $CaCl_2$-treated samples. Data are plotted as in panel D.

(F) NS-EM 2D class averages (top) and mutations (bottom) in two CA09 NA mutants derived from N1-CA09-sNAp-130 and N1-CA09-sNAp-155, respectively, that explore the roles of spaces A, B, and D in tetramer closure and expression.

Structural and Bioinformatic Analysis of Closed State Stabilizing Mutations

To obtain more information on the effects of our tetramer-stabilizing mutations, we determined a cryo-EM structure of N1-CA09-sNAp-155 at 3.2 Å resolution (**Figures 3.3 and S3.3**). 2D class averages obtained from vitrified samples showed closed NA tetramers resembling those previously observed in crystal structures, and the 3D reconstruction confirmed that N1-CA09-sNAp-155 forms a closed tetramer in solution (**Figure 3.3A**). The structure is highly similar to N1 CA09 crystal structures (1.18 and 1.83 Å backbone RMSD to PDB 4B7Q over one and all four chains of the tetramer, respectively). The main differences were in a few solvent-exposed loops that were poorly ordered in N1-CA09-sNAp-155, including the C-terminal region from residues 458–469 and the 150- and 430-loops. The apparent flexibility of the 150- and 430-loops is consistent with previous structural observations and computational modeling of these regions (Amaro et al., 2009, 2011; Russell et al., 2006). Additionally, a backbone segment adjacent to the space A mutations was slightly rearranged such that W455 packed closely against the introduced mutations and W457 moved away from its native position at the interface. Despite this rearrangement, none of the mutated positions in spaces A, B, and D showed substantial changes in their main chain coordinates and, other than their interactions with W455 and W457, the intended interactions were formed. For example, P99 and T196 (T195 in N2 numbering) in space A form a central hydrophobic contact across the interface that closely matches the same interaction seen in the NA structures used for homology-directed design (**Figures 3.3B and 3.4A**). Likewise, I177 (I176 in N2 numbering) provides additional hydrophobic packing in both N1-CA09-sNAp-155 and the NAs of other subtypes relative to N1 CA09, while I205 adds further packing that was favored by Rosetta. In space B, the Rosetta-derived Q408M and the homology-inspired Y100L and R419V simultaneously provide improved hydrophobic packing and decrease the number of partially buried polar groups at the interface.

In contrast to intuitive stabilization mechanisms such as the cavity-filling mutations employed in space A, the N5 NA-inspired space D mutation E165S does not have an obvious structural explanation. Crystal structures of N2, N3, N4, and N5 NAs all show less bulky residues at position 165, including S, T, and V (**Figure 3.4A**). Depending on the rotameric orientation of S165, it could either stabilize the loop region from residues 160–165, which makes modest interface contacts, or possibly interact with a bridging water molecule hydrogen-bonded to the peptide backbone of the neighboring subunit (**Figures 3.3B** and **3.4A**). Interestingly, in all known NA structures a substantial cavity surrounds D103, adjacent to the 160-loop and near the inter-protomeric interface, raising the possibility that the E165S mutation may function by helping pre-organize this region during tetramer assembly. Structures of N2 and N3 NAs also show partial filling of this cavity compared to N1, N4, and N5 NAs, with the side chains involved either forming hydrogen bond networks within the cavity or filling it with hydrophobic packing. In N1 CA09, the higher entropy of the native E165 side chain compared to smaller residues may destabilize this region.

To better understand NA sequence-structure relationships, a comprehensive dataset of

unique NA sequences from all available influenza A viruses isolated before December 31, 2019 was compiled, and the mutational frequencies of key positions in spaces A and D were evaluated within each subtype (**Figure 3.4B**). As expected, some variation was observed in the amount of sequence diversity at each position, ranging from universal conservation of the tyrosine nucleophile in the catalytic site (Y402 and Y406 in N1 and N2 numbering, respectively) to high diversity at several surface-exposed positions (e.g., position 386 in N1 NAs) that is possibly due to immune selection. However, sequence diversity within each subtype was generally low: positions of mean entropy in N1 and N2 NAs, for which far greater numbers of unique sequences were available compared to the animal-derived N3, N4, and N5 subtypes, showed ~97% conservation of the predominant amino acid.

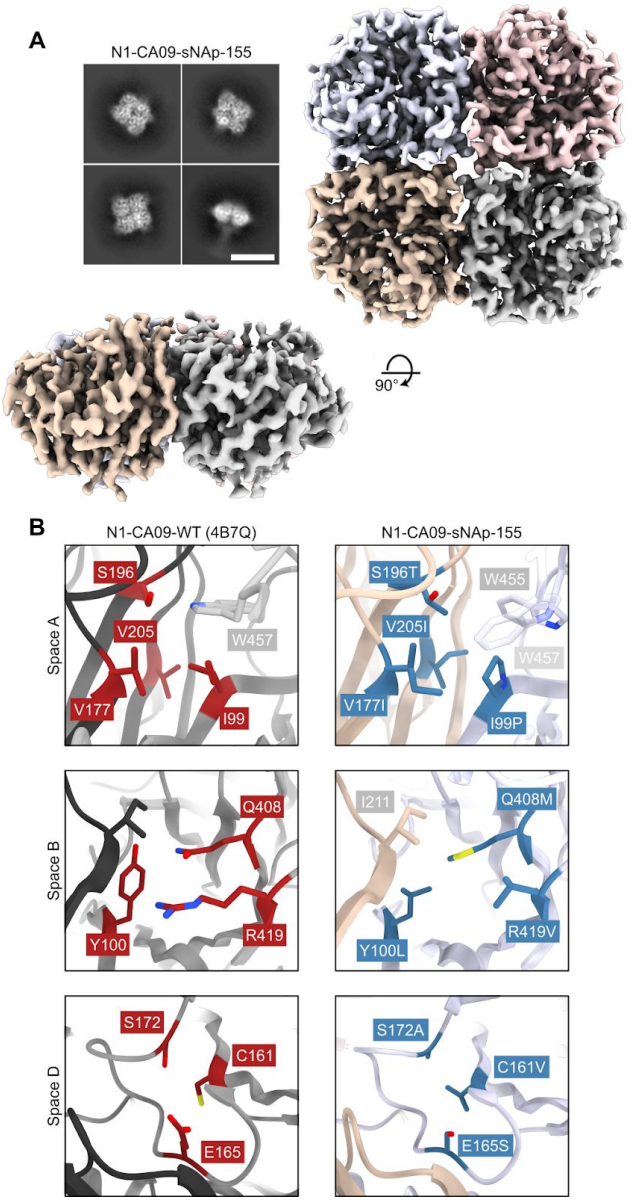

Figure 3.3. Cryo-EM structure of N1-CA09-sNAp-155
(A) Cryo-EM 2D class averages for N1-CA09-sNAp-155 showing fully closed tetramers (scale bar, 10nm) (top left). Cryo-EM map, colored by individual head domain, viewed down the four-fold symmetry axis (top right) and an orthogonal view (bottom left).
(B) Snapshots of the three major regions targeted for mutation: WT N1-CA09 (PDB 4B7Q, left), with residues targeted for mutation indicated (red). Space A (top), Space B (middle), and space D (bottom). Corresponding regions in the N1-CA09-sNAp-155 single particle reconstruction (right), with mutated residues indicated (blue) and non-mutated residues involved in packing colored by chain as in (A).

Fewer than 0.05% of the 4,422 animal and 13,735 human N1 NA sequences included in our dataset contain any of the five stabilizing mutations at positions 99, 165, 177, 196, and 205, with the vast majority of sequences instead conserving the less stable identities observed in N1-CA09-WT. Position 99 was the most variable, with valine present in ~9.8% of the sequences. We predict that both isoleucine and valine at position 99 favor the open state; 99.9% of N1 NA sequences contain one of these two residues. NAs from N2 (dataset of 8,888 animal and 23,121 human sequences), N3 (942 animal sequences), and N4 (242 animal sequences) are also highly conserved at most of these positions and share multiple features

that are distinct from N1 NAs, despite the close phylogenetic relationship between N1 and N4 (**Figure 3.1A**). For example, P99 and T196 (195 in N2 numbering) are nearly completely conserved in all three subtypes, forming a consistent hydrophobic contact that we employed in the sNAp designs. In contrast, position 177 (176 in N2 numbering) in space A is more variable in N2 and N3 NAs, with multiple identities appearing frequently, while N4 has a universally conserved valine at this position. N2-IN11-WT (A/Indiana/10/2011), which we found to be predominantly closed (**Figure 3.1C**), contains a methionine at position 176, showing that this substitution can favor the closed state similarly to isoleucine. N5 NAs have converged on a different solution in space A, maintaining complete conservation of the distinctive Y203, which both fills the cavity and accepts a hydrogen bond from the backbone amide of residue 99, thereby achieving the same outcome as P99 and T196 (**Figure 3.4A–B**). In space D, further similarities are observed among the more stable subtypes (N2, N3, N4, and N5) at position 165, with less flexible smaller or beta-branched amino acids (A/S/T/V/I) found in >99.9% of all sequences in these subtypes, with valine, serine, and threonine most prevalent by far.

These structural and bioinformatic analyses provide sequence-based signatures that appear to explain the conformational differences we observed in recombinant NAs by NS- and cryo-EM. Specifically, the combination of a small side chain at position 165 and a well-packed space A correlates with the stability of the closed tetrameric conformation.

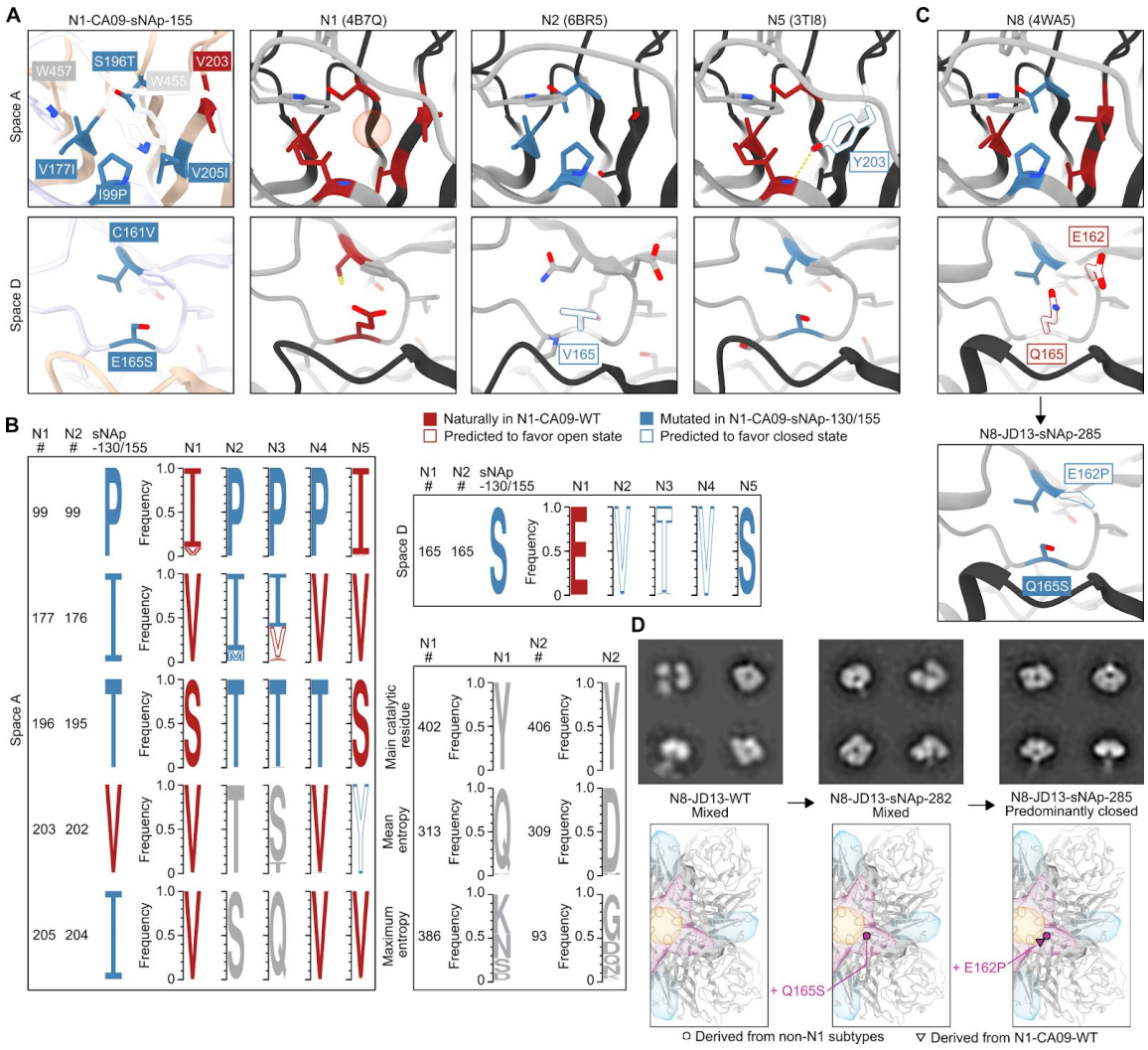

Figure 3.4. Structural and Bioinformatic Analysis of Closed State-Stabilizing Mutations

(A) Zoomed-in views of space A- and D-stabilizing mutations in the N1-CA09-sNAp-155 cryo-EM structure and corresponding regions in predominantly open N1 (PDB ID 4B7Q) and predominantly closed N2 (PDB ID 6BR5) and N5 (PDB ID 3TI8) NAs. The red sphere in N1 highlights the position of a structured water molecule in the space A cavity.

(B) Sequence logos for N1-CA09-sNAp-155 and naturally occurring NAs at positions that can alter NA tetrameric conformation, derived from a compiled database of all unique sequences from each subtype prior to December 31st, 2019.

(C) (Top) Spaces A and D in a representative crystal structure of an N8 NA (PDB ID 4WA5) and (Bottom) design model for space D of N8-JD13-sNAp-285.

(D) Mutation schematics and NS-EM comparing N8-JD13-WT, N8-JD13-sNAp-282, and N8-JD13-sNAp-285.

Design of Stabilized Closed Tetrameric N8 NA

Our finding that recombinant N8-JD13-WT forms a mixture of open and closed tetramers (**Figure 3.1C**) is consistent with a previous report showing that N8 NAs can form monomers and dimers, while a number of infection-elicited N8 NA-specific antibodies recognized a quaternary epitope (Saito et al., 1994), an observation that provides an incentive for tetramer stabilization.

We applied the lessons learned from stabilizing N1 CA09 to generate closed N8 NA tetramers. Analysis of existing N8 NA crystal structures showed hydrophobic packing in space A to be similar to that of N4 NAs, featuring P99 and T196. However, space D contained the large, polar Q165 and a notable difference from other subtypes with a glutamate at position 162 instead of a proline (**Figure 3.4C**). This combination of a well-packed space A and a more "open-like" space D appeared to explain its heterogeneous conformational phenotype. Although Q165S alone (N8-JD13-sNAp-282) was insufficient, the combination of E162P and Q165S (N8-JD13-sNAp-285) provided complete stabilization of the closed state of N8 as assessed by NS-EM, further emphasizing the cooperative effects of spaces A and D on stabilization (**Figure 3.4D**). While N8-JD13-sNAp-285 showed only small improvements in its primary T_m in the presence of either Ca^{2+} or EDTA relative to N8-JD13-WT, the stabilizing mutations minimized an earlier partial unfolding transition at 45–55°C, consistent with its more homogeneous adoption of the closed state (**Figure S3.4A**). A similar effect on T_{agg} was observed (**Figure S3.4B**). Finally, N8-JD13-sNAp-285 was still catalytically active, although slightly less so than N8-JD-WT (**Figure S3.4C**).

Mutation of Stabilizing Residues in N2 NA Prevents Closed Tetramer Formation

Given the clear stabilizing effects of key positions in spaces A and D, we hypothesized that mutating them to amino acids observed in more open subtypes would destabilize the closed N2-WI05-WT tetramer. Mutations were made separately in each space to make space A more strongly resemble N1 NAs and space D resemble N1 or N8 NAs, while avoiding steric clashes (**Figure S3.4D**). The V165E mutation in space D alone was sufficient to induce massive structural changes including dissociation of the heads, but also led to the formation of soluble aggregates. V165Q resulted in a more subtle effect, causing about half of the tetrameric particles to adopt the open state while the rest remained closed. In space A, an I176V/T195S double mutant remained closed, but the addition of P99I led to formation of unassembled monomers and aggregates. We next combined V165Q with I176V and T195S and found that the protein formed either open tetramers or lower-order oligomers (**Figure S3.4D**). Thermal denaturation of this triple mutant destabilized NA protein (desNAp), N2-WI05-desNAp-255, showed a decreased T_m, a strongly redshifted baseline in its intrinsic fluorescence emission spectrum, and no apparent stabilization by Ca^{2+} (**Figure S3.4E**). Enzymatic activity was also abolished in N2-WI05-desNAp-255 (**Figure S3.4F**). Together, these data indicate that the same design rules that enabled stabilization of the closed tetrameric state of N1 CA09 and N8 JD13 could be applied in reverse to destabilize the closed state of N2 WI05. Although the loss of enzymatic activity in N2-WI05-desNAp-255 makes it tempting to speculate that the closed tetrameric state may be more important for the function of N2 WI05 than for N1 CA09 and N8 JD13, we hesitate to do so as it is difficult to disentangle the role of the tetrameric conformation from the potential deleterious effects of mutations within each protomer.

Design of Additional Closed Recombinant N1 NA Tetramers

To assess their portability, the closed state-stabilizing mutations from N1-CA09-sNAp-155 were introduced into the NA of N1 MI15, from the same post-2009 human lineage as CA09. We found that the sNAp-155 mutations were insufficient for complete closure, as N1-MI15-sNAp-155 adopted a mixture of the open and closed states (**Figures 3.5A**).

Intrigued by the possible requirement of an ordered space D for closure, we focused on redesigning the aqueous cavity surrounding D103 to stabilize N1 MI15. This cavity is adjacent to, but not immediately at, the inter-protomer interface. After generating a homology model of N1-MI15 using PDB ID 4B7Q as a template, we applied our Rosetta-based homology-directed design strategy to this space. The protocol again sampled mutations observed in structures of NAs from other subtypes, novel mutations, and combinations of the two, and in this case also evaluated intra- and inter-protomeric disulfide bonds. Among 20 designs building on N1-MI15-sNAp-155, four were found to heavily favor the closed state, with three showing only closed particles in electron micrographs (**Figures 3.5A** and **S3.5A**). These designs utilized N2-inspired proline mutations (N1-MI15-sNAp-165 and -176), an N2-inspired T131Q mutation that provides both improved packing and hydrogen bonding in the cavity (N1-MI15-sNAp-174 and -176), and homology-directed hydrophobic filling of the cavity (N1-MI15-sNAp-183). Mirroring the results obtained with other sNAps, the stability of N1-MI15-sNAp-174 (which required only a single mutation for closure beyond the sNAp-155 mutations) was relatively insensitive to Ca^{2+}; the T_m of the sNAp was 14.7°C higher than N1-MI15-WT in the presence of EDTA (**Figure 3.5B**); and its T_{agg} was also higher in both EDTA and Ca^{2+} (**Figure 3.5C**). N1-MI15-sNAp-174 remained catalytically active, although at reduced levels compared to its open WT counterpart (**Figure S3.5B**). The success of these designs established multiple sets of mutations that stabilize closed N1 NA tetramers—including several that do not make direct contact across the interface—and highlight the cavity in space D as a key determinant of closed tetramer stability.

We obtained a structure of the N1-MI15-sNAp-174 tetramer at 3.2 Å resolution using cryo-EM (**Figures 3.5D** and **S3.6**). The structure, which strongly resembled the overall structure of N1-CA09-sNAp-155 (backbone RMSD of 0.77 and 0.80 Å over one and all four subunits of the tetramer, respectively), confirmed that N1-MI15-sNAp-174 adopts the closed tetrameric state in solution. The backbone rearrangement in space A involving W455 and W457 observed in the N1-CA09-sNAp-155 structure was also found in N1-MI15-sNAp-174, although W457 was not resolved. The new T131Q mutation helps fill the space D cavity as intended while forming a hydrogen bond to the side chain of S442 (**Figure 3.5E**). We conclude that even seemingly subtle sidechain changes adjacent to the inter-protomeric interface can substantially impact the stability of the closed tetramer.

We next applied the sNAp-155 mutations to more distantly related N1 NAs from the avian H5N1 strain A/Vietnam/1203/2004 (VN04) and an earlier, pre-pandemic lineage of human H1N1, A/WSN/1933 (WSN33). The resultant N1-VN04-sNAp-155 and N1-WSN33-sNAp-155 formed predominantly open tetramers (**Figures S3.5C,D**). We reasoned that making the sequences of these sNAps more like N1-CA09-sNAp-155 and N1-MI15-sNAp-174 overall should stabilize them in the closed tetrameric state. We therefore combined mutations identified during stabilization of N1 CA09 and N1 MI15 with conversion of divergent amino acids at other positions to the WT residues observed in N1 CA09 and N1 MI15, an approach similar to the Repair-and-Stabilize strategy recently developed for stabilization of HIV-1 Env trimers (Rutten et al., 2018). Only buried positions were mutated to reduce the chances of unintended effects on antigenicity. N1-VN04-sNAp-354 combined the T131Q substitution in space D that stabilized N1-MI15-sNAps with mutation of three nearby residues to the identities in N1-CA09-WT: I106V, V163I, and A166V. This sNAp formed exclusively closed tetramers as determined by NS-EM,

suggesting that this strategy could be broadly applied to stabilize the closed tetrameric state of NA (**Figure S3.5C**).

We then undertook stabilization of the more divergent N1-WSN33-sNAp-155 using sequence information only as a rigorous test of our approach. The sequence of N1 WSN33 NA differs from N1 CA09 and N1 MI15 at many positions in both the space D cavity and the rest of the tetrameric interface. In addition to the sNAp-155 mutation set, substitution of six residues across spaces A, B, and D (G105S, I106V, A157T, V163I, A166V, and R210G; N1-WSN33-sNAp-366) substantially improved the frequency of closed tetramers observed by NS-EM, demonstrating that there are inherent differences in interface stability between N1 WSN33 and N1 CA09/N1 MI15 that can be altered by focusing purely on the interface and the space D cavity (**Figure S3.5D**). The addition of T131Q to this set of mutations resulted in a sNAp (N1-WSN33-sNAp-367) that further reduced levels of open tetramers to predominantly favor the closed state. In contrast, the addition of the space D hydrophobic repacking mutations used in N1-MI15-sNAp-183 (N1-WSN-sNAp-375) appeared to be slightly deleterious towards closure, with only about half of the particles observed by NS-EM adopting the closed state. To determine if sequence differences distant from the interface contribute to closed tetramer formation, eight buried residues distributed throughout the globular head of N1-WSN-sNAp-375 were changed to the amino acids in N1-CA09-WT, resulting in the predominantly closed N1-WSN-sNAp-378 (**Figure S3.5D**). These data suggest that while spaces A and D are key for closure, packing interactions distant from the interface can allosterically influence the effectiveness of interface-stabilizing mutations. Transfer of general packing residues from one strain to another thus offers an additional strategy for altering closure while maintaining native surface antigenicity. Together, the strategies we provide should be widely applicable across many N1 NAs as well as NAs from other subtypes.

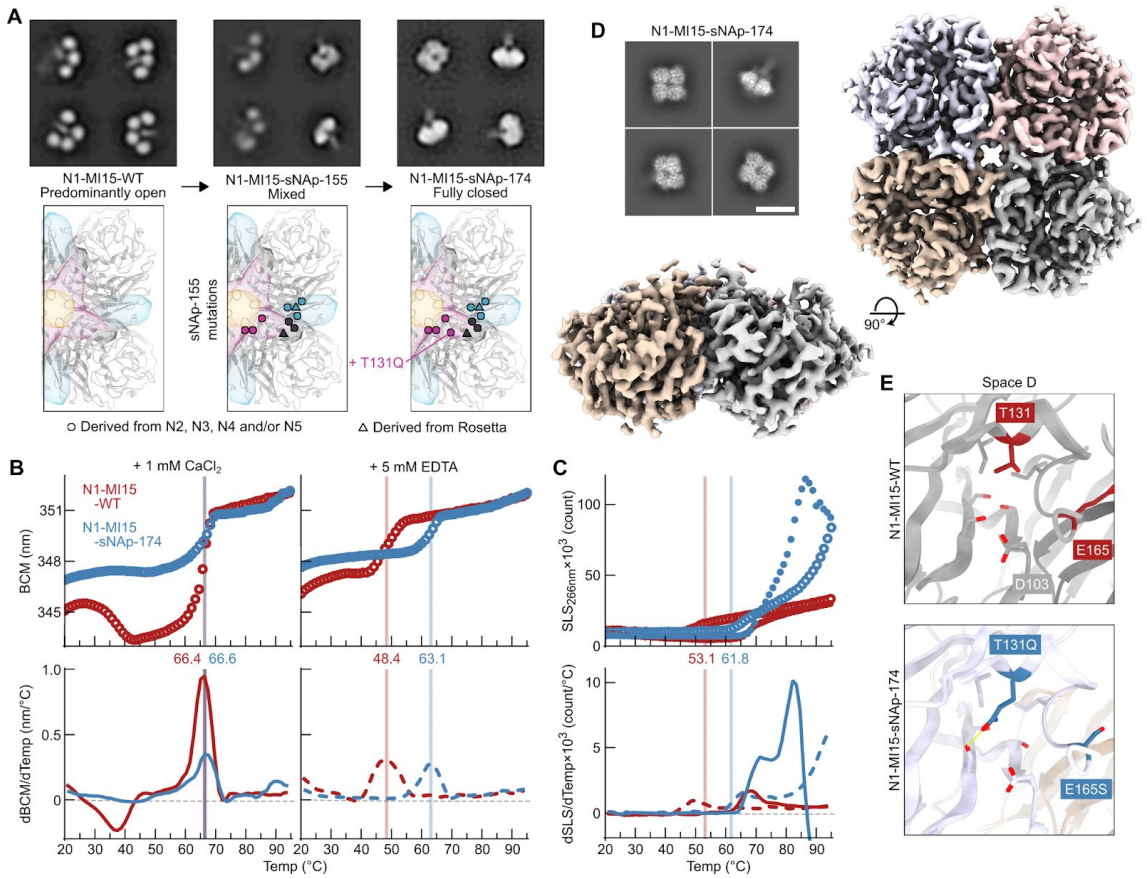

Figure 3.5. Design and Structural Characterization of N1-MI15-sNAp-174

(A) Application of sNAp-155 mutations to N1 MI15 and addition of the space D stabilizing mutation T131Q resulted in fully closed N1-MI15-sNAp-174 tetramers.

(B) Thermal denaturation of N1-MI15-WT and N1-MI15-sNAp-c174 in the presence of 1 mM $CaCl_2$ (closed circles and solid lines) or 5 mM EDTA (open circles and dashed lines), monitored by intrinsic tryptophan fluorescence. Top panels show raw data, while lower panels show smoothed first derivatives used to calculate melting temperatures. The barycentric mean (BCM) of the fluorescence emission spectra is plotted.

(C) SLS during thermal denaturation of N1-MI15-WT and N1-MI15-sNAp-c174 in the presence of 1 mM $CaCl_2$ or 5 mM EDTA, with aggregation temperatures shown for $CaCl_2$-treated samples. Data are plotted as in panel B.

(D) Representative 2D class averages (scale bar, 10 nm) (top left) and final 3D density (bottom left and right) from cryo-EM of N1-MI15-sNAp-174.

(E) Space D cavity in N1-MI15-WT (top; from PDB ID 4B7Q) and N1-MI15-sNAp-174 (bottom; cryo-EM reconstruction). All residues shown as sticks in the WT model are conserved between N1-CA09-WT and N1-MI15-WT.

Effects of N1 NA Tetramer Closure on its Antigenic Profile

To determine whether stabilizing NA tetramers in the closed conformation alters the antigenicity of recombinant NA, we assessed the binding kinetics of mAbs that recognize different antigenic sites on N1 NAs (**Figure 3.6A**). The murine mAb CD6, isolated from a mouse infected with a sublethal dose of A/California/07/2009 (H1N1) virus, recognizes a quaternary epitope that spans two neighboring NA protomers (Wan et al., 2015). CD6 is highly protective and potently inhibits

viral replication *in vitro*. The second mAb, 1G01, isolated from a human immediately after H3N2 virus infection, is the broadest anti-NA antibody described to date, providing protection against many influenza A and B viruses through targeting the highly conserved catalytic site (Stadlbauer et al., 2019). We measured antibody binding affinities to the open N1-CA09-WT and closed N1-CA09-sNAp-130 by biolayer interferometry. While both proteins were recognized by 1G01 IgG with similar affinity in the presence of $CaCl_2$, the antibody bound to N1-CA09-WT with much lower affinity than to N1-CA09-sNAp-130 in the presence of EDTA (**Figure 3.6B**). Strikingly, the quaternary epitope-specific CD6 IgG showed only minimal binding to N1-CA09-WT regardless of the presence of Ca^{2+} ions, indicating that the CD6 epitope was not properly formed in the open N1-CA09-WT. In contrast, the same antibody readily and avidly bound to N1-CA09-sNAp-130 in the presence or absence of Ca^{2+} (**Figure 3.6B**). This observation, which is consistent with our thermal stability data, again suggests that Ca^{2+} can assist stabilization of the closed tetrameric state, although it is not sufficient for closure on its own. These data further illuminate the difference in tetrameric conformation between open NAs and sNAps in solution, and demonstrate that tetramer closure better preserves antigenic sites—including a quaternary epitope—targeted by highly protective, infection-elicited antibodies.

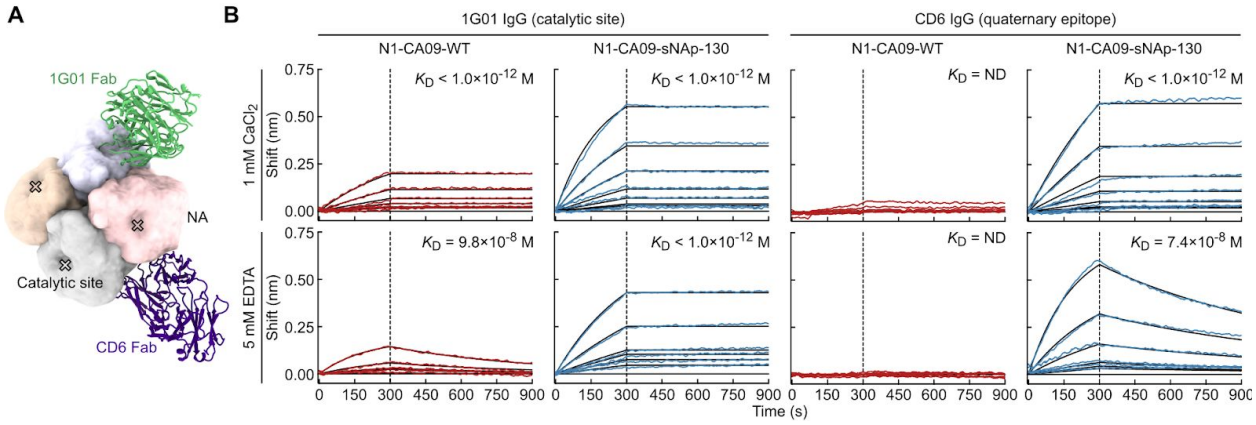

Figure 6. Antigenic Effects of N1 NA Tetramer Closure

(A) Models of Fabs of murine CD6 (purple) and human 1G01 (green) bound to CA09 NA. CD6 binds a quaternary epitope that spans two protomers, while 1G01 binds within and around the catalytic pocket. Models were generated by aligning structural models of Fabs of CD6 (PDB ID 4QNP) and 1G01 (PDB ID 6Q23) to a single tetramer of CA09 NA (PDB ID 4B7Q).

(B) Binding kinetics of anti-NA mAbs to N1-CA09-WT and N1-CA09-sNAp-130. Biolayer interferometry sensorgrams of 1G01 IgG (left) and CD6 IgG (right) binding to N1-CA09-WT (red) and N1-CA09-sNAp-130 (blue). Upper and lower sensorgrams were measured in buffers containing 1 mM $CaCl_2$ and 5 mM EDTA, respectively. Experimental data (colored traces) were fitted (black lines) with the binding equations describing a 2:1 interaction.

Discussion

We have shown that recombinant NA tetramers from several different influenza strains and subtypes adopt a previously unreported open tetrameric conformation, while others form the crystallographically observed closed tetramer. These data may help explain reports of differing stabilities among NAs from various subtypes (Sultana et al., 2014) and are consistent with observations that NA protomers have a tendency to dissociate (Saito et al., 1994; Zhu et

al., 2019). Furthermore, structural characterization of H and HN glycoproteins as well as G proteins from several paramyxoviruses, which share the beta propeller fold and stalk-dependent tetramerization of influenza NA, have revealed that their head domains form weak and dynamic tetramers, often arranged as dimers of dimers (Aguilar et al., 2016; Yuan et al., 2005). However, as mentioned earlier, several lines of evidence suggest that NA forms closed tetramers on the surface of influenza virions. Such differences between native transmembrane and recombinant soluble forms of glycoproteins are not uncommon. For example, many recombinant class I fusion proteins require stabilizing mutations to maintain their native prefusion conformations (Graham et al. 2019). Nevertheless, more data will be required to define the tetrameric conformation of NA on the surface of diverse influenza virus strains and subtypes.

To stabilize recombinant NAs in the closed tetrameric state, we used a homology-directed design strategy similar to the recently reported Repair-and-Stabilize approach applied to HIV envelope trimers (Rutten et al., 2018). Our method combines computational protein design with knowledge of the sequences and structural phenotypes of homologous NAs. We identified several structural features that work together, sometimes non-intuitively, to stabilize the closed NA tetramer: direct interactions between subunits at the tetrameric interface, pre-organization of the tetrameric interface within each subunit by second-shell interactions, and general stabilization of the structure of each subunit by packing interactions distant from the interface. Two regions of the NA head, which we refer to as spaces A and D, appear to have a particularly strong influence on NA stability and conformation. Whereas mutations in space A and the space D cavity stabilize the closed tetrameric state by improving atomic packing in these interface or interface-proximal regions, the stabilizing mechanism of other mutations is less clear. For example, there is no obvious structural rationale for the stabilizing effect of the E/Q165S mutation, yet this position—which stood out when multiple sequence alignments of several NA subtypes were compared—is a critical determinant of the stability of the closed tetrameric state. Although such mutations would not be identified by typical design approaches based on structure alone, they are clearly prioritized by the homology-directed design strategy used here. A stabilizing mutation in an N9 NA that also would likely have been passed over in purely structure-based analyses was recently identified using a similar homology-directed approach (Zhu et al., 2019). The success of homology-based mutations reflects the sensitivity and complexity of the determinants of NA stability and highlights the valuable yet cryptic design space accessible to homology-directed design. In this way, our work provides both an important step as well as a roadmap towards the design of stabilizing mutations that could be more universally applied to NAs from diverse influenza strains and subtypes.

Multiple naturally occuring stabilizing and destabilizing mutations in space D have been described previously (McKimm-Breschkin et al., 2019; Wang et al., 2019). Our identification of several homology-inspired and novel second-shell stabilizing mutations clearly indicates that the large, polar cavity surrounding D103 is suboptimal from the perspective of structural stability. Nevertheless, the backbone positions of the residues surrounding this cavity are strongly conserved in all non-bat influenza subtypes, and D103 itself—which caps the N terminus of the 110-helix—is nearly completely conserved across all known non-bat influenza A sequences. While many side chain substitutions are found in this space in influenza B NAs, including at position 103, the local backbone conformation is still mostly conserved. We speculate that this

conserved, structurally suboptimal feature plays a role in the biological function of the enzyme. In contrast, neuraminidase-like proteins from the N10 and N11 subtypes found in bats show vastly different backbone conformations in this region, do not have an aspartate at position 103, and characteristically reorder the nearby 110-helix into less compact loops (Li et al., 2012; Tong et al., 2013). Given that these NA-like proteins have not been shown to have NA activity and are predicted to have different functions, this observation further suggests a functional role for this region in non-bat influenza viruses.

Our results have several significant implications for previous and future studies of influenza NA. Importantly, we found that several commonly used assays—SEC, enzymatic activity, and thermal stability—were generally unable to distinguish between the open and closed forms of the enzyme due to inherent differences between NA from different strains, although decreased sensitivity of thermal stability to Ca^{2+} was loosely correlated with closure. Structural characterization by EM was required to establish whether each NA adopted the open or closed tetrameric state, or a mixture of the two. Intriguingly, protective mAbs that bind a quaternary epitope or the catalytic site also distinguished the open and closed forms. mAb binding was also sensitive to the presence of Ca^{2+}, emphasizing the importance of considering exposure to Ca^{2+} in NA antibody discovery and antigenic analyses. We propose that with the identification of additional NA-specific mAbs with the desired properties, antigenic characterization could become a rapid, widely accessible, and powerful tool for assessing NA tetrameric conformation. Beyond enabling simplified screening of sNAp designs across additional strains and subtypes, such antigenic characterization could provide a simple and accurate method for assessing NA conformation during vaccine development. In the meantime, knowledge of the conformational state of recombinant NA tetramers will be crucial for appropriately interpreting the outcomes of experiments using them, and we propose the use of at least NS-EM with 2D class averaging until appropriate and adequately characterized mAbs are available for this purpose.

Our data suggest that the recombinant NA proteins used in many previous studies, while presumed to be in the crystallographically observed tetrameric state based on biochemical assays, may have been in fact in the open conformation. This disconnect could lead to erroneous interpretations of experimental outcomes. For example, previous immunological analyses of sera from infected humans or mice immunized with whole virions showed that N2-directed responses appeared to be stronger than those against N1, and that N2-specific human mAbs had higher affinities than N1-specific mAbs (Chen et al., 2018; Rajendran et al., 2017). However, such measurements could have been influenced by the use of recombinant N1 and N2 NAs in the open and closed conformations, respectively, in ELISA assays. If so, our understanding of NA immunogenicity may be incomplete or compromised, particularly for NAs that form metastable tetramers in recombinant form.

The sNAps and design methods we describe here should enable new approaches to structure-based design of NA antigens to include in future influenza vaccines. As interest in NA-based antibodies and vaccines rekindles, the utility of stable and well-defined recombinant antigens will be vital for progress, as highlighted by the transformational effects of the development of prefusion-stabilized class I viral fusion proteins (Graham et al., 2019; Hsieh et al., 2020; Sanders and Moore, 2017). First, sNAp-based probes may improve serological assays for NA-specific antibodies elicited by infection or immunization, as well as the isolation of

NA-specific B cells and mAbs. Their enhanced stability and monodispersity will expedite rapid structure determination of antibody/NA complexes, which will provide valuable information on mechanisms of antibody-mediated protection. More directly, sNAps may themselves be superior NA-based immunogens. We note that recombinant native N1 NA heads fused to hVASP tetramerization domains, which we predict to adopt the open conformation, have previously been shown to elicit protective immunity against viral challenge in mice, suggesting that the metastable open state can nonetheless be useful as an immunogen (McMahon et al., 2020; Wohlbold et al., 2015). The increased affinity of an N1 sNAp towards the quaternary epitope-specific mAb CD6 and the broadly protective mAb 1G01 suggest that sNAp-based immunogens may be more likely to elicit protective antibody responses targeting these sites of vulnerability and other quaternary epitopes, at least for recombinant NAs that do not naturally form closed tetramers. Finally, the increased physical stability of sNAps may help overcome product stability issues that have historically plagued recombinant NAs, enabling the design and evaluation of next-generation NA-based influenza vaccines.

Contributors and acknowledgements

I would like to thank Julia Lederhofer, Neil P. King and Masaru Kanekiyo for their leadership and strong contributions to this project. I would also like to thank Oliver J. Acton, Yaroslav Tsybovsky, Sally Kephart, Christina Yap, Rebecca A. Gillespie, Adrian Creanga, Tyler Stephens, Deleah Pettie, Michael Murphy, Andrew J. Borst, Young-Jun Park, Kelly K. Lee, Barney S. Graham and David Veesler for contributions. As well, I would like to thank Jeffrey Boyington and Guillaume Stewart-Jones for design insights; John Mascola for advisory support; and Harry Kleanthous, members of the King laboratory, and members of the Influenza Program at the Vaccine Research Center for comments on the manuscript. This study was supported by the intramural research program of the Vaccine Research Center, National Institute of Allergy and Infectious Diseases, National Institutes of Health (M.K. and B.S.G.); a generous gift from the Open Philanthropy Project (N.P.K.); a generous gift from the Audacious Project (N.P.K.); the National Institute of General Medical Sciences (R01GM120553, D.V.); the National Institute of Allergy and Infectious Diseases (DP1AI158186 and HHSN272201700059C to DV); a Pew Biomedical Scholars Award (D.V.); an Investigators in the Pathogenesis of Infectious Disease Award from the Burroughs Wellcome Fund (D.V.); and the University of Washington Arnold and Mabel Beckman cryo-EM center. This study has been funded in part with Federal funds from the Frederick National Laboratory for Cancer Research, National Institutes of Health, under Contract No. HHSN261200800001E (Y.T., T.S.). Molecular graphics and analyses performed with UCSF ChimeraX, developed by the Resource for Biocomputing, Visualization, and Informatics at the University of California, San Francisco, with support from National Institutes of Health R01-GM129325 and the Office of Cyber Infrastructure and Computational Biology, National Institute of Allergy and Infectious Diseases.

Supplemental figures

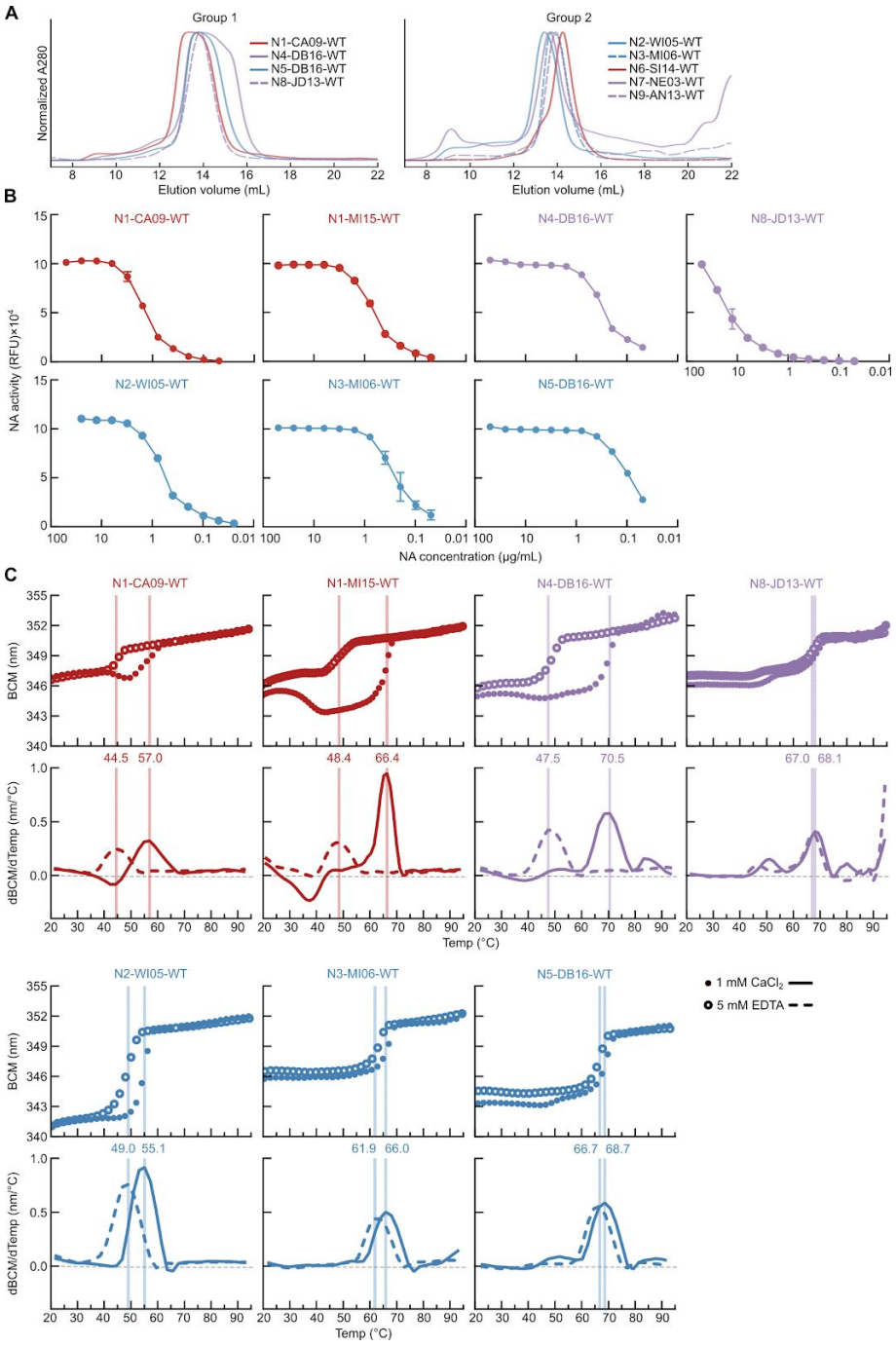

Figure S3.1. Preparative SEC, enzymatic activity, and nanoDSF of recombinant WT NA tetramers, Related to Figure 3.1

(A) Preparative SEC of recombinant NAs from all nine non-bat influenza A subtypes on a Superdex 200 Increase 10/300 GL column.

(B) Enzymatic activity of purified recombinant NAs. RFU, relative fluorescence units. Error bars denote the standard deviation for each dilution, performed in duplicate.

(C) Thermal denaturation of WT NA tetramers in the presence of 1 mM $CaCl_2$ (closed circles and solid lines) or 5 mM EDTA (open circles and dashed lines), monitored by intrinsic tryptophan fluorescence. The barycentric mean (BCM) of the fluorescence emission spectra is plotted. Top panels show raw data, while lower panels show smoothed first derivatives used to calculate melting temperatures, which are indicated by vertical lines.

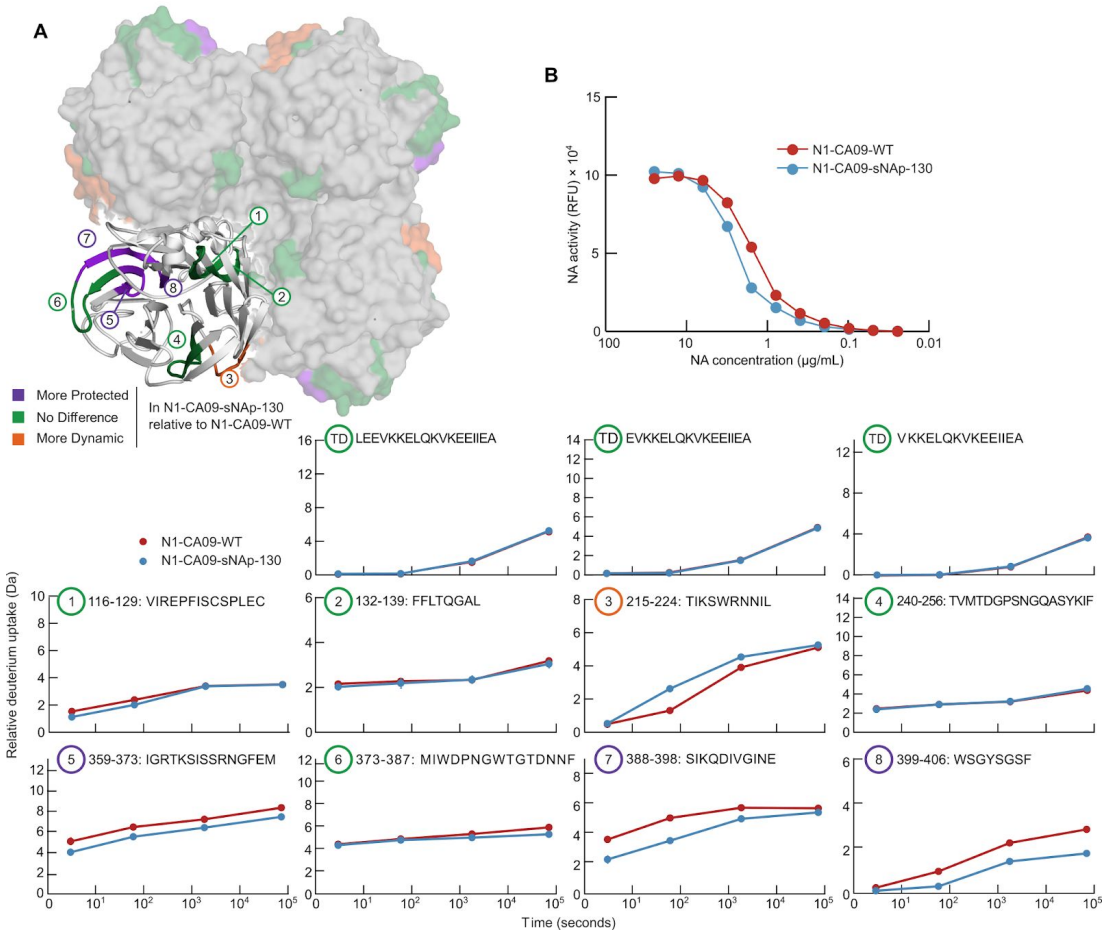

Figure S3.2. Hydrogen-Deuterium Exchange and Catalytic Activity of Unmodified and Stabilized N1 CA09 NA tetramers, Related to Figure 3.2

(A) (Top left) Peptide segments, numbered 1 to 8, mapped onto the structure of N1 NA (PDB ID 4B7Q). Colors indicate whether the peptide is more protected (purple) or more dynamic (orange) in N1-CA09-sNAp-130 compared to N1-CA09-WT. Green indicates peptides where there is no difference in deuterium exchange between variants. (Bottom) Kinetics of hydrogen-deuterium exchange for numbered peptides and peptides from the tetramerization domain (TD) at multiple timepoints up to 20 h. Each point is an average of duplicate measurements (N1-CA09-WT) and triplicate measurements (N1-CA09-sNAp-130), except for a limited number of replicates that were discarded due to low signal to noise. Standard deviations for all measurements were smaller than the points plotted.

(B) Enzymatic activity of N1-CA09-WT and N1-CA09-sNAp-130. RFU, relative fluorescence units. Performed in duplicate, with error bars smaller than the plotted points and not shown.

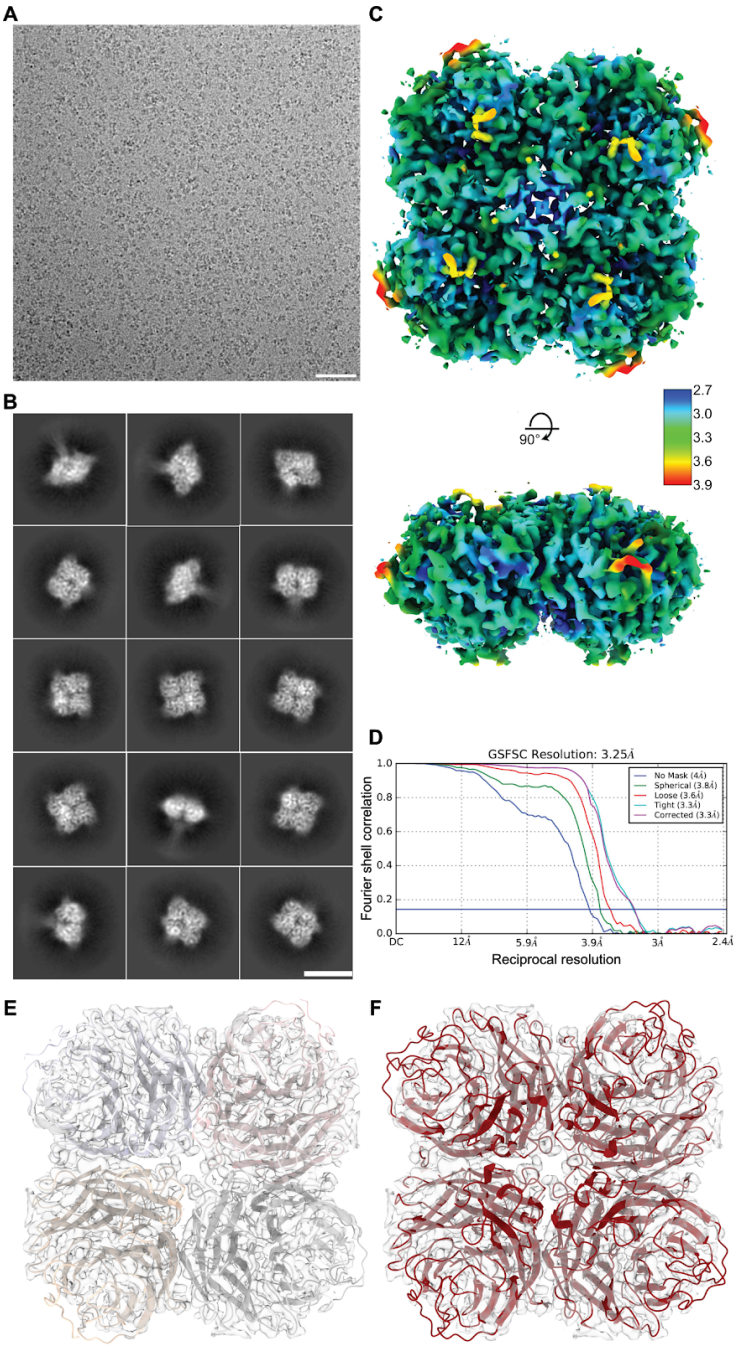

Figure S3.3. Cryo-EM analysis of N1-CA09-sNAp-c155, Related to Figure 3.3

(A) Representative micrograph of N1-CA09-sNAp-c155. Scale bar, 50 nm.

(B) 2D class averages of N1-CA09-sNAp-c155. Scale bar, 10 nm.

(C) Orthogonal views of the cryo-EM reconstruction of N1-CA09-sNAp-c155. Map is colored according to local resolution as indicated by color scale (in Å).

(D) Gold standard FSC for cryo-EM reconstruction.

(E) N1-CA09-sNAp-155 model coloured by chain shown in transparent density showing overall tetramer conformation of map.

(F) N1-CA09-WT (4B7Q, red) rigid-body docked into the N1-CA09-sNAp-c155 map, showing overall agreement with tetramers observed by X-ray crystallography.

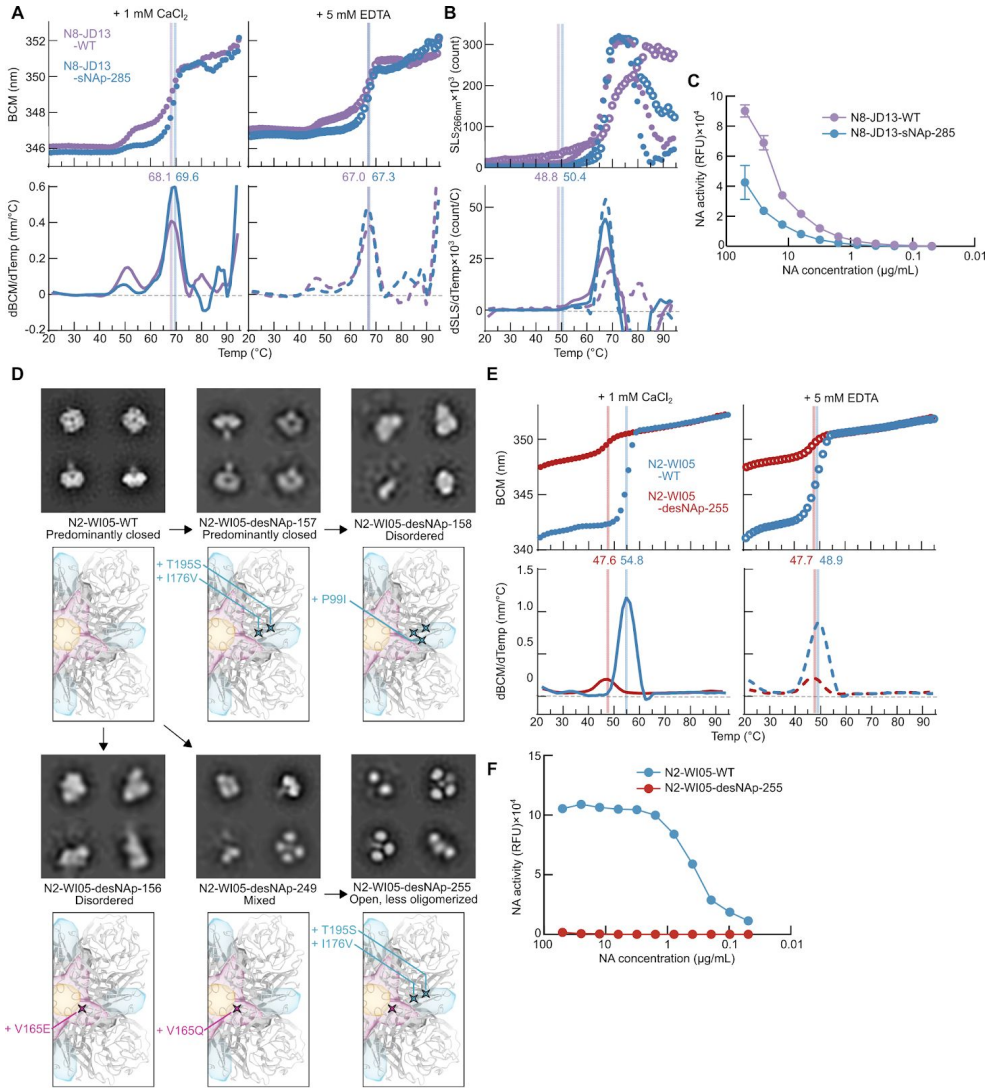

Figure S3.4. Structural, Biophysical, and Biochemical Characterization of a Stabilized N8 NA Tetramer and Destabilized N2 NA Tetramers, Related to Figure 3.4

(A) Thermal denaturation of N8-JD18-WT and N8-JD13-sNAp-285 in the presence of 1 mM $CaCl_2$ (closed circles and solid lines) or 5 mM EDTA (open circles and dashed lines), monitored by intrinsic tryptophan fluorescence. Data are presented as in Figure 2D.

(B) SLS during thermal denaturation of N8-JD18-WT and N8-JD13-sNAp-285 in the presence of 1 mM $CaCl_2$ or 5 mM EDTA. Data are presented as in Figure 2E.

(C) Enzymatic activity of N8-JD13-WT and N8-JD13-sNAp-285. RFU, relative fluorescence units. Error bars denote the standard deviation for each dilution, performed in duplicate.

(D) Mutation of predicted stabilizing residues in N2 NA to less stable counterparts observed in N1 or N8 and corresponding NS-EM 2D class averages. All numbers are listed in N2 numbering in which positions 99, 165, 176 and 195 are equivalent to positions 99, 165, 177 and 196 in N1 numbering, respectively.

(E) Thermal denaturation of N2-WI05-WT and N2-WI05-desNAp-255 in the presence of 1 mM $CaCl_2$ or 5 mM EDTA, monitored by intrinsic tryptophan fluorescence. Data are presented as in Figure 2D.

(F) Enzymatic activity of N2-WI05-WT and N2-WI05-desNAp-255. RFU, relative fluorescence units. Error bars are smaller than the plotted points and not shown.

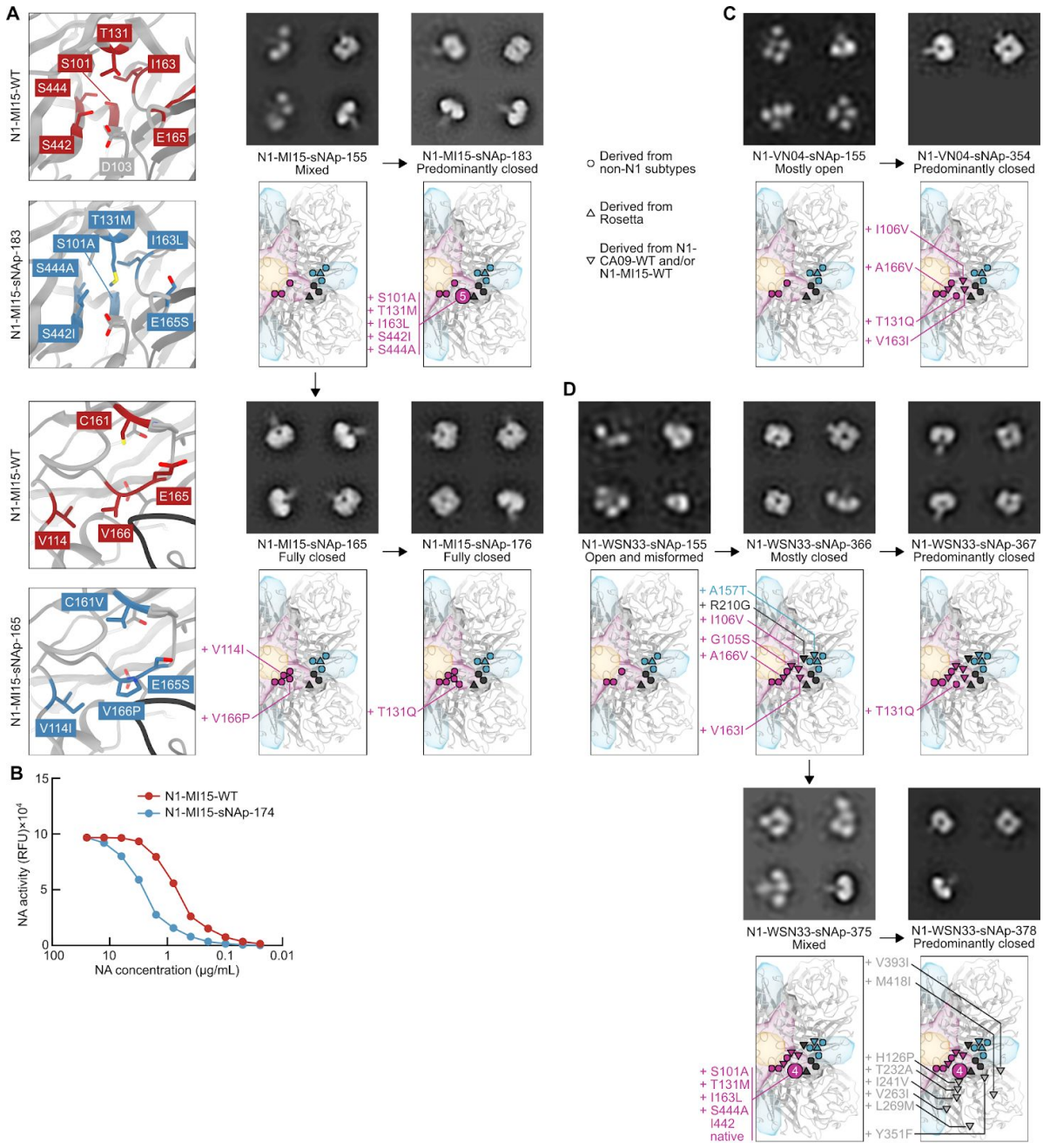

Figure S3.5. Design of Additional Closed Recombinant N1 NA Tetramers, Related to Figure 3.5

(A) Multiple mutations used to successfully design sNAps for N1 MI15. Structural models were derived from a Rosetta-generated homology model of N1 MI15 NA based on PDB ID 47BQ.

(B) Enzymatic activity of N1-MI15-WT compared to N1-MI15-sNAp-174, performed in duplicate. RFU, relative fluorescence units. Error bars are smaller than the plotted points and not shown.

(C) Design of a predominantly closed N1 VN04 sNAp using sNAp-155 mutations in addition to T131Q and three other mutations in space D that are derived from N1 CA09 and N1 MI15.

(D) Design of multiple N1 WSN33 sNAps using homology-directed mutations in combination with strain-specific mutations derived from N1 CA09 and N1 MI15. The mutations added to finalize N1-WSN33-sNAp-375 utilize the same mutation set featured in N1-MI15-sNAp-183. I442 was already native to N1 WSN33.

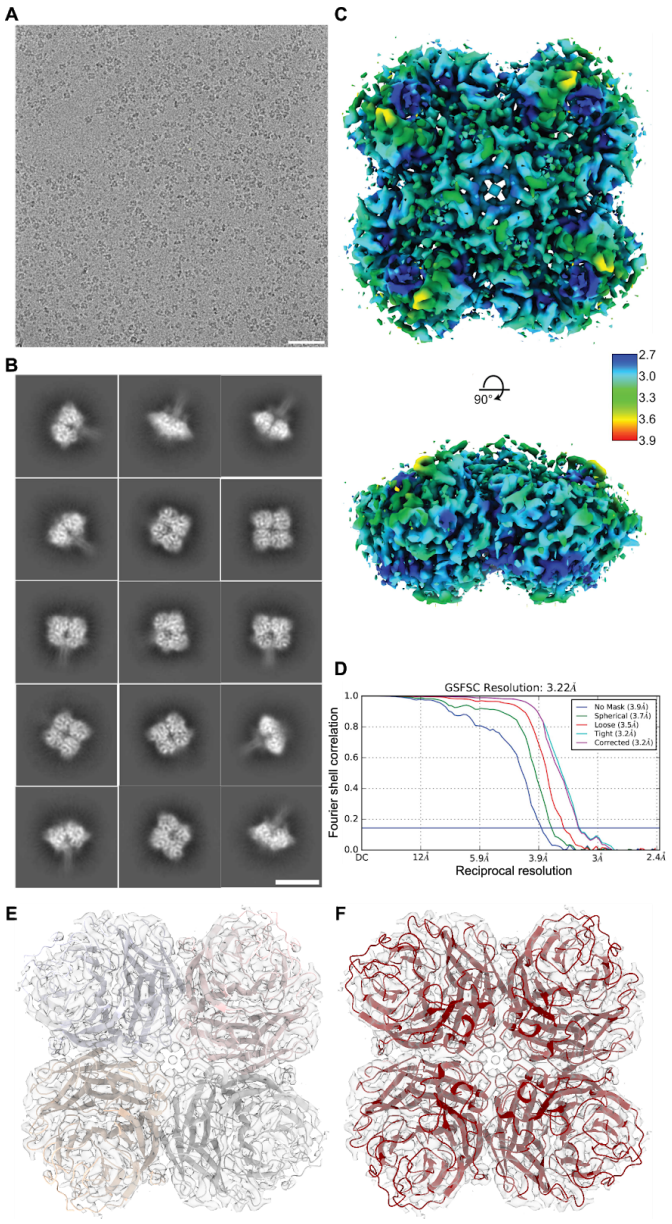

Figure S3.6. Cryo-EM analysis of N1-MI15-sNAp-c174, Related to Figure 3.5

(A) Representative micrograph of N1-MI15-sNAp-c174. Scale bar, 50 nm.

(B) 2D class averages of N1-MI15-sNAp-c174. Scale bar, 10 nm.

(C) Orthogonal views of the cryo-EM reconstruction of N1-CA09-sNAp-c155. Map is colored according to local resolution as indicated by color scale (in Å).

(D) Gold standard FSC for cryo-EM reconstruction.

(E) N1-CA09-sNAp-174 model coloured by chain shown in transparent density showing overall tetramer conformation of map

(F) N1-CA09-WT (4B7Q, red) rigid-body docked into the N1-MI15-sNAp-c174 map, showing overall agreement with tetramers observed by X-ray crystallography.

Materials and Methods

Protein expression and purification

NA constructs were expressed by transient transfection in Expi293F cells (ThermoFisher Scientific) at a density of 2.5×10^6 cells/ml using the ExpiFectamine™ 293 Transfection Kit (ThermoFisher Scientific). The supernatants were harvested 5 days post-transfection and centrifuged at 4000 rpm to remove cell debris. Proteins were purified from clarified supernatants by immobilized metal affinity chromatography (IMAC) using either Ni^{2+}- or Co^{2+}-containing resin. For Ni^{2+}-based IMAC, clarified supernatants were incubated for 2 h at room temperature with Ni^{2+} Sepharose High Performance histidine-tagged protein purification resin (Cytiva) and bound protein eluted using 50 mM Tris pH 8.0, 0.5 M NaCl, 300 mM imidazole. For Co^{2+}-based resin, clarified supernatants were flowed over Talon resin (Takara), and bound protein eluted in 20 mM Tris pH 8.0, 300 mM NaCl, 300 mM imidazole. Eluted proteins were further purified by SEC into phosphate-buffered saline (PBS) or 25 mM Tris pH 8.0, 150 mM NaCl, 5% glycerol using a Superdex 200 Increase 10/300 column (Cytiva).

Negative stain EM sample preparation and analysis

NS-EM and particle image averaging was used to assess whether the head domains of recombinant NA proteins adopted the open or closed tetrameric structure. Proteins were diluted to between 0.1–0.2 mg/mL using either 10 mM HEPES pH 7.0, 150 mM NaCl or 10 mM Tris pH 7.5, 150 mM NaCl. Samples were adsorbed to glow-discharged carbon-coated copper grids. The grids were either washed with a drop of the same buffer three times and stained with 0.75% uranyl formate, or blotted and stained directly with 0.75% uranyl formate. Images were recorded with sampling ranging between 1.9 Å/pixel and 2.2 Å/pixel, depending on the microscope. Data were collected on either an FEI Tecnai T20 electron microscope equipped with an FEI Eagle CCD camera and operated at 200 kV using SerialEM (Takaba et al., 2020), or on an FEI Tecnai 12 Spirit 120kV electron microscope equipped with a Gatan Ultrascan 4000 CCD camera. Particles were selected from the micrographs automatically using either in-house software (Yaroslav Tsybovsky, unpublished) or were picked in a reference-free manner in cisTEM (Grant et al., 2018). For the latter datasets, particles were extracted after correcting for the effect of the CTF for each micrograph with cisTEM (Grant et al., 2018). Depending on user, dataset, and microscope, particles were either extracted into 120×120-pixel boxes with a final pixel size of 2.2 Å/pixel or extracted with a box size of 176×176 pixels and binned to a final box size of 44×44 pixels (to a pixel size of 6.4 Å/pixel). Reference-free 2D classification was performed using either Relion 1.4 or Relion 3.1 (Scheres, 2015; Zivanov et al., 2018). Representative 2D class averages for all datasets were chosen based on the unambiguous identification of NA particle quality and conformational state, with qualitative descriptions based on overall class average appearance and/or semi-quantitative measurements of particles assigned to each class when distinct populations could be reliably measured. A designation of “fully closed” was assigned to samples where only closed particles were resolved into interpretable 2D class averages. “Predominantly closed” NA variants were assigned to samples with 2D class averages of the closed state comprising >80% of well-resolved NA tetramers, with open or poorly resolvable classes containing the remaining <20% of particles. “Mostly closed” was assigned to NA variants where roughly three quarters of particles were classified into the closed conformation. “Mostly open” was assigned when roughly one quarter of particles were observed

as closed. “Predominantly open” was assigned for samples with clearly >80% of resolvable particles being classified in an open conformation. “Mixed” was assigned to any sample in between “mostly closed” and “mostly open”.

Thermal denaturation and static light scattering

Non-equilibrium melting temperatures were determined using an UNcle (UNchained Labs) based on the barycentric mean of intrinsic tryptophan fluorescence emission spectra collected from 20–95°C using a thermal ramp of 1°C per minute in buffers of 25 mM Tris pH 8.0, 150 mM NaCl and 5% glycerol supplemented with either 1 mM $CaCl_2$ or 5 mM EDTA. Static light scattering (SLS) data was simultaneously collected. Melting temperatures were defined as the maximum point of the first derivative of the melting curve, with first derivatives calculated using GraphPad Prism software after smoothing with four neighboring points using 2nd order polynomial settings. Aggregation temperatures were defined as the first positive data point above baseline of the first derivative of SLS, with the first derivative similarly calculated using GraphPad Prism.

Enzymatic activity

Neuraminidase activity was measured with the NA-Fluor™ Influenza Neuraminidase Assay Kit (ThermoFisher Scientific) according to the manufacturer’s protocol. Briefly, two-fold serial dilutions of each NA protein were made in a black 96-well, flat bottom plate, starting from protein stocks at concentrations of 25–50 µg/mL. The wells in column 12 were left empty for background controls. NA-Fluor Substrate was prepared according to the manufacturer’s protocol and added to each well. Plates were incubated for 1 h at 37°C and reactions were stopped with NA-Fluor Stop Solution. Plates were read using an excitation wavelength range of 350–365 nm and an emission wavelength range of 440–460 nm. Background control wells were subtracted for each protein serial dilution. Protein concentrations were plotted versus relative fluorescence unit (RFU) values.

Structure-based design using Rosetta

All calculations in Rosetta were made using versions v2017.18-dev59451, v2019.21-dev60746, or v2019.45-dev61026. For design of N1 CA09 sNAps, residue positions were manually sorted into spaces A, B, C, and D based on perceived local interactions in the inter-protomeric interface of N1-CA09-WT (PDB ID 4B7Q). The sequence of PDB ID 4B7Q contains an additional Y351F mutation compared to the sequence used for N1-CA09-WT, which was maintained in all designs. Based on either amino acid appearing at this position in multiple closed and open constructs described in this manuscript, we do not expect that this mutation has an impact on closure. Representative structures of N2 (PDB ID 6BR5), N3 (PDB ID 4HZV), N4 (PDB ID 2HTV), and N5 (PDB ID 3TI8) NAs were analyzed and residue identities at each of the positions were recorded. The four-fold symmetry axis of N1-CA09-WT was aligned with [0,0,1] and a single protomer was saved in .pdb format. A design protocol was written using RosettaScripts (Fleishman et al., 2011) that takes the aligned protomer and a custom resfile as inputs, with the resfile dictating the side chain identities and conformations sampled during design. Briefly, the protocol applies two rounds of design based on the input resfile, with side chain and backbone energy minimization applied after each design step. Both design and

minimization steps were allowed to repack or minimize residues within 5 Å of all mutable or packable residues listed in the resfile. Multiple resfiles were set up for each space. One set of resfiles was designed to place specific substitutions from N2 (PDB ID 4H52), N3, N4, or N5 NA structures into N1-CA09-WT using the 'PIKAA' option. Other sets used the 'PIKAA' option to allow Rosetta's packer to choose between residue identities from the N1, N2, N3, N4, or N5 NAs. A final set used the 'PIKAA' option to add further residue identities that were not observed in the N1, N2, N3, N4, or N5 structures to identify novel mutations. Design models and scores were manually inspected to identify interactions across the interface that appeared structurally feasible. Favorable interactions were iteratively retested in resfiles and manually refined to finalize a diverse set of designs for each space. Twenty-six designs targeted individual spaces, while six designs consisted of combinations of designs to all four spaces that were manually picked and combined.

A slightly modified protocol was used to design N1 MI15 sNAps that contained additional mutations in space D. Due to the lack of a crystal structure for N1 MI15, N1 CA09 (PDB-ID 4B7Q) was used as a template for a homology model. All design trajectories were performed while adding sNAp-155 mutations (I99P, Y100L, C161V, E165S, S172A, V177I, S196T, V205I, Q408M, R419V) in addition to mutational differences between N1 CA09 and N1 MI15 (N200S, V241I, N248D, V264I, N270K, I314M, I321V, N369K, N386K, K432E). Beyond those mutations, the design process focused entirely on residues within space D with resfile inputs drawn from either crystal structures of other non-bat NA subtypes or other identities not naturally observed in all subtypes. Disulfide mutations were designed outside of Rosetta based on distances between pairs of residues.

Hydrogen-deuterium exchange mass spectrometry

For each time point, 40 pmol of N1-CA09-WT and N1-CA09-sNAp-130 were incubated in deuterated buffer (85% D2O, pH* 7.4) for 3, 60, 1,800, or 72,000 s at room temperature and subsequently mixed with an equal volume of ice-cold quench buffer (4 M urea, 200 mM tris(2-chlorethyl) phosphate (TCEP), 0.2% formic acid) to a final pH* of 2.5. Samples were immediately frozen in liquid nitrogen and stored at 80°C until analysis. Fully deuterated samples were prepared by digesting 40 pmol of undeuterated sample over a pepsin column, followed by concentration under vacuum, resuspension in deuterated buffer at 65°C for 1 hour, and then quenching/freezing. Zero time point samples were prepared as previously described (Verkerke et al. 2016). A 3 s exchange was performed at the beginning and end of the longest exchange reaction to monitor protein stability under the experiment conditions. Online pepsin digestion was performed and analyzed by LC-MS-IMS utilizing a Waters Synapt G2-Si Q-TOF mass spectrometer as previously described (Verkerke et al. 2016). Deuterium uptake analysis was performed using HX-Express v2 (Guttman et al. 2013; Weis et al. 2006). The relative deuterium exchange was corrected for in-exchange using the zero time point. Internal exchange standards (Pro-Pro-Pro-Ile [PPPI] and Pro-Pro-Pro-Phe [PPPF]) were included in each reaction to ensure that conditions were consistent throughout all of the labeling reactions.

Cryo-electron microscopy sample preparation, data collection, and image processing

sNAp proteins were diluted to 1–1.5 μM in buffer (10 mM Tris, pH 7.5, 150 mM NaCl) and 3 μL sample loaded onto a freshly glow-discharged 1.2/1.2 UltrAuFoil grid (300 mesh) prior to plunge

freezing using a vitrobot Mark IV (ThermoFisher Scientific) with a blot force of -1 and 3.5–4.5 s blot time at 100% humidity and 4°C.

Data were acquired on an FEI Glacios transmission electron microscope operated at 200 kV and equipped with a Gatan K2 Summit direct detector. Automated data collection was carried out using Leginon (Suloway et al., 2005) at a nominal magnification of 36,000× with a pixel size of 1.16 Å. The dose rate was adjusted to 8 counts/pixel/s, and each movie was acquired in counting mode fractionated in 50 frames of 200 ms. For the N1-CA09-sNAp-c155 and N1-MI15-sNAp-174 complexes, 1,034 and 1,099 micrographs were collected, respectively, with a defocus range between -0.5 and -2.5 µm. For the N1-CA09-WT complex, 605 micrographs were collected with a defocus range between -1.0 and -3.0 µm. Movie frame alignment, estimation of microscope CTF parameters, and automatic particle picking and extraction were carried out using Warp (Tegunov and Cramer, 2019). Particles were extracted unbinned into a box size of 204 pixels.

For the N1-CA09-WT dataset, three rounds of reference-free 2D classification were performed using cryoSPARC (Punjani et al., 2017). After each round, well-defined images corresponding to NA tetramers were selected and re-classified until 2D classification stabilized. For the N1-CA09-sNAp-c155 and N1-MI15-sNAp-c174 datasets, two rounds of reference-free 2D classification were performed in cryoSPARC, again selecting for well defined images. Particles selected post-2D classification were subjected to two rounds of 3D classification in Relion (Scheres, 2012) without imposing symmetry (angular sampling 7.5° for 25 iterations followed by 1.8° with local searches for a further 25 iterations). For each dataset, ab initio models were generated in cryoSPARC as reference maps for 3D classification (Punjani et al., 2017). Refinements of 3D maps were carried out using non-uniform refinement along with per-particle defocus refinement as implemented in cryoSPARC (Punjani et al., 2019). Particles were transferred back into Relion to perform Bayesian polishing (Zivanov et al., 2018, 2019) before an additional round of non-uniform refinement, per-particle defocus refinement, and finally one more round of non-uniform refinement imposing four-fold symmetry. Local resolution estimation, filtering, and sharpening were carried out in cryoSPARC (Cardone et al., 2013). All reported resolutions were determined using gold-standard Fourier shell correlation (FSC) calculations with a cutoff criterion of 0.143 (Rosenthal and Henderson, 2003) and FSC curves were corrected for the effects of soft masking by high-resolution noise substitution (Chen et al., 2013).

Cryo-EM model building and analysis

UCSF Chimera (Pettersen et al., 2004) and Coot (Emsley et al., 2010) were used to fit atomic models (PDB ID 4B7Q) into the cryoEM maps and point mutations were made manually in Coot. Models were refined and relaxed using Rosetta using both sharpened and unsharpened maps (Frenz et al., 2019; Wang et al., 2016) and validated using Molprobity (Chen et al., 2010), Phenix (Liebschner et al., 2019), and EMRinger (Barad et al., 2015). Figures were generated using UCSF ChimeraX (Goddard et al., 2018).

Collection of NA sequences and entropy calculations

Comprehensive sequence datasets for each NA subtype were downloaded from GISAID (www.gisaid.org). Each dataset included animal and human sequences longer than 1,350

nucleotides deposited before January 14, 2020. Sequences were aligned using Mafft v7 for large numbers of short sequences (Katoh et al., 2019). Sequences with more than 135 ambiguous bases or large gaps were eliminated. To calculate amino acid frequencies, we truncated NA sequences to retain only the globular head of NA ectodomain. Unique amino acid sequences of the NA head domain were selected using CD-HIT with the "Sequence identity cut-off" set at 1.0 (St Clair et al., 1991). Sequence logos were generated using WebLogo 3 (Crooks et al., 2004), http://weblogo.threeplusone.com/). From aligned sequences containing gaps, entropy calculations were measured using the dms_tools2 python library (https://jbloomlab.github.io/dms_tools2/). Representative positions for maximum and mean entropies were the individual positions with entropy values that were highest or closest to the mean calculated using all positions in a given sequence, respectively.

Biolayer interferometry

All biosensors were hydrated in PBS prior to use. Recombinant NA tetramers were immobilized on HIS2 biosensors (fortéBio) through their hexahistidine tags. After briefly dipping in assay buffer (25 mM Tris pH 8, 150 mM NaCl, 5% glycerol, 1% BSA) supplemented with either 1 mM $CaCl_2$ or 5 mM EDTA, the biosensors were dipped in a two-fold dilution series of IgG for 5 min. Biosensors were then dipped in the assay buffer (with either $CaCl_2$ or EDTA) to allow IgG to dissociate from NA for 10 min. All assay steps were performed at 30°C with agitation set at 1,000 rpm in the Octet HTX instrument (fortéBio). Correction to subtract non-specific baseline drift was carried out by subtracting the measurements recorded for a sensor loaded with the NA in the same buffer with no antibody. Data analysis and curve fitting were carried out using Octet analysis software (version 11). Experimental data were fitted with the binding equations describing a 2:1 (bivalent binding) interaction. Global analyses of the complete data sets assuming binding was reversible (full dissociation) were carried out using nonlinear least-squares fitting allowing a single set of binding parameters to be obtained simultaneously for all concentrations used in each experiment.

Poems

“Closure”	“Golden Joinery”	“Flu Journey”
Neuraminidase	Protein kintsugi	Hundreds of designs
Shifting clover form now clear	Essence of NA restored	In the search for NA truth
sNAp tetramers closed	Beauty through EM	Four protomers meet

Neuraminidase, neuraminidase,
Such a sweet taste,
We desired to express you as a recombinant protein,
But you decided to be open/closed/mixed in shape and not clean.
Why oh why are you not beautiful closed and decide to be mixed in shape?
You weren’t easy to stabilize, like other proteins.
You certainly got our passion and love to change your clover,
To create a beautiful closed tetramer, giving you a nano makeover.
Only changing your inside, filling cavities and other spaces.
One of many mysteries might be solved,
However, there is still so much more to discover, we need others involved.

References

Aguilar, H.C., Henderson, B.A., Zamora, J.L., and Johnston, G.P. (2016). Paramyxovirus Glycoproteins and the Membrane Fusion Process. Curr Clin Microbiol Rep *3*, 142–154.

Air, G.M. (2012). Influenza neuraminidase. Influenza Other Respi. Viruses *6*, 245–256.

Amaro, R.E., Cheng, X., Ivanov, I., Xu, D., and McCammon, J.A. (2009). Characterizing loop dynamics and ligand recognition in human- and avian-type influenza neuraminidases via generalized born molecular dynamics and end-point free energy calculations. J. Am. Chem. Soc. *131*, 4702–4709.

Amaro, R.E., Swift, R.V., Votapka, L., Li, W.W., Walker, R.C., and Bush, R.M. (2011). Mechanism of 150-cavity formation in influenza neuraminidase. Nat. Commun. *2*, 388.

Barad, B.A., Echols, N., Wang, R.Y.-R., Cheng, Y., DiMaio, F., Adams, P.D., and Fraser, J.S. (2015). EMRinger: side chain-directed model and map validation for 3D cryo-electron microscopy. Nat. Methods *12*, 943–946.

Boyken, S.E., Chen, Z., Groves, B., Langan, R.A., Oberdorfer, G., Ford, A., Gilmore, J.M., Xu, C., DiMaio, F., Pereira, J.H., et al. (2016). De novo design of protein homo-oligomers with modular hydrogen-bond network-mediated specificity. Science *352*, 680–687.

Broecker, F., Zheng, A., Suntronwong, N., Sun, W., Bailey, M.J., Krammer, F., and Palese, P. (2019). Extending the Stalk Enhances Immunogenicity of the Influenza Virus Neuraminidase. J. Virol. *93*, e00840–19.

Bucher, D.J., and Kilbourne, E.D. (1972). A 2 (N2) neuraminidase of the X-7 influenza virus recombinant: determination of molecular size and subunit composition of the active unit. J. Virol. *10*, 60–66.

Cardone, G., Heymann, J.B., and Steven, A.C. (2013). One number does not fit all: mapping local variations in resolution in cryo-EM reconstructions. J. Struct. Biol. *184*, 226–236.

Chen, T.-W., Wardill, T.J., Sun, Y., Pulver, S.R., Renninger, S.L., Baohan, A., Schreiter, E.R., Kerr, R.A.,

Orger, M.B., Jayaraman, V., et al. (2013). Ultrasensitive fluorescent proteins for imaging neuronal activity. Nature *499*, 295–300.

Chen, V.B., Arendall, W.B., 3rd, Headd, J.J., Keedy, D.A., Immormino, R.M., Kapral, G.J., Murray, L.W., Richardson, J.S., and Richardson, D.C. (2010). MolProbity: all-atom structure validation for macromolecular crystallography. Acta Crystallogr. D Biol. Crystallogr. *66*, 12–21.

Chen, Y.-Q., Wohlbold, T.J., Zheng, N.-Y., Huang, M., Huang, Y., Neu, K.E., Lee, J., Wan, H., Rojas, K.T., Kirkpatrick, E., et al. (2018). Influenza Infection in Humans Induces Broadly Cross-Reactive and Protective Neuraminidase-Reactive Antibodies. Cell *173*, 417–429.e10.

Colman, P.M. (1994). Influenza virus neuraminidase: structure, antibodies, and inhibitors. Protein Sci. *3*, 1687–1696.

Colman, P.M., Varghese, J.N., and Laver, W.G. (1983). Structure of the catalytic and antigenic sites in influenza virus neuraminidase. Nature *303*, 41–44.

Colman, P.M., Laver, W.G., Varghese, J.N., Baker, A.T., Tulloch, P.A., Air, G.M., and Webster, R.G. (1987). Three-dimensional structure of a complex of antibody with influenza virus neuraminidase. Nature *326*, 358–363.

Couch, R.B., Atmar, R.L., Franco, L.M., Quarles, J.M., Wells, J., Arden, N., Niño, D., and Belmont, J.W. (2013). Antibody correlates and predictors of immunity to naturally occurring influenza in humans and the importance of antibody to the neuraminidase. J. Infect. Dis. *207*, 974–981.

Crooks, G.E., Hon, G., Chandonia, J.-M., and Brenner, S.E. (2004). WebLogo: a sequence logo generator. Genome Res. *14*, 1188–1190.

Dai, M., Guo, H., Dortmans, J.C.F.M., Dekkers, J., Nordholm, J., Daniels, R., van Kuppeveld, F.J.M., de Vries, E., and de Haan, C.A.M. (2016). Identification of Residues That Affect Oligomerization and/or Enzymatic Activity of Influenza Virus H5N1 Neuraminidase Proteins. J. Virol. *90*, 9457–9470.

Duan, S., Govorkova, E.A., Bahl, J., Zaraket, H., Baranovich, T., Seiler, P., Prevost, K., Webster, R.G., and Webby, R.J. (2014). Epistatic interactions between neuraminidase mutations facilitated the emergence of the oseltamivir-resistant H1N1 influenza viruses. Nat. Commun. *5*, 5029.

Emsley, P., Lohkamp, B., Scott, W.G., and Cowtan, K. (2010). Features and development of Coot. Acta Crystallogr. D Biol. Crystallogr. *66*, 486–501.

Fleishman, S.J., Leaver-Fay, A., Corn, J.E., Strauch, E.-M., Khare, S.D., Koga, N., Ashworth, J., Murphy, P., Richter, F., Lemmon, G., et al. (2011). RosettaScripts: a scripting language interface to the Rosetta macromolecular modeling suite. PLoS One *6*, e20161.

Frenz, B., Rämisch, S., Borst, A.J., Walls, A.C., Adolf-Bryfogle, J., Schief, W.R., Veesler, D., and DiMaio, F. (2019). Automatically Fixing Errors in Glycoprotein Structures with Rosetta. Structure *27*, 134–139.e3.

Fujisaki, S., Takashita, E., Yokoyama, M., Taniwaki, T., Xu, H., Kishida, N., Sato, H., Tashiro, M., Imai, M., and Odagiri, T. (2012). A single E105K mutation far from the active site of influenza B virus neuraminidase contributes to reduced susceptibility to multiple neuraminidase-inhibitor drugs. Biochem. Biophys. Res. Commun. *429*, 51–56.

Gilchuk, I.M., Bangaru, S., Gilchuk, P., Irving, R.P., Kose, N., Bombardi, R.G., Thornburg, N.J., Creech, C.B., Edwards, K.M., Li, S., et al. (2019). Influenza H7N9 Virus Neuraminidase-Specific Human Monoclonal Antibodies Inhibit Viral Egress and Protect from Lethal Influenza Infection in Mice. Cell Host Microbe *26*, 715–728.e8.

Goddard, T.D., Huang, C.C., Meng, E.C., Pettersen, E.F., Couch, G.S., Morris, J.H., and Ferrin, T.E. (2018). UCSF ChimeraX: Meeting modern challenges in visualization and analysis. Protein Sci. *27*,

14–25.

Graham, B.S., Gilman, M.S.A., and McLellan, J.S. (2019). Structure-Based Vaccine Antigen Design. Annu. Rev. Med. *70*, 91–104.

Grant, T., Rohou, A., and Grigorieff, N. (2018). cisTEM, user-friendly software for single-particle image processing. Elife *7*, e35383.

Gulati, U., Hwang, C.-C., Venkatramani, L., Gulati, S., Stray, S.J., Lee, J.T., Laver, W.G., Bochkarev, A., Zlotnick, A., and Air, G.M. (2002). Antibody epitopes on the neuraminidase of a recent H3N2 influenza virus (A/Memphis/31/98). J. Virol. *76*, 12274–12280.

Han, N., Ng, J.T.Y., Li, Y., Mu, Y., and Huang, Z. (2020). Plasticity of the 340-Loop in Influenza Neuraminidase Offers New Insight for Antiviral Drug Development. Int. J. Mol. Sci. *21*, 5655.

Harris, A., Cardone, G., Winkler, D.C., Heymann, J.B., Brecher, M., White, J.M., and Steven, A.C. (2006). Influenza virus pleiomorphy characterized by cryoelectron tomography. Proc. Natl. Acad. Sci. U. S. A. *103*, 19123–19127.

Harris, A.K., Meyerson, J.R., Matsuoka, Y., Kuybeda, O., Moran, A., Bliss, D., Das, S.R., Yewdell, J.W., Sapiro, G., Subbarao, K., et al. (2013). Structure and accessibility of HA trimers on intact 2009 H1N1 pandemic influenza virus to stem region-specific neutralizing antibodies. Proc. Natl. Acad. Sci. U. S. A. *110*, 4592–4597.

Hocart, M., Grajower, B., Donabedian, A., Pokorny, B., Whitaker, C., and Kilbourne, E.D. (1995). Preparation and characterization of a purified influenza virus neuraminidase vaccine. Vaccine *13*, 1793–1798.

Hsieh, C.-L., Goldsmith, J.A., Schaub, J.M., DiVenere, A.M., Kuo, H.-C., Javanmardi, K., Le, K.C., Wrapp, D., Lee, A.G.-W., Liu, Y., et al. (2020). Structure-based Design of Prefusion-stabilized SARS-CoV-2 Spikes. bioRxiv.

Jiang, L., Fantoni, G., Couzens, L., Gao, J., Plant, E., Ye, Z., Eichelberger, M.C., and Wan, H. (2016). Comparative Efficacy of Monoclonal Antibodies That Bind to Different Epitopes of the 2009 Pandemic H1N1 Influenza Virus Neuraminidase. J. Virol. *90*, 117–128.

Katoh, K., Rozewicki, J., and Yamada, K.D. (2019). MAFFT online service: multiple sequence alignment, interactive sequence choice and visualization. Brief. Bioinform. *20*, 1160–1166.

Kilbourne, E.D., Christenson, W.N., and Sande, M. (1968). Antibody response in man to influenza virus neuraminidase following influenza. J. Virol. *2*, 761–762.

Kilbourne, E.D., Couch, R.B., Kasel, J.A., Keitel, W.A., Cate, T.R., Quarles, J.H., Grajower, B., Pokorny, B.A., and Johansson, B.E. (1995). Purified influenza A virus N2 neuraminidase vaccine is immunogenic and non-toxic in humans. Vaccine *13*, 1799–1803.

Krammer, F., Fouchier, R.A.M., Eichelberger, M.C., Webby, R.J., Shaw-Saliba, K., Wan, H., Wilson, P.C., Compans, R.W., Skountzou, I., and Monto, A.S. (2018). NAction! How Can Neuraminidase-Based Immunity Contribute to Better Influenza Virus Vaccines? MBio *9*, e02332–17.

Kühnel, K., Jarchau, T., Wolf, E., Schlichting, I., Walter, U., Wittinghofer, A., and Strelkov, S.V. (2004). The VASP tetramerization domain is a right-handed coiled coil based on a 15-residue repeat. Proc. Natl. Acad. Sci. U. S. A. *101*, 17027–17032.

Kwon, J.J., Choi, W.-S., Jeong, J.H., Kim, E.-H., Lee, O.-J., Yoon, S.-W., Hwang, J., Webby, R.J., Govorkova, E.A., Choi, Y.K., et al. (2018). An I436N substitution confers resistance of influenza A(H1N1)pdm09 viruses to multiple neuraminidase inhibitors without affecting viral fitness. J. Gen. Virol. *99*, 292–302.

Leman, J.K., Weitzner, B.D., Lewis, S.M., Adolf-Bryfogle, J., Alam, N., Alford, R.F., Aprahamian, M., Baker, D., Barlow, K.A., Barth, P., et al. (2020). Macromolecular modeling and design in Rosetta: recent methods and frameworks. Nat. Methods *17*, 665–680.

Li, Q., Sun, X., Li, Z., Liu, Y., Vavricka, C.J., Qi, J., and Gao, G.F. (2012). Structural and functional characterization of neuraminidase-like molecule N10 derived from bat influenza A virus. Proc. Natl. Acad. Sci. U. S. A. *109*, 18897–18902.

Liebschner, D., Afonine, P.V., Baker, M.L., Bunkóczi, G., Chen, V.B., Croll, T.I., Hintze, B., Hung, L.W., Jain, S., McCoy, A.J., et al. (2019). Macromolecular structure determination using X-rays, neutrons and electrons: recent developments in Phenix. Acta Crystallogr D Struct Biol *75*, 861–877.

Liu, W.-C., Lin, C.-Y., Tsou, Y.-T., Jan, J.-T., and Wu, S.-C. (2015). Cross-Reactive Neuraminidase-Inhibiting Antibodies Elicited by Immunization with Recombinant Neuraminidase Proteins of H5N1 and Pandemic H1N1 Influenza A Viruses. J. Virol. *89*, 7224–7234.

Madsen, A., Dai, Y.-N., McMahon, M., Schmitz, A.J., Turner, J.S., Tan, J., Lei, T., Alsoussi, W.B., Strohmeier, S., Amor, M., et al. (2020). Human Antibodies Targeting Influenza B Virus Neuraminidase Active Site Are Broadly Protective. Immunity *53*, 852–863.

Maguire, J.B., Boyken, S.E., Baker, D., and Kuhlman, B. (2018). Rapid Sampling of Hydrogen Bond Networks for Computational Protein Design. J. Chem. Theory Comput. *14*, 2751–2760.

Malby, R.L., Tulip, W.R., Harley, V.R., McKimm-Breschkin, J.L., Laver, W.G., Webster, R.G., and Colman, P.M. (1994). The structure of a complex between the NC10 antibody and influenza virus neuraminidase and comparison with the overlapping binding site of the NC41 antibody. Structure *2*, 733–746.

McAuley, J.L., Gilbertson, B.P., Trifkovic, S., Brown, L.E., and McKimm-Breschkin, J.L. (2019). Influenza Virus Neuraminidase Structure and Functions. Front. Microbiol. *10*, 39.

McKimm-Breschkin, J.L., Williams, J., Barrett, S., Jachno, K., McDonald, M., Mohr, P.G., Saito, T., and Tashiro, M. (2013). Reduced susceptibility to all neuraminidase inhibitors of influenza H1N1 viruses with haemagglutinin mutations and mutations in non-conserved residues of the neuraminidase. J. Antimicrob. Chemother. *68*, 2210–2221.

McKimm-Breschkin, J.L., Barrett, S., McKenzie-Kludas, C., McAuley, J., Streltsov, V.A., and Withers, S.G. (2019). Passaging of an influenza A(H1N1)pdm09 virus in a difluoro sialic acid inhibitor selects for a novel, but unfit I106M neuraminidase mutant. Antiviral Res. *169*, 104542.

McMahon, M., Strohmeier, S., Rajendran, M., Capuano, C., Ellebedy, A.H., Wilson, P.C., and Krammer, F. (2020). Correctly folded - but not necessarily functional - influenza virus neuraminidase is required to induce protective antibody responses in mice. Vaccine *38*, 7129–7137.

Memoli, M.J., Shaw, P.A., Han, A., Czajkowski, L., Reed, S., Athota, R., Bristol, T., Fargis, S., Risos, K., Powers, J.H., et al. (2016). Evaluation of Antihemagglutinin and Antineuraminidase Antibodies as Correlates of Protection in an Influenza A/H1N1 Virus Healthy Human Challenge Model. MBio *7*, e00417–16.

Monto, A.S., Petrie, J.G., Cross, R.T., Johnson, E., Liu, M., Zhong, W., Levine, M., Katz, J.M., and Ohmit, S.E. (2015). Antibody to Influenza Virus Neuraminidase: An Independent Correlate of Protection. J. Infect. Dis. *212*, 1191–1199.

Murphy, B.R., Kasel, J.A., and Chanock, R.M. (1972). Association of serum anti-neuraminidase antibody with resistance to influenza in man. N. Engl. J. Med. *286*, 1329–1332.

Pettersen, E.F., Goddard, T.D., Huang, C.C., Couch, G.S., Greenblatt, D.M., Meng, E.C., and Ferrin, T.E. (2004). UCSF Chimera--a visualization system for exploratory research and analysis. J. Comput. Chem.

25, 1605–1612.

Punjani, A., Rubinstein, J.L., Fleet, D.J., and Brubaker, M.A. (2017). cryoSPARC: algorithms for rapid unsupervised cryo-EM structure determination. Nat. Methods *14*, 290–296.

Punjani, A., Zhang, H., and Fleet, D.J. (2019). Non-uniform refinement: Adaptive regularization improves single particle cryo-EM reconstruction. bioRxiv.

Rajendran, M., Nachbagauer, R., Ermler, M.E., Bunduc, P., Amanat, F., Izikson, R., Cox, M., Palese, P., Eichelberger, M., and Krammer, F. (2017). Analysis of Anti-Influenza Virus Neuraminidase Antibodies in Children, Adults, and the Elderly by ELISA and Enzyme Inhibition: Evidence for Original Antigenic Sin. MBio *8*, e02281–16.

Rosenthal, P.B., and Henderson, R. (2003). Optimal determination of particle orientation, absolute hand, and contrast loss in single-particle electron cryomicroscopy. J. Mol. Biol. *333*, 721–745.

Russell, R.J., Haire, L.F., Stevens, D.J., Collins, P.J., Lin, Y.P., Blackburn, G.M., Hay, A.J., Gamblin, S.J., and Skehel, J.J. (2006). The structure of H5N1 avian influenza neuraminidase suggests new opportunities for drug design. Nature *443*, 45–49.

Rutten, L., Lai, Y.-T., Blokland, S., Truan, D., Bisschop, I.J.M., Strokappe, N.M., Koornneef, A., van Manen, D., Chuang, G.-Y., Farney, S.K., et al. (2018). A Universal Approach to Optimize the Folding and Stability of Prefusion-Closed HIV-1 Envelope Trimers. Cell Rep. *23*, 584–595.

Saito, T., Taylor, G., Laver, W.G., Kawaoka, Y., and Webster, R.G. (1994). Antigenicity of the N8 influenza A virus neuraminidase: existence of an epitope at the subunit interface of the neuraminidase. J. Virol. *68*, 1790–1796.

Sanders, R.W., and Moore, J.P. (2017). Native-like Env trimers as a platform for HIV-1 vaccine design. Immunol. Rev. *275*, 161–182.

Scheres, S.H.W. (2012). RELION: implementation of a Bayesian approach to cryo-EM structure determination. J. Struct. Biol. *180*, 519–530.

Scheres, S.H.W. (2015). Semi-automated selection of cryo-EM particles in RELION-1.3. J. Struct. Biol. *189*, 114–122.

Schulman, J.L., Khakpour, M., and Kilbourne, E.D. (1968). Protective effects of specific immunity to viral neuraminidase on influenza virus infection of mice. J. Virol. *2*, 778–786.

da Silva, D.V., Nordholm, J., Madjo, U., Pfeiffer, A., and Daniels, R. (2013). Assembly of subtype 1 influenza neuraminidase is driven by both the transmembrane and head domains. J. Biol. Chem. *288*, 644–653.

Smith, B.J., Huyton, T., Joosten, R.P., McKimm-Breschkin, J.L., Zhang, J.G., Luo, C.S., Lou, M.Z., Labrou, N.E., and Garrett, T.P.J. (2006). Structure of a calcium-deficient form of influenza virus neuraminidase: implications for substrate binding. Acta Crystallogr. D Biol. Crystallogr. *62*, 947–952.

Smith, G.E., Sun, X., Bai, Y., Liu, Y.V., Massare, M.J., Pearce, M.B., Belser, J.A., Maines, T.R., Creager, H.M., Glenn, G.M., et al. (2017). Neuraminidase-based recombinant virus-like particles protect against lethal avian influenza A(H5N1) virus infection in ferrets. Virology *509*, 90–97.

Stadlbauer, D., Zhu, X., McMahon, M., Turner, J.S., Wohlbold, T.J., Schmitz, A.J., Strohmeier, S., Yu, W., Nachbagauer, R., Mudd, P.A., et al. (2019). Broadly protective human antibodies that target the active site of influenza virus neuraminidase. Science *366*, 499–504.

St Clair, E.W., Kenan, D., Burch, J.A., Jr, Keene, J.D., and Pisetsky, D.S. (1991). Anti-La antibody production by MRL-1pr/1pr mice. Analysis of fine specificity. J. Immunol. *146*, 1885–1892.

Suloway, C., Pulokas, J., Fellmann, D., Cheng, A., Guerra, F., Quispe, J., Stagg, S., Potter, C.S., and Carragher, B. (2005). Automated molecular microscopy: the new Leginon system. J. Struct. Biol. *151*, 41–60.

Sultana, I., Gao, J., Markoff, L., and Eichelberger, M.C. (2011). Influenza neuraminidase-inhibiting antibodies are induced in the presence of zanamivir. Vaccine *29*, 2601–2606.

Sultana, I., Yang, K., Getie-Kebtie, M., Couzens, L., Markoff, L., Alterman, M., and Eichelberger, M.C. (2014). Stability of neuraminidase in inactivated influenza vaccines. Vaccine *32*, 2225–2230.

Takaba, K., Maki-Yonekura, S., and Yonekura, K. (2020). Collecting large datasets of rotational electron diffraction with ParallEM and SerialEM. J. Struct. Biol. *211*, 107549.

Taylor, G. (1996). Sialidases: structures, biological significance and therapeutic potential. Curr. Opin. Struct. Biol. *6*, 830–837.

Tegunov, D., and Cramer, P. (2019). Real-time cryo-electron microscopy data preprocessing with Warp. Nat. Methods *16*, 1146–1152.

Tong, S., Zhu, X., Li, Y., Shi, M., Zhang, J., Bourgeois, M., Yang, H., Chen, X., Recuenco, S., Gomez, J., et al. (2013). New world bats harbor diverse influenza A viruses. PLoS Pathog. *9*, e1003657.

Varghese, J.N., Laver, W.G., and Colman, P.M. (1983). Structure of the influenza virus glycoprotein antigen neuraminidase at 2.9 A resolution. Nature *303*, 35–40.

van der Vries, E., Collins, P.J., Vachieri, S.G., Xiong, X., Liu, J., Walker, P.A., Haire, L.F., Hay, A.J., Schutten, M., Osterhaus, A.D.M.E., et al. (2012). H1N1 2009 pandemic influenza virus: resistance of the I223R neuraminidase mutant explained by kinetic and structural analysis. PLoS Pathog. *8*, e1002914.

Wan, H., Yang, H., Shore, D.A., Garten, R.J., Couzens, L., Gao, J., Jiang, L., Carney, P.J., Villanueva, J., Stevens, J., et al. (2015). Structural characterization of a protective epitope spanning A(H1N1)pdm09 influenza virus neuraminidase monomers. Nat. Commun. *6*, 6114.

Wang, H., Dou, D., Östbye, H., Revol, R., and Daniels, R. (2019). Structural restrictions for influenza neuraminidase activity promote adaptation and diversification. Nat Microbiol *4*, 2565–2577.

Wang, R.Y.-R., Song, Y., Barad, B.A., Cheng, Y., Fraser, J.S., and DiMaio, F. (2016). Automated structure refinement of macromolecular assemblies from cryo-EM maps using Rosetta. Elife *5*, e17219.

Wohlbold, T.J., Nachbagauer, R., Xu, H., Tan, G.S., Hirsh, A., Brokstad, K.A., Cox, R.J., Palese, P., and Krammer, F. (2015). Vaccination with adjuvanted recombinant neuraminidase induces broad heterologous, but not heterosubtypic, cross-protection against influenza virus infection in mice. MBio *6*, e02556.

Xu, X., Zhu, X., Dwek, R.A., Stevens, J., and Wilson, I.A. (2008). Structural characterization of the 1918 influenza virus H1N1 neuraminidase. J. Virol. *82*, 10493–10501.

Yuan, P., Thompson, T.B., Wurzburg, B.A., Paterson, R.G., Lamb, R.A., and Jardetzky, T.S. (2005). Structural studies of the parainfluenza virus 5 hemagglutinin-neuraminidase tetramer in complex with its receptor, sialyllactose. Structure *13*, 803–815.

Zanin, M., Duan, S., Wong, S.-S., Kumar, G., Baviskar, P., Collin, E., Russell, C., Barman, S., Hause, B., and Webby, R. (2017). An Amino Acid in the Stalk Domain of N1 Neuraminidase Is Critical for Enzymatic Activity. J. Virol. *91*, e00868–16.

Zhu, X., Turner, H.L., Lang, S., McBride, R., Bangaru, S., Gilchuk, I.M., Yu, W., Paulson, J.C., Crowe, J.E., Jr, Ward, A.B., et al. (2019). Structural Basis of Protection against H7N9 Influenza Virus by Human Anti-N9 Neuraminidase Antibodies. Cell Host Microbe *26*, 729–738.e4.

Zivanov, J., Nakane, T., Forsberg, B.O., Kimanius, D., Hagen, W.J., Lindahl, E., and Scheres, S.H. (2018). New tools for automated high-resolution cryo-EM structure determination in RELION-3. Elife *7*, e42166.

Zivanov, J., Nakane, T., and Scheres, S.H.W. (2019). A Bayesian approach to beam-induced motion correction in cryo-EM single-particle analysis. IUCrJ *6*, 5–17.

Chapter 4: Investigation of the effects of particle size and antigen valency on peptide epitope immunogenicity using precisely defined designed protein nanomaterials

Summary

Multivalent presentation of antigen is known to increase the intensity and longevity of humoral immune responses induced by vaccination. Self-assembling proteins are a promising platform for multivalent antigen presentation that allows the production of immunogens with precisely defined molecular compositions and three-dimensional structures. However, the limited set of naturally occurring protein scaffolds available has slowed investigation of the effects of two key structural parameters, immunogen size and antigen valency, on immunogenicity. New computational methods for designing novel self-assembling proteins with atomic-level accuracy present a unique opportunity to explore these aspects of structure-based vaccine design. We generated a series of seven self-assembling protein immunogens with a range of precisely defined sizes and antigen valencies by genetically fusing a peptide antigen derived from the L2 coat protein of human papillomavirus to several computationally designed protein nanomaterials. Including controls for trimeric nanoparticle subunits, we immunized mice with immunogens ranging in size from ~5–25 nm and displaying 3, 12, 24, 60, and 120 copies of the antigen. Anti-L2 serum antibody titers measured shortly after immunization and six months later were generally correlated with increasing immunogen size and antigen valency. These results clearly identify antigen valency as a key parameter for structure-based vaccine design and highlight the potential of designed protein nanomaterials as a powerful and flexible platform for designing next-generation vaccines.

Introduction

Early vaccine development focused on the use of attenuated or inactivated whole pathogens, an approach that was highly effective in eliminating or greatly reducing the threat of several diseases (Ehreth 2003; Rappuoli et al. 2014). However, there are several important diseases for which whole-pathogen approaches are not practical or have failed (Nabel 2013). This fact, coupled with a demand for improved safety profiles and manufacturing methods, has shifted the focus of modern vaccine development towards vectored approaches (Ewer et al. 2016; Swadling et al. 2014; Ondondo 2014) and subunit vaccines, which contain antigenic fragments of the pathogen but no live components (Kanekiyo, Ellis, and King 2019). Unlike vaccines derived from whole pathogens, the composition and formulation of subunit vaccines is not predefined and must be optimized to induce the desired immune response. Several enabling technologies have been developed recently that are transforming vaccine development from a trial-and-error process to one more amenable to rational design (Koff et al. 2013; Nabel 2013). For diseases in which humoral responses are required for immunity, the three-dimensional structure of the immunogen is a major factor, both at the level of the antigen conformation as well as its presentation to B cells. For example, presenting antigen in repetitive arrays through either conjugation or genetic fusion to carrier proteins has been shown numerous times to induce more robust and durable humoral immune responses (Yassine et al. 2015; Kanekiyo et al. 2013; Kanekiyo et al. 2015; Yassine et al. 2015; Kanekiyo et al. 2013; Sliepen et al. 2015; J. Jardine et al. 2013; Kato et al. 2020; Irvine and Read 2020; J. Jardine et al. 2013), even to the point of overriding self-tolerance mechanisms (Frietze, Peabody, and Chackerian 2016). In

humans, the effects of multivalent antigen presentation have been most comprehensively documented in studies of the commercial virus-like particle vaccines for human papillomaviruses (Schiller and Lowy 2015; Zhao et al. 2013). In addition to increasing avidity, multivalent antigen presentation is thought to more strongly activate B cells through bivalent ligation and/or clustering of B-cell receptors (BCRs) (Martin F. Bachmann and Jennings 2010; M. F. Bachmann and Zinkernagel 1997). Developing new methods for multivalent antigen presentation therefore represents an important opportunity for overcoming the often limited immunogenicity of subunit vaccines.

Self-assembling proteins offer many advantages as platforms for the multivalent display of heterologous antigens (López-Sagaseta et al. 2016). They can form highly ordered, monodisperse structures similar in size to viruses, and offer defined abilities to present antigens via genetic fusion. Most of the self-assembling proteins that have been investigated as vaccine scaffolds fall into two main classes. Virus-like particles (VLPs), often derived from the capsid proteins of plant viruses or bacteriophage, have been extensively explored as platforms for the multivalent display of peptide and small protein epitopes (Frietze, Peabody, and Chackerian 2016; Correia et al. 2014). The high valencies that can be achieved using these platforms result in robust immunogenicity of these otherwise relatively non-immunogenic antigens. More recently, several non-viral self-assembling proteins, which appear to be more tolerant with respect to genetic fusions than many VLPs, have been used to multivalently scaffold larger and more complex antigens, including those derived from influenza hemagglutinin (Yassine et al. 2015; Kanekiyo et al. 2013), HIV Env (Zhou et al. 2014; Krebs et al. 2014; J. G. Jardine et al. 2015; He et al. 2016; McGuire et al. 2016) and Epstein-Barr virus (Kanekiyo et al. 2015). Commonly used non-viral scaffolds include lumazine synthase (60 subunits) (J. Jardine et al. 2013), E2p (60 subunits) (He et al. 2016), encapsulin (60 subunits) (Kanekiyo et al. 2015), ferritin (24 subunits) (Kanekiyo et al. 2015; Yassine et al. 2015; Kanekiyo et al. 2013; Sliepen et al. 2015) and C4b-binding protein (7 subunits) (Ogun et al. 2008; Li et al. 2016). Designed self-assembling peptides have also been used as particulate scaffolds to present peptide antigens (Kaba et al. 2012; Karch et al. 2016).

Recently, new computational methods have enabled the design of various structural classes of self-assembling protein nanomaterials with atomic-level accuracy (Hsia et al. 2016; Bale et al. 2016; King et al. 2014, 2012; Gonen et al. 2015; Fallas et al. 2017). Multiple designed tetrahedral and icosahedral nanoparticles have been investigated as immunogens displaying diverse antigens from HIV (Antanasijevic et al. 2020); (Brouwer et al. 2019), respiratory syncytial virus (Marcandalli et al. 2019), plasmodium falciparum (Bruun et al. 2018), SARS-COV-2 (Walls et al. 2020) and influenza (Ueda et al. 2020). The vast number and diversity of possible nanomaterials that could be designed using these methods opens the door to systematic investigation of the structural correlates of immunogenicity in multivalent immunogens. Here we used a variety of precisely defined designed self-assembling protein nanomaterials, ranging from 24-subunit assemblies with tetrahedral symmetry to 120-subunit assemblies with icosahedral symmetry, as scaffolds to evaluate the effects of antigen valency and immunogen size on the immunogenicity of a model peptide antigen. Peptides derived from the L2 coat protein of human papillomavirus (HPV) have proven to be simple yet effective epitopes for eliciting neutralizing antibody responses against HPV when multimerized on VLPs (Tumban et al. 2011, 2012, 2013; Tyler, Tumban, Peabody, et al. 2014). We genetically fused

an optimized consensus epitope that induces neutralizing responses against a number of HPV types (Tyler, Tumban, Dziduszko, et al. 2014) to four designed nanomaterials with a wide yet precisely defined range of valencies. Anti-L2 antibody titers from immunized mice were compared across the set of immunogens and to closely related trimeric control proteins bearing the peptide epitope. Our results demonstrate that the immunogenicity of the displayed epitope increases in proportion to antigen valency, thereby emphasizing the importance of maximizing this feature in the structure-based design of novel self-assembling immunogens.

Results

To investigate the relationship between immunogen size, antigen valency, and immunogenicity, we generated a set of nine immunogens derived from four distinct designed protein nanomaterial scaffolds (**Figure 4.1**). The four scaffolds vary in terms of their subunit composition, symmetry, and size. Two of the scaffolds, T33-31 and T33-15, are two-component, 24-subunit assemblies with tetrahedral symmetry, each comprising four copies of two distinct trimeric protein building blocks (King et al. 2014; Bale et al. 2015). T33-31 has a diameter of 11 nm, while T33-15 has a radius of 13 nm. The third scaffold, I3-01, is a 25 nm, 60-subunit assembly with icosahedral symmetry constructed from 20 copies of a single trimer (Hsia et al. 2016). The fourth scaffold, I53-50, comprises 20 trimers and 12 pentamers that form a 25 nm, 120-subunit assembly with icosahedral symmetry (Bale et al. 2016).

The N terminus of each subunit in these scaffolds is exposed on the scaffold exterior, enabling multivalent display of the L2 peptide epitope (MAGTGGRTGYVPLGTRPPTVVDV) via N-terminal genetic fusion. For each two-component scaffold (T33-15, T33-31, and I53-50), the L2 peptide was fused to one or both subunits to generate pairs of immunogens that were identical in all respects other than antigen valency. Combined with the single L2 peptide fusion to I3-01, this resulted in seven total nanomaterial immunogens displaying 12, 24, 60, or 120 epitopes. To control for the effects of higher-order assembly, two additional immunogens were made by fusing the L2 peptide to two wild-type trimeric proteins that were used as starting points for the computational design of one building block in each of the four scaffolds (PDB IDs 1wa3 (Fullerton et al. 2006) and 1ufy (unpublished)). These trimers lack the computationally designed interfaces that drive nanomaterial assembly and display three epitopes per oligomer.

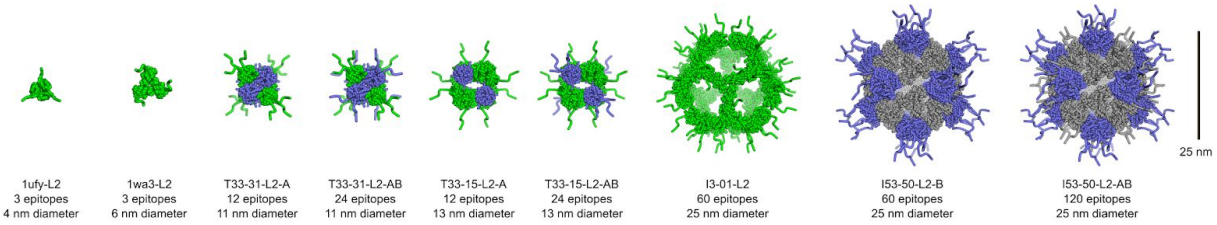

Figure 4.1. Overview of L2-displaying nanomaterials.
Seven total nanoparticle immunogens were designed, which were chosen based on varied sizes and epitope valencies. Within each construct, different protein components are displayed in different colors. Wild-type trimeric immunogens without nanomaterial interfaces were also designed to control for the identity of protein components (left). In all cases, the peptide epitope was genetically fused to the N-terminus of protein components as shown.

The novel immunogens were expressed in *Escherichia coli* cells and purified by either immobilized metal affinity chromatography or heat purification followed by ammonium sulfate precipitation. In all cases, a final size-exclusion chromatography (SEC) step was used to isolate either fully assembled nanomaterials or trimeric controls. Analytical SEC of the purified materials revealed predominantly single peaks at the expected elution volumes, indicating the formation of monodisperse assemblies (**Figure 4.2**). This was confirmed by negative stain electron microscopy, which showed fields of uniform particles that were indistinguishable from previous characterizations of the unmodified scaffolds (Hsia et al. 2016; Bale et al. 2016, 2015; King et al. 2014). As expected, large assemblies were not observed for peptide fusions to the wild-type trimer controls. SDS-PAGE analysis indicated that each immunogen was highly pure and that the two-component immunogens contained a 1:1 ratio of the two subunits (**Figure 4.2, bottom right**).

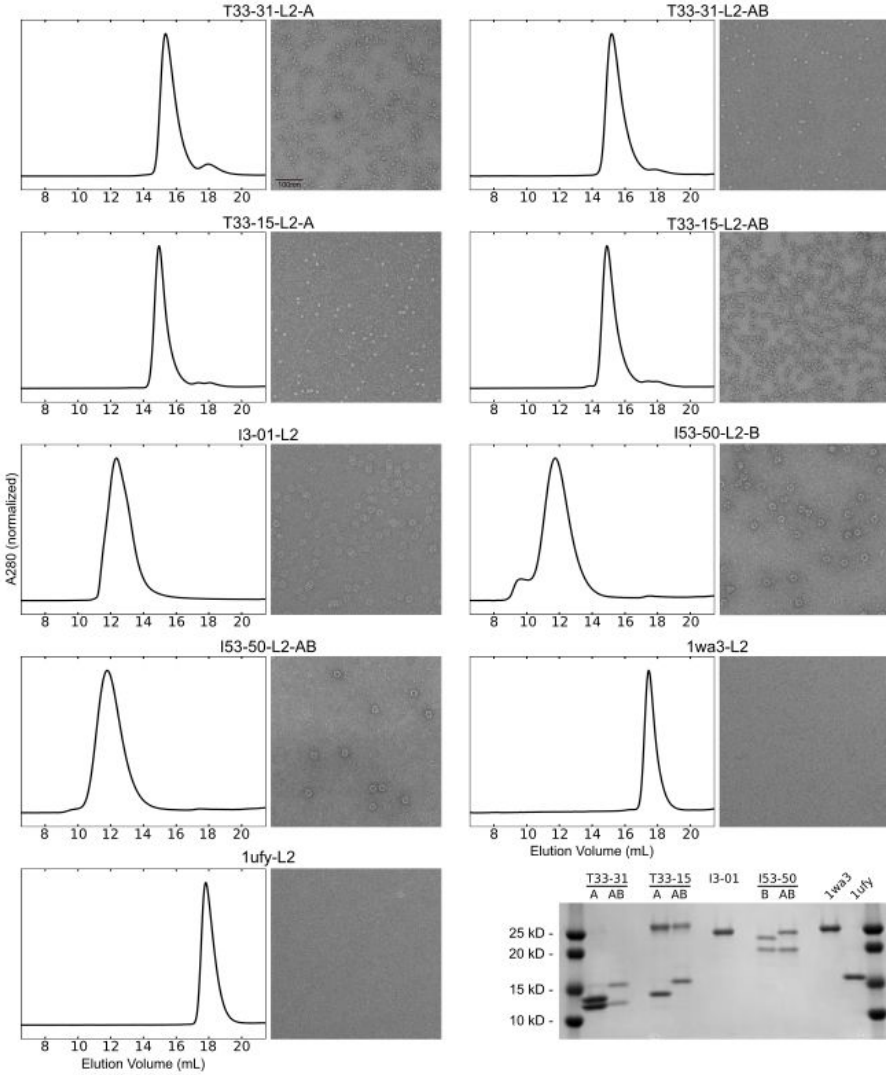

Figure 4.2. Biochemical characterization of L2-displaying nanomaterials.
Correct size and characteristics of produced immunogens were assessed by size-exclusion chromatography and negative stain electron microscopy. SDS-PAGE confirmed protein identities and revealed the expected shifts in mobility for subunits bearing fused peptide epitopes (bottom right).

To assess the immunogenicity of the L2-displaying nanomaterials, groups of BALB/c mice were immunized and followed for up to seven months. Mice were given two 5 μg doses of each immunogen intramuscularly at weeks 0 and 4 without adjuvant, and sera were collected three weeks after each immunization and at the conclusion of the study. Serum IgG antibody titers against the L2 peptide and the nanomaterial platforms were assessed by ELISA. In general, anti-L2 antibody titers correlated with peptide valency and the size of the nanomaterial. After a single immunization, the smaller tetrahedral nanomaterials elicited weak antibody responses against L2 (**Fig. 4.3A**), while the larger diameter and higher valency I3-01 and I53-50 nanomaterials elicited slightly higher antibody levels, although this difference was not statistically significant. The levels of antibody induced against the underlying nanomaterial scaffolds followed a similar pattern: the larger I3-01 and I53-50 nanoparticles elicited higher responses than the T33 materials (**Fig. 4.3B**). Anti-L2 antibody titers after two immunizations are shown in Fig. 3C. Among the three pairs of immunogens based upon the same scaffold but displaying differing numbers of the L2 epitopes, the immunogen displaying more copies of the epitope elicited (on average) slightly higher anti-L2 antibodies in two cases (T33-31 and T33-15), although the observed differences were not significant. The trimeric controls that displayed only three copies of the L2 peptide elicited weak antibody responses even after two immunizations. This trend persisted in samples obtained six months after the booster immunization, as the levels of anti-L2 antibody induced by the several nanoparticle immunogens were largely unchanged (**Fig. 4.3D**). Antibodies elicited by the designed nanoparticles were all found to be IgG1 (not shown).

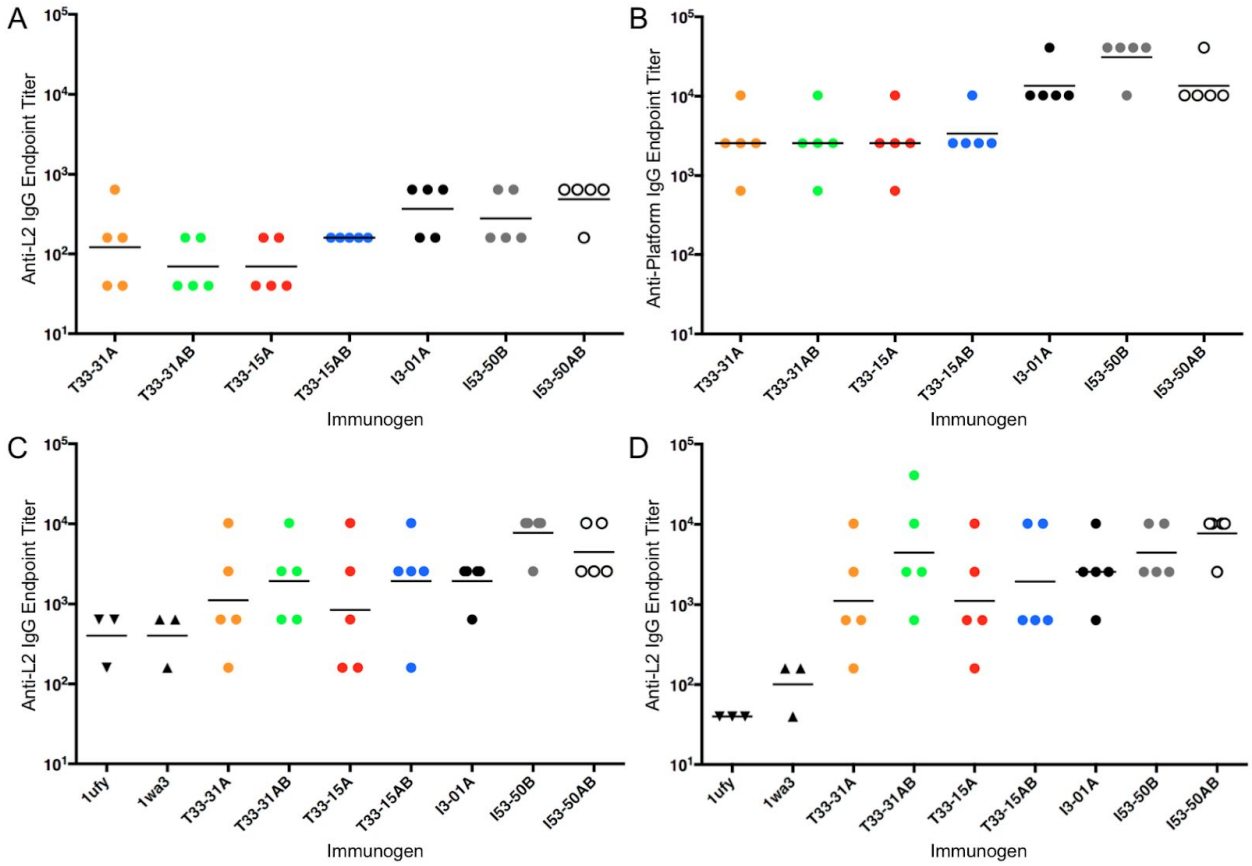

Figure 4.3. Immunogenicity of L2-displaying nanomaterials in mice
In all cases, IgG titers were determined by end-point titration ELISA. Groups of Balb/c mice were immunized twice intramuscularly with 5ug of each immunogen at a four-week interval. (A) Short-term IgG titers against the L2 peptide epitope were measured three weeks after the first immunization. (B) At the same time, IgG titers against unmodified nanomaterial constructs were measured. (C) Short-term IgG titers after the second immunization were similarly measured. (D) Long-term IgG titers were measured six months after the second immunization.

Discussion

As multivalent antigen presentation on self-assembling proteins becomes an increasingly promising and common approach to structure-based vaccine design, understanding the correlation between specific structural properties of multimerization platforms and the immunological responses they elicit will be critical for directing future design strategies. Methods for designing novel self-assembling proteins could play an important role by enabling the design of multivalent display platforms in which specific structural features are varied systematically. Given their ability to form highly ordered and monodisperse structures, self-assembling proteins could in principle permit atomic-level dissection of structural correlates of immunogenicity. Here we took a first step in this direction by engineering a series of precisely defined protein nanomaterial immunogens ranging in size from 5–25 nm that display 3, 12, 24, 60, or 120 copies of a model peptide epitope. We found that larger immunogens displaying more copies of the epitope induced higher epitope-specific antibody titers, confirming previous observations that higher antigen valency correlates with increased immunogenicity (Kato et al. 2020;

Marcandalli et al. 2019). Interestingly, within this overall trend, pairs of immunogens based on the same self-assembling scaffold yet displaying differing numbers of epitopes showed relatively small variations in immunogenicity. This may suggest that, at least for peptide epitopes, antigen valency and immunogen size are roughly equally important factors.

Designed protein nanomaterials, in addition to being used as probes for systematic and high-resolution interrogation of structural correlates of immune responses, can be envisioned as multimerization scaffolds for next-generation vaccines. The high degree or order observed in computationally designed protein nanomaterials, which are very monodisperse and structurally defined at the atomic level (Hsia et al. 2016; Bale et al. 2016; King et al. 2014, 2012), is a desirable property for next-generation vaccine candidates. As shown here, direct genetic fusion of epitopes to the nanomaterial subunits results in reproducibly manufacturable immunogens with precisely defined numbers of epitopes. A key next question will be whether designed nanomaterials like those presented here can scaffold more complex antigens, such as viral glycoproteins. Displaying such proteins on VLPs has proven challenging, reflecting an apparent sensitivity of the folding and/or assembly of many VLP subunits to genetic fusion of large, complex antigens (Mateu 2011; Smith, Hawes, and Bundy 2013). This has driven the use of conjugation techniques based on robust small molecule-protein reactions (Correia et al. 2014) and protein-peptide conjugation systems such as SpyTag-SpyCatcher (Zakeri et al. 2012; K. D. Brune et al. 2016; K. Brune et al. 2017). However, recent demonstrations that complex antigens can be displayed via genetic fusion on a small number of stable, non-viral self-assembling proteins (J. Jardine et al. 2013; Kanekiyo et al. 2015; Yassine et al. 2015; Kanekiyo et al. 2013; Krebs et al. 2014; He et al. 2016; McGuire et al. 2016), combined with the robust stability of many computationally designed proteins (Kuhlman et al. 2003; Brunette et al. 2015; Koga et al. 2012), suggest that designed protein nanomaterials like those presented here could be a robust and versatile platform for multivalent display of a wide variety of antigens.

In summary, we have used a set of highly monodisperse self-assembling protein nanomaterials to investigate the relationship between the valency of a displayed peptide epitope, overall immunogen size, and immunogenicity. Our results demonstrate that within the ranges tested, the immunogenicity of peptide antigens increases with increasing antigen valency and immunogen size. The data motivate the exploration of larger self-assembling protein nanomaterials displaying as many copies of an antigen as possible as vaccine scaffolds. In addition, this work establishes computationally designed protein nanomaterials as a novel platform for structure-based vaccine design.

Contributors and acknowledgements

I would like to thank Julianne Peabody, Joost Snijder, David Veesler, Bryce Chackerian, and Neil P. King for contributing to this project.

Materials and Methods

Genetic insertion of L2 peptides onto the N-terminus of nanoparticle subunits

As described in the main text, the constructs based on I3-01, 1wa3-wt and 1ufy-wt consisted of a single protein, while constructs based on T33-15, T33-31 and I53-50 consisted of a pair of proteins. Optimized consensus L2 sequences with a 4-residue linker (ASGS) were cloned onto the amino-terminus of mentioned protein subunits and wildtype trimers, and genes

were inserted into the pET29b plasmid as previously described. For I3-01_L2-A, the N-terminal hexahistidine tag was removed and replaced by the L2 peptide and linker. All constructs were sequenced to confirm the presence of L2 peptide inserts.

Protein expression and purification

Expression plasmids were transformed into BL21(DE3) *E. coli* cells, and all constructs were expressed as previously described [27463675]. For purification, constructs based on T33-15, T33-31, I53-50, 1wa3-wt and 1ufy-wt were purified using previously described methods [27463675]. The construct based on I3-01 was purified using an alternate method. Cells were lysed by sonication in 25mM TRIS pH 8.0, 150mM NaCl, 1mM DTT supplemented with 1mM phenylmethanesulfonyl fluoride, 0.1mg/mL DNase and 0.1mg/mL RNase. Ammonium sulfate was added to the lysate to a concentration of 60%, and the mixture was lightly mixed for 10 minutes before collecting the precipitate by centrifugation. The precipitate was resuspended in 25mM TRIS pH 8.0, 150mM NaCl, 1mM DTT and was then heated at 70°C for 10min. The supernatant was cleared by centrifugation and filtered through 0.22uM filters (Millipore). Proteins were purified from the filtered supernatant by size exclusion chromatography on a Superose 6 Increase 10/300 gel filtration column (GE Life Sciences).

Analytical size exclusion chromatography

Analytical SEC was performed on a Superose 6 Increase 10/300 gel filtration column (GE Life Sciences) using 25 mM TRIS pH 8.0, 150 mM NaCl, 1 mM DTT as the running buffer. The purified constructs were loaded onto the column with each component present at subunit concentrations varying from 15-50 μM for each subunit present.

Negative stain electron microscopy

Samples were diluted to final concentrations ranging between 0.1 and 0.01 g/L. Volumes of 3-4 μL of the samples were loaded onto glow-discharged, carbon-coated copper grids. After 30 seconds, excess sample was blotted from the grid with Whatman 1 filter paper and subsequently stained twice in 3 μL of 2% (w/v) uranyl formate. Grids were loaded in a FEI Tecnai Spirit transmission electron microscope equipped with a US4000 CCD camera. Images were acquired at a magnification of 52000 at a defocus of approximately -1 μm.

Immunization of mice and measurement of antibody responses

Endotoxin was removed from all purified constructs by a phase extraction with Triton X-114 as previously described (2170533). All animal work was done in accordance with National Institutes of Health and University of New Mexico guidelines. Groups of five Balb/c mice were immunized twice at a four-week interval. Immunizations were performed intramuscularly (i.m.) using 5 μg of nanoparticles without exogenous adjuvant. Sera from all experimental groups were collected three weeks after each immunization and six months after the boost. Sera was assessed by ELISA for IgG antibodies against the L2 peptide and the nanoparticle platform. A peptide ELISA was used to measure the titer of anti-L2(65- 85) IgG in sera. ELISA plates were coated with 1 μg of the HPV16 (65-85) peptide (synthesized by American Peptide Company as described above) conjugated to streptavidin using SMPH. In order to measure antibody titers against the platform, ELISA plates were coated with 500ng of

unmodified nanoparticles (T33-15, T33-31, I3-01, and I53-50). ELISAs were performed as described (Tumban et al. 2011). Briefly, peptide-coated wells were blocked for 2 hours at room temperature with 0.5% non-fat dry milk in PBS buffer. Four-fold serial dilutions of sera were added to each well and incubated for 2 hours at room temperature. Horseradish peroxidase (HRP)-labeled goat anti-mouse IgG (Jackson Immunoresearch, West Grove) at a dilution of 1∶5,000 was applied for 1 hour as a secondary antibody. The plates were developed with 3,3',5,5'-tetramethylbenzidine (TMB; Calbiochem), neutralized with an equal volume of 1% HCl, and reactivity was determined by measuring the mean optical density (OD) values at 450nm. End-point dilution IgG titers were calculated as the highest dilution at which the OD450 value was over twice the background of negative control samples.

References

Antanasijevic, Aleksandar, George Ueda, Philip J. M. Brouwer, Jeffrey Copps, Deli Huang, Joel D. Allen, Christopher A. Cottrell, et al. 2020. "Structural and Functional Evaluation of de Novo-Designed, Two-Component Nanoparticle Carriers for HIV Env Trimer Immunogens." *PLoS Pathogens* 16 (8): e1008665.

Bachmann, Martin F., and Gary T. Jennings. 2010. "Vaccine Delivery: A Matter of Size, Geometry, Kinetics and Molecular Patterns." *Nature Reviews. Immunology* 10 (11): 787–96.

Bachmann, M. F., and R. M. Zinkernagel. 1997. "Neutralizing Antiviral B Cell Responses." *Annual Review of Immunology* 15: 235–70.

Bale, Jacob B., Shane Gonen, Yuxi Liu, William Sheffler, Daniel Ellis, Chantz Thomas, Duilio Cascio, et al. 2016. "Accurate Design of Megadalton-Scale Two-Component Icosahedral Protein Complexes." *Science* 353 (6297): 389–94.

Bale, Jacob B., Rachel U. Park, Yuxi Liu, Shane Gonen, Tamir Gonen, Duilio Cascio, Neil P. King, Todd O. Yeates, and David Baker. 2015. "Structure of a Designed Tetrahedral Protein Assembly Variant Engineered to Have Improved Soluble Expression." *Protein Science: A Publication of the Protein Society* 24 (10): 1695–1701.

Brouwer, Philip J. M., Aleksandar Antanasijevic, Zachary Berndsen, Anila Yasmeen, Brooke Fiala, Tom P. L. Bijl, Ilja Bontjer, et al. 2019. "Enhancing and Shaping the Immunogenicity of Native-like HIV-1 Envelope Trimers with a Two-Component Protein Nanoparticle." *Nature Communications* 10 (1): 4272.

Brune, Karl, Can Buldun, Yuanyuan Li, Iona Taylor, Florian Brod, Sumi Biswas, and Mark Howarth. 2017. "Dual Plug-and-Display Synthetic Assembly Using Orthogonal Reactive Proteins for Twin Antigen Immunization." *Bioconjugate Chemistry*, April. https://doi.org/10.1021/acs.bioconjchem.7b00174.

Brune, Karl D., Darren B. Leneghan, Iona J. Brian, Andrew S. Ishizuka, Martin F. Bachmann, Simon J. Draper, Sumi Biswas, and Mark Howarth. 2016. "Plug-and-Display: Decoration of Virus-Like Particles via Isopeptide Bonds for Modular Immunization." *Scientific Reports* 6 (January): 19234.

Brunette, T. J., Fabio Parmeggiani, Po-Ssu Huang, Gira Bhabha, Damian C. Ekiert, Susan E. Tsutakawa, Greg L. Hura, John A. Tainer, and David Baker. 2015. "Exploring the Repeat Protein Universe through Computational Protein Design." *Nature* 528 (7583): 580–84.

Bruun, Theodora U. J., Anne-Marie C. Andersson, Simon J. Draper, and Mark Howarth. 2018. "Engineering a Rugged Nanoscaffold To Enhance Plug-and-Display Vaccination." *ACS Nano* 12 (9): 8855–66.

Correia, Bruno E., John T. Bates, Rebecca J. Loomis, Gretchen Baneyx, Chris Carrico, Joseph G. Jardine, Peter Rupert, et al. 2014. "Proof of Principle for Epitope-Focused Vaccine Design." *Nature* 507 (7491): 201–6.

Ehreth, Jenifer. 2003. "The Global Value of Vaccination." *Vaccine* 21 (7-8): 596–600.

Ewer, Katie J., Teresa Lambe, Christine S. Rollier, Alexandra J. Spencer, Adrian Vs Hill, and Lucy Dorrell. 2016. "Viral Vectors as Vaccine Platforms: From Immunogenicity to Impact." *Current Opinion in Immunology* 41 (August): 47–54.

Fallas, Jorge A., George Ueda, William Sheffler, Vanessa Nguyen, Dan E. McNamara, Banumathi Sankaran, Jose Henrique Pereira, et al. 2017. "Computational Design of Self-Assembling Cyclic

Protein Homo-Oligomers." *Nature Chemistry* 9 (4): 353–60.
Frietze, Kathryn M., David S. Peabody, and Bryce Chackerian. 2016. "Engineering Virus-like Particles as Vaccine Platforms." *Current Opinion in Virology* 18 (June): 44–49.
Fullerton, Stephen W. B., Jennifer S. Griffiths, Alexandra B. Merkel, Manoj Cheriyan, Nathan J. Wymer, Michael J. Hutchins, Carol A. Fierke, Eric J. Toone, and James H. Naismith. 2006. "Mechanism of the Class I KDPG Aldolase." *Bioorganic & Medicinal Chemistry* 14 (9): 3002–10.
Gonen, Shane, Frank DiMaio, Tamir Gonen, and David Baker. 2015. "Design of Ordered Two-Dimensional Arrays Mediated by Noncovalent Protein-Protein Interfaces." *Science* 348 (6241): 1365–68.
He, Linling, Natalia de Val, Charles D. Morris, Nemil Vora, Therese C. Thinnes, Leopold Kong, Parisa Azadnia, et al. 2016. "Presenting Native-like Trimeric HIV-1 Antigens with Self-Assembling Nanoparticles." *Nature Communications* 7 (June): 12041.
Hsia, Yang, Jacob B. Bale, Shane Gonen, Dan Shi, William Sheffler, Kimberly K. Fong, Una Nattermann, et al. 2016. "Design of a Hyperstable 60-Subunit Protein Icosahedron." *Nature* 535 (7610): 136–39.
Irvine, Darrell J., and Benjamin J. Read. 2020. "Shaping Humoral Immunity to Vaccines through Antigen-Displaying Nanoparticles." *Current Opinion in Immunology* 65 (August): 1–6.
Jardine, Joseph G., Takayuki Ota, Devin Sok, Matthias Pauthner, Daniel W. Kulp, Oleksandr Kalyuzhniy, Patrick D. Skog, et al. 2015. "HIV-1 VACCINES. Priming a Broadly Neutralizing Antibody Response to HIV-1 Using a Germline-Targeting Immunogen." *Science* 349 (6244): 156–61.
Jardine, Joseph, Jean-Philippe Julien, Sergey Menis, Takayuki Ota, Oleksandr Kalyuzhniy, Andrew McGuire, Devin Sok, et al. 2013. "Rational HIV Immunogen Design to Target Specific Germline B Cell Receptors." *Science* 340 (6133): 711–16.
Kaba, Stephen A., Margaret E. McCoy, Tais A. P. F. Doll, Clara Brando, Qin Guo, Debleena Dasgupta, Yongkun Yang, et al. 2012. "Protective Antibody and CD8+ T-Cell Responses to the Plasmodium Falciparum Circumsporozoite Protein Induced by a Nanoparticle Vaccine." *PloS One* 7 (10): e48304.
Kanekiyo, Masaru, Wei Bu, M. Gordon Joyce, Geng Meng, James R. R. Whittle, Ulrich Baxa, Takuya Yamamoto, et al. 2015. "Rational Design of an Epstein-Barr Virus Vaccine Targeting the Receptor-Binding Site." *Cell* 162 (5): 1090–1100.
Kanekiyo, Masaru, Daniel Ellis, and Neil P. King. 2019. "New Vaccine Design and Delivery Technologies." *The Journal of Infectious Diseases* 219 (Suppl_1): S88–96.
Kanekiyo, Masaru, Chih-Jen Wei, Hadi M. Yassine, Patrick M. McTamney, Jeffrey C. Boyington, James R. R. Whittle, Srinivas S. Rao, Wing-Pui Kong, Lingshu Wang, and Gary J. Nabel. 2013. "Self-Assembling Influenza Nanoparticle Vaccines Elicit Broadly Neutralizing H1N1 Antibodies." *Nature* 499 (7456): 102–6.
Karch, Christopher P., Jianping Li, Caroline Kulangara, Sara M. Paulillo, Senthil K. Raman, Sharareh Emadi, Anmin Tan, et al. 2016. "Vaccination with Self-Adjuvanted Protein Nanoparticles Provides Protection against Lethal Influenza Challenge." *Nanomedicine: Nanotechnology, Biology, and Medicine*, September. https://doi.org/10.1016/j.nano.2016.08.030.
Kato, Yu, Robert K. Abbott, Brian L. Freeman, Sonya Haupt, Bettina Groschel, Murillo Silva, Sergey Menis, Darrell J. Irvine, William R. Schief, and Shane Crotty. 2020. "Multifaceted Effects of Antigen Valency on B Cell Response Composition and Differentiation In Vivo." *Immunity* 53 (3): 548–63.e8.
King, Neil P., Jacob B. Bale, William Sheffler, Dan E. McNamara, Shane Gonen, Tamir Gonen, Todd O. Yeates, and David Baker. 2014. "Accurate Design of Co-Assembling Multi-Component Protein Nanomaterials." *Nature* 510 (7503): 103–8.
King, Neil P., William Sheffler, Michael R. Sawaya, Breanna S. Vollmar, John P. Sumida, Ingemar André, Tamir Gonen, Todd O. Yeates, and David Baker. 2012. "Computational Design of Self-Assembling Protein Nanomaterials with Atomic Level Accuracy." *Science* 336 (6085): 1171–74.
Koff, Wayne C., Dennis R. Burton, Philip R. Johnson, Bruce D. Walker, Charles R. King, Gary J. Nabel, Rafi Ahmed, Maharaj K. Bhan, and Stanley A. Plotkin. 2013. "Accelerating next-Generation Vaccine Development for Global Disease Prevention." *Science* 340 (6136): 1232910.
Koga, Nobuyasu, Rie Tatsumi-Koga, Gaohua Liu, Rong Xiao, Thomas B. Acton, Gaetano T. Montelione, and David Baker. 2012. "Principles for Designing Ideal Protein Structures." *Nature* 491 (7423): 222–27.
Krebs, Shelly J., Sean P. McBurney, Dina N. Kovarik, Chelsea D. Waddell, J. Pablo Jaworski, William F. Sutton, Michelle M. Gomes, et al. 2014. "Multimeric Scaffolds Displaying the HIV-1 Envelope MPER Induce MPER-Specific Antibodies and Cross-Neutralizing Antibodies When Co-Immunized with

gp160 DNA." *PloS One* 9 (12): e113463.
Kuhlman, Brian, Gautam Dantas, Gregory C. Ireton, Gabriele Varani, Barry L. Stoddard, and David Baker. 2003. "Design of a Novel Globular Protein Fold with Atomic-Level Accuracy." *Science* 302 (5649): 1364–68.
Li, Yuanyuan, Darren B. Leneghan, Kazutoyo Miura, Daria Nikolaeva, Iona J. Brian, Matthew D. J. Dicks, Alex J. Fyfe, et al. 2016. "Enhancing Immunogenicity and Transmission-Blocking Activity of Malaria Vaccines by Fusing Pfs25 to IMX313 Multimerization Technology." *Scientific Reports* 6 (January): 18848.
López-Sagaseta, Jacinto, Enrico Malito, Rino Rappuoli, and Matthew J. Bottomley. 2016. "Self-Assembling Protein Nanoparticles in the Design of Vaccines." *Computational and Structural Biotechnology Journal* 14: 58–68.
Marcandalli, Jessica, Brooke Fiala, Sebastian Ols, Michela Perotti, Willem de van der Schueren, Joost Snijder, Edgar Hodge, et al. 2019. "Induction of Potent Neutralizing Antibody Responses by a Designed Protein Nanoparticle Vaccine for Respiratory Syncytial Virus." *Cell* 176 (6): 1420–31.e17.
Mateu, Mauricio G. 2011. "Virus Engineering: Functionalization and Stabilization." *Protein Engineering, Design & Selection: PEDS* 24 (1-2): 53–63.
McGuire, Andrew T., Matthew D. Gray, Pia Dosenovic, Alexander D. Gitlin, Natalia T. Freund, John Petersen, Colin Correnti, et al. 2016. "Specifically Modified Env Immunogens Activate B-Cell Precursors of Broadly Neutralizing HIV-1 Antibodies in Transgenic Mice." *Nature Communications* 7 (February): 10618.
Nabel, Gary J. 2013. "Designing Tomorrow's Vaccines." *The New England Journal of Medicine* 368 (6): 551–60.
Ogun, Solabomi A., Laurence Dumon-Seignovert, Jean-Baptiste Marchand, Anthony A. Holder, and Fergal Hill. 2008. "The Oligomerization Domain of C4-Binding Protein (C4bp) Acts as an Adjuvant, and the Fusion Protein Comprised of the 19-Kilodalton Merozoite Surface Protein 1 Fused with the Murine C4bp Domain Protects Mice against Malaria." *Infection and Immunity* 76 (8): 3817–23.
Ondondo, Beatrice O. 2014. "The Influence of Delivery Vectors on HIV Vaccine Efficacy." *Frontiers in Microbiology* 5 (August): 439.
Rappuoli, Rino, Mariagrazia Pizza, Giuseppe Del Giudice, and Ennio De Gregorio. 2014. "Vaccines, New Opportunities for a New Society." *Proceedings of the National Academy of Sciences of the United States of America* 111 (34): 12288–93.
Schiller, John T., and Douglas R. Lowy. 2015. "Raising Expectations for Subunit Vaccine." *The Journal of Infectious Diseases* 211 (9): 1373–75.
Sliepen, Kwinten, Gabriel Ozorowski, Judith A. Burger, Thijs van Montfort, Melissa Stunnenberg, Celia LaBranche, David C. Montefiori, John P. Moore, Andrew B. Ward, and Rogier W. Sanders. 2015. "Presenting Native-like HIV-1 Envelope Trimers on Ferritin Nanoparticles Improves Their Immunogenicity." *Retrovirology* 12 (September): 82.
Smith, Mark Thomas, Anna K. Hawes, and Bradley Charles Bundy. 2013. "Reengineering Viruses and Virus-like Particles through Chemical Functionalization Strategies." *Current Opinion in Biotechnology* 24 (4): 620–26.
Swadling, Leo, Stefania Capone, Richard D. Antrobus, Anthony Brown, Rachel Richardson, Evan W. Newell, John Halliday, et al. 2014. "A Human Vaccine Strategy Based on Chimpanzee Adenoviral and MVA Vectors That Primes, Boosts, and Sustains Functional HCV-Specific T Cell Memory." *Science Translational Medicine* 6 (261): 261ra153.
Tumban, Ebenezer, Julianne Peabody, David S. Peabody, and Bryce Chackerian. 2011. "A Pan-HPV Vaccine Based on Bacteriophage PP7 VLPs Displaying Broadly Cross-Neutralizing Epitopes from the HPV Minor Capsid Protein, L2." *PloS One* 6 (8): e23310.
———. 2013. "A Universal Virus-like Particle-Based Vaccine for Human Papillomavirus: Longevity of Protection and Role of Endogenous and Exogenous Adjuvants." *Vaccine* 31 (41): 4647–54.
Tumban, Ebenezer, Julianne Peabody, Mitchell Tyler, David S. Peabody, and Bryce Chackerian. 2012. "VLPs Displaying a Single L2 Epitope Induce Broadly Cross-Neutralizing Antibodies against Human Papillomavirus." *PloS One* 7 (11): e49751.
Tyler, Mitchell, Ebenezer Tumban, Agnieszka Dziduszko, Michelle A. Ozbun, David S. Peabody, and Bryce Chackerian. 2014. "Immunization with a Consensus Epitope from Human Papillomavirus L2 Induces Antibodies That Are Broadly Neutralizing." *Vaccine* 32 (34): 4267–74.
Tyler, Mitchell, Ebenezer Tumban, David S. Peabody, and Bryce Chackerian. 2014. "The Use of Hybrid

Virus-like Particles to Enhance the Immunogenicity of a Broadly Protective HPV Vaccine." *Biotechnology and Bioengineering* 111 (12): 2398–2406.

Ueda, George, Aleksandar Antanasijevic, Jorge A. Fallas, William Sheffler, Jeffrey Copps, Daniel Ellis, Geoffrey B. Hutchinson, et al. 2020. "Tailored Design of Protein Nanoparticle Scaffolds for Multivalent Presentation of Viral Glycoprotein Antigens." *eLife* 9 (August). https://doi.org/10.7554/eLife.57659.

Walls, Alexandra C., Brooke Fiala, Alexandra Schäfer, Samuel Wrenn, Minh N. Pham, Michael Murphy, Longping V. Tse, et al. 2020. "Elicitation of Potent Neutralizing Antibody Responses by Designed Protein Nanoparticle Vaccines for SARS-CoV-2." *Cell* 183 (5): 1367–82.e17.

Yassine, Hadi M., Jeffrey C. Boyington, Patrick M. McTamney, Chih-Jen Wei, Masaru Kanekiyo, Wing-Pui Kong, John R. Gallagher, et al. 2015. "Hemagglutinin-Stem Nanoparticles Generate Heterosubtypic Influenza Protection." *Nature Medicine* 21 (9): 1065–70.

Zakeri, Bijan, Jacob O. Fierer, Emrah Celik, Emily C. Chittock, Ulrich Schwarz-Linek, Vincent T. Moy, and Mark Howarth. 2012. "Peptide Tag Forming a Rapid Covalent Bond to a Protein, through Engineering a Bacterial Adhesin." *Proceedings of the National Academy of Sciences of the United States of America* 109 (12): E690–97.

Zhao, Qinjian, Shaowei Li, Hai Yu, Ningshao Xia, and Yorgo Modis. 2013. "Virus-like Particle-Based Human Vaccines: Quality Assessment Based on Structural and Functional Properties." *Trends in Biotechnology* 31 (11): 654–63.

Zhou, Tongqing, Jiang Zhu, Yongping Yang, Jason Gorman, Gilad Ofek, Sanjay Srivatsan, Aliaksandr Druz, et al. 2014. "Transplanting Supersites of HIV-1 Vulnerability." *PloS One* 9 (7): e99881.

Chapter 5: Biochemical, biophysical and immunogenic analysis of stabilizing mutations to the SARS-CoV-2 receptor binding domain

Summary

Improvements to the complete product profiles of promising SARS-CoV-2 vaccine candidates will be vital for the global distribution of effective vaccines in the midst and aftermath of the current pandemic. Immunogens based on the SARS-CoV-2 spike receptor binding domain (RBD) have shown promising potent immunogenicity and are being considered as second generation vaccine candidates. Here, based on a previously reported deep mutational scanning (DMS) study of the RBD, we designed and characterized stabilizing mutations in the context of SARS-CoV-2 vaccines, both for trimeric and nanoparticle-based RBD immunogens. Two stabilized RBD designs were selected from experimental screening as leading candidates, which both provided greatly improved expression yields in addition to enhanced thermal stability and resistance to aggregation, particularly in the context of nanoparticle immunogens. Both designs were shown to be immunogenically equivalent to immunogens based on the wildtype RBD, suggesting that stabilizing mutations to the RBD can be viably included in future RBD-based vaccines to assist manufacturability.

Introduction

The response of rapid vaccine design and development to the 2020 SARS-CoV-2 pandemic continues to be a massive test of modern vaccinology, as well as scalable vaccine manufacturing and distribution. Previous prototyping of preclinical vaccines against coronaviruses such as MERS-CoV and SARS-CoV-1 was vital for mounting such a fast response (Corbett et al. 2020; Pallesen et al. 2017; van Doremalen et al. 2020), emphasizing the importance of continued refinement of vaccines against possible viral threats. In considering future endemic and pandemic threats from SARS-CoV-2 and other coronaviruses, the ability to reliably design, maximally produce and widely distribute vaccines against any threatening coronavirus is a high priority, with ample room to improve the complete product profiles of existing vaccines against SARS-CoV-2 (Morens and Fauci 2020).

Vaccines against SARS-CoV-2 most frequently target the spike protein (S), which is a homotrimeric class I viral fusion protein (Krammer 2020; Huang et al. 2020). The S protomer is split into two key regions, S1 and S2, with S1 characterized by separated N- and C-terminal domains responsible for both receptor binding and suppressing conformational changes, and S2 containing metastable fusion machinery (Hoffmann et al. 2020; Walls, Park, et al. 2020; Wrapp et al. 2020). SARS-CoV-2 uses the C-terminal receptor binding domain (RBD) within S1 to bind to host cells using the ACE2 receptor, while other coronaviruses have shown multiple ways of recognizing diverse host receptors using either domain in S1 (Letko, Marzi, and Munster 2020; Kuhn et al. 2004; Zhou et al. 2020). The S antigen, whether studied as a whole trimer or in terms of individual domains, has been widely considered the most valuable target for protective antibody responses against coronaviruses (Buchholz et al. 2004; Corti et al. 2015; Pallesen et al. 2017). When considered as a complete ectodomain, maintenance of S trimers in their prefusion state is seen to be important for eliciting neutralizing antibody responses (Pallesen et al. 2017; Graham, Gilman, and McLellan 2019; Mercado et al. 2020), with many current clinical candidates utilizing stabilizing mutations that help favor this conformation (Keech et al. 2020;

Jackson et al. 2020; Polack et al. 2020; Krammer 2020). Even with stabilizing mutations, protein-based immunogens containing the full S trimeric ectodomain can suffer from limitations to stability and expression, which can particularly limit the development and scalability of protein-based vaccines (Hsieh et al. 2020).

An antigenic alternative to complete S trimeric ectodomains for vaccine development for SARS-CoV-2 and other coronaviruses is the isolated RBD, with the majority of neutralizing antibody responses against SARS-CoV-2 targeting this confined portion of S and often blocking ACE2 binding (Piccoli et al. 2020; Barnes et al. 2020; Brouwer et al. 2020; Liu et al. 2020; Robbiani et al. 2020; Seydoux et al. 2020; Tortorici et al. 2020; Wang et al. 2020; Wu et al. 2020). When expressed alone, monomeric RBDs are much less structurally heterogeneous compared with the metastable S ectodomain, and naturally support far higher expression yields (Walls, Fiala, et al. 2020). RBD-based vaccines have been investigated as genetic or protein-based vaccines when presented in various reengineered oligomeric states, including dimers (Dai et al. 2020), trimers (Mulligan et al. 2020) and highly valent nanoparticles (Walls, Fiala, et al. 2020; Cohen et al., 2020), with at least one candidate already clinically studied and others being investigated as second generation candidates. While the RBD is much smaller than S and could be more susceptible to escape mutations when targeted alone, simultaneous elicitation of responses against diverse epitopes on the RBD has been demonstrated by infection, clinical vaccines and preclinical vaccines, which could hedge against this possible downside (Piccoli et al. 2020; Walls, Fiala, et al. 2020; Sahin et al. 2020). RBDs from diverse coronaviruses have been confirmed to be capable of eliciting neutralizing responses against matched viruses (Dai et al. 2020), in all confirming the importance of this domain for targeted inclusion in future coronavirus vaccines.

Previous studies have identified mutations to the SARS-CoV-2 RBD that can greatly assist expression and stability of this domain (Starr et al. 2020). Such mutations have potential to maximize the impact of RBD-based vaccines by streamlining scalable manufacturing and distribution, but have not yet been studied in the context of vaccines. Here, we further explore and refine the design of stabilizing mutations to the RBD in the context of immunogens. Stabilizing mutations were found to assist the thermal and solution stabilities of RBD-containing immunogens, most particularly when displayed in oligomeric formats, while not impacting their established potent immunogenicity.

Results

As described in a referenced publication by Starr and Greaney et al. (Starr et al. 2020), deep mutational scanning (DMS) of the RBD was performed using yeast display to assess the effects of all possible mutations on expression levels and ACE2 affinity. To validate the results of this assay's analysis on expression levels, five RBD mutants were recloned for production as soluble monomers with affinity tags and secreted from HEK293F cells. As assessed by SDS-PAGE, expression levels were confirmed to be significantly higher for all five mutants, with equivalent yields maintained after immobilized metal affinity chromatography (IMAC) purification and centrifugal concentration (**Figure 5.1A**). Size exclusion chromatography (SEC) of IMAC eluates was used to quantify recovery yields from expression and purification (**Figure 5.1B**), which revealed relative yields of monomeric and dimeric disulfide-linked species (**Figure 5.1B-C**). The studied mutations ranged from ~2x to ~4.5x higher recovery compared to the

wildtype RBD, with all mutations except F392W increasing the relative recovery of disulfide-linked dimeric species. All mutants were measured for qualitative binding to ACE2 and the antibody CR3022 (Yuan et al. 2020) using biolayer interferometry (**Figure 5.1D**). Binding was seen to both by all mutations, although kinetics appeared slightly altered for binding to CR3022. Thermal stabilities of all mutants was measured using nano-differential scanning fluorimetry (nano-DSF) (**Figure 5.1E,F**), showing increases in melting temperatures (Tm) relative to wildtype for all mutations except Y365F.

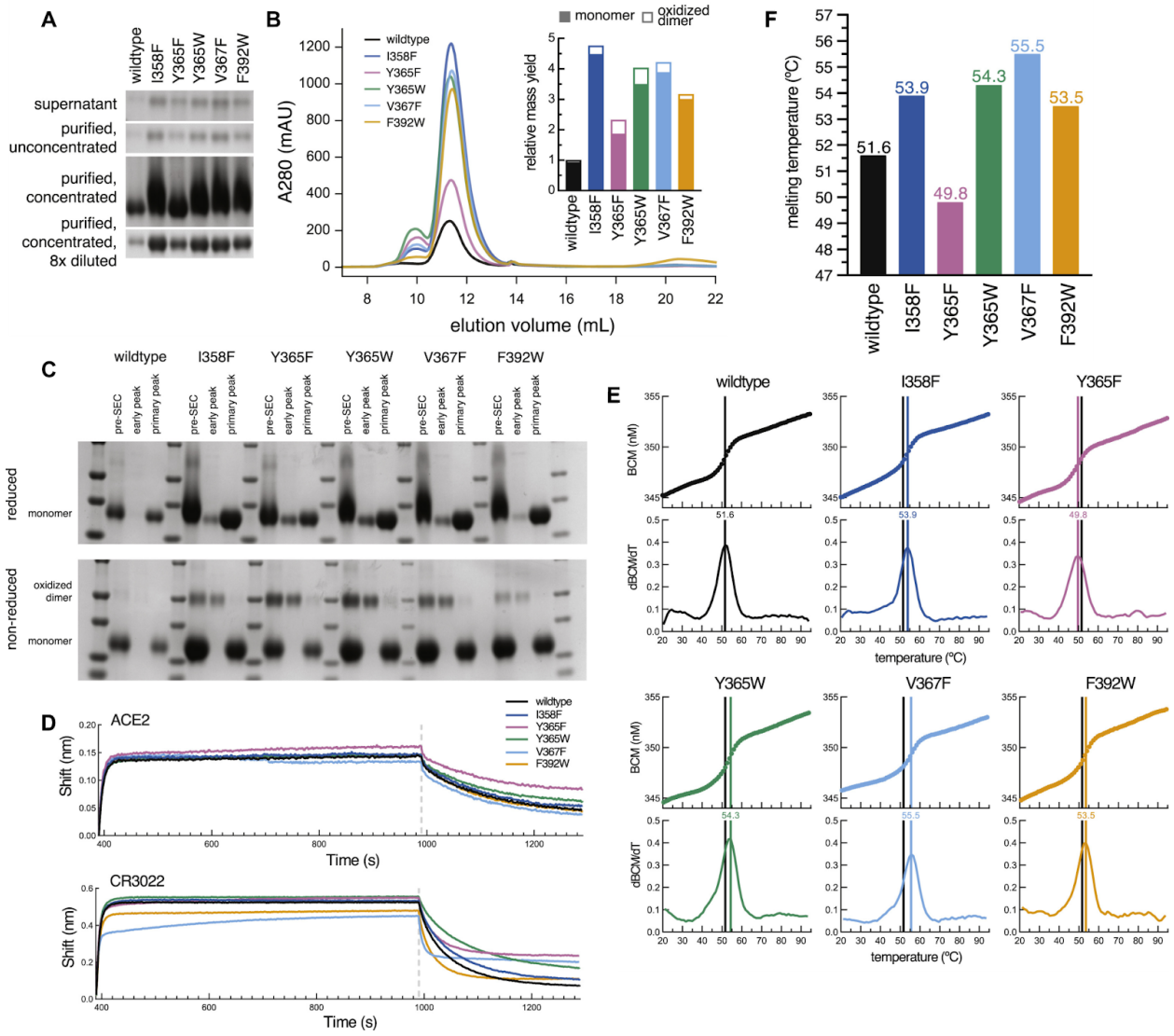

Figure 5.1: Experimental analysis of effects of individual stabilizing mutations to the SARS-CoV-2 RBD. **A)** Reducing SDS-PAGE of supernatants and IMAC eluates used to respectfully express and purify wildtype and mutant RBDs. **B)** SEC analysis of IMAC eluates to assess relative yields of wildtype and mutant RBDs. Inset shows relative mass yields compared to wildtype RBDs, with monomers and oxidized dimers quantified based on the integration of distinct peaks present. **C)** Reducing and non-reducing SDS-PAGE of wildtype and mutant RBD IMAC eluates before and after SEC. **D)** BLI of purified monomeric RBDs binding to immobilized ACE2 receptor and CR3022 antibody. **E)** Nano-DSF measuring the barycentric mean (BCM) of intrinsic tryptophan fluorescence. Melting temperatures were calculated

based on the maximum point of the smoothed first derivative. **F)** Quantitative values for melting temperatures.

Given that many studied vaccines are based on the RBD and there is a need for maximal scalable manufacturing and distribution of vaccines against SARS-CoV-2, we sought out to further refine mutations that are optimal for use SARS-CoV-2 vaccines and investigate such vaccines immunogenically. All mutations were structurally analyzed using PyMol and modelling in Rosetta using a cryo-EM structure of the complete S ectodomain (PDB ID 6VXX). With the exception of V367F, all mutations were observed to be hidden from solvent, which lowers the risk of unfavorable alterations to antigenicity. All mutations were observed to be near or within a recently-identified site that can bind linoleic acid (Toelzer et al. 2020; Bangaru et al. 2020), with Y365 identified as a key gating residue for this interaction and many other mutations involved in binding the lipid (**Figure 5.2C-E**). Rosetta calculations showed that, despite assisting stabilization and expression, the Y365W mutation carries a strong chance of introducing steric clashes in the context of the RBD in the full S ectodomain (data not shown). In combination with conformational changes observed in structures of S binding linoleic acid and crystal structures of other RBD complexes (Huo et al. 2020; Lan et al. 2020), plasticity of the backbone in this region was inferred.

While the individual mutants offered healthy increases in expression and stability, it is possible that combinations of mutations could further improve such properties. Rosetta protocols were developed that modelled one or more of I358F, Y365F, Y365W and/or F392W while allowing for nearby residues to also be mutated based on Rosetta's design algorithms. Design trajectories were also set up to redesign this region without forced inclusion of these four valuable mutations. To account for backbone plasticity, the developed protocols were assessed with and without movement allowed to the backbones surrounding the mutations, and were further assessed both in the context of the complete S ectodomain (PDB ID 6VXX) and a high resolution crystal structure of an RBD monomer (PDB ID 6YZ5). Seventeen repacked designs (abbreviated as "Rpk") that appeared structurally promising by filling of cavities and/or removal of buried polar groups were selected for experimental analysis, with some of the previously-studied individual mutations also included (**Figure 5.2B**). To prepare for testing in the context of RBD-based vaccines, designs were screened in the context of genetic fusion to the I53-50A nanoparticle trimeric component which can be incorporated into a studied RBD nanoparticle vaccine candidate (Walls, Fiala, et al. 2020). Repacked RBD amino acid sequences were therefore cloned in a vector for mammalian expression with the I53-50A sequence C-terminally appended and the two sequences joined by a 16-residue flexible Gly-Ser linker.

Designs were secreted in small scale from HEK293F cells alongside a comparable construct with a wildtype RBD. Supernatants were analyzed by reducing and non-reducing SDS-PAGE which showed increased expression for all constructs compared to wildtype (**Figure 5.2A**). Increased expression and antigenic intactness was additionally confirmed by greatly increased binding measured from supernatants to ACE2 and CR3022 by all designs (data not shown). Non-reducing SDS-PAGE also showed differences in amounts of disulfide-linked dimers present in each sample (**Figure 5.2A**), which have previously been observed for the genetic fusion of RBDs to I53-50A and are likely formed within RBDs of the same trimer.

Designs including the F392W mutation were observed to contain noticeably lower levels of disulfide-linked dimers, which is consistent with previous analysis of individual mutations to monomeric RBDs that also showed decreased presence of dimeric species (**Figure 5.1B-C**). Given the close proximity of this mutation to the disulfide between residues 391 and 525 (**Figure 5.2E**), the mutation likely disfavors off-target formation of this disulfide between different RBDs.

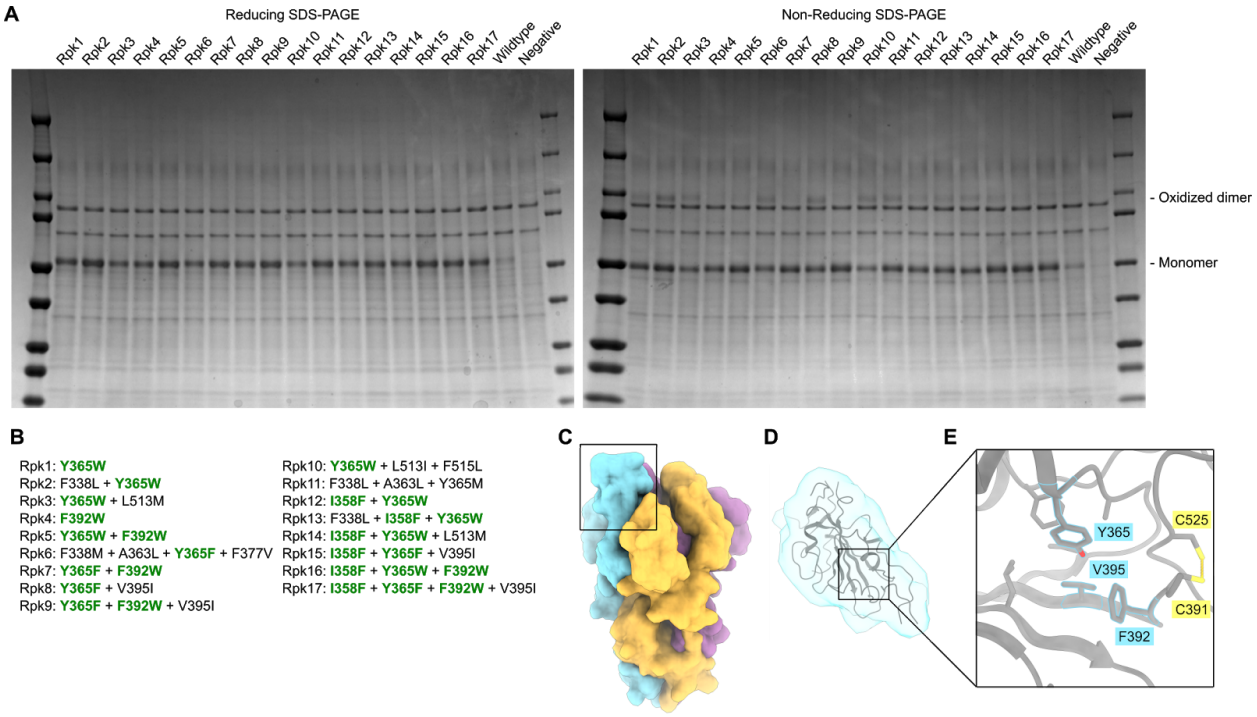

Figure 5.2: Screening of stabilized RBDs that include combinations of mutations. **A)** Reducing and non-reducing SDS-PAGE analysis of supernatants used to express designed repacked RBD ("Rpk") variants genetically fused to the I53-50A trimeric nanoparticle component. The wildtype control contains no mutations to the RBD, and the negative control uses a plasmid that does not encode for any secreted protein. Migration of monomeric and oxidized dimeric species are marked. **B)** List of mutations included in all constructs. Mutations listed in green were previously validated alone in Starr et al. 2020. **C)** Surface representation of the SARS-CoV-2 spike protein based on PDB-ID 6VYB, with the box highlighting the RBD. **D)** Cartoon chain and transparent surface representation of the SARS-CoV-2 RBD. **E)** Zoom-in on the region of the SARS-CoV-2 receptor binding domain that contains most designed mutations.

Since minimal covalent heterogeneity would be preferred for vaccine candidates, three designs containing F392W (Rpk4, Rpk5 and Rpk9) were scaled-up for more detailed analysis. Rpk4 only contained F392W, while Rpk5 additionally contained Y365W and Rpk9 contained Y365F and V395I, with mutations in both cases removing the nonideal buried polar group of Y365. Mutant RBD-I53-50A trimers (Rpk4-RBD-I53-50A, Rpk5-RBD-I53-50A and Rpk9-RBD-I53-50A) were purified by IMAC and SEC, and subsequently assembled as nanoparticles (Rpk4-RBD-I53-50, Rpk5-RBD-I53-50 and Rpk9-RBD-I53-50) by addition of a complementary pentameric I53-50B component with excess remaining components removed with an additional SEC step and particle formation confirmed by negative stain electron

microscopy (**Figure 5.3A**). I53-50 nanoparticles displaying RBDs have previously been characterized to require particular excipients to remain nanoparticle solubility, with combinations of glycerol, arginine and 3-[(3-cholamidopropyl)dimethylammonio]-1-propanesulfonate detergent (CHAPS) previously used. Nanoparticle samples for all three designs were dialyzed into buffered solutions with varied excipients to measure solution behaviors as measured by UV-Vis before and after a freeze-thaw cycle, with scattering qualitatively watched as a sign of aggregation (**Figure 5.3B**). All samples showed suitable solubility before and after freeze-thaw in Tris-buffered saline (TBS) supplemented with glycerol, arginine and CHAPS. In the presence of TBS alone, all nanoparticle samples showed significant signs of scattering, particularly after freezing, although spectra shape was better maintained before freeze-thaw in Rpk4-RBD-I53-50 and Rpk9-RBD-I53-50. Addition of 100mM arginine to TBS improved all samples though still with signs of scattering, which was most particularly worse for Rpk5-RBD-I53-50. Addition of both 100mM arginine and 5% glycerol allowed for healthy spectra for Rpk4-RBD-I53-50 and Rpk9-RBD-I53-50 samples that were indistinguishable before and after freeze-thaw, with significant scattering still observed for Rpk5-RBD-I53-50. Therefore, while the Y365W mutation included in the Rpk5 design has been helpful for expression and thermal stability, it appears deleterious to the solution stability of the I53-50 nanoparticle scaffold displaying RBDs.

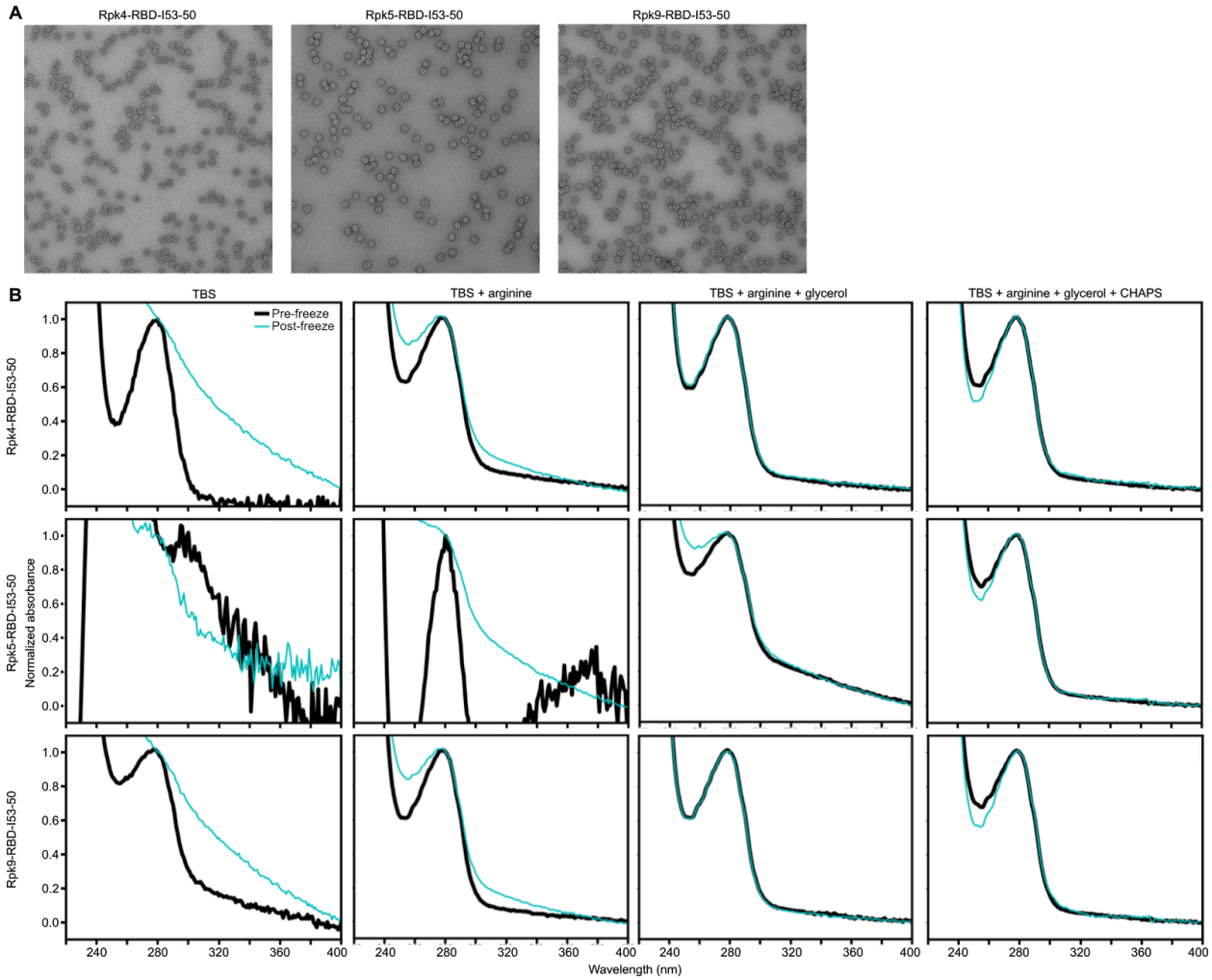

Figure 5.3: Assembly and solution stability of I53-50 nanoparticle immunogens displaying stabilized SARS-CoV-2 RBDs. **A)** Negative stain electron micrographs of Rpk4, Rpk5 and Rpk9 RBD designs displayed separately on I53-50 nanoparticles. **B)** UV-Vis spectra of Rpk4, Rpk5 and Rpk9 RBD designs displayed separately on I53-50 nanoparticles after dialysis into different buffer conditions, before (black) and after a freeze-thaw (blue) cycle. “TBS” refers to 50mM Tris pH 8.0, 150mM NaCl. “TBS + arginine” refers to 50mM Tris pH 8.0, 150mM NaCl, 100mM arginine. “TBS + arginine + glycerol” refers to 50mM Tris pH 8.0, 150mM NaCl, 100mM arginine, 5% glycerol. “TBS + arginine + glycerol + CHAPS” refers to 50mM Tris pH 7.0, 185mM NaCl, 100mM arginine, 4.5% glycerol, 0.75% CHAPS

Next, the physical stabilities of the stabilized Rpk4 and Rpk9 RBDs were compared to the wildtype RBD using hydrogen-deuterium exchange mass spectrometry (HDX-MS), nano-DSF, and static light scattering (SLS). All experiments were performed on wildtype and stabilized RBDs in the context of genetic fusions to I53-50A trimers. Relative to the wildtype RBD fusion (WT-RBD-I53-50A), HDX-MS showed increased local stability in two beta strands adjacent to the mutations in Rpk4-I53-50A and Rpk9-I53-50A, with a slightly stronger stabilizing effect observed for Rpk9 (**Figure 5.4A**). Tms were increased for both stabilized constructs as measured by nano-DSF, with a 2.0°C increase for Rpk4-RBD-I53-50A and a 4.5°C increase for Rpk9-RBD-I53-50A (**Figure 5.4B**). SLS measured over a temperature gradient showed clear

induction of aggregation for WT-RBD-I53-50A, however no measured aggregation for both Rpk4-RBD-I53-50A and Rpk9-RBD-I53-50A at both 266nm and 473nm (**Figure 5.4C-D**). In all, clear advantages in thermal stability were demonstrated for stabilized RBDs.

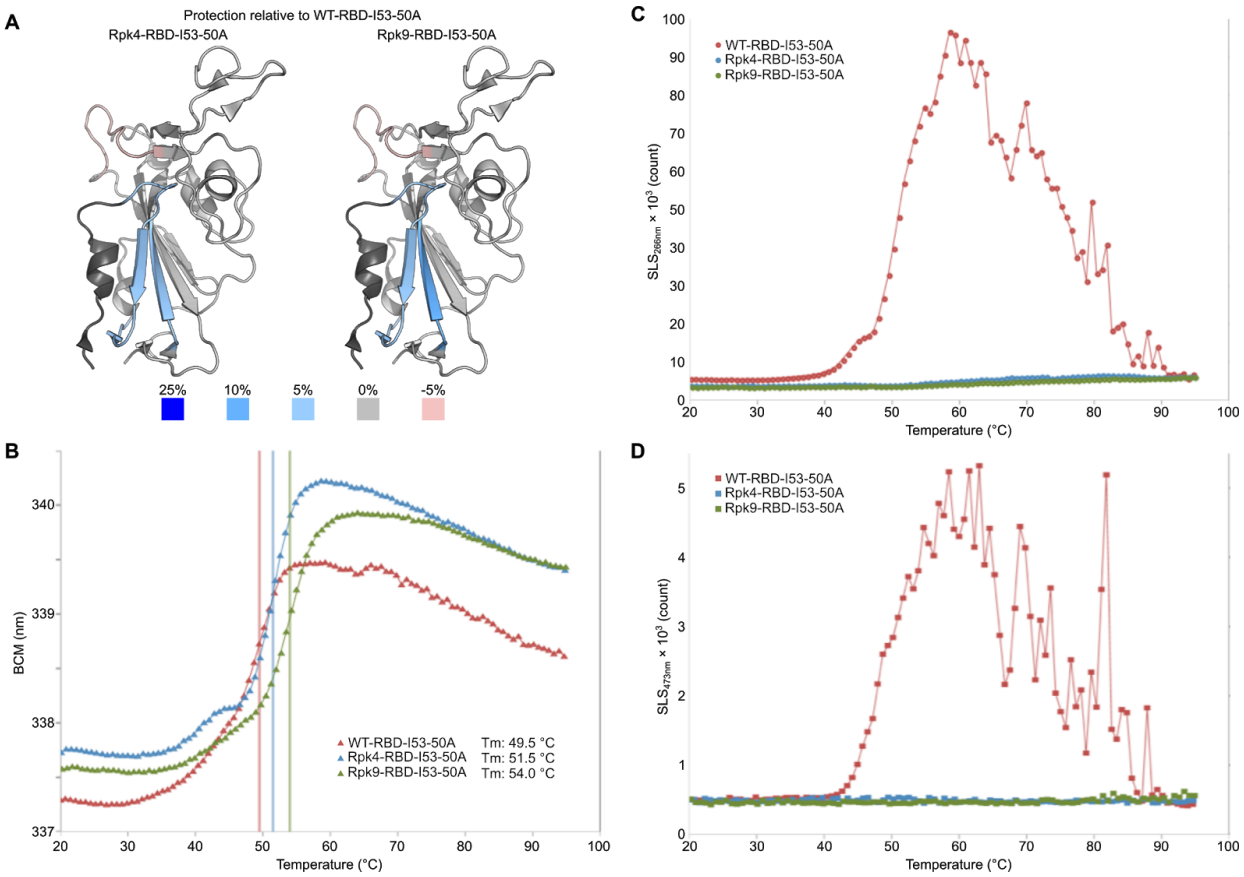

Figure 5.4: Hydrogen-deuterium exchange mass spectrometry (HDX-MS) and thermal stabilities of Rpk4 and Rpk9 RBD designs compared to wildtype RBD. **A)** Local stabilities of peptides in Rpk4 and Rpk9 genetically fused to I53-50A trimeric nanoparticle components as measured by HDX. Stability measured is relative to wildtype RBD genetically fused to I53-50A trimeric nanoparticle component, with data shown after 20hrs of exposure to deuterated water. **B)** Nano-DSF of wildtype, Rpk4 and Rpk9 RBDs genetically fused to I53-50A trimeric nanoparticle component measuring the barycentric mean (BCM) of intrinsic tryptophan fluorescence. Melting temperatures were calculated based on maximum points of first derivatives as calculated using UNcle analysis software. **C)** SLS from 266nm of wildtype, Rpk4 and Rpk9 RBDs genetically fused to I53-50A trimeric nanoparticle components measured over a temperature gradient. **D)** SLS from 273nm of wildtype, Rpk4 and Rpk9 RBDs genetically fused to I53-50A trimeric nanoparticle components measured over a temperature gradient.

Finally, the immunogenicity of stabilized RBDs was studied in mice. The wildtype RBD and stabilized RBDs were prepared in two formats: nanoparticles of RBD-I53-50A fusions assembled with the I53-50B component, and “unassembled controls” in which the trimer RBD-I53-50A fusion is mixed with a comparable pentameric scaffold that lacks the hydrophobic interface which drives assembly (“2OBX”) (Klinke et al. 2007). This comparison allows for study of the immunogenicity of different RBDs in trimeric and nanoparticle contexts, while also

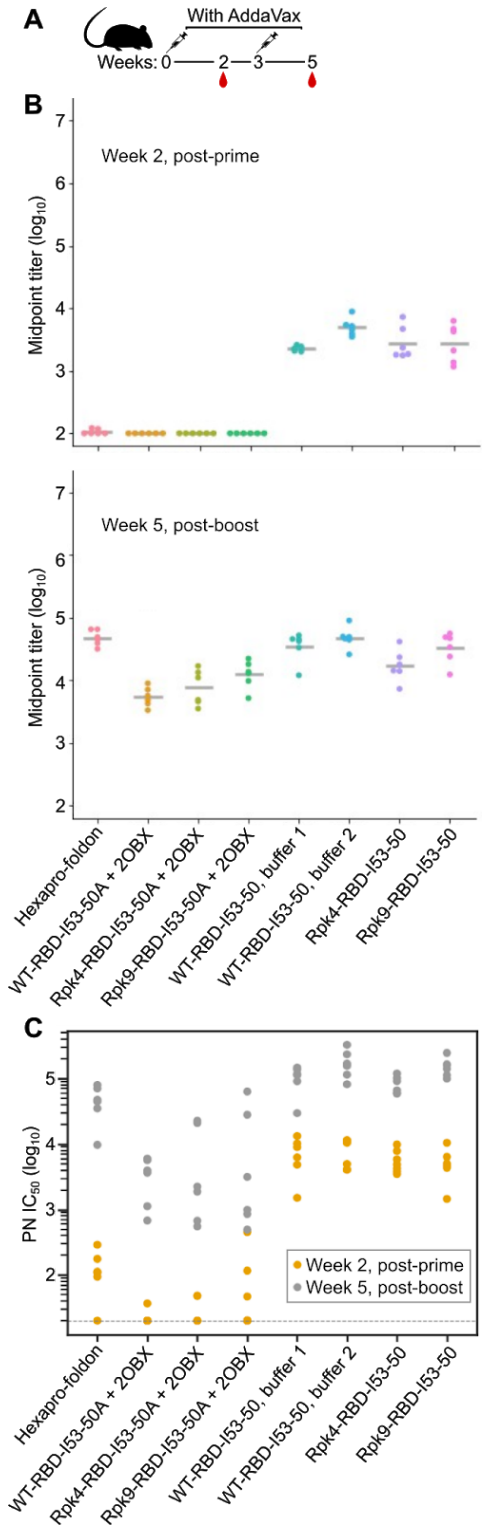

allowing for understanding of effects of nanoparticle assembly. All stabilized RBD-I53-50 immunogens were prepared in TBS supplemented with 100mM arginine and 5% glycerol, while the WT-RBD-I53-50 nanoparticle was also prepared in a buffer that further contains CHAPS to ensure proper solubility given that WT-RBD-I53-50 is not perfectly soluble with just 100mM arginine and 5% glycerol as excipients (data not shown). The “hexapro” prefusion-stabilized S antigen fused to T4 foldon (Hexapro-foldon) was included as a generally comparative control (Hsieh et al. 2020). Female BALB/c mice were immunized twice with each immunogen, with serum collection two weeks after each immunization (**Figure 5.5A**). All doses were administered in equimolar amounts of RBD with AddaVax adjuvant.

Binding titers were measured against Hexapro-foldon using enzyme-linked immunosorbent assays (ELISA), with all nanoparticle groups showing comparable signal after the prime and all other groups showing lower and negligible signal (**Figure 5.5B**). Binding signal increased for all groups after a boost with less separation between groups. Pseudovirus neutralization (PN) showed similar trends after the prime with a notable dominance by all nanoparticle groups (**Figure 5.5C**). PN strongly increased for all groups after a boost, with all nanoparticles and Hexapro-foldon showing the strongest signals. All nanoparticle groups showed comparable PN signals at both time points, while all unassembled controls showed lower signals that were comparable within that subset. In all, stabilized RBDs were found to be similarly immunogenic to the wildtype RBD when presented in both trimeric and particulate formats, with nanoparticle presentation shown to be vital for maximizing the immunogenicity of RBDs.

Figure 5.5: Immunogenicity of stabilized RBDs presented as trimers or nanoparticles. Female BALB/c mice (N=6 per group) were immunized twice with stabilized SARS-CoV-2 spike fused to the foldon trimerization domain (“hexapro-foldon”), nanoparticles displaying different RBD versions, or unassembled controls of the trimeric RBD-I53-50A fusions mixed with the “2OBX” pentamer that lacks the hydrophobic interface which drives nanoparticle assembly. “buffer 1” refers to 50mM Tris pH 7.0, 185mM NaCl, 100mM Arginine, 4.5% glycerol, 0.75% CHAPS while “buffer 2” refers to 50mM Tris pH 8.0, 150mM NaCl, 100mM Arginine, 5% glycerol. All immunizations used Addavax as adjuvant and administered equimolar amounts of SARS-CoV-2 RBD, with 5ug of hexapro-foldon and

0.88ug of total protein for all other groups used in each immunization. **A)** Immunization schedule in mice, with immunizations on weeks 0 and 3 with serum collection on weeks 2 and 5. **B)** Midpoint ELISA binding titers against hexapro-foldon measured at weeks 2 and 5. **C)** Pseudovirus neutralization (PN) titers measured at weeks 2 and 5. Values plotted are serum dilutions for which 50% of cell entry by pseudoviruses was blocked.

Discussion

Structure-based protein design strategies can be greatly assisted by detailed information that narrows the explorable sequence space to particularly valuable areas. Here, we demonstrate the direct applicability of DMS results to glycoprotein stabilization, with DMS results providing a clear focus on locations and identities of possible mutations and structural modeling in Rosetta further expanding this space. The success rate of tested designs with successfully increased expression was abnormally high compared to many other purely structure-based design experiments. This is due in part to the obviousness of DMS results, and in this case likely also to inferred conformational plasticities of the studied region of the RBD. Through detailed experimental characterization of RBDs presented as trimers or nanoparticles, narrowing criteria was used to select designs that improved expression, minimized off-target disulfides, improved solution behavior to minimize aggregation, and increased Tms all while maintaining equivalent immunogenicity to immunogens based on wildtype RBDs. Of the studied mutation sets, Rpk4 (F392W) is simpler due to its singular nature, but less stabilizing compared to Rpk9 (Y365F, F392W, V395I) which includes additional mutations which were shown particularly to improve thermal stability. Looking forward, this simple study strongly suggests that DMS has untapped promise as a broader tool for identifying stabilizing mutations in diverse glycoprotein antigens.

The similar immunogenicity observed between wildtype and stabilized RBD immunogens is not surprising, as the studied mutations are not expected to favor any advantageous conformation or alter surface immunogenicity. Beyond demonstrating this equivalence, the immunogenicity results shown here have implications for all forms of RBD-based immunogens, whether smaller oligomers or larger particles. Highly valent nanoparticle-based RBD immunogens are clearly far more immunogenic than comparable trimeric forms of RBDs, and offer a notable advantage from prime immunizations. While particulate presentation of the RBD outperforms trimeric spike alone, presentation of the RBD on a general trimeric scaffold is not as strongly neutralizing. This clarifies that removing the RBD from the spike may not be inherently advantageous compared to equally oligomeric antigens with complete S ectodomains, and emphasizes the particular advantage in potency given to highly valent nanoparticle-based RBD immunogens.

While the stabilizing mutations are not expected to impact the efficacy of RBD-based vaccines, they have particular properties that could assist modern challenges in scalable vaccine manufacturing and distribution. The greatly improved expression of stabilized RBDs could directly impact production bottlenecks of protein-based SARS-CoV-2 vaccines. It is possible that future SARS-CoV-2 vaccines will require updates to included strains due to antigenic drift, in which case such improvements to expression could be crucial for maximizing the scale of production. Improved thermal stability and resistance to aggregation could be particularly impactful for more reliable distribution, particularly in less developed countries. Finally, as we consider the possibility of future viral introductions to the human population, the

ability to reliably improve vaccine manufacturability using stabilizing mutations to this region of the RBD can inspire optimized vaccine designs against other coronaviruses, most notably the ever-threatening sarbecovirus family.

Contributors and acknowledgements
I would like to thank Brooke Fiala, Natalie Brunette, Minh Pham, Kate Crawford, Karla-Luise Herpoldt, Chengbo Chen, Tyler Starr, Jesse Bloom and Neil P. King for their leadership and extensive contributions to this project. I would also like to thank Jake Kraft, Mike Murphy, Deleah Pettie, Lauren Carter and Kelly Lee for direct contributions to this project.

Materials and Methods

Expression-enhancing mutant RBD purifications
Codon-optimized RBDs of SARS-CoV-2 with its unmutated sequence or with single mutations (I358F, Y365F, Y365W, V367F or F392W) were synthesized by IDT as gBlocks with an N-terminal EGT secretion signal (MGILPSPGMPALLSLVSLLSVLLMGCVA) and C-terminal Avi- and octa-histidine tags (GLNDIFEAQKIEWHEHHHHHHHHH) and cloned into the CMV/R (VRC 8400) mammalian expression vector. Plasmids were transfected into 200mL suspension Expi293F cells at 37°C in a humidified 8% CO2 incubator rotating at 130 rpm and harvested 3 days later. Clarified supernatants were purified in batch over Talon resin (Takara). After elution at 125mL in 20mM Tris pH 8.0, 300mM NaCl, 300mM imidazole, concentrated solutions of L-arginine (pH 8.0), CHAPS and glycerol were added to eluate to final concentrations of 100mM, 0.75%, and 5%, respectively, to prevent adhesion to concentrator membranes. To quantify yield, each sample was concentrated to a final volume of 1500uL, and 1000uL was applied to a Superdex 75 Increase 10/300 GL column (GE) pre-equilibrated with 50mM Tris pH 8.0, 185mM NaCl, 100mM L-arginine, 0.75% CHAPS and 5% glycerol. Peak integration was quantified using UNICORN software (GE), and relative quantity from the SEC trace was corrected for unique extinction coefficients and molecular weights of each RBD mutant. Purified peaks from monomeric species were dialyzed three times into 25mM Tris (pH 8.0), 150mM NaCl and 5% glycerol at 4°C.

Biolayer interferometry
BLI binding assays were performed on an Octet Red instrument at 25°C with shaking at 1,000 RPM in the presence of 25mM Tris pH 8.0, 150mM NaCl and 5% glycerol. Anti-hIgG Capture (AHC) tips were loaded with human ACE2-Fc or CR3022 at 0.02mg/mL for 300s prior to a baseline for 60s, association with monomeric RBDs at 500nM for 600s, and dissociation for 300s.

Thermal denaturation and melting point calculations
Non-equilibrium measurements of melting temperatures were determined from thermal denaturation melt curves using an UNcle (UNchained Labs) based on the barycentric mean of intrinsic tryptophan fluorescence, with data collected from 20-95°C using a thermal ramp of 1°C per minute in a background of 25mM Tris pH 8.0, 150mM NaCl and 5% glycerol. Melting temperatures were defined as the maximum point of the first derivative of the melting curve, with

first derivatives calculated using GraphPad Prism software after smoothing with four neighboring points using 2nd order polynomial settings.

References

Bangaru, Sandhya, Gabriel Ozorowski, Hannah L. Turner, Aleksandar Antanasijevic, Deli Huang, Xiaoning Wang, Jonathan L. Torres, et al. 2020. “Structural Analysis of Full-Length SARS-CoV-2 Spike Protein from an Advanced Vaccine Candidate.” *Science* 370 (6520): 1089–94.

Barnes, Christopher O., Anthony P. West Jr, Kathryn E. Huey-Tubman, Magnus A. G. Hoffmann, Naima G. Sharaf, Pauline R. Hoffman, Nicholas Koranda, et al. 2020. “Structures of Human Antibodies Bound to SARS-CoV-2 Spike Reveal Common Epitopes and Recurrent Features of Antibodies.” *Cell* 182 (4): 828–42.e16.

Brouwer, Philip J. M., Tom G. Caniels, Karlijn van der Straten, Jonne L. Snitselaar, Yoann Aldon, Sandhya Bangaru, Jonathan L. Torres, et al. 2020. “Potent Neutralizing Antibodies from COVID-19 Patients Define Multiple Targets of Vulnerability.” *Science* 369 (6504): 643–50.

Buchholz, Ursula J., Alexander Bukreyev, Lijuan Yang, Elaine W. Lamirande, Brian R. Murphy, Kanta Subbarao, and Peter L. Collins. 2004. “Contributions of the Structural Proteins of Severe Acute Respiratory Syndrome Coronavirus to Protective Immunity.” *Proceedings of the National Academy of Sciences of the United States of America* 101 (26): 9804–9.

Cohen, Alexander A., Priyanthi N. P. Gnanapragasam, Yu E. Lee, Pauline R. Hoffman, Susan Ou, Leesa M. Kakutani, Jennifer R. Keeffe, et al. n.d. “Neutralization of SARS-CoV-2 and Zoonotic Coronavirus Threats by Mosaic Nanoparticle Vaccination.” https://doi.org/10.1101/2020.11.17.387092.

Corbett, Kizzmekia S., Darin K. Edwards, Sarah R. Leist, Olubukola M. Abiona, Seyhan Boyoglu-Barnum, Rebecca A. Gillespie, Sunny Himansu, et al. 2020. “SARS-CoV-2 mRNA Vaccine Design Enabled by Prototype Pathogen Preparedness.” *Nature* 586 (7830): 567–71.

Corti, Davide, Jincun Zhao, Mattia Pedotti, Luca Simonelli, Sudhakar Agnihothram, Craig Fett, Blanca Fernandez-Rodriguez, et al. 2015. “Prophylactic and Postexposure Efficacy of a Potent Human Monoclonal Antibody against MERS Coronavirus.” *Proceedings of the National Academy of Sciences of the United States of America* 112 (33): 10473–78.

Dai, Lianpan, Tianyi Zheng, Kun Xu, Yuxuan Han, Lili Xu, Enqi Huang, Yaling An, et al. 2020. “A Universal Design of Betacoronavirus Vaccines against COVID-19, MERS, and SARS.” *Cell* 182 (3): 722–33.e11.

Doremalen, Neeltje van, Elaine Haddock, Friederike Feldmann, Kimberly Meade-White, Trenton Bushmaker, Robert J. Fischer, Atsushi Okumura, et al. 2020. “A Single Dose of ChAdOx1 MERS Provides Protective Immunity in Rhesus Macaques.” *Science Advances* 6 (24): eaba8399.

Graham, Barney S., Morgan S. A. Gilman, and Jason S. McLellan. 2019. “Structure-Based Vaccine Antigen Design.” *Annual Review of Medicine* 70 (January): 91–104.

Hoffmann, Markus, Hannah Kleine-Weber, Simon Schroeder, Nadine Krüger, Tanja Herrler, Sandra Erichsen, Tobias S. Schiergens, et al. 2020. “SARS-CoV-2 Cell Entry Depends on ACE2 and TMPRSS2 and Is Blocked by a Clinically Proven Protease Inhibitor.” *Cell* 181 (2): 271–80.e8.

Hsieh, Ching-Lin, Jory A. Goldsmith, Jeffrey M. Schaub, Andrea M. DiVenere, Hung-Che Kuo, Kamyab Javanmardi, Kevin C. Le, et al. 2020. “Structure-Based Design of Prefusion-Stabilized SARS-CoV-2 Spikes.” *Science* 369 (6510): 1501-1505.

Huang, Yuan, Chan Yang, Xin-Feng Xu, Wei Xu, and Shu-Wen Liu. 2020. “Structural and Functional Properties of SARS-CoV-2 Spike Protein: Potential Antivirus Drug Development for COVID-19.” *Acta Pharmacologica Sinica* 41 (9): 1141–49.

Huo, Jiangdong, Audrey Le Bas, Reinis R. Ruza, Helen M. E. Duyvesteyn, Halina Mikolajek, Tomas Malinauskas, Tiong Kit Tan, et al. 2020. “Neutralizing Nanobodies Bind SARS-CoV-2 Spike RBD and Block Interaction with ACE2.” *Nature Structural & Molecular Biology* 27 (9): 846–54.

Jackson, Lisa A., Evan J. Anderson, Nadine G. Rouphael, Paul C. Roberts, Mamodikoe Makhene, Rhea N. Coler, Michele P. McCullough, et al. 2020. “An mRNA Vaccine against SARS-CoV-2 - Preliminary Report.” *The New England Journal of Medicine* 383 (20): 1920–31.

Keech, Cheryl, Gary Albert, Iksung Cho, Andreana Robertson, Patricia Reed, Susan Neal, Joyce S. Plested, et al. 2020. “Phase 1-2 Trial of a SARS-CoV-2 Recombinant Spike Protein Nanoparticle Vaccine.” *The New England Journal of Medicine* 383 (24): 2320–32.

Klinke, Sebastián, Vanesa Zylberman, Hernán R. Bonomi, Ilka Haase, Beatriz G. Guimarães, Bradford C. Braden, Adelbert Bacher, Markus Fischer, and Fernando A. Goldbaum. 2007. “Structural and Kinetic Properties of Lumazine Synthase Isoenzymes in the Order Rhizobiales.” *Journal of Molecular Biology* 373 (3): 664–80.

Krammer, Florian. 2020. “SARS-CoV-2 Vaccines in Development.” *Nature* 586 (7830): 516–27.

Kuhn, J. H., W. Li, H. Choe, and M. Farzan. 2004. “Angiotensin-Converting Enzyme 2: A Functional Receptor for SARS Coronavirus.” *Cellular and Molecular Life Sciences: CMLS* 61 (21): 2738–43.

Lan, Jun, Jiwan Ge, Jinfang Yu, Sisi Shan, Huan Zhou, Shilong Fan, Qi Zhang, et al. 2020. “Structure of the SARS-CoV-2 Spike Receptor-Binding Domain Bound to the ACE2 Receptor.” *Nature* 581 (7807): 215–20.

Letko, Michael, Andrea Marzi, and Vincent Munster. 2020. “Functional Assessment of Cell Entry and Receptor Usage for SARS-CoV-2 and Other Lineage B Betacoronaviruses.” *Nature Microbiology* 5 (4): 562–69.

Liu, Lihong, Pengfei Wang, Manoj S. Nair, Jian Yu, Micah Rapp, Qian Wang, Yang Luo, et al. 2020. “Potent Neutralizing Antibodies against Multiple Epitopes on SARS-CoV-2 Spike.” *Nature* 584 (7821): 450–56.

Mercado, Noe B., Roland Zahn, Frank Wegmann, Carolin Loos, Abishek Chandrashekar, Jingyou Yu, Jinyan Liu, et al. 2020. “Single-Shot Ad26 Vaccine Protects against SARS-CoV-2 in Rhesus Macaques.” *Nature* 586 (7830): 583–88.

Morens, David M., and Anthony S. Fauci. 2020. “Emerging Pandemic Diseases: How We Got to COVID-19.” *Cell* 182 (5): 1077–92.

Mulligan, Mark J., Kirsten E. Lyke, Nicholas Kitchin, Judith Absalon, Alejandra Gurtman, Stephen Lockhart, Kathleen Neuzil, et al. 2020. “Phase I/II Study of COVID-19 RNA Vaccine BNT162b1 in Adults.” *Nature* 586 (7830): 589–93.

Pallesen, Jesper, Nianshuang Wang, Kizzmekia S. Corbett, Daniel Wrapp, Robert N. Kirchdoerfer, Hannah L. Turner, Christopher A. Cottrell, et al. 2017. “Immunogenicity and Structures of a Rationally Designed Prefusion MERS-CoV Spike Antigen.” *Proceedings of the National Academy of Sciences of the United States of America* 114 (35): E7348–57.

Piccoli, Luca, Young-Jun Park, M. Alejandra Tortorici, Nadine Czudnochowski, Alexandra C. Walls, Martina Beltramello, Chiara Silacci-Fregni, et al. 2020. “Mapping Neutralizing and Immunodominant Sites on the SARS-CoV-2 Spike Receptor-Binding Domain by Structure-Guided High-Resolution Serology.” *Cell* 183 (4): 1024–42.e21.

Polack, Fernando P., Stephen J. Thomas, Nicholas Kitchin, Judith Absalon, Alejandra Gurtman, Stephen Lockhart, John L. Perez, et al. 2020. “Safety and Efficacy of the BNT162b2 mRNA Covid-19 Vaccine.” *The New England Journal of Medicine* 383 (27): 2603–15.

Robbiani, Davide F., Christian Gaebler, Frauke Muecksch, Julio C. C. Lorenzi, Zijun Wang, Alice Cho, Marianna Agudelo, et al. 2020. “Convergent Antibody Responses to SARS-CoV-2 in Convalescent Individuals.” *Nature* 584 (7821): 437–42.

Sahin, Ugur, Alexander Muik, Evelyna Derhovanessian, Isabel Vogler, Lena M. Kranz, Mathias Vormehr, Alina Baum, et al. 2020. “COVID-19 Vaccine BNT162b1 Elicits Human Antibody and T1 T Cell Responses.” *Nature* 586 (7830): 594–99.

Seydoux, Emilie, Leah J. Homad, Anna J. MacCamy, K. Rachael Parks, Nicholas K. Hurlburt, Madeleine F. Jennewein, Nicholas R. Akins, et al. 2020. “Characterization of Neutralizing Antibodies from a SARS-CoV-2 Infected Individual.” *bioRxiv : The Preprint Server for Biology*, May. https://doi.org/10.1101/2020.05.12.091298.

Starr, Tyler N., Allison J. Greaney, Sarah K. Hilton, Daniel Ellis, Katharine H. D. Crawford, Adam S. Dingens, Mary Jane Navarro, et al. 2020. “Deep Mutational Scanning of SARS-CoV-2 Receptor Binding Domain Reveals Constraints on Folding and ACE2 Binding.” *Cell* 182 (5): 1295–1310.e20.

Toelzer, Christine, Kapil Gupta, Sathish K. N. Yadav, Ufuk Borucu, Andrew D. Davidson, Maia Kavanagh Williamson, Deborah K. Shoemark, et al. 2020. “Free Fatty Acid Binding Pocket in the Locked Structure of SARS-CoV-2 Spike Protein.” *Science* 370 (6517): 725–30.

Tortorici, M. Alejandra, Martina Beltramello, Florian A. Lempp, Dora Pinto, Ha V. Dang, Laura E. Rosen, Matthew McCallum, et al. 2020. “Ultrapotent Human Antibodies Protect against SARS-CoV-2 Challenge via Multiple Mechanisms.” *Science* 370 (6519): 950–57.

Walls, Alexandra C., Brooke Fiala, Alexandra Schäfer, Samuel Wrenn, Minh N. Pham, Michael Murphy, Longping V. Tse, et al. 2020. “Elicitation of Potent Neutralizing Antibody Responses by Designed

Protein Nanoparticle Vaccines for SARS-CoV-2." *Cell* 183 (5): 1367–82.e17.
Walls, Alexandra C., Young-Jun Park, M. Alejandra Tortorici, Abigail Wall, Andrew T. McGuire, and David Veesler. 2020. "Structure, Function, and Antigenicity of the SARS-CoV-2 Spike Glycoprotein." *Cell* 181 (2): 281–92.e6.
Wang, Chunyan, Wentao Li, Dubravka Drabek, Nisreen M. A. Okba, Rien van Haperen, Albert D. M. E. Osterhaus, Frank J. M. van Kuppeveld, Bart L. Haagmans, Frank Grosveld, and Berend-Jan Bosch. 2020. "A Human Monoclonal Antibody Blocking SARS-CoV-2 Infection." *Nature Communications* 11 (1): 2251.
Wrapp, Daniel, Nianshuang Wang, Kizzmekia S. Corbett, Jory A. Goldsmith, Ching-Lin Hsieh, Olubukola Abiona, Barney S. Graham, and Jason S. McLellan. 2020. "Cryo-EM Structure of the 2019-nCoV Spike in the Prefusion Conformation." *Science* 367 (6483): 1260–63.
Wu, Yan, Feiran Wang, Chenguang Shen, Weiyu Peng, Delin Li, Cheng Zhao, Zhaohui Li, et al. 2020. "A Noncompeting Pair of Human Neutralizing Antibodies Block COVID-19 Virus Binding to Its Receptor ACE2." *Science* 368 (6496): 1274–78.
Yuan, Meng, Nicholas C. Wu, Xueyong Zhu, Chang-Chun D. Lee, Ray T. Y. So, Huibin Lv, Chris K. P. Mok, and Ian A. Wilson. 2020. "A Highly Conserved Cryptic Epitope in the Receptor Binding Domains of SARS-CoV-2 and SARS-CoV." *Science* 368 (6491): 630–33.
Zhou, Peng, Xing-Lou Yang, Xian-Guang Wang, Ben Hu, Lei Zhang, Wei Zhang, Hao-Rui Si, et al. 2020. "A Pneumonia Outbreak Associated with a New Coronavirus of Probable Bat Origin." *Nature* 579 (7798): 270–73.